Development of new buffer layers and rapid annealing process for efficient Sb Se thin-film solar cells

Yandi Luo

COLLEGE SCIENCES DE LA MATIERE
DOCTORAL DES MOLECULES
BRETAGNE ET MATERIAUX

Université de Rennes

THESE DE DOCTORAT DE

L'UNIVERSITE DE RENNES

ECOLE DOCTORALE N° 638
Sciences de la Matière, des Molécules et Matériaux
Spécialité : *Sciences des matériaux*

Par
Yandi LUO

Development of new buffer layers and rapid annealing process for efficient Sb_2Se_3 thin-film solar cells

Thèse présentée et soutenue sur le Campus de Beaulieu à Rennes le 11 Octobre 2024
Unité de recherche : UMR 6226 Institut des Sciences Chimiques de Rennes

Rapporteurs avant soutenance :

Raquel CABALLERO MESA	Tenured Scientist	CSIC Madrid
Stéphane JOBIC	Directeur de Recherche	CNRS-Nantes Université

Composition du Jury :

Président :	Judikael Le Rouzo	Professeur	Aix-Marseille Université
Examinateurs :	Raquel CABALLERO MESA	Tenured Scientist	CSIC Madrid
	Stéphane JOBIC	Directeur de Recherche	CNRS-Nantes Université
	Judikael Le Rouzo	Professeur	Aix-Marseille Université
Dir. de thèse :	Xianghua ZHANG	Directeur de Recherche	CNRS-Université de Rennes
Co-Dir. de thèse :	Guang-Xing LIANG	Professeur	University of Shenzhen
Co-encadrant:	Michel CATHELINAUD	Ingénieur de Recherche	CNRS-Université de Rennes
Invité(s) :			
	Zheng-Hua SU	Professeur	University of Shenzhen

ACKNOWLEDGEMENT

The research works presented here are accomplished in the College of Physics and Energy of Shenzhen University in China and the Equipe Verres et Céramiques of ISCR of Université de Rennes in France. Completing this PhD has been a challenging and rewarding journey, one that I could not have undertaken alone. I would like to express my deepest gratitude to those who have supported me and helped me throughout this process.

First and foremost, I would like to express my deepest gratitude to my doctoral supervisors, Prof. Xianghua Zhang and Prof. Guangxing Liang, for their invaluable guidance, patience, and support in experimental exploration and thesis writing. Prof. Zhang and Prof. Liang have a serious and rigorous scientific research attitude, pioneering and innovative scientific research thinking deeply inspired and educated me. Prof. Zhang's insightful feedback has been instrumental in shaping this thesis. When revising the thesis, Prof. Zhang helped me analyze the questions and guided me to think about the way and direction of answering the questions. Prof. Liang often taught me how to grasp the main points of an article during the discussion and gave me a lot of valuable advice, guidance, and help in experiment operation, data analysis, and paper writing. I am very grateful for the encouragement, support, patience, and meticulous guidance they gave me.

I would like to thank the judges for accepting the thesis. I would like to express my sincere gratitude to Prof. CALLABERO MESA Raquel and Prof. JOBIC Stéphane for accepting me as a reporter for my dissertation, and to Prof. LE ROUZO Judikael for participating in the defense of my doctoral degree. I would also like to thank Prof. Jean-Francois and Prof. Zhongkuan Luo for reviewing my CSI report every year. I would like to thank Dr. Michel Cathelinaud for helping me with experiment conducting, thesis

revision, and a lot of puzzles solved in the lab. I would like to thank Thierry Jouan and Antoine Gautier for their help in technical support and my experiment.

Besides, I want to thank Ms. Hongli Ma for her care and assistance both for my work and life during my stay in France. I still remember the moment I arrived in Rennes in 2023, Ms. Ma came to pick me up at the railway station, drove me to the apartment and helped me check in, made me feel as warm as family.

During my studies in China, I would like to give my thanks to Prof. Zhenghua Su, Prof. Shuo Chen, Prof. Juguang Hu, Prof. Rong Tang, Prof. Zhuanghao Zheng, and Ms. Jun Zhao at Shenzhen University for their help and support in the experiment. I would like to thank Xingye Chen, Tong Wu, Meng Wei, Guojie Chen, ZixuanYu, Mingdong Chen, Jinhong Lin, Ping LUO, and Yi Fu for their company, care, and assistance both in experiment and life, and for the wonderful time in Shenzhen University.

Moreover, I would like to thank my Chinese compatriots, Zheng Wang, Hongjiao Wang, Jiajie Zhang, Zeyu Ge, and Lilin Wu for their help and for bringing a lot of happiness in Rennes.

Last but not least, to my family, I owe a debt of gratitude for your unconditional love, support, and understanding, and for always being there for me.

This dissertation is a testament to the collective support and encouragement I have received from all these remarkable.

SOMMAIRE

RÉSUMÉ DÉTAILLÉ EN FRANÇAIS

1. Introduction

L'énergie solaire est une source d'énergie durable et renouvelable dérivée du rayonnement solaire, ce qui en fait l'une des ressources les plus abondantes et les plus respectueuses de l'environnement, capable de satisfaire au besoin énergie de l'humanité. Les cellules photovoltaïques (PV) convertissent directement la lumière en électricité grâce à l'effet photovoltaïque. Les cellules solaires en silicium cristallin restent une technologie dominante dans l'industrie PV avec un rendement de conversion d'énergie (PCE) de plus de 26%, offrant une solution éprouvée et fiable pour exploiter l'énergie solaire.

Le dispositif photovoltaïque à couches minces (TFPV) a été développé avec les avantages d'une faible consommation de matériaux et de la flexibilité et des progrès remarquables ont été réalisés au cours des dernières années. Les PCE certifiés de CdTe, $Cu(In,Ga)Se_2$ (CIGS), et les cellules solaires à couches minces de perovskites hybrides ont dépassé 22%. Cependant, l'utilisation de matières toxiques comme le cadmium (Cd) et le plomb (Pb), ainsi que la rareté de l'indium (In), du gallium (Ga) et du tellure (Te), limitent considérablement leur commercialisationà grande échelle avec une part de marché en constate diminution ces dernières années. Les chalcogénures inorganiques sont une autre classe de matériaux à l'étude les PV applications. La Kesterite $Cu_2ZnSn(S_x,Se_{1-x})_4$ a suscité un intérêt scientifique significatif en éliminant les éléments rares dans le CIGS. Ces cellules solaires à couche mince, nommées CZTSSe ont atteint un rendement de 14,9%, encore loin de celui du CIGS. Des progrès importants sont encore nécessaires avant une commercialisation réelle.

Ainsi, de nouveaux absorbeurs, avec des éléments abondants et non toxiques sont toujours l'objet de recherche. De ce point de vue, le sélénium d'antimoine (Sb_2Se_3), a été considéré comme un matériau prometteur pour des applications photovoltaïques. Sb_2Se_3 présente des caractéristiques photoélectriques remarquables, avec un band-gap approprié (1,1-1,3 eV), un coefficient d'absorption élevé ($> 10^5$ cm^{-1}), et une mobilité décente des porteurs de charge supérieure à 10 $cm^2/V{\cdot}s$. Il ne possède qu'une seule phase orthorhombique stable, ce qui permet d'obtenir facilement une couche mince de

Sb_2Se_3 sans phase secondaire. Les compositions élémentaires abondantes sur terre du Sb_2Se_3 ainsi que sa fabrication facile promettent une fabrication à faible coût. L'application du Sb_2Se_3 dans les dispositifs photovoltaïques comme absorbeur de lumière a été explorée par Nair et al. dans les années 2000, produisant un rendement de conversion plutôt faible de 0,66%. Les cellules solaires à base de Sb_2Se_3 en couche mince ont connu ensuite un développement rapide. En 2022, un PCE de 10,57 % a été obtenu grâce à une nouvelle technologie de dépôt chimique par bain de couches minces en solution. L'augmentation de l'efficacité du dispositif est largement attribuée à l'amélioration de la qualité de l'hétérojonction formée entre la couche absorbante et la couche tampon.

Dans ce travail, nous proposons de doper la couche tampon de CdS avec de l'aluminium et de développer un traitement thermique rapide pour la couche absorbante. L'objectif est d'optimiser l'alignement des bandes d'energie, d'améliorer le transport des porteurs de charge et de minimiser la perte par recombinaison due aux défaut à la surface et dans la majorité du Sb_2Se_3. En outre, nous avons essayé de développer une couche tampon à base de ZnSnO pour remplacer le CdS largement utilisé.

2. Cellules solaires à couche mince de Sb_2Se_3 utilisant une couche tampon CdS dopée Al^{3+}

Pour les cellules solaires à couche mince de Sb_2Se_3, la couche tampon la plus efficace reste le CdS.

Cependant, plusieurs études ont montré que le principal facteur contribuant à la dégradation du rendement des ces cellules solaires est la forte densité de défauts ($\approx 10^{11}$ cm^{-3}) présents à l'interface entre Sb_2Se_3 et CdS. En outre, le décalage de bande de conduction (CBO) insatisfaisant à l'hétérojonction Sb_2Se_3/CdS a été considéré comme un facteur majeur limitant les performances de ces cellules solaires. Plusieurs approches, telles que la modification de l'interface et le dopage, ont été utilisées pour améliorer la qualité de l'hétérojonction, afin d'améliorer le transport des porteurs de charge en minimisant la recombinaison due aux défauts.

Dans ce travail, la couche tampon CdS a été dopée par des ions Al^{3+} et l'effet de ce dopage sur différentes propriétés, en particulier l'alignement bandes d'énergie et le transport des porteurs de charge des cellules solaires Sb_2Se_3/CdS:Al a été particulièrement étudié.

2.1 Préparation de cellules solaires à couche mince de Sb_2Se_3

Pour la fabrication des cellules solaires Sb_2Se_3, un verre recouvert d'une couche de Mo comme contact arrière a été utilisé comme substrat. La fabrication des couches minces Sb_2Se_3 en sélénisant une couche métallique précurseur de Sb, obtenues par pulvérisation de magnétrons.

Une couche tampon de sulfure de cadmium (CdS) a ensuite été déposée sur la couche mince de Sb_2Se_3 en utilisant la technique de dépôt chimique en solution (chemical bath deposition, CBD). Une solution Al^{3+} à concentration différente (0,1, 0,3, 0,5 et 0,7 M) est ensuite déposée à la surface du CdS par spin-coating, avant un traitement thermique à différentes températures (260, 280, 300 et 320 °C) et pour différentes durées (1, 3, 5 et 7 min). Ce procédé est schématisé sur la Figure 1. La couche conductrice transparente en oxyde d'indium et d'étain (ITO) a ensuite été déposées par pulvérisation magnétron sur le CdS dopé. Les électrodes Ag ont été évaporées thermiquement sur la surface de l'ITO pour former un contact métallique. La surface des cellules solaires a été divisée en petits carrés avec une zone active identique. La configuration "substrat" de ces cellules est Mo/Sb_2Se_3/CdS:Al/ITO/Ag.

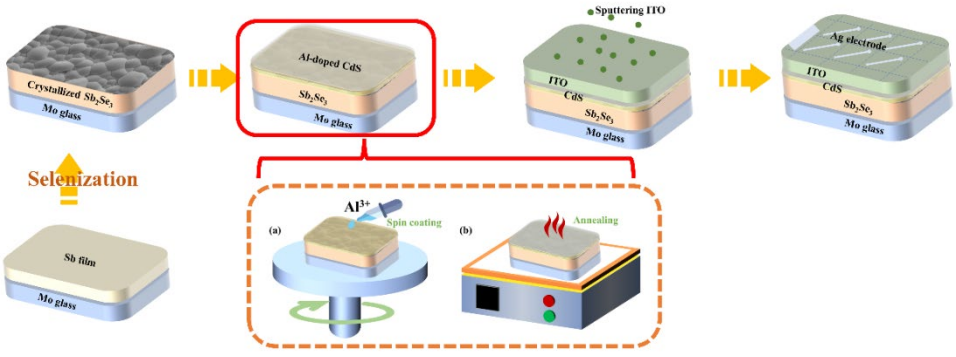

Figure 1 *L'illustration schématique du procédé de fabrication des cellules solaires Sb_2Se_3 à structure "substrat" avec la couche tampon CdS dopée aux Al^{3+}.*

2.2 Caractérisation de la couche d'absorbeur Sb_2Se_3

Les couches minces de Sb_2Se_3 ont été étudiées avec la diffraction aux rayons X et le résultat représentatif est montré sur la Figure 2a. Il est évident que les pics de diffraction correspondaient bien à Sb_2Se_3 orthorhombique (carte JCPDS N° 15-0861) sans aucune phase secondaire détectable. Il a été constaté que la couche a une orientation préférentielle [hk1].

La Figure 2b montre l'image électronique de la surface de la couche mince. Une surface bien cristallisée, compacte et uniforme est observée, sans défaut/porosité visible. La taille moyenne des grains était de ≈ 1,2 µm, assze grande pour limiter des pertes de recombinaison aux des joints de grain.

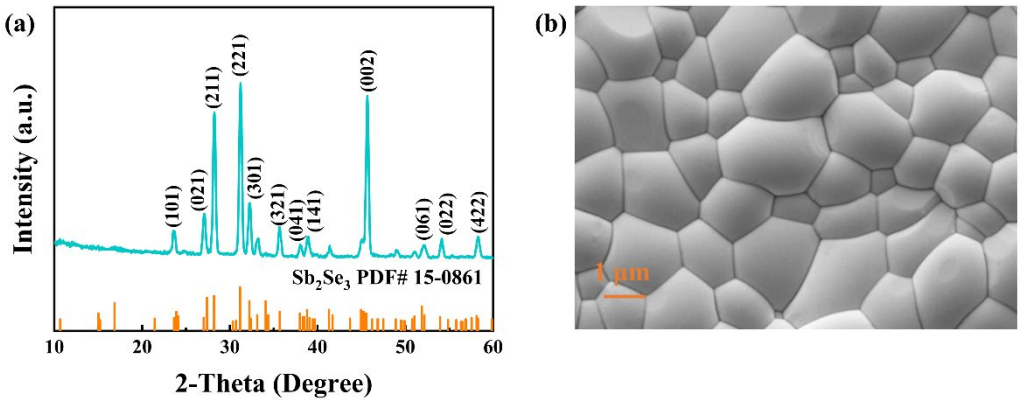

Figure 2 *(a) Spectre de XRD d'une couche Sb_2Se_3. (b) Image SEM de la surface de cette couche.*

Par conséquent, une couche de Sb_2Se_3 de haute qualité avec une orientation préférée, une cristallinité élevée, des grains de cristal assez grands et une surface compacte a été obtenue, ce qui pourrait être favorable pour l'amélioration des performances des cellules solaires.

2.3 Caractérisation des couches tampons CdS dopées Al

Les cellules solaires avec une couche de CdS dopé aux Al^{3+} avec diverses concentrations (0, 0,1, 0,3, 0,5 et 0,7 M) ont été dénommées, A0, A1, A2, A3 et A4 respectivement.

La caractérisation par spectroscopie photoélectronique à rayons x (XPS) a été effectuée pour étudier l'effet de dopage. L'échantillon avec du CdS sans dopage (A0) et un échantillon représentatif avec du CdS dopé (A3) ont été sélectionnés pour l'étude. Les pics principaux des éléments Cd et S ont été assignés à CdS. Un pic additionnel attribué à Al 2p a été observé dans l'échantillon A3 (Figure 3) avec une énergie de liaison de 74,5 eV, ce qui indique que les ions d'aluminium ont bien été incorporés dans la couche de CdS.

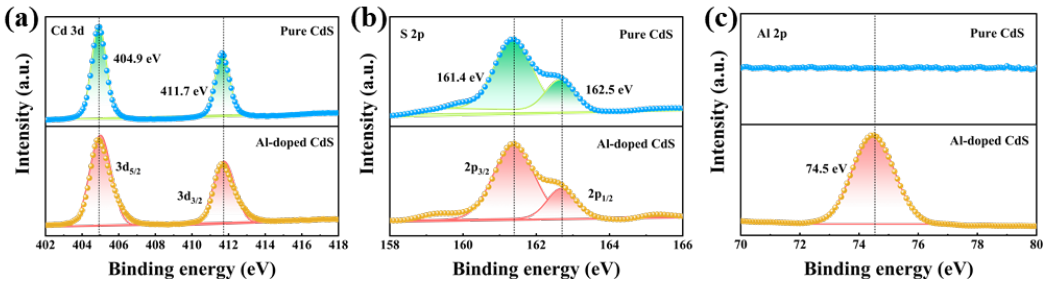

Figure 3 *Analyse XPS de Cd 3d (a), S 2p (b) et Al 2p (c) pour les CdS sans et avec le dopage à l'aluminium. (a) et (c) pour le CdS non dopé et (b) et (d) pour le CdS dopé.*

Pour examiner les propriétés électriques à la surface des échantillons, des mesures au microscope à force atomique équipée d'une sonde de Kelvin (KPFM) (Figure 4) ont été effectuées. Ce résultat indiquait une variation moins importante du niveau de Fermi et de bande d'énergie dans les échantillons de CdS doppés. Par conséquent, une différence de potentiel de contact V_{CPD} plus faible dans les échantillons de CdS doppés aux Al^{3+} est bénéfique pour l'extraction et la collecte des porteurs de charge, donc favorable à une amélioration du rendement des cellules solaires.

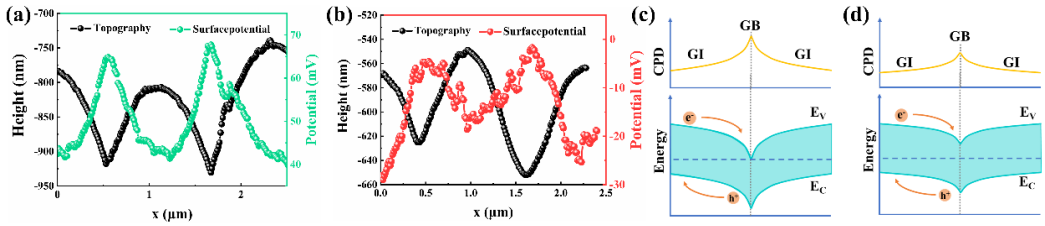

Figure 4 *Analyse KPFM des échantillons représentatifs de CdS sans dopage (A0) et de CdS dopés aux Al^{3+} (A3). (a), (b) topographie et profil potentiel de Surface. (c), (d) les diagrammes schématiques correspondant aux résultats KPFM.*

2.4 Caractérisation de hétérojonctions Sb_2Se_3/CdS:Al

Des mesures au microscope électronique en Transmission (TEM) ont été effectuées sur l'échantillon A3 pour l'étude de l'hétérojonction Sb_2Se_3/CdS:Al.

Les images HAADF-STEM (Figure 5b1) obtenues près de la région de l'interface Sb_2Se_3/CdS:Al (le rectangle jaune de la Figure 5a2), permettent de mesurer une distance inter-planaire de 0.329 nm, correspondant bien au plan (111) du CdS hexagonal.

La variation de l'intensité HAADF (Figure 5c1) montre clairement que les sites de Cd ont été parfois occupés par un autre cation qui possède un numéro atomique plus petit, à savoir les atomes Al provenant du dopage. Tous les éléments sont distribués de façon homogène dans l'absorbeur et la couche tampon, confirmant ainsi un dopage réussi des ions d'alumnium avec une interface lisse Sb_2Se_3/CdS:Al.

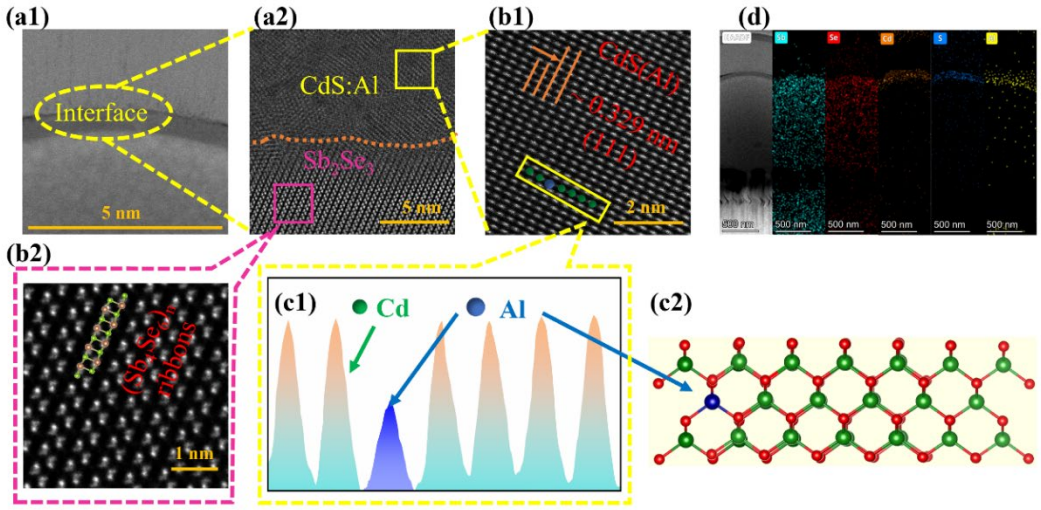

Figure 5 *Caractérisation TEM de la meilleure cellule solaire Sb_2Se_3/CdS:Al. (a1) image TEM transversale de l'hétérojonction Sb_2Se_3/CdS:Al. (a2) image HRTEM de l'hétérojonction. Imagehaute résolution de la couche tampon de CdS:Al, (b1) et de l'absorbeur Sb_2Se_3 (b2). (c1) les profils d'intensité des signaux HAADF. (c2) la configuration atomique du CdS:Al. (d) la cartographie des éléments à l'interface Sb_2Se_3/CdS:Al.*

2.5 Effets de la concentration de dopage Al sur les performances photovoltaïques

Les courbes de densité de courant−tension (*J*−*V*) des cellules solaires représentatives A1, A3 et A0 sous éclairement standard AM 1,5 G sont indiquées sur la Figure 6a. Les cellules A0 et A1 présentent un PCE de 6.82% et 7.01%, respectivement. En revanche, un PCE plus élevé de 8,41 % a été obtenu pour la cellule A3, avec une amélioration simultanée de FF à 60,9 % et de J_{SC} à 28,3 mA cm^{-2}.

La cellule A3 a montré une amélioration considérable du rendement quantique dans la région visible de 400 à 700 nm, par rapport à la cellule avec du CdS non dopé (Figure 6b). Cette amélioration est sans doute due à une meilleure absorption de la lumière ainsi qu'une diminution de la recombinaison des porteurs de charge à l'interface Sb_2Se_3/CdS:Al. Les valeurs J_{SC} intégrées pour les cellules A1, A3 et A0 étaient respectivement de 21,61, 25,33 et 21,10 mA cm^{-2}, en bon accord avec les mesures *J*−*V*.

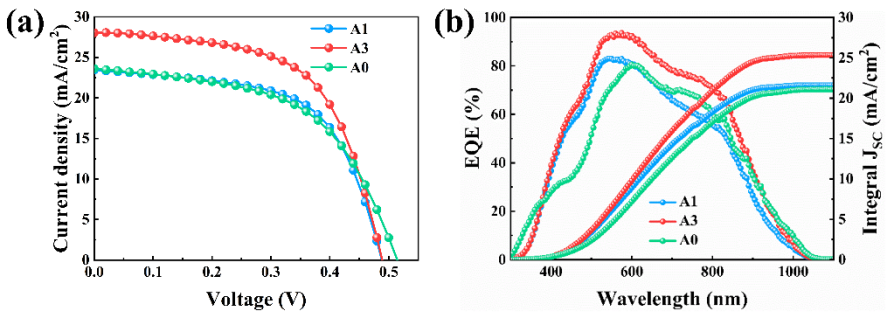

Figure 6 *(a) courbes densité de courant-tension (J−V) et (b) efficacité quantique externe (EQE).*

2.6 Alignement des bandes d'énergie des cellules solaires Sb_2Se_3/CdS:Al

Les diagrammes schématiques de l'alignement des bandes d'énergie pour les cellules solaires utilisant une couche tampon de CdS sans et avec dopage Al, sont représentés à la Figure 7. Le CdS pur présente un alignement de bandes du type "cliff-like" avec un offset des bandes de conduction (CBO) de −0,21 eV. Ceci atténue la courbure des bandes et abaisse les barrières pour les porteurs de charge se rapprochant de l'interface, augmentant ainsi la probabilité de recombinaison de charge par des défauts à l'interface. En revanche, la cellule avec du CdS dopé Al présente un alignement de bandes " spike-like" avec un CBO de 0,19 eV, ce qui empêche les porteurs de charge de s'accumuler à proximité de l'hétérojonction. La recombinaison peut donc être efficacement minimisée.

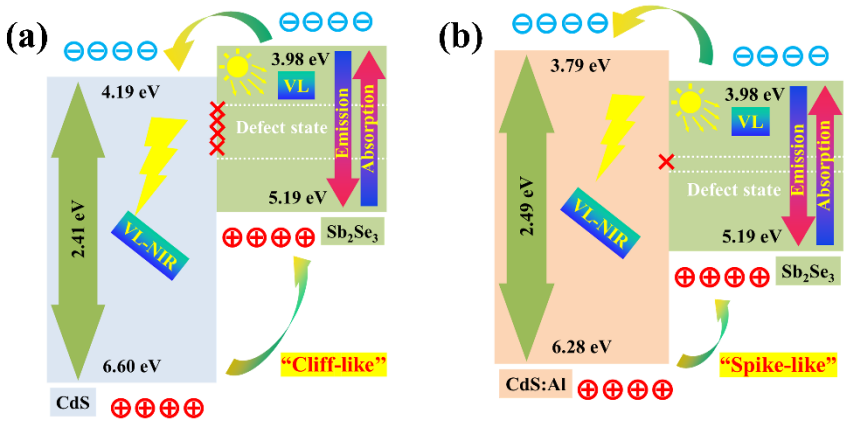

Figure 7 *Illustration schématique de l'alignement des bandes pour les cellules avec CdS (a) et CdS dopés Al^{3+}(b).*

2.7 Etude de défauts des cellules solaires Sb_2Se_3/CdS:Al

Les mesures capacitance-tension ($C-V$) et le profilage de capacitance (DLCP) ont été effectués pour étudier la densité de défauts d'interface des cellules solaires, qui peut être calculée comme la soustraction du N_{DLCP} du N_{CV}. Plus précisément, la valeur calculée pour la cellule A0 était de $4{,}90\times10^{16}$ cm^{-3}, et la valeur correspondante pour les cellules A1 et A3 a diminué pour atteindre $3{,}93\times10^{16}$ et $3{,}08\times10^{16}$ cm^{-3}, respectivement. Ces mesures confirment donc une densité de défauts d'interface plus faible et une perte de recombinaison réduite à l'interface Sb_2Se_3/CdS:Al de la cellule A3 (Figure 8a).

L'analyse par spectroscopie transitoire en profondeur (DLTS) montre qu'un défaut de piège à trous et un défaut de piège à électrons ont été trouvés dans les deux dispositifs, qui sont désignés respectivement par H1 et E1. Selon les résultats calculés du niveau d'énergie, les défauts de type E1 et H1 peuvent être attribués respectivement au défaut de vacance de Se (V_{Se}) et à l'antistite au sélénium (Se_{Sb}). On a notamment obtenu une diminution de la densité des défauts et de la section de capture pour le dispositif Sb_2Se_3 dopé Al^{3+} (A3), ce qui a permis d'améliorer les performances du dispositif (Figure 8b, c).

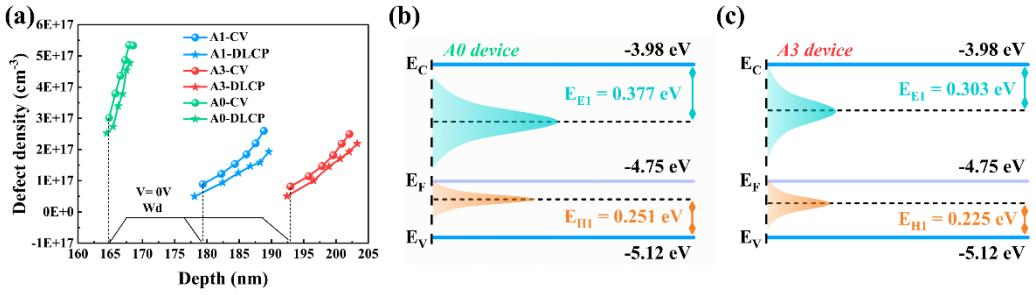

Figure 8 (a) *Profilage C-V et DLCP. (b), (c) niveaux d'énergie des défauts.*

En résumé, nous avons démontré une stratégie efficace de dopage des Al^{3+} dans la couche tampon CdS par une méthode simple de spin-coating associé à un post-traitement thermique. Les cellules PV à base de Sb_2Se_3 avec une configuration type "substrat" Mo/Sb_2Se_3/CdS:Al/ITO/Ag ont été mises au point. L'alignement des bandes

d'énergie de l'hétérojonction Sb_2Se_3/CdS:Al a été amélioré, donnant ainsi un rendement de 8,41% pour les cellules PV à base de Sb_2Se_3.

3. Recuit thermique rapide des cellules solaires PV à base de Sb_2Se_3

Ces dernières années, des progrès significatifs ont été reportés dans l'amélioration du rendement des cellules PV à base de Sb_2Se_3, avec un record actuel de 10,57%. Des défis persistent dans le contrôle de la croissance des cristaux, en particulier en ce qui concerne le mécanisme de nucléation pendant le processus de sélénisation du Sb_2Se_3. Ce processus joue un rôle souvent déterminant sur la qualité de la couche absorbeur. Nous avons ainsi décidé d'étudier systématiquement l'impact du procédé de sélénisation sur la qualité de la couche mince de Sb_2Se_3 en utilisant un traitement thermique rapide (RTP).

3.1 Préparation et caractérisation des couches minces Sb_2Se_3

Comme discuté auparavant, une couche mince de Sb métallique, déposée sur un substrat de verre de vitre recouvert d'une couche de Mo par pulvérisation magnétron, est utilisée comme précurseur. La couche de Sb_2Se_3 a été préparée par un procédé thermique rapide, illustré sur la Figure 9. La durée de pré-sélénisation varie de 60 s à 300 s à un intervalle de 60 s pour déterminer la meilleure durée.

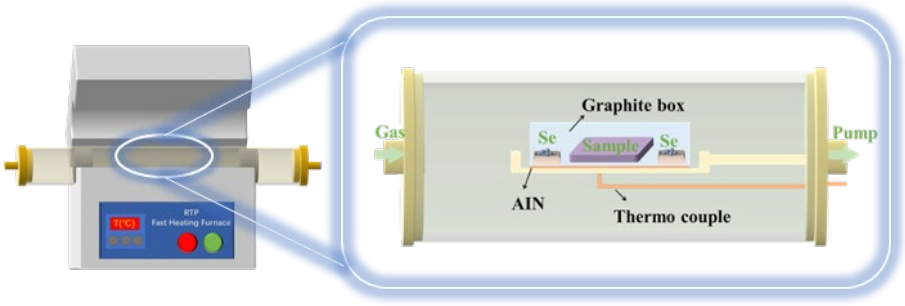

Figure 9 *Le procédé de préparation RTP des couches minces de Sb_2Se_3*

3.2 Influence du temps de pré-sélénisation sur la morphologie et la cristallinité des couches minces Sb_2Se_3

Pour plus de clarté, les échantillons Sb_2Se_3 préparés par RTP avec une durée de sélénisation de 60, 120, 180, 240 et 300 s ont été désignés R60, R120, R180, R240 et R300, respectivement.

La Figure 10 montre les résultats de XRD des couches minces qui ont subi une sélénisation pendant différentes durées (60, 120, 180, 240 et 300 s) à 410 °C. Il est évident que tous les pics de diffraction de l'échantillon R60 correspondent à Sb orthorhombique (JCPDS# 35-0732). Les pics appartenant à Sb peuvent encore être observables dans l'échantillon R120; Ensuite, l'échantillon R180 présente clairement les pics de diffraction (211) et (221) attribués à la phase orthorhombique de Sb_2Se_3. Pour l'échantillon R240, les pics sont en bon accord avec la phase orthorhombique de Sb_2Se_3 (JCPDS# 15-0861), indiquant une orientation préférentielle intéressante [hk1] et l'absence de toute phase secondaire détectable.

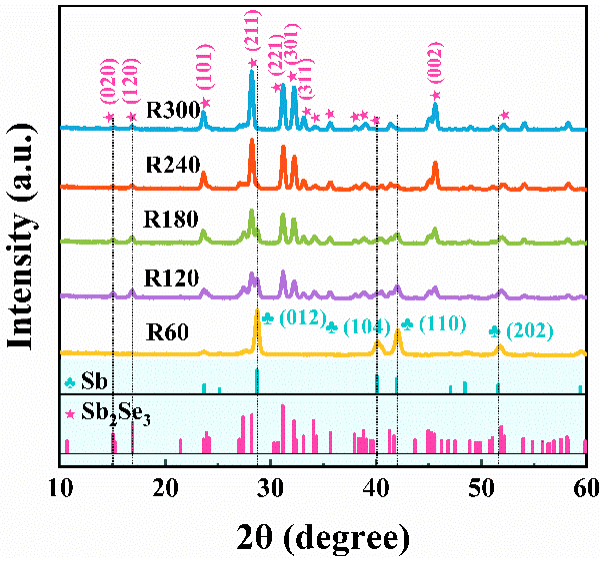

Figure 10 *Les XRD des couches Sb après une pré-sélénisation à 410°C pendant différentes durées*

Les images SEM de surface des interfaces des couches minces de Sb_2Se_3 avec différentes durées de sélénisation sont présentées à la Figure 11. La Figure 11a montre une surface avec de petits grains attribués au Sb métallique. Avec l'augmentation de la durée de sélénisation, les grains de Sb_2Se_3 apparaissent irrégulièrement à la surface et forment graduellement des grains plus grands. Avec une sélénisation au-delà de 240 s,

les couches minces de Sb_2Se_3 ont montré une excellente compacité et uniformité. Avec une pré-sélénisation prolongée, des porosités apparaissent à l'interface Sb_2Se_3/Mo.

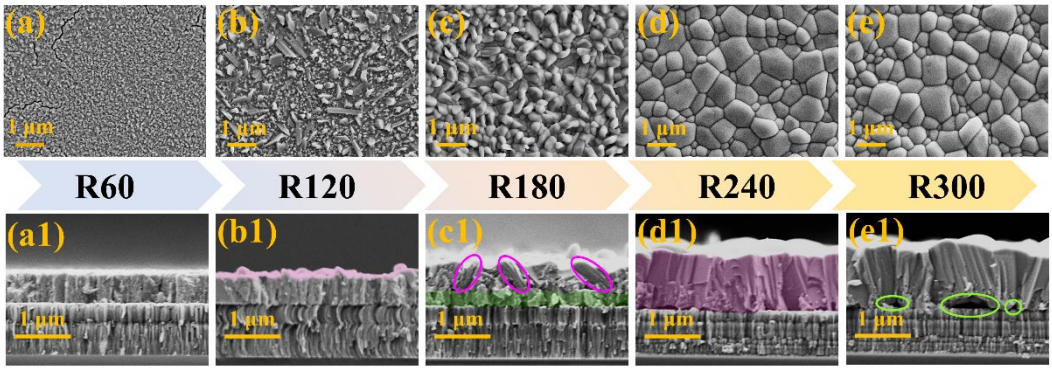

Figure 11 *Les images SEM de surface (a-e) et des interfaces (a1-e1) des couches minces Sb_2Se_3 avec une durée de pré-sélénisation de 60, 120, 180, 240 et 300 s à 410 °C.*

3.3 Performances photovoltaïques des cellules solaires à couche mince de Sb_2Se_3

Les couches minces R60, R120, R180, R240 et R300 ont ensuite été sélénisées à 390°C pendant 15 minutes. La fabrication du dispositif peut être vue dans "2.1 préparation des cellules solaires à couche mince Sb_2Se_3". Une configuration de substrat de Mo/ Sb_2Se_3/CdS:Al/ITO/Ag A été utilisée pour fabriquer les cellules PV. Les courbes *J-V* des cellules représentatives avec différentes conditions de préparation des couches d'absorbeurs de Sb_2Se_3 sont montrées à la Figure 12. La cellule utilisant l'absorbeur R240 présente une performance nettement supérieure avec une V_{OC} la plus élevée de 495 mV, un FF de 62,95 % et une J_{SC} également la plus élevée de 28,97 mA/cm^2, donnant ainsi le meilleur rendement de 9,03 % sous l'illumination solaire AM 1,5 G. Comme le montre le spectre de rendement quantique EQE (Figure 12b), la cellule R240 montre une photo-réponse considérablement améliorée dans le domaine spectral de 550 à 1000 nm, grâce à l'amélioration de la couche d'absorbeur.

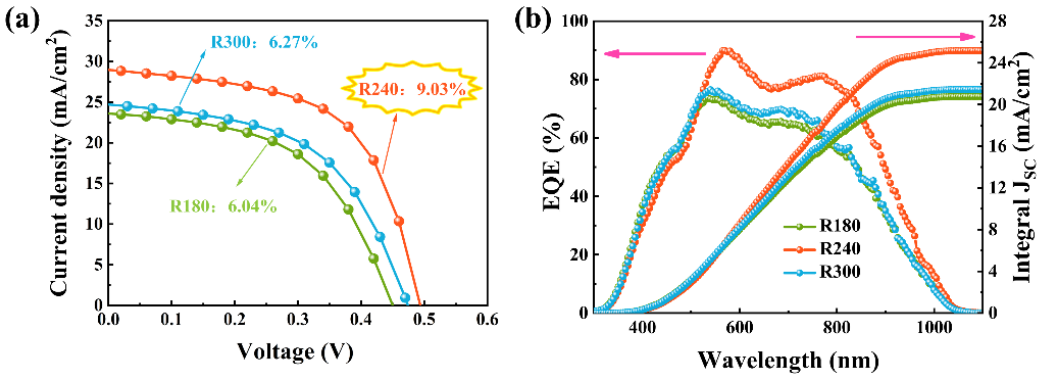

Figure 12 *(a) Courbes J-V. (b) Spectres de rendement quantique EQE.*

3.4 Analyse d'alignement de bandes d'énergie des cellules PV

La Figure 13 illustre le sommet de la bande de valence (VBM), le minimum de la bande de conduction (CBM) et le niveau de Fermi (E_F) calculés pour analyser l'alignement des bandes d'énergie. Les décalages VBM et CBM pour ces trois échantillons montrent un bon alignement avec la couche tampon, facilitant ainsi significativement le transport des porteurs de charge. L'échantillon R240 présente une valeur CBO (conduction band offset) la plus favorable. Un tel alignement de bandes «de type spike-like» empêche efficacement les porteurs de charge de recombiner avec les défauts à l'interface, ce qui est bien évidement favorable à l'amélioration de performances des cellules PV.

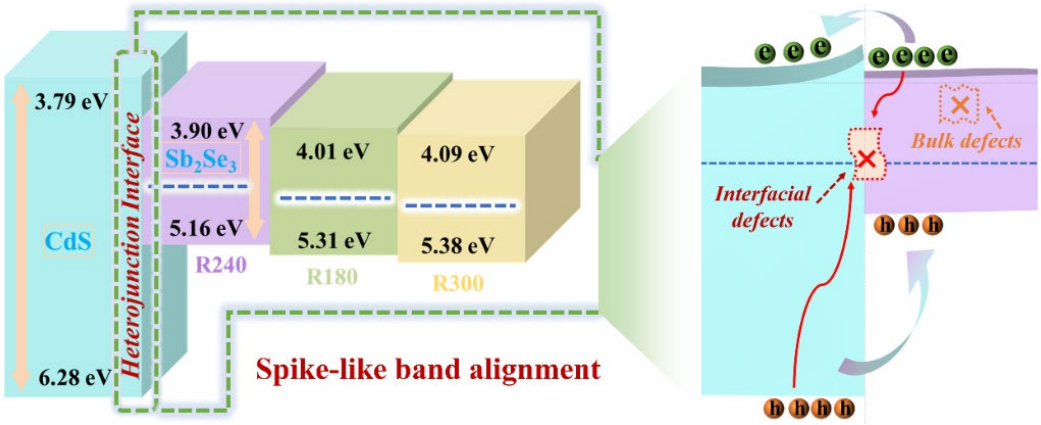

Figure 13 *Schéma de l'alignement des bandes pour les échantillons R180 (vert), R240 (violet) et R300 (jaune).*

3.5 Analyse des propriétés de défauts des cellules PV de Sb_2Se_3

Les techniques *C−V* et DLCP ont été utilisées pour caractériser les cellules PV, notamment en ce qui concerne la densité des défauts électroniques. Les résultats sont résumés sur la figure 14. La cellule R240 présente a montré une densité de défauts de $3{,}92\times10^{16}$ cm^{-3} à la jonction, significativement plus faible que les autres cellules. Ceci est certainement en relation avec la qualité de cet absorbeur en couche mince avec une très bonne compacité et des cristaux relativement gros.

La spectroscopie d'admittance a été utilisée pour évaluer la densité des défauts dans l'absorbeur et un seul type de défauts a été mis en évidence. En tenant compte du procédé de fabrication de Sb_2Se_3 par sélénisation du Sb, les défauts de V_{Se} et/ou de SbSe sont sans doute les plus probables. Notamment, la cellule R240 avec la couche d'absorbeur la plus performante possède une énergie d'activation des défauts la plus faible avec une densité de défauts plus faible, grâce à une qualité améliorée de la couche d'absorbeur (Figure 14b,c).

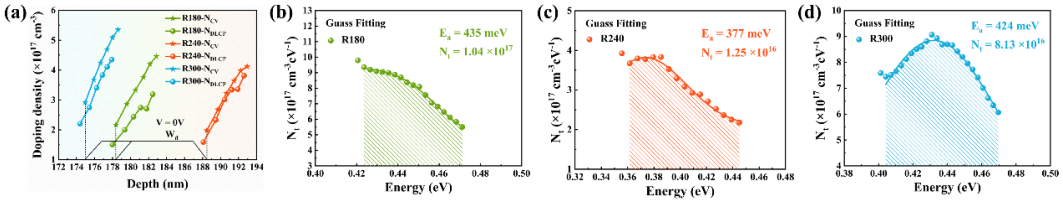

Figure 14 *(a) Résultats C−V et DLCP, (b)-(d) énergie d'activation des défauts et densités de défauts à partir des spectres d'admission.*

3.6 Analyse de la dynamique du transport des porteurs de charge

La spectroscopie d'absorption transitoire (TAS) a été utilisée pour évaluer la dynamique de transport des porteurs de charge photo-générés dans trois cellules PV représentatives. Une durée de vie très élevée de 7,5 ns a été mesurée dans la cellule R240 surement grâce à la qualité globale de cet absorbeur, discutée auparavant. Ce niveau de durée de vie est comparable à celles mesurées dans les meilleures cellules solaires en couche mince de Sb_2Se_3. Une longue durée de vie des porteurs de charge photo-générés contribue à l'amélioration du J_{SC} dans les cellules PV.

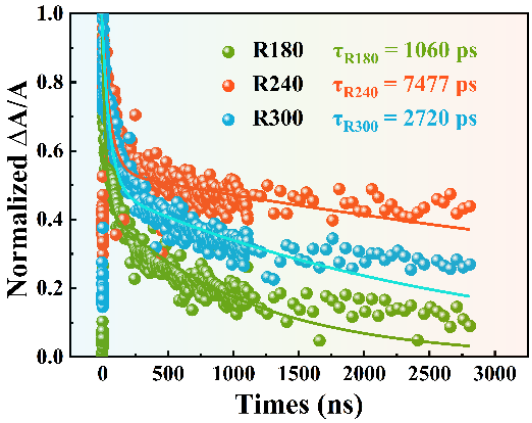

Figure 15 *Déclin de l'absorption photoinduite à 720 nm pour l'échantillon R180, l'échantillon R240 et l'échantillon R300.*

4. Cellules solaires à couche mince de Sb_2Se_3 avec couche tampon de ZnSnO

À ce jour, une couche mince de CdS déposée par bain chimique est couramment utilisée comme couche de transport d'électrons (ETL) dans les cellules solaires Sb_2Se_3. Ceci pose un problème très sérieux pour des applications futures en raison de la toxicité du Cd. En plus de sa nature toxique, le band gap relativement faible (2,4 eV) de CdS provoque également une perte de lumière dans les courtes longueurs d'onde. Par conséquent, il est crucial de remplacer les CdS par un ETL non toxique et avec un band gap plus large. Dans ce travail, nous avons proposé des couches de ZnSnO (ZTO) déposées par co-pulvérisation magnétron pour remplacer le CdS en formant des jonctions ZTO/Sb_2Se_3. L'effet du ratio Zn/Sn dans la couche ZTO sur les performances des cellules solaires type substrat (verre/Mo/Sb_2Se_3/ZTO/ITO/Ag) et le mécanisme de transfert de charges ont été étudiés systématiquement.

4.1 Préparation de l'hétérojonction Sb_2Se_3/ZTO

La pulvérisation par magnétron a été utilisée pour la fabrication de couches minces de précurseurs métalliques Sb. Par la suite, le précurseur métallique Sb a été soumis à une sélénisation pour produire une couche mince de Sb_2Se_3.

Pour le dépôt de $Zn_{1-x}Sn_xO$ ETL, des cibles de ZnO et SnO_2 ont été utilisées dans la co-pulvérisation. Le procédé est schématisé sur la Figure 16. La composition des

couches de ZTO a été contrôlée en variant les puissances appliquées aux cibles ZnO et SnO_2 pendant la co-pulvérisation. Le tableau 1 montre les compositions de ZTO étudiées dans ce travail.

La fabrication des cellules solaires peut être vue dans Chapitre "2.2 préparation des cellules solaires à couche mince Sb_2Se_3".

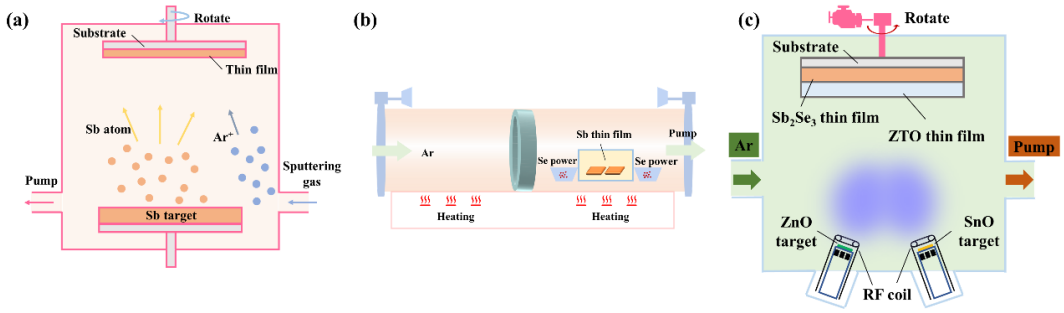

Figure 16 *Illustration schématique du procédé de fabrication de (a) dépôt de Sb, (b) couche mince de Sb_2Se_3 par post-sélénisation, (c) couche tampon ZTO déposée par co-pulvérisation.*

Table 1 *Paramètres de co-pulvérisation et bandgap optique des ZTO.*

Sample	Sn/(Zn+Sn)	E_g (eV)	Power ratio ZnO:SnO_2
ZnO	0	3.209	–
ZTO 1	0.29	3.166	8 : 2
ZTO 2	0.38	3.418	6 : 4
ZTO 3	0.43	3.754	1 : 1
ZTO 4	0.56	3.642	4 : 6
SnO_2	1	3.247	–

4.2 Analyse de band gap optique des couches minces de ZTO

La Figure 17a montre la transmission des couches $Zn_{1-x}Sn_xO$ avec différents rapports Sn/(Zn+Sn). Le band gap optique est obtenu par l'extrapolation de l'absorption. Le plus grand bandgap a été obtenu avec un rapport Sn/(Zn+Sn) de 0,43.

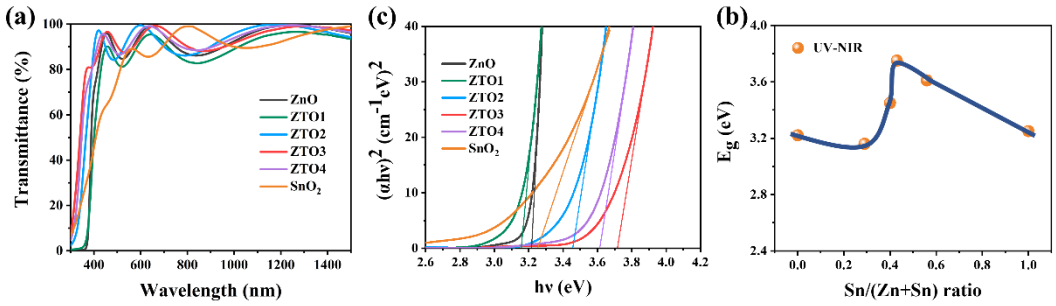

Figure 17 *(a) Transmission des couches $Zn_{1-x}Sn_xO$. (b) Tracé Tauc de $(\alpha hv)^2$ versus hv. (c) Band gap en fonction du rapport de Sn/(Zn+Sn).*

4.3 Analyse de la structure des bandes d'énergie de l'hétérojonction Sb_2Se_3/ZTO

Sur la Figure 18, on peut observer que le décalage de la bande de conduction (CBO) pour les cellules PV ZTO2 et ZTO3 a été mesuré respectivement à 0,27 eV et 0,18 eV. Ceci indique une courbure de bande type "spike-like" à l'interface, qui n'empêche pas le transport d'électrons, favorable pour obtenir un dispositif efficace. L'hétérojonction Sb_2Se_3/ZTO3 montre le meilleur alignement des bandes.

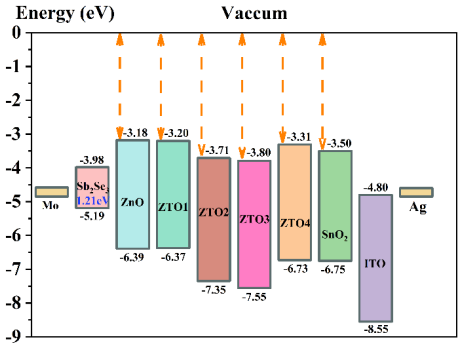

Figure 18 *Alignement des bandes d'énergie des cellules PV Sb_2Se_3/ZTO.*

4.4 Performances des cellules solaires Sb_2Se_3/ZTO

La cellule ZTO2 présente un J_{SC} de 20,26 $mAcm^{-2}$, un V_{OC} de 354 mV et un FF de 37,06 %, ce qui donne un PCE de 2,50 %. La cellule ZTO3 possède un PCE de 3,44% avec une amélioration évidente de Voc à 364 mV, de J_{SC} à 23,23 $mAcm^{-2}$, et de FF à 40,63% .

L'analyse du rendement quantique EQE des cellules ZTO2 et ZTO3 montre des réponses semblables dans le domaine spectral de 300 à 1100 nm. Les cellules solaires

à ZTO possèdent un rendement quantique amélioré, par rapport aux cellules avec une couche tampon de CdS, en dessous de 520 nm. Ceci peut être expliqué par un bandgap plus large des ZTO, ce qui permet de mieux utiliser les photos de courtes longueurs d'onde.

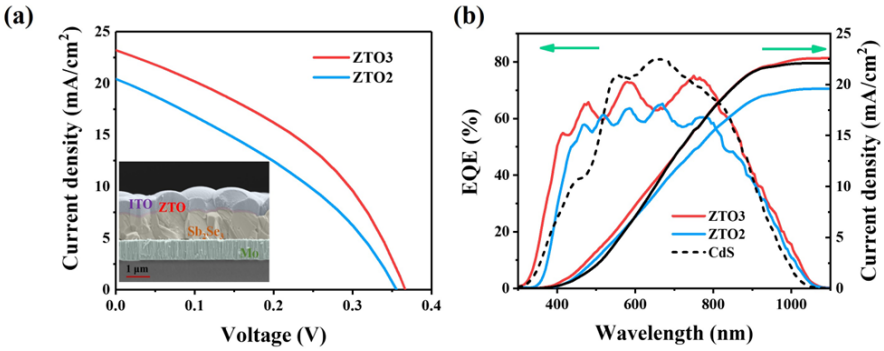

Figure 19 *(a) Courbes J-V. (b) Spectres EQE.*

4.5 Analyse des défauts dans les cellules solaires Sb_2Se_3/ZTO

Une grande différence est visible entre les courbes N_{CV} et N_{DLCP} pour la cellule ZTO2 par rapport au ZTO3. Ces résultats montrent qu'une couche de ZTO optimisée est très importante pour minimiser les défauts à l'interface Sb_2Se_3/ZTO.

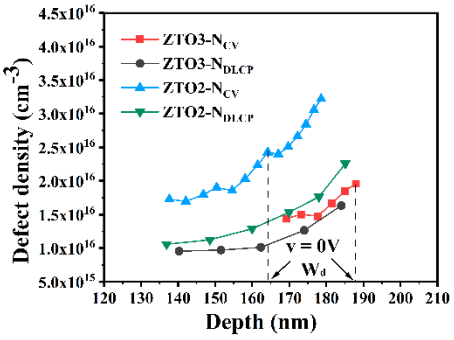

Figure 20 *Densité des défauts dans les cellules PV ZTO2 et ZTO3.*

En résumé, des cellules solaires à base de Sb_2Se_3 avec la configuration Glass/Mo/Sb_2Se_3/ZTO/ITO/Ag ont d'abord été développés. Il a été démontré que la composition de ZTO est très importante pour le rendement des cellules PV. Avec la couche tampon optimisée de $Zn_{0.57}Sn_{0.43}O$, un rendement intéressant de 3,44% a été obtenu.

5. Conclusions

Sb_2Se_3 est un nouveau matériau absorbeur, possédant des propriétés globales très intéressantes pour applications photovoltaïques en couches minces. Cette thèse porte sur des cellules solaires à couche mince de Sb_2Se_3 préparées avec un procédé de sélénisation des précurseurs métalliques de Sb. Ce travail est particulièrement centré sur l'optimisation la couche tampon et l' absorbeur. Pour minimiser le défaut à l'interface de la jonction et dans l'absorbeur en Sb_2Se_3, l'accent a été mis sur le développement d'un procédé de recuit thermique rapide afin d'améliorer la qualité de la couche de Sb_2Se_3. Le dopage de la couche tampon en CdS a été également étudié dans le but d'améliorer l'alignement des bandes d'énergie. Tous ces efforts ont permis d'obtenir des cellules solaires avec un rendement de 9.03%, proche de l'état de l'art avec d'autres procédés.

En outre, des cellules solaires à base de Sb_2Se_3 avec une couche tampon de ZnSnO, donc sans l'élément toxique Cd, ont été développés dans ce travail. Un rendement, encore modeste mais très encourageant, de 3,44 % a été obtenu, montrant une possibilité d'éliminer le cadmium, présent dans les meilleures cellules solaires à base de Sb_2Se_3.

GENERAL INTRODUCTION

With the continuous development of our society, energy crisis and environmental pollution are among the biggest challenges to global sustainability and well-being. There is an urgent need for finding sustainable and renewable alternative energy resources. As one of the most interesting environmentally friendly energy sources, solar energy is abundant and renewable, making it a promising solution to address both the energy crisis and environmental pollution.

Photovoltaic (PV) solar cells directly convert sunlight into electricity using solar panels made of semiconductor materials based on the photovoltaic effect. The crystalline silicon solar cells remain a dominant technology in the solar industry with a power conversion efficiency (PCE) of more than 26%, offering a proven and reliable solution for harvesting solar energy. The thin-film photovoltaic (TFPV) device with the advantages of low material consumption and flexibility has been intensively studied. The certified PCE of CdTe, Cu(In,Ga)Se_2 (CIGS), and perovskites thin-film solar cells have exceeded 22%. However, the toxicity of cadmium (Cd) and plumbum (Pb), the scarcity of indium (In), gallium (Ga), and tellurium (Te) are the important issues limiting their further large-scale development. To solve these problems, some alternative eco-friendly, intrinsically stable, and cost-effective absorber thin film materials have attracted considerable interest over the past several decades.

Among various photoactive materials, antimony selenide (Sb_2Se_3) has emerged as an alternative and promising candidate for the next-generation thin-film solar cells due to its superior stability, low toxicity, high element abundance, and attractive optical and electronic properties. It possesses a suitable band gap, and high absorption coefficient. Additionally, it has only one stable phase with a one-dimensional (1D) crystal orthorhombic structure, which avoids the issues of complicated preparation and secondary phase. A Shockley−Queisser (SQ) theory determined PCE exceeding 30% exhibits great potential in the application of TFPV devices. With the efforts of

researchers, the efficiency of Sb_2Se_3 solar cells has increased from <3% to an encouraging 10.57% over the past decade. However, this efficiency is still considerably lower than the theoretical limits (PCE = 30%). The issues of heterojunction interface quality, complex defects in Sb_2Se_3 material, and the Cd-based buffer layer are still the key scientific problems limiting the further development of Sb_2Se_3 thin-film solar cells. This thesis is on the performance improvement of Sb_2Se_3 thin-film solar cells. The scientific approach is the following. Firstly, the energy band alignment will be improved to overcome the challenge of interface recombination of photogenerated charge carriers. The crystal growth process of the absorber layer will be carefully optimized in order to facilitate the separation and the transport of the charge carriers. Finally, preliminary research will also be conducted on replacing the widely used CdS buffer layer to develop Cd-free Sb_2Se_3 thin-film solar cells.

This thesis is divided into four chapters. The first chapter provides an overview of the photovoltaic materials and solar cells, with the focus on the materials of Sb_2Se_3 and its applications in photovoltaics. After that, Chapter 2 is dedicated to the heterojunction interface engineering by doping the CdS buffer layer with Al^{3+}. In Chapter 3, an efficient absorber growth process by rapid thermal processing is studied and the crystal growth mechanism of Sb_2Se_3 will be discussed. The last chapter focuses on the preparation of Cd-free Sb_2Se_3 thin-film solar cells with an alternative buffer layer of ZnSnO film.

Chapter I: Photovoltaic materials and solar cells

1.1 Introduction

Energy shortage and environmental pollution have emerged as two major issues in social development. Fossil fuels, such as coal, natural gas, and oil are non-renewable resources and release greenhouse gases like carbon dioxide during their utilization, leading to adverse effects on the environment. [1-3] As the foundation for human survival and progress, energy has also become a significant indicator of societal advancement and a crucial driver for facilitating sustainable development. Countries worldwide are placing increasing emphasis on renewable energy sources.[4-6] However, renewable energy sources such as wind, hydroelectricity, tidal power, biomass, and geothermal energy can only serve as supplementary sources to the primary energy supply due to their uneven distribution, limited stability, and low reserves. This situation compels us to seek cost-effective, reliable, and secure renewable energy resources. Solar energy stands out among various renewable energy sources for its earth-abundant storage, low cost, and wide distribution. Additionally, utilizing solar energy not only avoids pollution but also has negligible negative impact on the ecosystem. Furthermore, it does not disrupt the Earth's thermal equilibrium, making it a highly promising option for future energy utilization.[7] The global annual energy consumption is around 600-700 exajoules (EJ), while the total solar radiation received by the Earth each year is about 5.5 million EJ. The annual global energy consumption by humans is equivalent to the solar energy received by Earth's surface in just 40 minutes.[1, 8, 9] If solar energy can be utilized more efficiently, it will contribute to addressing the global demand for energy and environmental issues.

Photovoltaic technologies are a crucial method for harnessing solar energy and have garnered increasing global attention. Solar cells, developed based on the photovoltaic effect, represent a mature technological solution for efficiently capturing solar energy. According to the principle of Detailed Balance Limit, the theoretical maximum power conversion efficiency (PCE) of single-junction solar cells can be determined to be 33.7%, while that of tandem multijunction solar cells exceeds 45%.[10-12] According to

International Energy Agency (IEA) data, there has been a significant increase in global solar PV capacity additions in the past five years (Figure 1.1). In 2023, the global solar PV capacity additions reached over 420 GW, making an impressive 85% increase from 228 GW in 2022 (Figure 1.2). This remarkable growth broke a new record and surpassed any other renewable energy technology. Hence, it appears that there is plenty more growth ahead for solar cells.

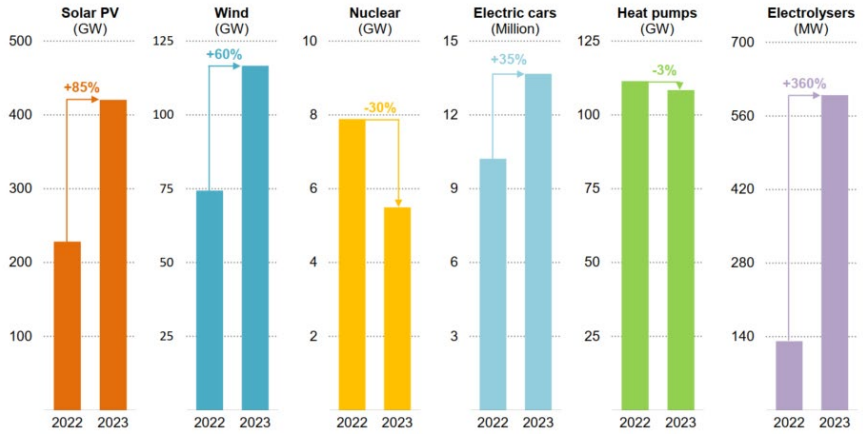

Figure 1.1 *Annual development of selected clean energy technologies, 2022 and 2023. "Annual development" refers to sales and capacity additions. GW=gigawatt, MW=megawatt, Mn=million.*[13]

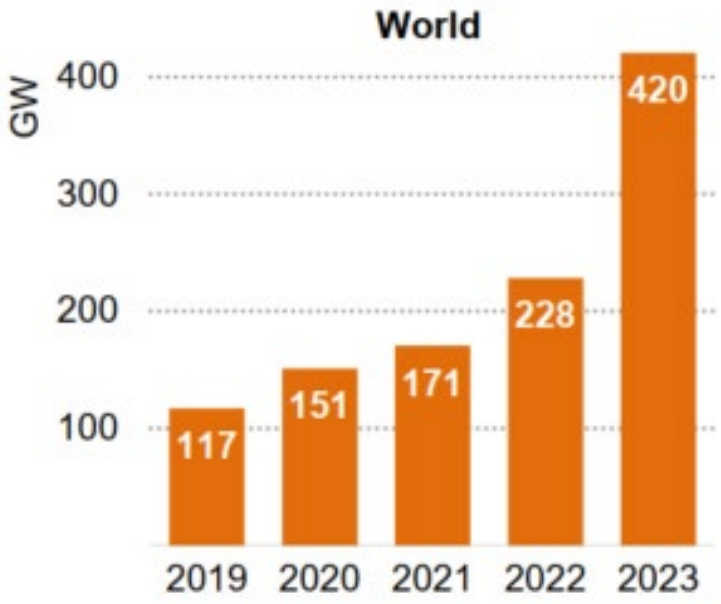

Figure 1.2 *Global solar PV capacity additions from 2019 to 2023.*[13]

1.2 Photovoltaic solar cells

1.2.1 Development of solar cells

Solar cell technology has been the subject of extensive research and innovation for several decades. The latest advancements in solar cell efficiency have been continuously documented by the US National Renewable Energy Lab (NREL), as depicted in Figure 1.3. The origins of solar cell technology can be traced back to the 19th century when Alexandre-Edmond Becquerel discovered the photovoltaic effect in 1839.[14] In 1905, Einstein provided a theoretical explanation for the photovoltaic effect.[15] In 1883, Charles Fritts constructed the first solar cells using selenium wafers on a thin layer of gold, delivering a PCE of less than 1%.[16]

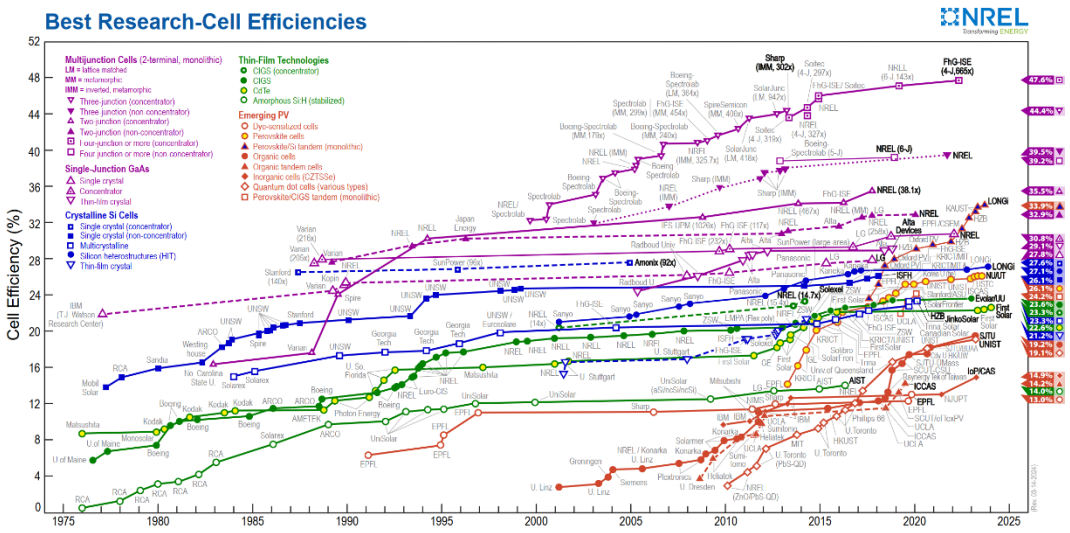

Figure 1.3 *Solar cell development and the record efficiencies in lab by NREL.*[16]

In the 1950s, researchers at Bell Labs developed the first silicon solar cell with a significantly improved efficiency of about 6%, making it the beginning of modern solar cell technology.[17] Over the years, researchers have focused on enhancing the efficiency of solar cells through materials optimization, structural improvements, and fabrication techniques, leading to the development of various types of solar cells. Based

on their development process, solar cells are divided into three categories: silicon-based solar cells, thin-film solar cells, and emerging solar cells.

(1) Silicon-based solar cells represent the most mature technology with the widest application in the solar cell market.[18] This is due to their outstanding long-term stability and well-established manufacturing process. Professor Gao's team has published an article in the journal Nature Energy, reporting a crystalline silicon heterojunction solar cell with a conversion efficiency of 26.81%, which currently represents the highest efficiency for silicon-based photovoltaics in the world.[19]

(2) Thin-film solar cells were developed owing to their advantages of low material consumption and flexibility. The primary light-absorbing materials include amorphous silicon (a-Si), cadmium telluride (CdTe), gallium arsenide (GaAs), and copper indium gallium selenide (CIGS).[20-24]

The inability of these solar cells to accommodate the growing energy demand in the future is due to the high cost associated with their production and the imperative to prioritize environmental protection. As a result, researchers are currently focusing on developing new types of solar cells.

(3) The emerging solar cells represented by inorganic compound thin-film solar cells, quantum dot solar cells, dye-sensitized solar cells, organic solar cells, and perovskite solar cells, have been extensively studied and significant progress has been achieved. Among them, inorganic compound thin-film solar cells are particularly promising due to their low material consumption, long-term stability, and flexibility.

1.2.2 The working principle of solar cells

Solar cells also referred to as photovoltaic cells in the field of physics or PV cells, are remarkable devices that serve as a prime example of the direct conversion of light energy into electrical energy. Essentially, a solar cell functions as a p-n junction diode and can instantaneously output voltage and generate current within specific illumination conditions, based on the photoelectric effect.

The structure of solar cells typically comprises multiple layers designed to efficiently convert sunlight into electrical energy. A standard solar cell structure typically includes a substrate, p-n junction, positive and negative electrodes, as shown in Figure 1.4. The substrate serves as the base upon which subsequent layers are deposited. Common substrate materials include glass, silicon, or plastic. The p-n junction is the essential component of solar cells, consisting of p-type semiconductors and n-type semiconductors. The negative and positive electrodes of the solar cell are connected to an n-type semiconductor and a p-type semiconductor, respectively, to collect current.

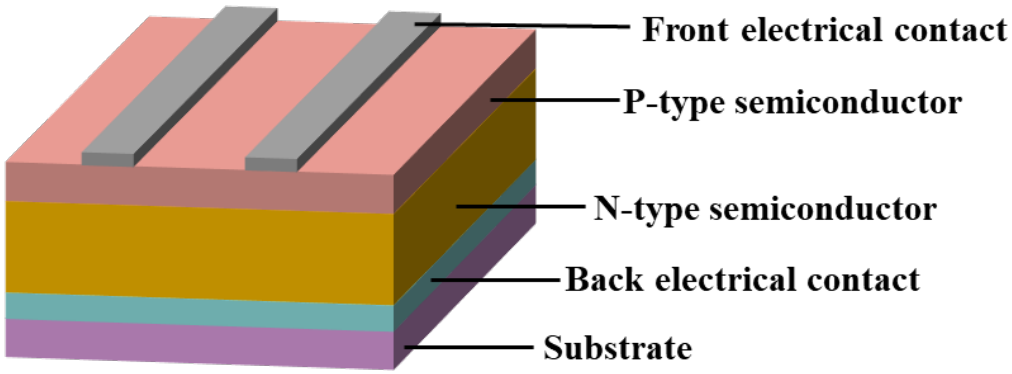

Figure 1.4 *Schematic configuration of a typical solar cell.*

The working principle of solar cells is based on the photovoltaic effect of semiconductor p-n junction, which generates electromotive force and current caused by the change in charge distribution within an illuminated object. In the case of typical solar cells, when sunlight illuminates the p-n junction, light photons can easily enter the junction via the p-type layer (Figure 1.5). A large number of electron-hole pairs are generated in the absorber owing to the sufficient energy supplied by the absorbed photons. The incident light disrupts the thermal equilibrium of the p-n junction, causing photoelectrons to flow into the n-type region driven by the built-in electric field, while holes in the depletion region rapidly migrate to the p-type side. Once a new equilibrium is established in the depletion region, a photogenerated electric field forms opposite to the built-in electric field, resulting in a photogenerated voltage across both sides of the

p-n junction. When an external circuit with a small load is connected at the ends of n-type and p-type regions, it will generate a current in a closed loop.

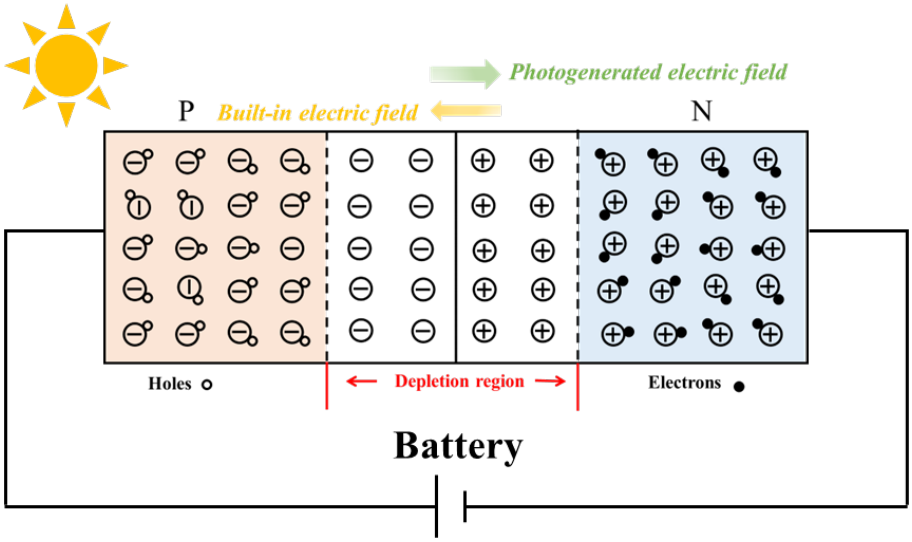

Figure 1.5 *Schematic diagram of the photovoltaic effect of p-n junction for solar cells.*

1.2.3 The key parameters of solar cells

(1) Current–voltage (*I*–*V*) characteristics of solar cells

An equivalent circuit model is a theoretical circuit diagram that represents the electrical behavior of a solar cell under varying conditions, providing valuable insights into its characteristics, and is widely utilized for analysis and simulation. An ideal solar cell may be modeled by a current source in parallel with a diode. The diode represents the junction formed within the solar cell, which allows the flow of current in one direction. Therefore, the most commonly used equivalent circuit model for a solar cell is the single-diode model. Figure 1.6a illustrates the ideal equivalent circuit model of a solar cell. I_L represents the photogenerated current, which is the current generated by the solar cell due to the incident light. I_D represents the diode current, which is influenced by the external load. I denote the output current. Therefore, based on the equivalent circuit model, the current density–voltage characteristics can be expressed by the following equation:

$$J = J_D - J_L = J_0\left[exp\left(\frac{qV}{k_BT}\right) - 1\right] - J_L \quad (1\text{-}1)$$

where q is the elementary charge, k_B represents the Boltzmann constant, and T denotes the Kelvin temperature. Similarly, J_D is the diode current density, J_L is the photogenerated current and J_0 is the diode reverse saturation current density.

However, it is necessary to consider the series resistance caused by carrier transport across the entire solar cells. Additionally, various detrimental defects from the material itself and the environment of the solar cells can lead to undesired current leakage impacting the current density–voltage characteristics. Therefore, the practical equivalent circuit model of a solar cell can be represented as shown in Figure 1.6b. This equivalent circuit model typically consists of several components that model the electrical characteristics of a solar cell, as summarized in the following equation:

$$J = J_0\left[exp\left(\frac{q(V-R_SJA_S)}{AK_BT}\right) - 1\right] + \frac{(V-R_SJA_S)}{R_{sh}A_S} - J_L \quad (1\text{-}2)$$

where A_s is the active surface area and A is the ideality factor (A>1). R_s is series resistance, which signifies the resistance encountered by the current as it flows through the semiconductor material of the solar cell and the electrodes. R_{sh} stands for parallel resistance, indicating the shunting effect or leakage current in the solar cell. Generally, J_L is dependent on the light intensity received by the solar cell.

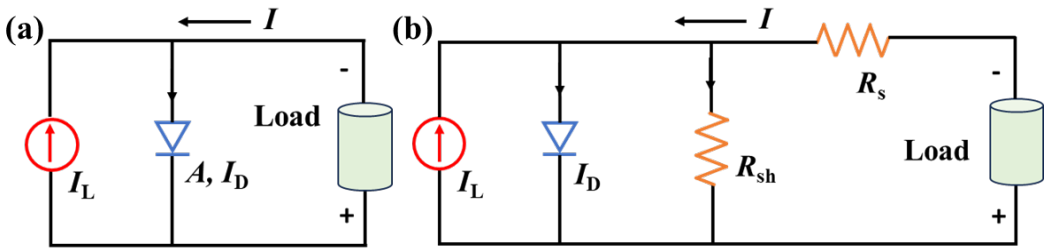

Figure 1.6 *The ideal (a) and practical (b) equivalent circuit model of a solar cell.*

(2) Performance parameters of solar cells

The performance of a photovoltaic solar cell depends on the lighting conditions and the standard test conditions include the AM1.5 solar spectrum distribution, with a spectral irradiance of about 1000W/m^2 and a temperature of about 25±2°C. The typical *I–V* characteristics in both illuminated and dark conditions can be represented by Figure 1.7

based on the equation (1-2), showing that the dark characteristic of solar cells follows a common diode rectification curve. Key performance parameters for solar cells typically include open-circuit voltage (V_{OC}), short-circuit current (I_{SC}), fill factor (FF), and power conversion efficiency (η, also known as E_{ff} or PCE).[25]

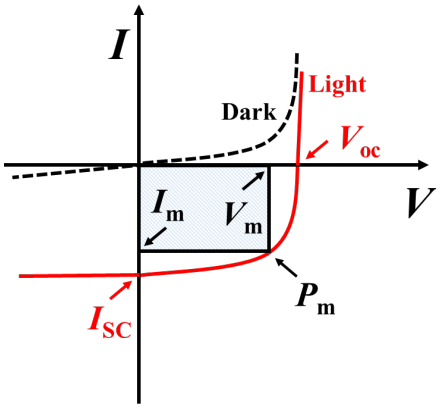

Figure 1.7 *Typical I–V characteristics of a photovoltaic solar cell in both illuminated and dark conditions.*

(a) Open–circuit voltage (V_{OC})

V_{OC} of a solar cell refers to the voltage across its terminals when no external load is connected, resulting in no current flow. When exposed to sunlight without an external circuit, a solar cell generates a voltage due to the photovoltaic effect, with V_{OC} denoting the maximum voltage it can produce under illumination. The V_{OC} value is influenced by various factors such as material properties, semiconductor bandgap, sunlight intensity, and temperature. Generally, higher open circuit voltages indicate greater efficiency and improved performance of the solar cell.

(b) Short–circuit current (I_{SC})

I_{SC} represents the maximum current generated by a solar cell under illumination in the absence of external resistance. I_{SC} is mainly determined by the spectral distribution and intensity of incident light, as well as the active area of the cell exposed to light. Additionally, material properties of the absorber layer, such as optical absorption coefficient, carrier mobility, and thickness, can affect the values of I_{SC}.

(c) Fill factor (FF)

FF is a crucial parameter used to evaluate the performance of a solar cell, quantifying its efficiency in converting sunlight into electricity by measuring the uniformity of current flow across the cell. As shown in Figure 1.7, V_m and I_m represent the voltage and current at the optimal operating condition, while P_m denotes the maximum available power generated by the solar cell under the standard test conditions, expressed as $P_m = V_m * I_m$. The FF can be visually represented by the *I–V* curves as the ratio of the different rectangular areas, which can be defined by the following equation:

$$FF = \frac{V_m \times I_m}{V_{oc} \times I_{sc}} = \frac{P_m}{V_{oc} \times I_{sc}} \quad (1\text{-}3)$$

The values of FF are directly affected by the resistance of the solar cell and the diodes losses, which can be characterized by R_{sh}, R_s, and A. Increasing the R_{sh} and decreasing R_s lead to a higher FF.

(d) Power conversion efficiency (PCE)

PCE is a critical parameter assessing the performance of solar cells. PCE is expressed as the ratio of the P_m of the solar cell to the power of the incident light (P_{in}):[26]

$$PCE = \frac{P_m}{P_{in}} \times 100\% = \frac{FF \times V_{oc} \times I_{sc}}{P_{in}} \times 100\% \quad (1\text{-}4)$$

The values of PCE can vary depending on factors such as the materials characteristics, cell structure, operating temperature, and environmental conditions. A higher PCE indicates a more effective solar cell, indicating greater conversion of solar energy into electricity.

(3) Theoretical efficiency of solar cells

The Shockley–Queisser limit, proposed by William Shockley and Hans Queisser in 1961 based on the detailed balance limit, is a fundamental theoretical boundary that defines the maximum achievable efficiency of a single-junction solar cell under ideal conditions.[10] A maximum efficiency of 30% was theoretically achievable using a

bandgap of 1.1 eV and approximating the solar spectrum with the 6000K black-body spectrum. Subsequently, the American Society for Testing and Materials (ASTM) defines the sunlight spectrum on the earth. Figure 1.8a depicts the schematic representation of the spectral irradiance outside the earth's atmosphere (AM 0) and on the earth's surface for direct sunlight, where AM stands for air mass and is defined by 1/cos(θ). International Standard (ASTM G173–03) defines two terrestrial spectral irradiance distributions of the sunlight spectrum on the earth, known as AM 1.5 D and AM 1.5 G. The AM 1.5D spectrum is associated with solar conversion systems utilizing light concentration through mirrors or lenses, as it only includes direct sunlight. In contrast, the AM 1.5G spectrum encompasses scattered light from the atmosphere and is applicable to PV systems without light concentration. The integrated power density for AM 1.5D and AM 1.5G spectral irradiance is 900.1 W/m^2 and 1000.4 W/m^2, respectively, significantly lower compared to the 1576.7 W/m^2 corresponding to the 6000K black-body spectrum used in Shockley and Queisser's model (Figure 1.8b).

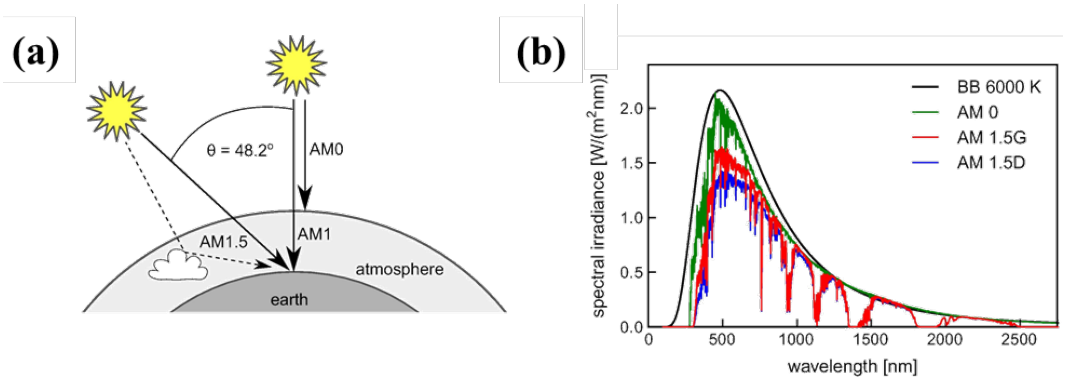

Figure 1.8 *(a) Schematic representation of the spectral irradiance outside the earth's atmosphere (AM 0) and on the earth's surface for direct sunlight shown by a solid arrow (AM 1.5D) and the direct sunlight together with the scattered contribution from the atmosphere (solid and dashed arrow) integrated over a hemisphere (AM 1.5G). (b) Spectral irradiance according to ASTM G173–03 in comparison to the spectrum used by Shockley and Queisser of a black body with a surface temperature of 6000 K (BB 6000 K).*[27]

In 2016, calculations were performed for a cell operated at 25 °C, illuminated by the AM 1.5G spectral irradiance according to ASTM G173–03 standard, and included a back surface mirror which increased the maximum solar conversion efficiency to 33.7% for a single-junction solar cell with a bandgap of 1.34 eV.[27]

It is crucial to emphasize that the calculation for the theoretical limit efficiency in the S–Q model is based on the following five prerequisites:

(a) The solar cell must absorb the incident photons with energy equal to or greater than its bandgap energy (E_g), assuming no transmission or reflection of photons.

(b) Each photon absorbed by the solar cells only excites an electron-hole pair.

(c) The only recombination mechanism of photogenerated carriers is radiative recombination in the solar cell, meaning that electron-hole pairs recombine by emitting photons rather than non-radiatively dissipating their energy as heat.

(d) The photon energies absorbed by the solar cell are assumed not to be reflected back out, but instead solely excite electron-hole pairs.

(e) Semiconductor materials fully comply with black body behavior, and absorb all photons with energy greater than the semiconductor bandgap, in addition to their own external radiation.

Under the above prerequisites, the maximum theoretical efficiency of solar cells is determined solely by the bandgap width of the semiconductor material and the ambient temperature.

1.3 Inorganic compound thin-film solar cells

The research on novel inorganic compound thin-film solar cells is based on the development of CdTe and CIGS thin-film solar cells. The successful progress of CdTe and CIGS solar cells provides valuable experience that can guide the research of novel inorganic compound thin-film solar cells.

1.3.1 CdTe thin-film solar cells

CdTe is a p-type binary monophasic compound belonging to the II-VI group with high carrier mobility. It is considered as an ideal compound semiconductor material for the fabrication of solar cells due to its intrinsic optoelectronic properties. CdTe possesses a favorable direct band gap of approximately 1.5 eV, which is close to the optimal band gap for solar cells, offering a theoretical efficiency of nearly 32%.[28] The high light absorption coefficient exceeding 5×10^5 cm^{-1} in the visible region, indicates that a thin film with a thickness of 2 μm is capable of absorbing 99% of light photons in the AM 1.5G spectrum. The high formation energy of intrinsic defects results in a relatively extended carrier lifetime of up to 30 ns.[29-33] Additionally, the fabrication and stoichiometric control of CdTe are facilitated by the higher vapor pressure of its constituent elements (Cd) compared to the CdTe compound, thereby suppressing the formation of undesired elemental secondary phases.[29] However, there are still a few drawbacks in CdTe. The presence of toxic (Cd) and scarce constituent elements (Te) limits the potential for sustainable large-scale manufacturing.

The development of CdTe thin-film solar cells has undergone significant progress over the years, leading to their emergence as a competitive technology in the solar energy industry. As early as 1963, General Electric Laboratory developed the first n-CdTe/p-Cu_2Te thin-film solar cells with an efficiency of 6%.[34] However, device instability caused by the diffusion of Cu ions into the CdTe layer promoted researchers to seek alternative materials to Cu_2Te. Until 1972, Bonnet and Rabenhorst proposed p-CdTe/n-CdS heterojunction solar cells with an efficiency of 6%, where the CdTe thin films were deposited on a Mo substrate using vapor transport deposition (VTD).[35] The improved efficiency of CdTe thin-film solar cells is attributed to the inter-diffusion between CdTe and CdS layers. Figure 1.9 illustrates the superstrate configuration of CdTe solar cells. In 1982, Tyan et al. utilized the close spaced sublimation method (CSS) to deposit CdTe thin films.[36] The introduction of oxygen during the deposition process not only reduces the crystallization temperature of CdTe thin films but also passivates defects in the films, resulting in an overall improvement of device performance and the achievement of

superstrate-structured CdTe thin-film solar cells with an efficiency exceeding 10%.[36] After 1990, Ferekids et al. introduced chlorine (Cl) treatment to activate the CdTe films leading to an efficiency enhancement of over 15%. This discovery established Cl treatment as a conventional technology for fabricating high-efficiency CdTe thin-film solar cells.[37] By 2001, NREL utilized CSS to fabricate CdTe thin film and incorporated Zn_2SnO_4 as the windows layer, attaining an efficiency of 15.8%.[38] Then in 2004, they achieved a CdTe polycrystalline thin-film solar cell with a total-area efficiency of 16.5% by using new materials and the modified device structure.[39] By 2015, the company First Solar achieved a record efficiency of 22.1% for CdTe thin-film solar cells.[40] Until now, the highest efficiency is 22.6%.[13] The progression of conversion efficiency of CdTe thin-film solar cells is illustrated in Figure 1.10.

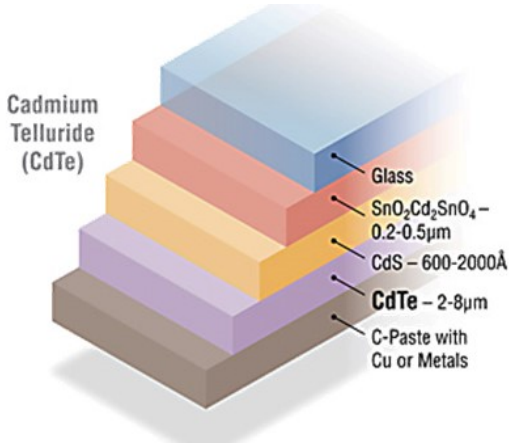

Figure 1.9 *The schematic configuration of CdTe thin-film solar cells.*[41]

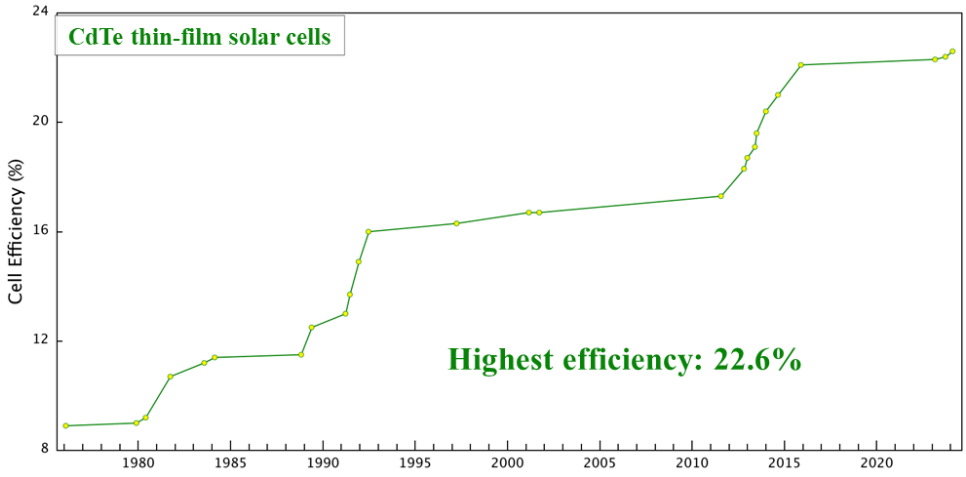

Figure 1.10 *The progression of conversion efficiency of CdTe thin-film solar cells.*[16]

1.3.2 CIGS thin-film solar cells

CIGS is a tetrahedrally bonded semiconductor with the chalcopyrite crystal structure, as illustrates in Figure 1.11. It is derived from $CuInSe_2$ (CIS) by substituting gallium (Ga) with indium (In), resulting in the compound $CuIn_{1-x}Ga_xSe_2$ (x = In/(In+Ga), 0<x<1). Upon heating, it transforms to the zincblende form, with the transition temperature decreasing from 1045 °C for x = 0 to 805 °C for x = 1. By modifying the composition, the band gap of CIGS can be continuously adjusted within the range of 1.0 eV-1.7 eV, giving the possibility to create a bandgap gradient. More importantly, this adjustment can result in a spatially distributed "V" shaped band gap profile, which has been demonstrated to not only introduce a back electric field on the back surface for enhanced electron collection efficiency but also widen the band gap at the interface to increase the V_{OC} values.[42]

The earliest research on CIGS thin-film solar cells can be dated back to 1976, when the University of Maine successfully prepared thin-film solar cells with a $CuInSe_2$/CdS substrate-structured by co-evaporation of $CuInSe_2$ and Se, achieving an efficiency of approximately 5%.[43] Since 1981, Mickelsen and Chen demonstrated a 9.4% efficiency using co-evaporation from elemental sources, sparking considerable interest in CIS-based thin-film solar cells.[44]

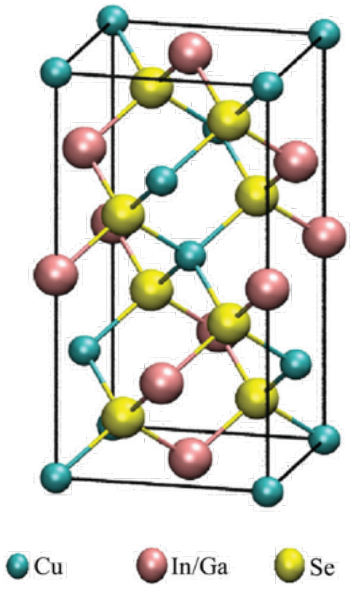

Figure 1.11 *The crystal structure of CIGS.*[45]

In the early 1980s, Boeing utilized co-evaporation technology to fabricate $CuInSe_2$ thin films, in which Cu, In and Se raw materials were placed in separate evaporation sources. The efficiency of $CuInSe_2$ thin film solar cells prepared by this thermal evaporation method was found to be close to 10%.[46] Emerged technologies including chemical bath deposition (CBD) and additive Cu-rich growth process were applied to the fabrication of $CuInSe_2$ thin-film solar cells. A 50 nm CBD-CdS thin film can not only minimize optical loss from CdS absorption but also uniformly cover the surface of the absorption layer, reducing leakage of $CuInSe_2$ thin-film solar cells. Additionally, the Cu-rich growth process effectively improves both morphology and electrical behavior. Then in the early 1990s, soda-lime glass was used as the substrate of $CuInSe_2$ thin-film solar cells, leading to the diffusion of Na elements into the absorption layer. This development became a key technology for enhancing device efficiency.[47] At the same time, a Mo/CIGS/CdS/ZnO structure device was constructed with Ga partially substituting In and S replacing Se, achieving an efficiency of 14%. The schematic configuration of CIGS thin-film solar cells is shown in Figure 1.12.

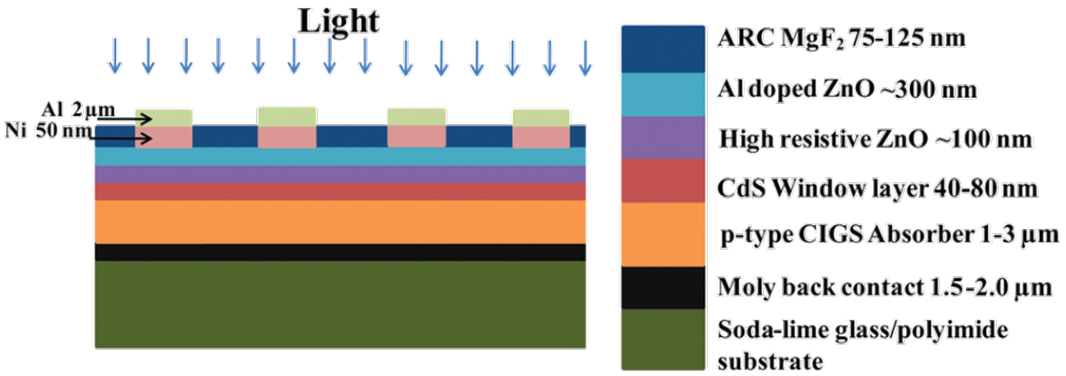

Figure 1.12 *The schematic cross-section of CIGS based thin-film solar cells.*[48]

In the mid-1990s, by precisely controlling the spatial distribution of Ga, In, and Cu, gradient energy bands on the front and back surfaces were achieved, which not only increased the V_{OC} but also enhanced the carrier collection efficiency. As a result, the PCE of CIGS thin-film solar cells has been consistently improved, reaching a PCE approach of 16%.[49] To date, the highest efficiency of 23.6% has been achieved by SolarFrontier.[16] The performance improvement of CIGS thin-film solar cells is shown

in Figure 1.13. Despite the increasing PCE, their production cost remains high due to the limited availability of raw materials In and Ga, high production temperature and low volume rate, which limits the market share of CIGS thin-film solar cells in the overall solar cells market.

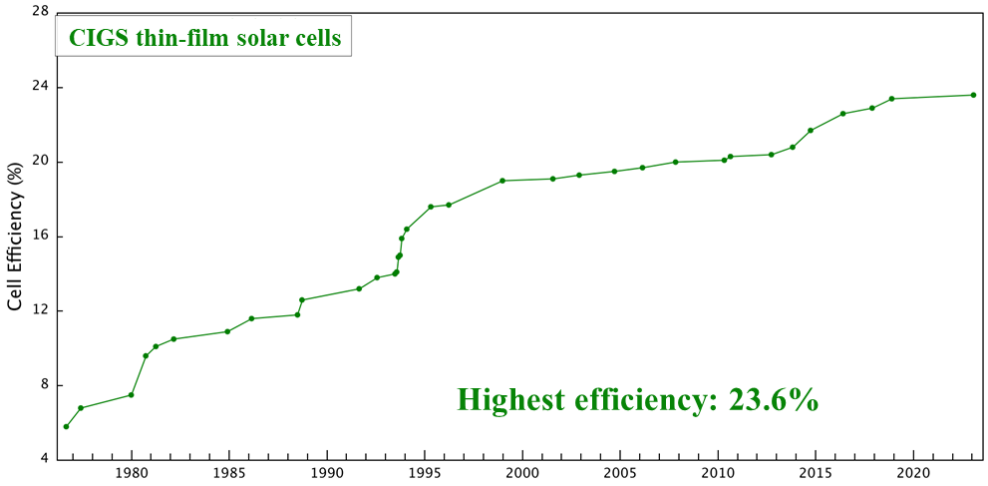

Figure 1.13 *The progression of conversion efficiency of CIGS thin-film solar cells.*[16]

1.4 Sb_2Se_3 thin-film solar cells

The rapid development of novel inorganic compound thin-film solar cells, such as Sb_2Se_3, has been driven by the successful research experience of CIGS and CdTe thin-film solar cells. Sb_2Se_3 thin-film solar cells have received extensive attention in recent years due to their unique material composition and structure.

1.4.1 Property of Sb_2Se_3

The main material properties parameters of Sb_2Se_3 are summarized in Table 1.1

(1) Basic material properties

Sb_2Se_3 is a member of the inorganic binary V-VI compound family and mainly exists naturally in the form of the mineral stibnite. Table 1.1 summarizes the basic material properties of Sb_2Se_3. It possesses an orthorhombic crystal structure with a space group

of Pnma 62, characterized by lattice constants a = 11.6330 Å, b = 11.7800 Å, and c = 3.9850 Å. The crystal structure of Sb_2Se_3 is depicted in Figure 1.14. Sb_2Se_3 exhibits a one-dimensional (1D) crystal structure composed of $(Sb_4Se_6)_n$ ribbons accumulated together by van der Waals (vdW) force in the *a*- and *b*-directions, while the $(Sb_4Se_6)_n$ ribbons are interconnected by Sb-Se covalent bonds in the *c*-direction. The minimum distance between two adjacent ribbons is determined to be 3.29 Å[50].

Table 1.1 Material properties of Sb_2Se_3.

Property	Symbol	Value	Reference
Space group		Pnma 62	[51]
Lattice parameters (Å)	*a*	11.6330	[51]
	b	11.7800	
	c	3.9850	
Relative molecular mass (g mol^{-1})	*Mr*	480.4	[52]
Density (g cm^{-3})	P	5.84	[51]
Melting point (K)	T_m	885	[53]
Band gap (eV)	$E_{g,d}$(direct)	1.17 (300K)	[54]
	$E_{g,i}$(indirect)	1.03 (300K)	
Absorption coefficient (cm^{-1})	A	$>10^5$	[55]
Relative dielectric constant	ε_r	14.3-19.8	[56]
Minority-carrier lifetime (ns)	τ_e	60	[50]
Diffusion length (μm)	$L_{e.c}$	1.7	[57]
Mobility ($cm^2 \cdot V^{-1} \cdot s^{-1}$)	μ_e	15	[51]
	μ_h	42	

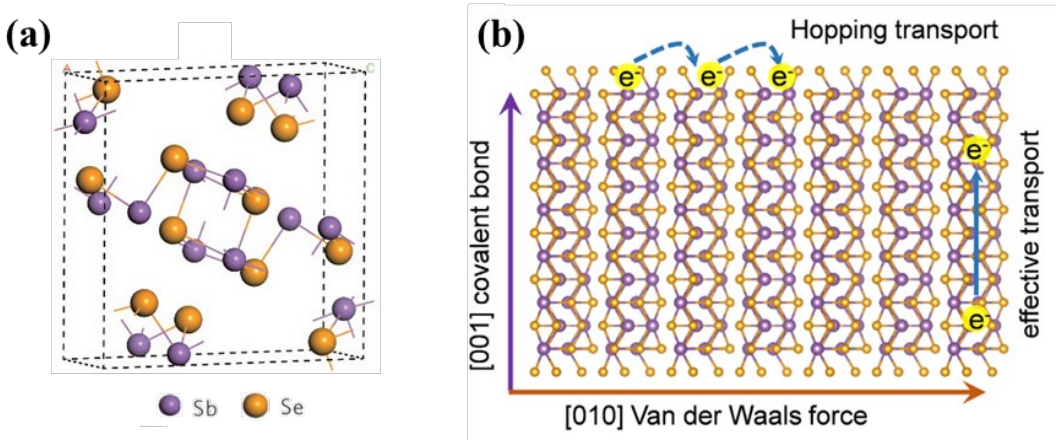

Figure 1.14 *(a) The crystal structure of Sb_2Se_3. (b) Anisotropic carrier transport along [010] and [001] directions.*[58] [59]

The low toxicity, and earth-abundance of Sb_2Se_3, along with its cost-effectiveness, are favorable for large-scale manufacturing. Sb_2Se_3 is not classified as highly toxic by the World major regulation authorities, nor does it appear in the lethal dose LD50 or lethal concentration LCt50 data. The elemental abundance of Sb and Se on the Earth's crust (0.2 and 0.05 ppm, respectively) exceeds that of Te (0.005 ppm) and In (0.049 ppm).[60] Additionally, according to the London Metal Exchange, the unit price of Sb and Se is approximately \$12.6/kg and \$69.1/kg, respectively, significantly lower than that of In (\$276.5/kg) and Te (\$82.9/kg). The significantly lower prices of Sb and Se compared to In and Te make Sb_2Se_3 an economically attractive material for photovoltaic applications.[61]

The melting point of Sb_2Se_3 is 885 K, significantly lower than that of CdTe (1366 K). Sb_2Se_3 exhibits only an orthorhombic phase at normal temperature and pressure, simplifying the composition and phase control. This reduces the occurrence of secondary phase and facilitates fabrication processing. The high vapor pressure of Sb_2Se_3 allows for its deposition using low temperature vacuum-based techniques. The crystallization temperature of amorphous Sb_2Se_3 is about 130 °C. It has been reported that micro-scale Sb_2Se_3 crystals can be obtained at a sintering temperature of 300 ~ 400 °C, indicating the possibility of flexible solar cell on polyimide (PT) substrate.

(2) Photoelectronic properties

In general, the selection of an appropriate light-absorbing material for an optimal solar cell depends not only on the optimal band gap and high absorption coefficient, but also on other comprehensive photo-electronic properties, such as high carrier mobility, long minority carrier lifetime, and diffusion length. As summarized in Table 1, Sb_2Se_3 with stoichiometric composition has an appropriate band gap of 1.17 for direct and 1.03 eV for indirect band gap at 300K, implying its potential as an absorber layer for solar cells. According to the (S−Q) detailed–balance limit, a single-junction solar cell with an optimal band gap of the absorber layer can yield a PCE exceeding 30%. Theoretical calculations demonstrate that Sb_2Se_3 has high density of state in the valence band (VB) and conduction band (CB), indicating its strong capacity for light harvesting. Additionally, the experimental results confirm that its absorption coefficient in the ultraviolet and visible spectrum of Sb_2Se_3 is greater than 10^5 cm^{-1}, suggesting that a 500 nm thin film can effectively absorb solar energy. Sb_2Se_3 thin films typically exhibit p-type semiconductor behavior, with conductivity values of 2×10^{-8} $\Omega\cdot cm^{-1}$ in the dark and 1×10^{-6} $\Omega\cdot cm^{-1}$ under AM 1.5G illuminate conditions.[55, 62]

The mobility of the charge carriers is crucial for solar cells as it dictates the carrier diffusion length. Since Sb_2Se_3 has an anisotropic crystal structure, it exhibits strong anisotropic features in carrier mobility. This is attributed to hop from one ribbon to the adjacent ribbon due to the 1D-ribbons like crystal structure when carrier transport along [hk0] orientations and the carriers. It has been reported that Sb_2Se_3 demonstrates greater mobility along [hk1≠0] orientations. Especially, the Sb_2Se_3 thin film demonstrates a preferred orientation of [221], resulting in maximum measured mobility values. Its electron mobility is determined to be 15 $cm^2\cdot V^{-1}\cdot s^{-1}$, while the hole mobility is 42 $cm^2\cdot V^{-1}\cdot s^{-1}$, surpassing that of CZTS (10 $cm^2\cdot V^{-1}\cdot s^{-1}$) and comparable to that of CdTe (μ_p=80 $cm^2\cdot V^{-1}\cdot s^{-1}$).

The minority carrier lifetime is a crucial parameter for solar cells as it directly impacts the minority carrier diffusion length and device performance. Chen et al. reported the first reliable minority carrier lifetime of Sb_2Se_3 via Time–Resolved Terahertz

spectroscopy (TRTS). Their findings revealed two lifetimes of 60 and 0.2 ns, corresponding to different recombination mechanisms. The longer lifetime of 60 ns was attributed to surface recombination, while the shorter lifetime was linked to the trapping process from the band edge to trap states.[63]

Furthermore, polycrystalline Sb_2Se_3 exhibits a significant dielectric constant (ε_r=14.3–19.8 at 852–1693 nm) (Figure 1.15), surpassing that of CdTe (ε_r=7.1) and comparable to that of CIGS (ε_r=13.6). The larger permittivity theoretically implies a smaller exciton binding energy and possibly immediate separation of electrons and holes upon photogeneration, resulting in reduced electron-hole recombination and ultimately device efficiency improvement.[64]

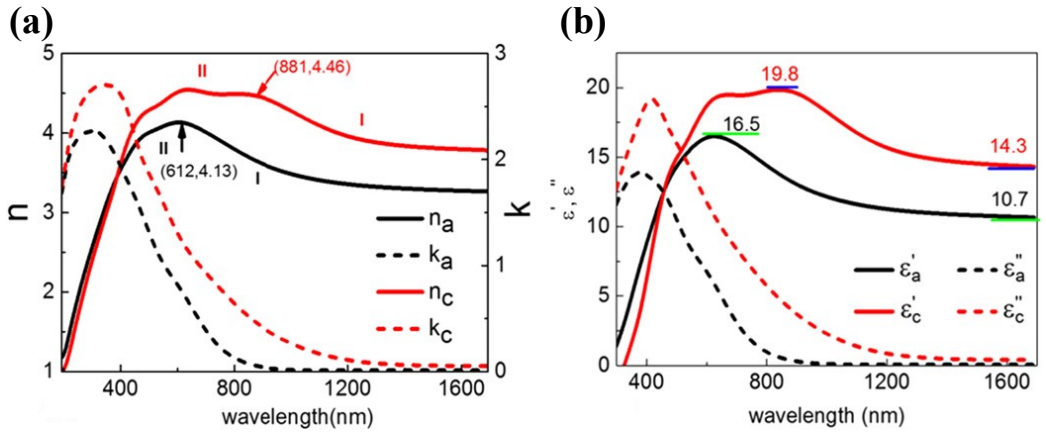

Figure 1.15 *(a) The refractive index and extinction coefficient of amorphous Sb_2Se_3 (a-Sb_2Se_3) and polycrystalline Sb_2Se_3 (c-Sb_2Se_3) films measured by ellipsometry in the wavelength range of 193–1693 nm. (b) The complex dielectric constant of a-Sb_2Se_3 and c-Sb_2Se_3 films versus photon wavelength. The blue and green short solid lines mark the typical values of the real part of the relative dielectric constant.*[64]

(3) Defect property

The distinctive one-dimensional crystal structure of Sb_2Se_3 leads to lower formation energies on surfaces parallel to the [001] direction, resulting in terminal surfaces that are essentially free of dangling bonds (Figure 1.16a). First-principle calculation reveals that non-radiative recombination at the grain boundaries (GBs) can be greatly reduced by appropriately adjusting the orientation of Sb_2Se_3 and by forming a benign grain

boundary in the (hk0) direction to eliminate dangling bonds at the GBs. In contrast, most light-absorbing materials with 3D crystal structure inevitably introduce defect states and recombination centers at the GBs due to the breakage of covalent bonds, which deteriorates device performance (Figure 1.16b).

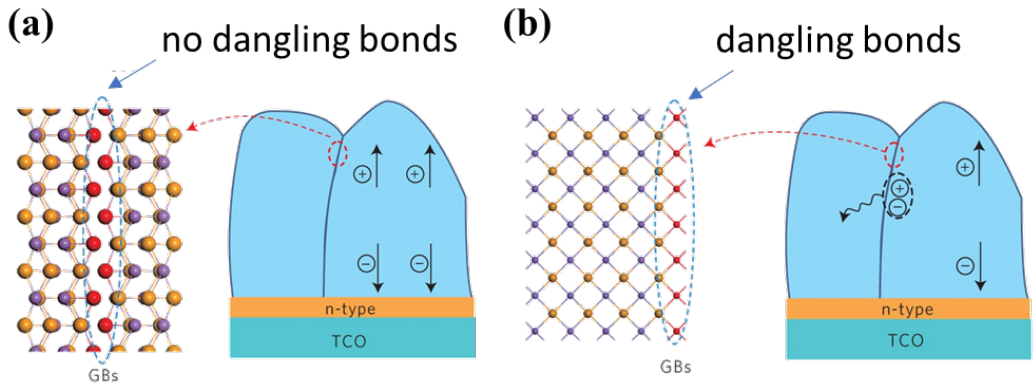

Figure 1.16 *(a) Sb_2Se_3 (orthorhombic) is composed of $(Sb_4Se_6)_n$ ribbons stacked in parallel in the [001] direction. All the atoms at the edge of these ribbons are saturated (highlighted as red spheres) and introduce no recombination loss at the GBs once they are oriented vertically onto the substrates. For clarity, we omitted from the image those $(Sb_4Se_6)_n$ ribbons that are present underneath this layer, but in a staggered manner. (b) CdTe possesses a 3D crystal structure and has dangling bonds (shown as red rods) at the grain boundaries (GBs), which act as defects that cause a recombination loss of the photogenerated carriers.*[58]

As a binary quasi-1D semiconductor, the intrinsic defects of Sb_2Se_3 primarily arise from vacancies and cations/anions anti-substitution, which were originally expected to be simple and easy to control (Figure 1.17). However, First principle calculations show that these defects are actually quite complicated in Sb_2Se_3 compared to traditional semiconductors like CdTe or GaAs. The low symmetry of the quasi-1D structure results in different behaviors for the same type of defects located on nonequivalent atomic sites, making point defects a challenging issue.[65-68]

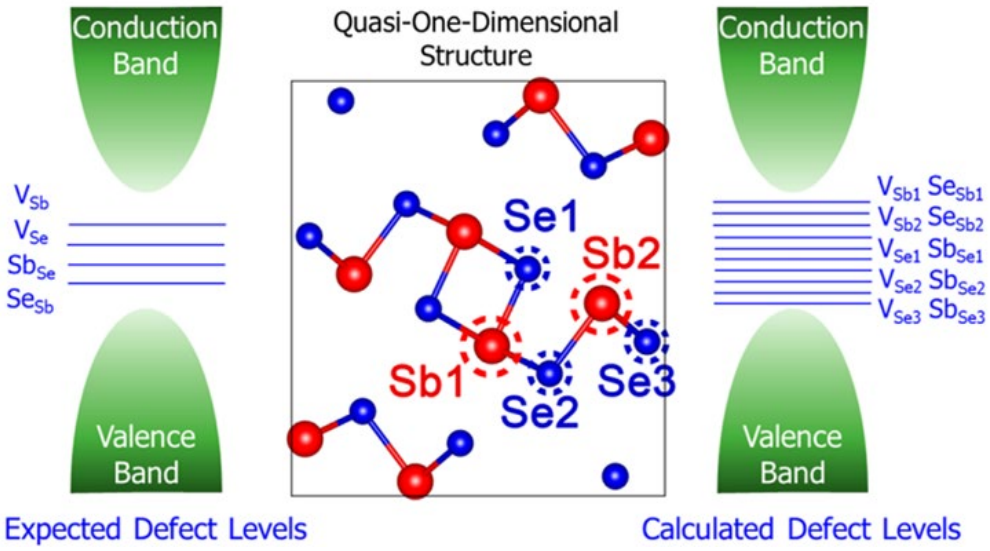

Figure 1.17 *Two nonequivalent Sb and three nonequivalent Se atomic sites in Sb_2Se_3 crystal. The expected defect levels and calculated defect levels of Sb_2Se_3.*[69]

The middle of Figure 1.17 displays the nonequivalent two Sb and three Se atomic sites within each $(Sb_4Se_6)_n$ atomic chain. Secondly, the formation of cations/anions anti-substitution defects is typically complicated in traditional binary compound semiconductor such as CdTe and GaAs. In contrast, the antisite defects Sb_{Se}, Se_{Sb}, even and $2Se_{Sb}$, exhibit higher concentration and may be dominant due to a larger gap and a weak van der Waals (vdW) interactions between the $[Sb_4Se_6]_n$ atomic chains. Furthermore, the formation of defects in Sb_2Se_3 is dependent on its chemical components (i.e., Sb-rich and Se-rich). Under Sb-rich conditions, the presence of Se vacancy (V_{Se}) and Sb antisite (Sb_{Se}) exist with a formation energy below 1.0 eV. Conversely, under Se-rich conditions, Se antisite (Se_{Sb}), and Sb vacancy (V_{Sb}) appear in Sb_2Se_3 with lower formation energy. However, generally speaking, the defect density of Sb_2Se_3 under Sb-rich condition is higher than that under Se-rich condition. As depicted in Figure 1.17, there are primarily 5 deep-level defects present in Sb_2Se_3, which pose significant challenges for the development of Sb_2Se_3 thin-film solar cells. The control of defects in Sb_2Se_3 films necessitates systematic and comprehensive investigation into the preparation process, composition control and doping engineering of Sb_2Se_3.

1.4.2 Preparation technology of Sb_2Se_3 thin film

Deposition of Sb_2Se_3 absorber thin films is of great effect for the preparation of Sb_2Se_3 solar cells. A high-quality light-absorbing film with benign surface morphology, preferred orientation, and minimal defect density can reduce non-radiative recombination losses in the device, leading to enhanced performance of solar cells. Over the past decade, numerous growth techniques have been developed for depositing Sb_2Se_3 thin films.

Physical deposition techniques, such as thermal evaporation (TE),[70] rapid thermal evaporation (RTE),[58, 71] magnetron sputtering deposition (MSD),[72-74] vapor transport deposition (VTD),[75, 76] close-spaced sublimation (CSS),[77-79] pulsed laser deposition (PLD),[80, 81] injection vapor deposition (IVD),[82] and chemical molecular beam deposition (CMBD)[83] are utilized for the for the growth of Sb_2Se_3. Additionally, chemical methods, including electrodeposition, chemical-bath deposition (CBD),[84] spin coating,[85, 86] and hydrothermal deposition[87] are employed for the preparation of Sb_2Se_3 film. The utilizaton of different deposition methods leads to distinct influences on the properties of Sb_2Se_3 films. Among all the physical and chemical preparation methods, the RTE, VTD, MSD, CSS, IVD, and CBD are well-established techniques for fabricating Sb_2Se_3 thin films. Hence, a brief introduction to these growth methods for Sb_2Se_3 deposition is provided below.

Chemical bath deposition (CBD). CBD is a solution-based technique used to deposit thin films from a liquid phase. This method is advantageous due to its cost-effectiveness, uniformity, and ability to produce high-quality films. To date, the highest efficiency of 10.57% for Sb_2Se_3 thin-film solar cells was achieved by a novel additive-assisted CBD technology using antimony potassium tartrate and sodium selenosulfate as antimony and selenide sources, respectively, along with thiourea and selenourea as additives to manipulate the deposition process (Figure 1.18). The physical properties of Sb_2Se_3

films have been greatly improved in terms of morphology, crystallinity, carrier transport properties, and defect density.

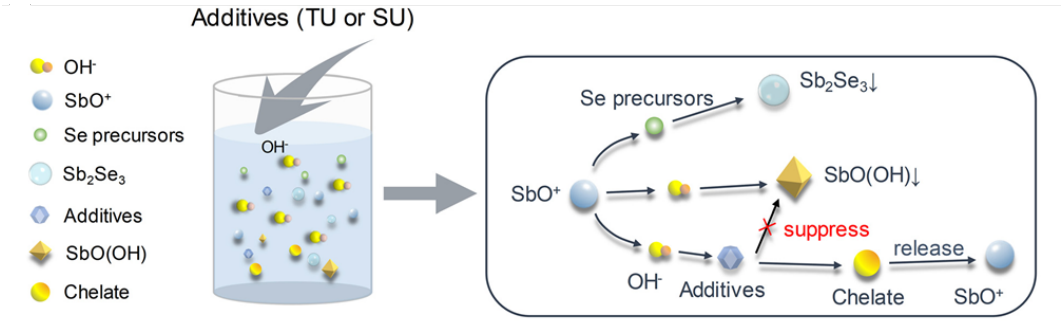

Figure 1.18 *Schematic diagram of the reaction mechanism during the Sb_2Se_3 film deposition.*[84]

Injection vapor deposition (IVD). This approach is characterized by the controlled injection of precursor materials in vapor form into a deposition chamber where they react and form a solid film on a substrate. The flow rate of the injection gas is identified as a critical factor influencing the quality of absorber layers and subsequent device functionality. The key advantages of VTD include precise regulation of deposition rate, film thickness, uniformity, and adaptability. Duan et al. reported an efficiency of 10.12% by IVD for photovoltaics with high-quality Sb_2Se_3 films, demonstrating smaller non-radiative recombination and fewer trap states in comparison to CSS-Sb_2Se_3 devices and Co-evaporation processed devices (Figure 1.19). This approach presents a promising avenue for the deposition of Sb_2Se_3 films.

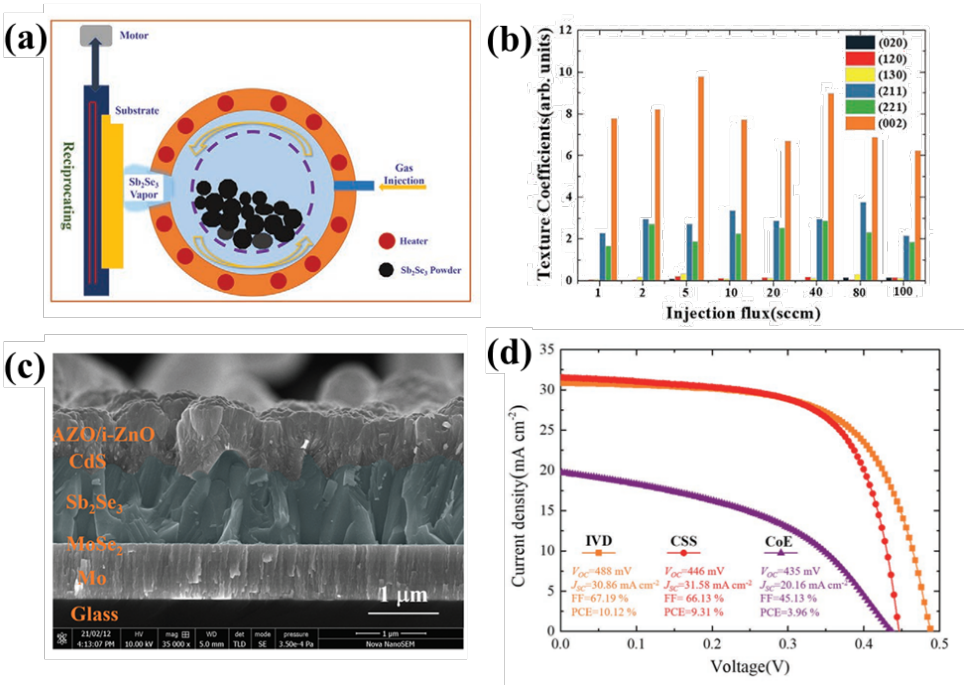

Figure 1.19 *(a) Schematic diagram of the injection vapor deposition system. (b) Texture coefficients of the Sb_2Se_3 thin films fabricated under different injection flux (1–100 sccm). (c) Cross-section of a completed Sb_2Se_3 thin-film solar cell fabricated by the IVD technique. (d) J–V curves of the Sb_2Se_3 solar cells.*[82]

Magnetron sputtering deposition (MSD). MSD is a widely utilized technology in thin film manufacturing due to its high compatibility. The deposition process for Sb_2Se_3 via MSD is carried out in full-vacuum conditions, with three distinct methods available. The first method involves obtaining Sb_2Se_3 through sputtering a high-purity, stoichiometric Sb_2Se_3 target. An alternative approach is the co-sputtering of Sb_2Se_3 and Se targets to deposit Sb_2Se_3 films. The third approach to preparing Sb_2Se_3 involves depositing a thin film of metallic Sb using radiofrequency MSD from a high-purity and dense Sb sputtering target, followed by selenization of the precursor thin films. Prof. Liang's group has recently utilized the MSD technique to enhance the efficiency of Sb_2Se_3 solar cells from 2.11% to 9.24%.[72, 88-93] Figure 1.20 shows the schematic illustration of the preparation process of the substrate-structured Sb_2Se_3 thin film by a combination of sputtered and selenized Sb precursors films.

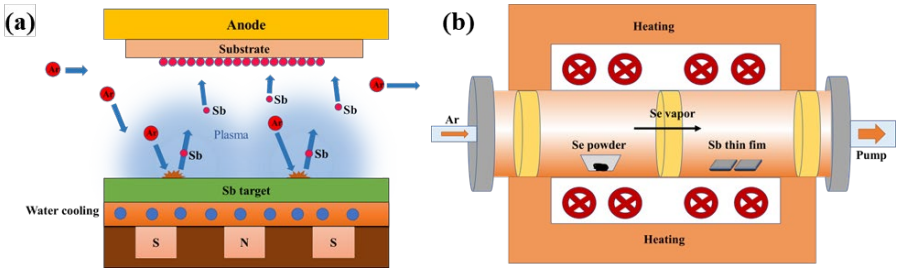

Figure 1.20 *(a) Sb precursor thin film deposited by RF magnetron sputtering, (b) Sb_2Se_3 thin film obtained by post-selenization heat treatment.*[94]

Close-spaced sublimation (CSS). This method offers cost-effective advantages and a high growth rate. It has been widely utilized for the deposition of semiconductor materials, particularly in the manufacturing of CdTe thin-film solar cells for commercial purposes. In CSS, the source material and substrate are positioned in close proximity, typically 1–5 mm apart within a graphite box. More recently, this technique has been employed for the fabrication of Sb_2Se_3 materials due to its high saturated vapor pressure. The highest reported efficiency achieved using the CSS method for Sb_2Se_3 solar cells is 9.2%, which was obtained from a substrate configuration of ZnO:Al/ZnO/CdS/TiO_2/Sb_2Se_3/$MoSe_2$/Mo (Figure 1.21).

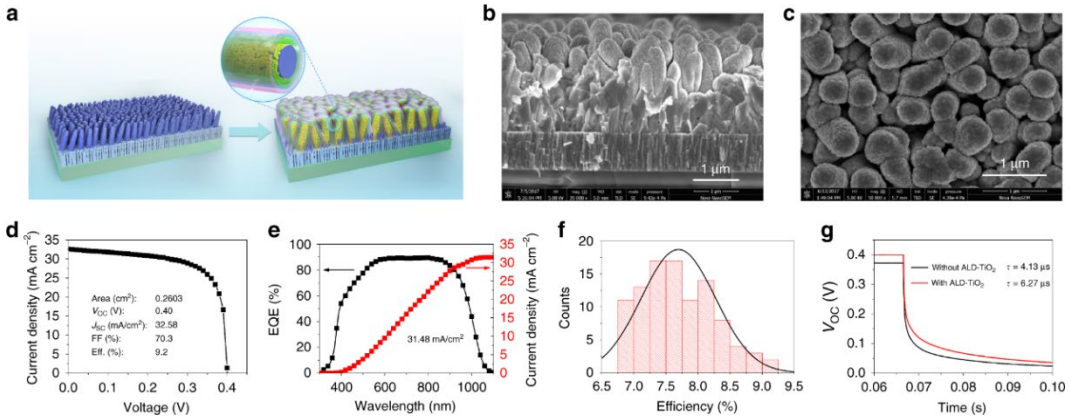

Figure 1.21 *(a) Schematic of the Sb_2Se_3 nanorod arrays on Mo-coated glass and finished Sb_2Se_3/CdS core/shell nanorod array solar cells. (b) Cross-sectional and (c) top view SEM images of the completed CdS/Sb_2Se_3 solar cells. (d) J–V curve and (e) EQE spectrum for the champion device (area=0.2603 cm^2). (f) Histogram of device efficiency over 100 individually fabricated solar cells. (g) V_{OC} decay curves of the solar cells with and without ALD-TiO_2 layer.*[77]

Rapid thermal evaporation (RTE). RTE is a vacuum process closely similar to CSS method but with a notably shorter growth period lasting only a few tens of seconds. RTE has demonstrated benefit in crystal nucleation and morphology control. The source-to-substrate distance is maintained at approximately 10 mm. Thin-film solar cells fabricated using RTE-deposited Sb_2Se_3 have attained a efficiency of 7% for a simple ITO/CdS/Sb_2Se_3/Au configuration.[95]

Vapor transport deposition (VTD). VTD is advantageous for producing uniform and large-area films with low cost, which are essential for the efficient performance of Sb_2Se_3 thin-film solar cells. In the VTD method, the substrate temperature and the distance between source and substrate are adjustable, making the heating temperature of the evaporation source, pressure in the quartz tube, and substrate temperature key factors in determining the quality of the final Sb_2Se_3 films. Wen et al achieved a certified efficiency of 7.6% for superstrate CdS/Sb_2Se_3 thin-film solar cells using the VTD technique in 2018 (Figure 1.22). More recently, Chen et al. have also fabricated the substrate-structured flexible Sb_2Se_3 thin-film solar cells through VTD, delivering an improved efficiency of 8.03% (Figure 1.23).

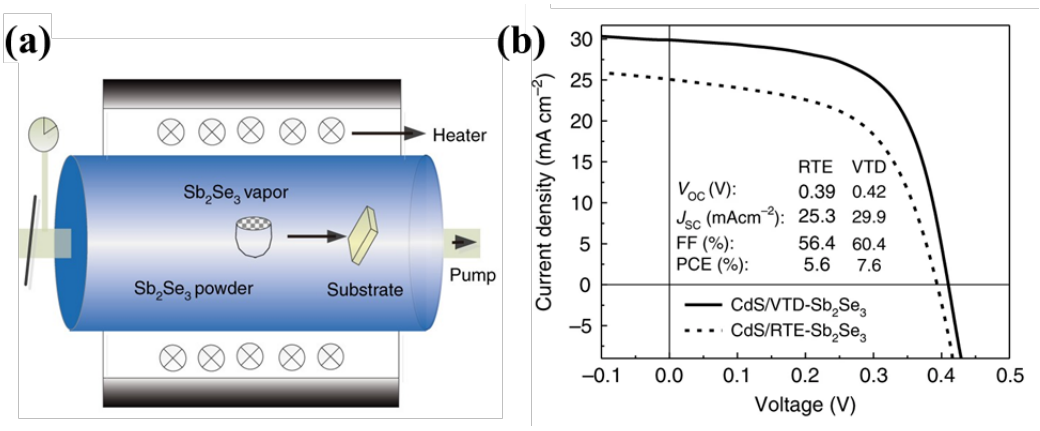

Figure 1.22 *(a) Schematics of VTD system for fabrication of CdS/Sb_2Se_3 solar cells. (b) The J–V curves of the best-performing VTD- and RTE-fabricated devices under AM1.5 G illumination.*[75]

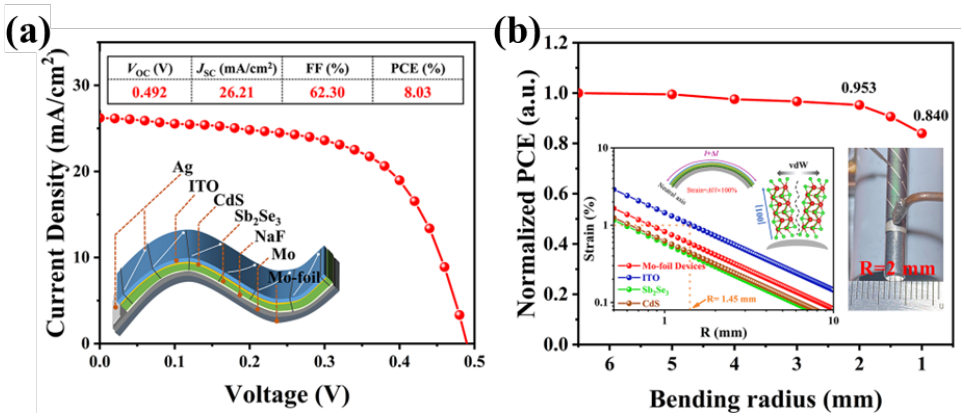

Figure 1.23 *(a) J–V curves of the representative Mo-foil Sb_2Se_3 thin-film solar cells, and a schematic configuration of the flexible device (insert). (b) The strain of the whole device.*[76]

1.4.3 Characterization techniques of Sb_2Se_3 thin-film solar cells

Characterizing Sb_2Se_3 thin-film solar cells involves various techniques to evaluate their structural, optical, electrical, and performance properties. Here are some common characterization techniques used for Sb_2Se_3 thin film and device.

(1) Characterization of Sb_2Se_3 thin film

X-ray diffraction (XRD) measurement

XRD is a powerful nondestructive technique used to characterize the crystal structure, phase purity, and crystallographic orientation of the Sb_2Se_3 thin films. It provides information on crystal structure, phase, preferred crystal orientation (texture), and other structural parameters, such as average grain size, crystallinity, strain, and crystal defects.

Scanning electron microscope (SEM) measurement

By precisely focusing a fine electron beam to scan the sample, the electrons interact with the surface, generating signals for surface mapping of the film. Detailed images of the film surface morphology and cross-sectional views can used to study the grain size and layer thickness.

Transmission Electron Microscopy (TEM) measurement

TEM analysis can offer high-resolution images and information on the microstructure, grain boundaries, and defects within the thin films.

Energy dispersive X-ray spectroscope (EDS) measurement

EDS is a method of analysis used to determine the elemental composition and chemical characteristics of a sample, often in combination with SEM and TEM.

UV-Vis Spectroscopy measurement

The optical absorption and transmission spectra are measured to obtain information on the bandgap and optical properties of the Sb_2Se_3 thin films.

Electron backscatter diffraction (EBSD) measurement

EBSD is a powerful technique used for characterizing the crystallographic structure of materials, particularly in SEM. By scanning the electron beam across the sample surface, an orientation map can be created showing the crystallographic orientation of grains.

X-ray photoelectron spectroscopy (XPS) measurements

XPS can be utilized for a wide variety of materials and offers valuable quantitative and chemical state data from the surface of the material under investigation. The elemental identity, chemical state, and quantity of a detected element can be determined from the binding energy and intensity of a photoelectron peak.

Ultraviolet photoelectron spectroscopy (UPS) measurements

UPS is used to investigate the valence band structure of materials, providing information on the density of states and the distribution of electrons.

Kelvin probe force microscopy (KPFM) measurements

KPFM measures the contact potential difference (CPD) between a conductive AFM tip and the sample surface, obtaining a map of the surface potential distribution. It is typically used to investigate the surface potential and charge distribution in photovoltaic materials.

(2) Measurements and characterization of Sb_2Se_3 solar cells

Current density–voltage (*J–V*) measurements

J–V measurements are used to determine the photovoltaic parameters, including V_{oc}, short–circuit current density (J_{sc}), FF, and overall PCE of the solar cells. This measurement is carried out under a light intensity of 100 mW/cm^2 AM 1.5 G.

External Quantum Efficiency (EQE) measurements

The wavelength-dependent response of a solar cell is analyzed through EQE measurements, which offer valuable insights into device performance, including optical loss mechanisms, carrier collection efficiency, and energy bandgap. Additionally, the maximum J_{SC} achieved by a solar cell can also be estimated from the EQE spectrum.

Capacitance-voltage (*C–V*) and drive-level capacitance profiling (DLCP) measurements

C–V and DLCP measurements study the variation of capacitance with applied voltage across a semiconductor device. *C–V* measurements are typically used for static characterization of doping density, while DLCP provides dynamic information about carrier mobility, trap states, and non-ideal effects. In solar cells, combined with *C–V* and DLCP measurements, the information on depletion region width, built-in potential, defect density can be determined.

Deep-level transient spectroscopy (DLTS) measurements

DLTS measures the change in capacitance of a solar cell. This change in capacitance is caused by the emission or capture of charge carriers at deep-level defects within the

band gap of the solar cells. Through analysis of the transient capacitance signal, it provides valuable information about the energy levels, capture cross-sections, and density of these defects.

Admittance spectroscopy (AS) measurements

AS is widely utilized for the examination of the electrical characteristics of materials, particularly semiconductors and dielectric materials. It offers insights into various processes such as carrier dynamics, defect states, and interface phenomena. In solar cells, AS can be used to analyze the performance and efficiency of solar cells by studying the carrier dynamics and defect states.

Transient absorption spectroscopy (TAS) measurements

TAS is a powerful technique used to study the charge carrier dynamics of excited states in solar cells. It provides insights into processes such as energy transfer, charge carrier dynamics, and photochemical reactions on ultrafast timescales.

1.4.4 Development of Sb_2Se_3 thin-film solar cells

Currently, research has primarily focused on three types of solar cells based on Sb_2Se_3: dye-sensitized solar cells, planar heterojunction superstrate-structured thin-film solar cells, and planar heterojunction substrate-structured thin-film solar cells. The typical structures are illustrated in Figure 1.24.

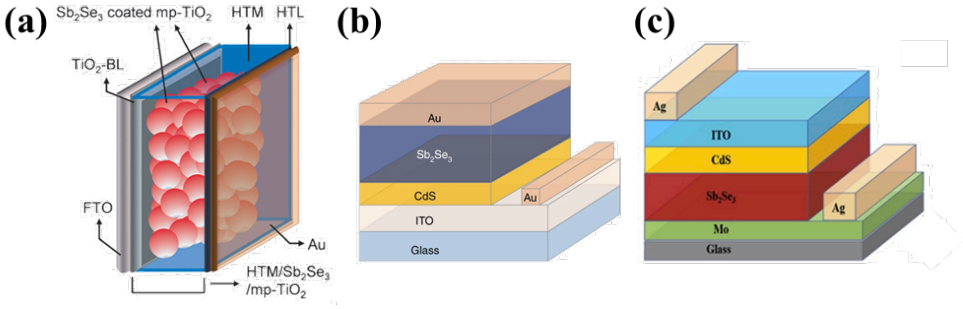

Figure 1.24 *The typical device structures. (a) mesoporous sensitized-type, (b) superstrate-type, and (c) substrate-type.*[54, 75, 94]

The photovoltaic performance of Sb_2Se_3 was first discovered in a photoelectrochemical device in 1982.[96] Then in 2009, Nair et al. explored the application of Sb_2Se_3 in photovoltaic devices as light-absorber layer, yielding a low conversion efficiency of 0.66% for the complex configuration of TCO/CdS/Sb_2Se_{3-x}:Sb_2O_3/PbS.[97] In 2012, Guijarro et al. demonstrated efficient charge photogeneration at a spiro-OMeTAD/Sb_2Se_3/Metal Oxide heterojunctions between Sb_2Se_3 nanocrystals and mesoporous TiO_2 films.[98] In 2013, Sb_2Se_3 thin films were deposited by solution methods, and the sensitized-type Sb_2Se_3 solar cells with a TCO/CdS/Sb_2Se_3-Sb_2O_3/PbS structure achieved a PCE of 3.21%.[54] However, there have been no reports of PCEs exceeding 3% for mesoporous solar cells enhanced with Sb_2Se_3 since then. The challenge of finding an appropriate Se source for depositing pure Sb_2Se_3, along with the uncontrolled morphology during the growth process of film in mesoporous TiO_2 scaffolds, has led to severe interfacial recombination and restrained the advancement of Sb_2Se_3-sensitized solar cells.

Significant advancements were made in the development of Sb_2Se_3 thin-film solar cells utilizing a planar-type device structure, which can be further categorized into superstrate and substrate structures. The following review will focus on the development of Sb_2Se_3 thin-film solar cells based on these two structures.

In 2014, Zhou employed a hydrazine (N_2H_4) solution method to deposit Sb_2Se_3 thin film on a buffer layer to fabricate a TiO_2/Sb_2Se_3 heterojunction solar cell, yielding an efficiency of 2.26%.[51] The device presented good stability since only a slight efficiency degradation (0.11%) could be seen after 24 hours of exposure to air at 60 °C. This marks the first reported superstrate configuration. In the same year, the device performance was enhanced by introducing a selenization process following thermal evaporation, resulting in an increased PCE of 3.7%. In 2015, RTE technology was proposed to optimize the substrate temperature during Sb_2Se_3 film deposition, leading to an effectively controlled crystal orientation and a significantly improved PCE of 5.6% (Figure 1.25).[58] This discovery reveals that the quasi-1D nature of Sb_2Se_3 can result in

benign grain boundaries by controlling the crystallographic orientation. That was the first-time crystal orientation was controlled for Sb_2Se_3 thin-film solar cells.

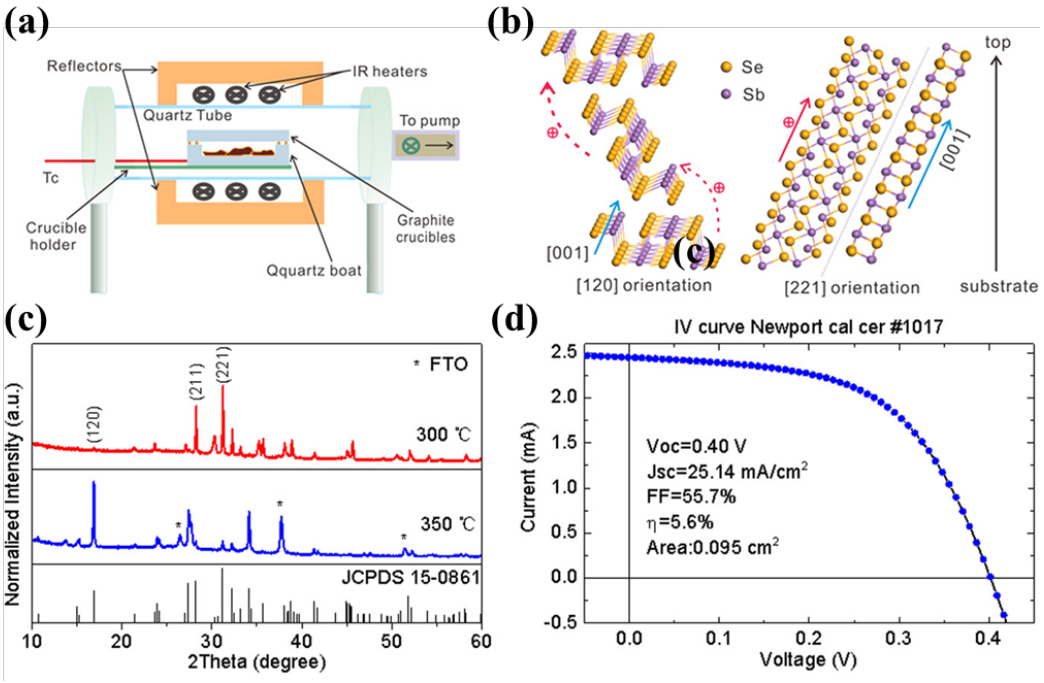

Figure 1.25 *(a) The schematic diagram of RTE equipment for Sb_2Se_3 film deposition. (b) Atomic structures of [120]- and [221]-oriented grains in Sb_2Se_3. The substrate is the CdS buffer layer on which the Sb_2Se_3 ribbons grow. (c) XRD patterns of Sb_2Se_3 film grown at different substrate temperature. (d) J–V characteristics of the FTO/CdS/ Sb_2Se_3/Au solar cell independently certified by the Newport Cooperation.*[58]

In 2017, Wang et al. utilized a ZnO buffer layer to induce the growth of Sb_2Se_3 thin films with preferred orientations of [221] and [211], achieving a certified PCE of 5.93%.[99] This device demonstrated nearly full compliance with the IEC61646 international standard due to its exceptional stability. Subsequently, Chen and Li et al introduced PbS colloidal quantum dot and organic CZ-TA as hole transport layers (HTLs) in a n-i-p configuration, boosting carrier collection efficiency and minimizing carrier recombination loss at the back contact, resulting in PCEs of 6.50% and 6.84%, respectively.[78, 100] In 2018, a monoatomic layer of Al_2O_3 prepared using the atomic layer deposition (ALD) method was employed to enhance the hole concentration of the Sb_2Se_3 films. A device with a configuration of FTO/CdS/p-Sb_2Se_3/p+-Sb_2Se_3/Al_2O_3/Au

achieved a PCE of 6.7%.[101] The PCE for RTE-based Sb_2Se_3 solar cells was further enhanced to 7.04% by the inverting the GBs (modifying the properties of GBs to optimize the electrical properties of Sb_2Se_3 films) through n-type $CuCl_2$ interstitial doping.[102] In 2019, precise control over the preferred orientation [211] and [221] of Sb_2Se_3 was achieved by utilizing high substrate temperature to re-evaporate lying seeds and to preserve standing seeds, resulting in a PCE of 7.62%.[71] In the same year, Wen developed a VTD technique for depositing Sb_2Se_3 thin films with improved crystallinity, leading to a reduction of the dominant deep defect density and achieving a PCE of 7.6%.[75] By 2022, the employment of additive-assisted CBD strategy significantly enhanced the quality of Sb_2Se_3 thin films, resulting in enhanced charge transport. This led to a certificated PCE of 10.57%, representing the highest PCE for Sb_2Se_3 solar cells.[84]

The development history of superstrate-structured Sb_2Se_3 thin-film solar cells exhibits three distinct inflection points, as depicted in Figure 1.26. These correspond to the technological advancements in crystal orientation control, the design of solar cells with p-i-n structure, and the utilization of the VTD technique, and additive-assisted CBD technique for preparing Sb_2Se_3 thin-films.

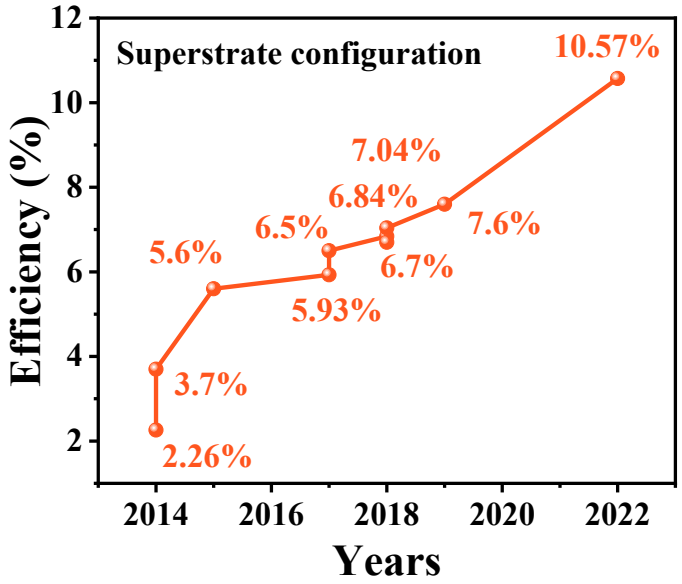

Figure 1.26 *The development history of PCE of superstrate-structured Sb_2Se_3 thin-film solar cells.*

Sb_2Se_3 thin-film solar cells, with a substrate-structured similar to CIGS thin-film solar cells, have attracted significant attention. The schematic of substrate configuration is depicted in Figure 1.24c. In 2014, Liu et al. reported the first substrate-structured Sb_2Se_3 solar cell (FTO/Sb_2Se_3/CdS/ZnO/ZnO:Al/Au), achieving an encouraging PCE of 2.16%.[70] In 2016, Sb_2Se_3 thin films were grown via the selenization of Sb metal precursor film, resulting in a PCE of 3.47% with the same configuration as CIGS (Mo/Sb_2Se_3/CdS/ZnO/Al:ZnO/Al-electrode).[103] In 2017, the Sb_2Se_3 thin films were deposited on a Mo-substrate through co-evaporation of Sb_2Se_3 and Se sources, combined with a Mo selenization process prior to the Sb_2Se_3 deposition, leading to a PCE of 4.25%.[104] Subsequently in 2018, an enhanced PCE of 6.71% was obtained by employing band alignment engineering with a $Cd_xZn_{1-x}S$ buffer layer (Figure 1.27).[105]

13

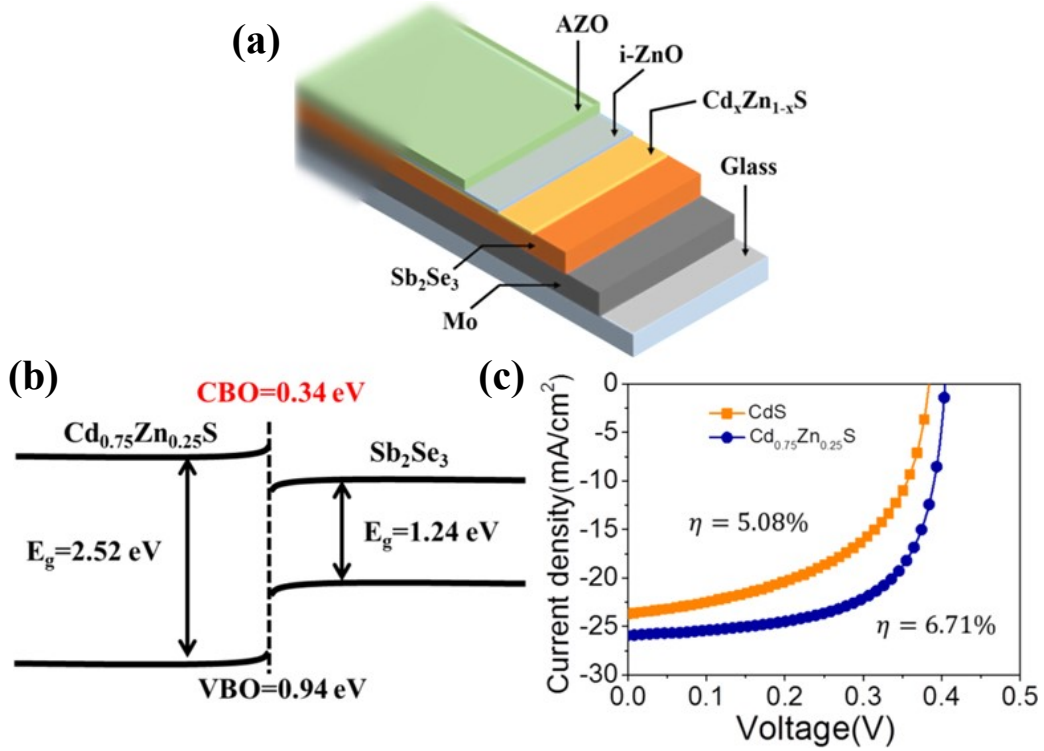

Figure 1.27 *(a) The device structure of Sb_2Se_3 solar cells. (b) Schematic of the band alignment of the Sb_2Se_3 absorber and $Cd_{0.75}Zn_{0.25}S$ buffer layer. (c) Light J−V characteristics of the solar cells with CdS and $Cd_{0.75}Zn_{0.25}S$ buffer layer.*[105]

Then in 2019, 1D [00l]-oriented Sb_2Se_3 core−shell nanorod arrays on selenized molybdenum-coated glass substrates by the CSS technique was developed, yielding a record PCE of 9.2% for Sb_2Se_3 solar cells. with a configuration of $Mo/Sb_2Se_3/TiO_2/CdS/ZnO/ITO/Ag$ using heterojunction interface engineering.[77]

In 2022, Duan et al. reported an IVD technique to fabricate compact Sb_2Se_3 with strong [001] orientation, revealing a PCE exceeding 10% (10.12%), which represents the highest PCE achieved for substrate-structured Sb_2Se_3 thin-film solar cells.[82]

Significant improvements in device performance have been reported for magnetron sputtering-based Sb_2Se_3 thin-film solar cells. In 2017, Liang et al. first reported an efficiency of 2.11% for substrate-structured solar cells with a Sb_2Se_3 absorber prepared using the magnetron sputtering technique.[72] In 2019, they proposed a two-step process for Sb_2Se_3 thin film fabrication, involving magnetron sputtering followed by a post-selenization treatment. Tuning the selenization parameters, resulted in a PCE of 6.06% for sputtered Sb_2Se_3 planar heterojunction solar cells, with an exceptional V_{OC} of 494 mV (Figure 1.28).[106] Subsequently, in 2020, they further improved the quality of Sb_2Se_3 films by an effective combination reaction involved with sputtered and selenized Sb precursor. Meanwhile, they found that the additional heterojunction (Sb_2Se_3/CdS) heat treatment can induce Cd and S interdiffusion, resulting in low deep-level defect and interface defect densities, thus achieving an efficiency of 6.84% (Figure 1.29).[94] Then in 2022, they proposed an effective interface engineering of heterojunction (HTJ) annealing treatment approach to overcome the large V_{oc} deficit, increasing the efficiency to 8.64% with a competitive V_{oc} of 0.52 V.[107] In 2023, the buried interface and heterojunction engineering were synergistically employed to enhance device characteristics, resulting in a comparable PCE of 9.24%, along with a higher J_{SC} of 29.47mA cm^{-2} and FF of 63.65% (Figure 1.30).[88]

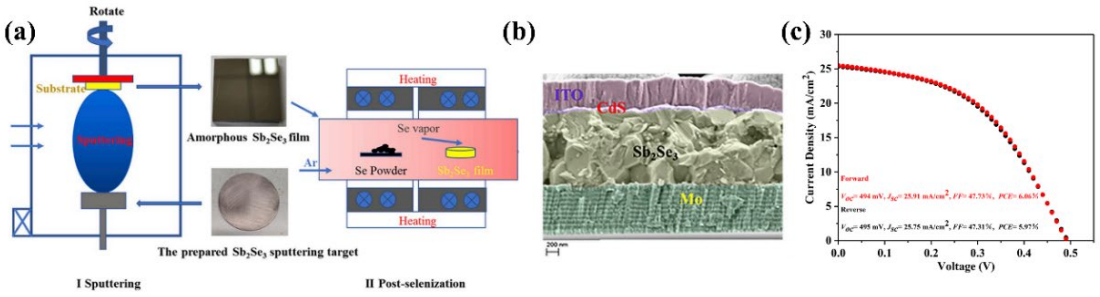

Figure 1.28 (a) *Schematic diagram of Sb_2Se_3 thin film. (b) SEM cross-sectional image of Sb_2Se_3 device. (c) J–V curves from different scanning direction of the champion device.*[106]

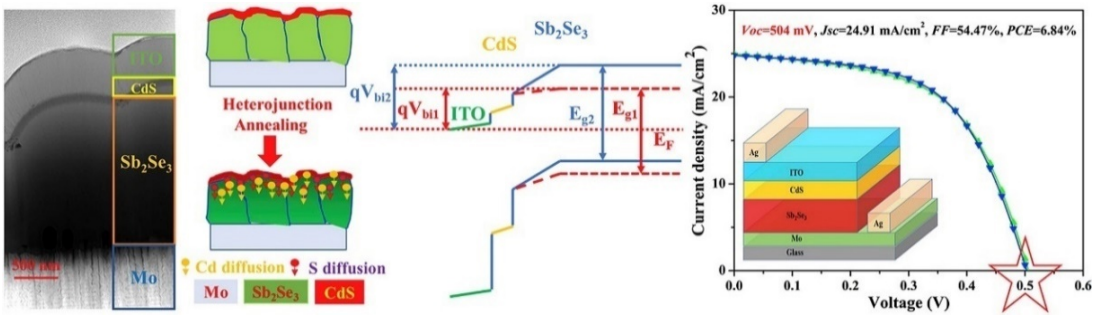

Figure 1.29 *Cross-sectional TEM image, schematic diagram of elemental inter-diffusion, the modified band alignment, and the J–V curves of the best devices.*[94]

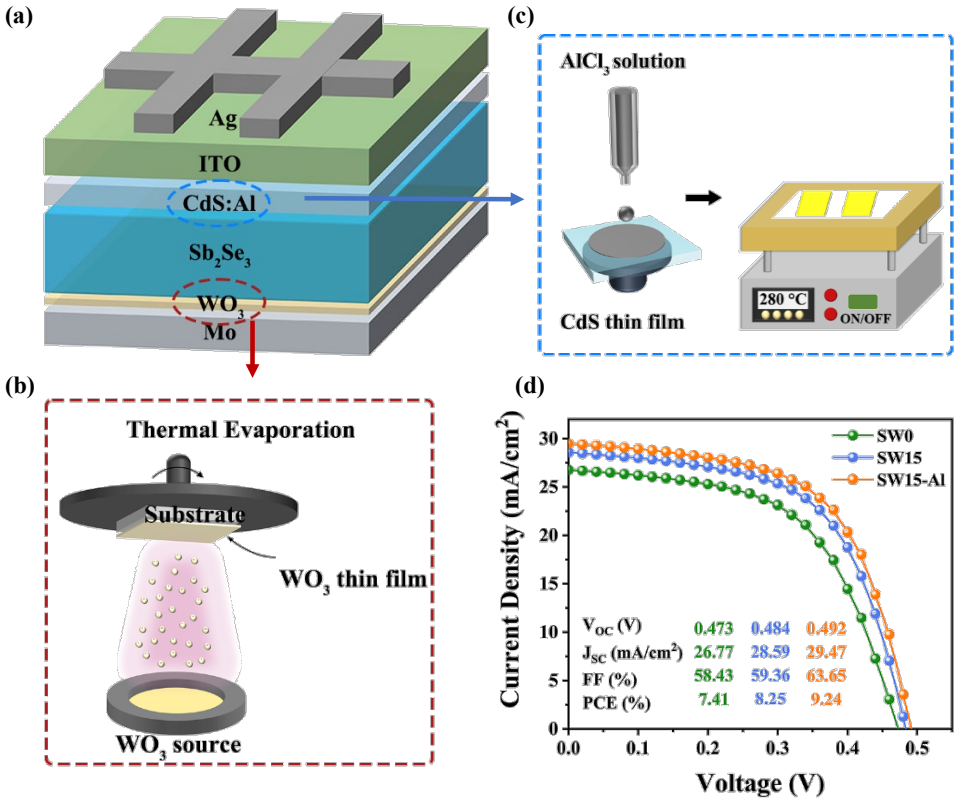

Figure 1.30 *Schematic diagram of production procedure and device photovoltaic performance. (a) Schematic configuration of Sb_2Se_3 device. (b) Deposition of the WO_3 buried interface layer. (c) Deposition of Al ion doping treatment of the CdS buffer layer. (d) J–V curves.*[88]

Similarly, Figure 1.31 illustrates the progression of PCE in substrate-structured Sb_2Se_3 thin-film solar cells. The increased PCE are attributed to key advancements in technology such as the employment of ZnCdS buffer layer for interfacial band alignment regulation, orientation control for nano arrays absorber growth, and heterojunction engineering to mitigate buried interface nonradiative recombination losses.

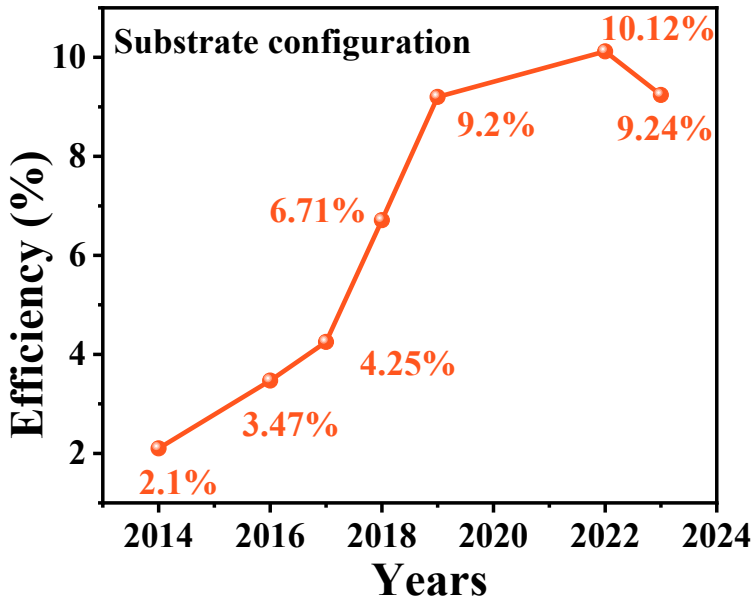

Figure 1.31 *The development history of PCE of substrate-structured Sb_2Se_3 thin-film solar cells.*

1.5 Conclusion and motivations

Sb_2Se_3 shows promising potential for the development of stable, non-toxic, cost-effective, and high-efficiency thin-film solar cells. The efficiency of Sb_2Se_3 thin-film solar cells has dramatically increased from 2.26% to 10.57% within only several years. However, in comparison to other mainstream solar cells such as c-Si, GaAs, CIGS, and CdTe, etc., the highest efficiency of Sb_2Se_3 thin-film solar cells remains considerably lower than the theoretical value and far inferior to that of the well-studied CIGS thin-film solar cells (23.6%). Several significant influencing factors indeed hinder the enhancement of device efficiency. Specifically, an outstanding heterojunction with optimized band alignment, effective carrier characteristics, and a suitable buffer layer is undeniably essential for achieving high efficiency in thin-film solar cells.

The objectives of this PhD work have been the following:

1) To optimize the interfacial band alignment of Sb_2Se_3/ CdS:Al heterojunction.

2) To optimize the absorber quality of Sb_2Se_3 thin-film solar cells by using rapid thermal processing (RTP) to improve the quality of the absorber layer.

3) To replace the toxic CdS film with a more environmentally friendly buffer layer, such as ZnSnO.

1.6 References

[1] IEA, World Energy Outlook 2023. 2023.

[2] MacDougall, A. H., Friedlingstein, P., The origin and limits of the near proportionality between climate warming and cumulative CO_2 emissions. *J. Clim.* 2015, 28(10), 4217-4230.

[3] Trenberth, K. E., Fasullo, J. T., Balmaseda, M. A., Earth's energy imbalance. *J. Clim.* 2014, 27(9), 3129-3144.

[4] Herzog, A. V., Lipman, T. E., Edwards, J. L., Kammen, D. M., Renewable energy: A viable choice. *Environ.: Sci. Policy Sustainable Dev.* 2001, 43, 20-8.

[5] Panwar, N. L., Kaushik, S. C., Kothari, S., Role of renewable energy sources in environmental protection: A review. *Renewable Sustainable Energy Rev.* 2011, 15(3), 1513-1524.

[6] Kannan, N., Vakeesan, D., Solar energy for future world: - A review. *Renewable Sustainable Energy Rev.* 2016, 62, 1092-1105.

[7] Rabaia, M. K. H., Abdelkareem, M. A., Sayed, E. T., Elsaid, K., Chae, K.-J., Wilberforce, T., Olabi, A. G., Environmental impacts of solar energy systems: A review. *Sci. Total Environ.* 2021, 754, 141989.

[8] IPCC, Renewable energy sources and climate change mitigation. 2024.

[9] Masters, G. M., The Solar Resource. In *Renewable and efficient Electric power systems*, 2004; pp 385-443.

[10] Shockley, W., Queisser, H. J., Detailed balance limit of efficiency of p-n junction solar cells. *J. Appl. Phys.* 1961, 32(3), 510-519.

[11] Nelson, J. A., *The physics of solar cells*. World Scientific Publishing Company: 2003.

[12] Green, M. A., Dunlop, E. D., Yoshita, M., Kopidakis, N., Bothe, K., Siefer, G., Hinken, D., Rauer, M., Hohl-Ebinger, J., Hao, X., Solar cell efficiency tables (Version 64). 2024, 32(7), 425-441.

[13] IEA, Clean Energy Market Monitor-March2024, IEA. *Paris https://www.iea.org/reports/clean-energy-market-monitor-march-2024* 2024, Licence: CC BY 4.0.

[14] Becquerel, M. E., Mémoire sur les effets électriques produits sous l'influence des rayons solaires.

C.R. Hebd. Seances Acad. Sci. 1839, 9, 561-567.

[15] Kapil, A., A Study on Einstein's explanation and Applications of photoelectric effect. 2015.

[16] https://www.nrel.gov/pv/interactive-cell-efficiency.html, CdTe-CIGS-PCE-NREL. 2024.

[17] Chapin, D. M., Fuller, C. S., Pearson, G. L., A new silicon p-n junction photocell for converting solar radiation into electrical power. *J. Appl. Phys.* 1954, 25(5), 676-677.

[18] Ziar, H., A global statistical assessment of designing silicon-based solar cells for geographical markets. *Joule* 2024, 8(6), 1667-1690.

[19] Lin, H., Yang, M., Ru, X. N., Wang, G. S., Yin, S., Peng, F. G., Hong, C. J., Qu, M. H., Lu, J. X., Fang, L., Han, C., Procel, P., Isabella, O., Gao, P. Q., Li, Z. G., Xu, X. X., Silicon heterojunction solar cells with up to 26.81% efficiency achieved by electrically optimized nanocrystalline-silicon hole contact layers. *Nat. Energy* 2023, 8(8), 789-799.

[20] Staebler, D. L., Wronski, C. R., Reversible conductivity changes in discharge-produced amorphous Si. *Appl. Phys. Lett.* 1977, 31(4), 292-294.

[21] Feng, Y., Wang, T. W., Yu, M. Z., Huang, J., Li, W., Hao, X., Zhang, J. Q., Wu, L. L., Coevaporated $Cd_{1-x}Mg_xTe$ thin films for CdTe solar cells. *Renewable Energy* 2020, 145, 13-20.

[22] Geisz, J. F., Friedman, D. J., Ward, J. S., Duda, A., Olavarria, W. J., Moriarty, T. E., Kiehl, J. T., Romero, M. J., Norman, A. G., Jones, K. M., 40.8% efficient inverted triple-junction solar cell with two independently metamorphic junctions. *Appl. Phys. Lett.* 2008, 93(12).

[23] Jackson, P., Hariskos, D., Lotter, E., Paetel, S., Wuerz, R., Menner, R., Wischmann, W., Powalla, M., New world record efficiency for $Cu(In,Ga)Se_2$ thin-film solar cells beyond 20%. *Prog. Photovoltaics Res. Appl.* 2011, 19(7), 894-897.

[24] Chopra, K. L., Paulson, P. D., Dutta, V., Thin-film solar cells: an overview. *Prog. Photovolt: Res. Appl.* 2004, 12(2-3), 69-92.

[25] Osbel Almora, D. B., Guillermo C. Bazan, Carlos I. Cabrera, Sule Erten-Ela, Karen Forberich, Fei Guo, Jens Hauch, Anita W. Y. Ho-Baillie, T. Jesper Jacobsson, Rene A. J. Janssen, Thomas Kirchartz, Nikos Kopidakis, Maria A. Loi, Richard R. Lunt, Xavier Mathew, Michael D. McGehee, Jie Min, David B. Mitzi, Mohammad K. Nazeeruddin, Jenny Nelson, Ana F. Nogueira, Ulrich W. Paetzold, Barry P. Rand, Uwe Rau, Henry J. Snaith, Eva Unger, Lídice Vaillant-Roca, Chenchen Yang, Hin-Lap Yip, and Christoph J. Brabec*, Device Performance of Emerging Photovoltaic Materials (Version 3). *Adv. Energy*

Mater. 2023, (2203313).

[26] Almora, O., Baran, D., Bazan, G. C., Berger, C., Cabrera, C. I., Catchpole, K. R., Erten-Ela, S., Guo, F., Hauch, J., Ho-Baillie, A. W. Y., Jacobsson, T. J., Janssen, R. A. J., Kirchartz, T., Kopidakis, N., Li, Y. F., Loi, M. A., Lunt, R. R., Mathew, X., McGehee, M. D., Min, J., Mitzi, D. B., Nazeeruddin, M. K., Nelson, J., Nogueira, A. F., Paetzold, U. W., Park, N.-G., Rand, B. P., Rau, U., Snaith, H. J., Unger, E., Vaillant-Roca, L., Yip, H. L., Brabec, C. J., Device performance of emerging photovoltaic materials (Version 1). *Adv. Energy Mater.* 2021, 11(11), 2002774.

[27] Rühle, S., Tabulated values of the Shockley–Queisser limit for single junction solar cells. *Sol. Energy* 2016, 130, 139-147.

[28] Romeo, A., Artegiani, E., CdTe-Based Thin Film Solar Cells: Past, Present and Future. *Energies* 2021, 14(6), 1684.

[29] Powalla, M., Paetel, S., Ahlswede, E., Wuerz, R., Wessendorf, C. D., Magorian Friedlmeier, T. J. A. P. R., Thin-film solar cells exceeding 22% solar cell efficiency: An overview on CdTe-, Cu(In,Ga)Se_2-, and perovskite-based materials. *Appl. Phys. Rev.* 2018, 5(4), 041602.

[30] Ma, J., Kuciauskas, D., Albin, D., Bhattacharya, R., Reese, M., Barnes, T., Li, J. V., Gessert, T., Wei, S.-H., Dependence of the minority-carrier lifetime on the stoichiometry of CdTe using time-resolved photoluminescence and first-principles calculations. *Phys. Rev. Lett.* 2013, 111(6), 067402.

[31] Burst, J. M., Duenow, J. N., Albin, D. S., Colegrove, E., Reese, M. O., Aguiar, J. A., Jiang, C. S., Patel, M. K., Al-Jassim, M. M., Kuciauskas, D., Swain, S., Ablekim, T., Lynn, K. G., Metzger, W. K., CdTe solar cells with open-circuit voltage breaking the 1 V barrier. *Nat. Energy* 2016, 1(3), 16015.

[32] Jensen, S. A., Burst, J. M., Duenow, J. N., Guthrey, H. L., Moseley, J., Moutinho, H. R., Johnston, S. W., Kanevce, A., Al-Jassim, M. M., Metzger, W. K., Long carrier lifetimes in large-grain polycrystalline CdTe without $CdCl_2$. *Appl. Phys. Lett.* 2016, 108(26), 263903.

[33] Yang, J. H., Park, J. S., Kang, J., Metzger, W., Barnes, T., Wei, S. H., Tuning the Fermi level beyond the equilibrium doping limit through quenching: The case of CdTe. *PhRvB* 2014, 90(24), 245202.

[34] Cusano, D. A., CdTe solar cells and photovoltaic heterojunctions in II–VI compounds. *Solid·State Electron.* 1963, 6(3), 217-232.

[35] Bonnet, D., Rabenhorst, H., New Results on the Development of a Thin Film p-CdTe/n-CdS Heterojunction Solar Cell. *Proceedings of the 9th Photovoltaic Specialists Conference* 1972, 129-131.

[36] Tyan, Y. S., Perez-Albuerne, E. A. In *Efficient thin-film CdS/CdTe solar cells*, 1982; pp 794-800.

[37] Britt, J., Ferekides, C., Thin-film CdS/CdTe solar cell with 15.8% efficiency. *Appl. Phys. Lett.* 1993, 62(22), 2851-2852.

[38] Wu, X., Asher, S., Levi, D. H., King, D. E., Yan, Y., Gessert, T. A., Sheldon, P., Interdiffusion of CdS and Zn_2SnO_4 layers and its application in CdS/CdTe polycrystalline thin-film solar cells. *J. Appl. Phys.* 2001, 89(8), 4564-4569.

[39] Wu, X. Z., High-efficiency polycrystalline CdTe thin-film solar cells. *Sol. Energy* 2004, 77(6), 803-814.

[40] Osborne, M., First Solar pushes CdTe cell efficiency to record 22.1%. https://www.pv-tech.org/first-solar-pushes-cdte-cell-efficiency-to-record-22-1/. *Thin-Film* 2016.

[41] https://www.nrel.gov/pv/cadmium-telluride-solar-cells.html, CdTe configuration. 2024.

[42] Ramanujam, J., Bishop, D. M., Todorov, T. K., Gunawan, O., Rath, J., Nekovei, R., Artegiani, E., Romeo, A., Flexible CIGS, CdTe and a-Si:H based thin film solar cells: A review. *Prog. Mater Sci.* 2020, 110, 100619.

[43] Kazmerski, L. L., White, F. R., Morgan, G. K., Thin-film $CuInSe_2$/CdS heterojunction solar cells. *Appl. Phys. Lett.* 1976, 29(4), 268-270.

[44] Mickelsen, R. A., Chen, W. S. In *Development of a 9.4% efficient thin-film $CuInSe_2$/CdS solar cell*, Photovoltaic Specialists Conference, 1981; pp 800-804.

[45] Islam, S., Rashid, M. J., Akhtaruzzaman, M., Takashi, S., Kazmi, J., Karim, M. R., Alnaser, I. A., Sobayel, K., Exploration of $Cd_{1-x}Zn_xSe$ as a window layer for CIGS based solar cell with PEDOT: PSS as back surface field layer. *Materials Research Express* 2024, 10, 126405.

[46] Mickelsen, R. A., Chen, W. S., Hsiao, Y. R., Lowe, V. E., Polycrystalline thin-film $CuInSe_2$/CdZnS solar cells. *IEEE Trans. Electron Devices* 1984, 31(5), 542-546.

[47] Rockett, A., Granath, K., Asher, S., Al Jassim, M. M., Hasoon, F., Matson, R., Basol, B., Kapur, V., Britt, J. S., Gillespie, T., Marshall, C., Na incorporation in Mo and $CuInSe_2$ from production processes. *Sol. Energy Mater. Sol. Cells* 1999, 59(3), 255-264.

[48] Ramanujam, J., Singh, U. P., Copper indium gallium selenide based solar cells – a review. *Energy Environ. Sci.* 2017, 10(6), 1306-1319.

[49] Gabor, A. M., Tuttle, J. R., Albin, D. S., Contreras, M. A., Noufi, R., Hermann, A. M., High-

efficiency CuInxGa$_{1-x}$Se$_2$ solar cells made from (In$_x$,Ga$_{1-x}$)$_2$Se$_3$ precursor films. *Appl. Phys. Lett.* 1994, 65(2), 198-200.

[50] Hadke, S., Huang, M. L., Chen, C., Tay, Y. F., Chen, S. Y., Tang, J., Wong, L., Emerging chalcogenide thin films for solar energy harvesting devices. *Chem. Rev.* 2022, 122(11), 10170-10265.

[51] Zhou, Y., Leng, M. Y., Xia, Z., Zhong, J., Song, H. B., Liu, X. S., Yang, B., Zhang, J. P., Chen, J., Zhou, K. H., Han, J. B., Cheng, Y. B., Tang, J., Solution-processed antimony selenide heterojunction solar cells. *Adv. Energy Mater.* 2014, 4(8), 1301846.

[52] Madelung, O., *Semiconductors*. 3 ed.; Springer Science & Business Media: 2012; p XIV, 691.

[53] Zeng, K., Xue, D. J., Tang, J., Antimony selenide thin-film solar cells. *Semicond. Sci. Technol.* 2016, 31(6).

[54] Choi, Y. C., Mandal, T. N., Yang, W. S., Lee, Y. H., Im, S. H., Noh, J. H., Seok, S. I., Sb$_2$Se$_3$-sensitized inorganic-organic heterojunction solar cells fabricated using a single-source precursor. *Angew. Chem. Int. Ed. Engl.* 2014, 53(5), 1329-1333.

[55] Mavlonov, A., Razykov, T., Raziq, F., Gan, J., Chantana, J., Kawano, Y., Nishimura, T., Wei, H., Zakutayev, A., Minemoto, T., Zu, X., Li, S., Qiao, L., A review of Sb$_2$Se$_3$ photovoltaic absorber materials and thin-film solar cells. *Sol. Energy* 2020, 201, 227-246.

[56] Wang, C., Lu, S., Li, S., Wang, S., Lin, X., Zhang, J., Kondrotas, R., Li, K., Chen, C., Tang, J., relative dielectric Efficiency improvement of flexible Sb2Se3 solar cells with non-toxic buffer layer via interface engineering. *Nano Energy* 2020, 71.

[57] Chen, C., Bobela, D. C., Yang, Y., Lu, S. C., Zeng, K., Ge, C., Yang, B., Gao, L., Zhao, Y., Beard, M. C., Tang, J., diffusion length - Characterization of basic physical properties of Sb$_2$Se$_3$ and its relevance for photovoltaics. *Front. Optoelectron.* 2017, 10(1), 18-30.

[58] Zhou, Y., Wang, L., Chen, S. Y., Qin, S. K., Liu, X. S., Chen, J., Xue, D. J., Luo, M., Cao, Y. Z., Cheng, Y. B., Sargent, E. H., Tang, J., 5.6% RTP-Thin-film Sb$_2$Se$_3$ photovoltaics with oriented one-dimensional ribbons and benign grain boundaries. *Nature Photonics* 2015, 9(6), 409-415.

[59] Chen, C., Li, K. H., Tang, J., Sb$_2$Se$_3$-Ten years of Sb$_2$Se$_3$ thin film solar cells. *Solar RRL* 2022, 6(2200094).

[60] *Mineral commodity summaries 2020*; Reston, VA, 2020; p 204.

[61] *Mineral commodity summaries 2023*; Reston, VA, 2023.

[62] Mavlonov, A., Razykov, T., Raziq, F., Gan, J. T., Chantana, J., Kawano, Y., Nishimura, T., Wei, H. M., Zakutayev, A., Minemoto, T., Zu, X. T., Li, S. A., Qiao, L., A review of Sb_2Se_3 photovoltaic absorber materials and thin-film solar cells. *Sol. Energy* 2016, 201, 227-246.

[63] Chen, C., Bobela, D. C., Yang, Y., Lu, S. C., Zeng, K., Ge, C., Yang, B., Gao, L., Zhao, Y., Beard, M. C., Tang, J., Characterization of basic physical properties of Sb_2Se_3 and its relevance for photovoltaics. *Frontiers of Optoelectronics* 2017, 10(1), 18-30.

[64] Chen, C., Li, W. Q., Zhou, Y., Chen, C., Luo, M., Liu, X. S., Zeng, K., Yang, B., Zhang, C. W., Han, J. B., Tang, J., Optical properties of amorphous and polycrystalline Sb_2Se_3 thin films prepared by thermal evaporation. *Appl. Phys. Lett.* 2015, 107(4).

[65] Chen, C., Tang, J., Open-circuit voltage loss of antimony chalcogenide solar cells: status, origin, and possible solutions. *ACS Energy Lett.* 2020, 5(7), 2294-2304.

[66] Lei, H., Chen, J., Tan, Z., Fang, G., Review of Recent Progress in Antimony Chalcogenide-Based Solar Cells: Materials and Devices. *Solar Rrl* 2019, 3(6).

[67] Mo, A. M., Feng, Y., Yang, B. X., Dang, W., Liang, X. Y., Cao, W. J., Guo, Y. N., Chen, T., Li, Z. Q., Controlling unintentional defects enables high-efficient antimony selenide solar cells. *Adv. Funct. Mater.* 2024, 34(29), 2316292.

[68] Lian, W. T., Cao, R., Li, G., Cai, H. L., Cai, Z. Y., Tang, R. F., Zhu, C. F., Yang, S. F., Chen, T., Distinctive deep-level defects in non-stoichiometric Sb_2Se_3 photovoltaic materials. *Adv. Sci.* 2022, 9(9), 2105268.

[69] Huang, M. L., Xu, P., Han, D., Tang, J., Chen, S. Y., Complicated and unconventional defect properties of the quasi-one-dimensional photovoltaic semiconductor Sb_2Se_3. *ACS Appl. Mater. Interfaces* 2019, 11(17), 15564-15572.

[70] Liu, X. S., Chen, J., Luo, M., Leng, M. Y., Xia, Z., Zhou, Y., Qin, S. K., Xue, D. J., Lv, L., Huang, H., Niu, D. M., Tang, J., Thermal evaporation and characterization of Sb_2Se_3 thin film for substrate Sb_2Se_3/CdS solar cells. *ACS Appl Mater Interfaces* 2014, 6(13), 10687-10695.

[71] Li, K. H., Chen, C., Lu, S. C., Wang, C., Wang, S. Y., Lu, Y., Tang, J., Orientation engineering in low-dimensional crystal-structural materials via seed screening. *Adv. Mater.* 2019, 31(44), 1903914.

[72] Liang, G. X., Zhang, X. H., Ma, H. L., Hu, J. G., Fan, B., Luo, Z. K., Zheng, Z. H., Luo, J. T., Fan, P., Facile preparation and enhanced photoelectrical performance of Sb_2Se_3 nano-rods by magnetron

sputtering deposition. *Sol. Energy Mater. Sol. Cells* 2017, 160, 257-262.

[73] Spaggiari, G., Pattini, F., Bersani, D., Calestani, D., De Iacovo, A., Gilioli, E., Mezzadri, F., Sala, A., Trevisi, G., Rampino, S., Growth and structural characterization of Sb_2Se_3 solar cells with vertical Sb_4Se_6 ribbon alignment by RF magnetron sputtering. *Journal of Physics D: Applied Physics* 2021, 54(38), 385502.

[74] Shongalova, A., Correia, M. R., Teixeira, J. P., Leitão, J. P., González, J. C., Ranjbar, S., Garud, S., Vermang, B., Cunha, J. M. V., Salomé, P. M. P., Fernandes, P. A., Growth of Sb_2Se_3 thin films by selenization of RF sputtered binary precursors. *Sol. Energy Mater. Sol. Cells* 2018, 187, 219-226.

[75] Wen, X. X., Chen, C., Lu, S. C., Li, K. H., Kondrotas, R., Zhao, Y., Chen, W. H., Gao, L., Wang, C., Zhang, J., Niu, G. D., Tang, J., Vapor transport deposition of antimony selenide thin film solar cells with 7.6% efficiency. *Nat. Commun.* 2018, 9(2179), 2179.

[76] Chen, M. D., Ishaq, M., Ren, D. L., Ma, H. L., Su, Z. H., Fan, P., Le Coq, D., Zhang, X. H., Liang, G. X., Chen, S., Interface optimization and defects suppression via NaF introduction enable efficient flexible Sb_2Se_3 thin-film solar cells. *J. Energy Chem.* 2024, 90, 165-175.

[77] Li, Z. Q., Liang, X. Y., Li, G., Liu, H. X., Zhang, H. Y., Guo, J. X., Chen, J. W., Shen, K., San, X. Y., Yu, W., Schropp, R. E. I., Mai, Y. H., 9.2%-efficient core-shell structured antimony selenide nanorod array solar cells. *Nat. Commun.* 2019, 10, 125.

[78] Li, D.-B., Yin, X., Grice, C. R., Guan, L., Song, Z., Wang, C., Chen, C., Li, K., Cimaroli, A. J., Awni, R. A., Zhao, D., Song, H., Tang, W., Yan, Y., Tang, J., 6.84% p-i-n-Stable and efficient CdS/Sb_2Se_3 solar cells prepared by scalable close space sublimation. *Nano Energy* 2018, 49, 346-353.

[79] Li, G., Li, Z. Q., Chen, J. W., Chen, X., Qiao, S., Wang, S. F., Xu, Y., Mai, Y. H., Self-powered, high-speed Sb_2Se_3/Si heterojunction photodetector with close spaced sublimation processed Sb_2Se_3 layer. *J. Alloys Compd.* 2018, 737, 67-73.

[80] Yang, K., Li, B., Zeng, G. G., Sb_2Se_3 thin film solar cells prepared by pulsed laser deposition. *Journal of Alloys Compounds* 2019, 821, 153505.

[81] Yu, L., Chen, J., Fu, Z.-W., Pulsed laser deposited heterogeneous mixture of Li_2Se–Sb_2Se_3 nanocomposite as a new storage lithium material. *Electrochim. Acta* 2010, 55(3), 1258-1264.

[82] Duan, Z. T., Liang, X. Y., Feng, Y., Ma, H. Y., Liang, B. L., Wang, Y., Luo, S. P., Wang, S. F., Schropp, R. E. I., Mai, Y. H., Li, Z. Q., Sb_2Se_3 thin-film solar cells exceeding 10% power conversion efficiency

enabled by injection vapor deposition technology. *Adv. Mater.* 2022, 34(30), 2202969.

[83] Razykov, T. M., Shukurov, A. X., Atabayev, O. K., Kuchkarov, K. M., Ergashev, B., Mavlonov, A. A., Growth and characterization of Sb_2Se_3 thin films for solar cells. *Sol. Energy* 2018, 173, 225-228.

[84] Zhao, Y. Q., Wang, S. Y., Li, C., Che, B., Chen, X. L., Chen, H. Y., Tang, R. F., Wang, X. M., Chen, G. L., Wang, T., Gong, J. B., Chen, T., Xiao, X. D., Li, J. M., Regulating deposition kinetics via a novel additive-assisted chemical bath deposition technology enables fabrication of 10.57%-efficiency Sb_2Se_3 solar cells. *Energy Environ. Sci.* 2022, 15, 5118-5128.

[85] Kim, J., Yang, W., Oh, Y., Lee, H., Lee, S., Shin, H., Kim, J., Moon, J., Self-oriented Sb_2Se_3 nanoneedle photocathodes for water splitting obtained by a simple spin-coating method. *J. Mater. Chem. A* 2017, 5(5), 2180-2187.

[86] Wang, X. M., Tang, R. F., Yin, Y. W., Ju, H. X., Li, S. A., Zhu, C. F., Chen, T., Interfacial engineering for high efficiency solution processed Sb_2Se_3 solar cells. *Sol. Energy Mater. Sol. Cells* 2019, 189, 5-10.

[87] Liu, D., Tang, R. F., Ma, Y. Y., Jiang, C. H., Lian, W. T., Li, G., Han, W. H., Zhu, C. F., Chen, T., Direct hydrothermal deposition of antimony triselenide films for efficient planar heterojunction solar cells. *ACS Appl. Mater. Interfaces* 2021, 13(16), 18856-18864.

[88] Chen, G. J., Luo, Y. D., Abbas, M., Ishaq, M., Zheng, Z. H., Chen, S., Su, Z. H., Zhang, X. H., Fan, P., Liang, G. X., Suppressing buried interface nonradiative recombination losses toward high-efficiency antimony triselenide solar cells. *Adv. Mater.* 2023, 36(5), 2308522.

[89] Luo, P., Imran, T., Ren, D. L., Zhao, J., Wu, K. W., Zeng, Y. J., Su, Z. H., Fan, P., Zhang, X. H., Liang, G. X., Chen, S., Electron transport layer engineering induced carrier dynamics optimization for efficient Cd-free Sb_2Se_3 thin-film solar cells. *Small* 2023, 20(4), 2306516.

[90] Lin, J. H., Chen, G. J., Ahmad, N., Muhammad, I., Chen, S., Su, Z. H., Fan, P., Zhang, X. H., Zhang, Y., Liang, G. X., Back contact interfacial modification mechanism in highly-efficient antimony selenide thin-film solar cells. *J. Energy Chem.* 2023, 80, 256-264.

[91] Luo, Y. D., Chen, M. D., Tang, R., Azam, M., Chen, S., Zheng, Z. H., Su, Z. H., Fan, P., Ma, H. L., Liang, G. X., Zhang, X. H., Energy band alignment for Cd-free antimony triselenide substrate structured solar cells by Co-sputtering ZnSnO buffer layer. *Sol. Energy Mater. Sol. Cells* 2022, 240, 111721.

[92] Lin, J. H., Mahmood, A., Chen, G. J., Ahmad, N., Chen, M. D., Fan, P., Chen, S., Tang, R., Liang, G. X., Crystallographic orientation control and defect passivation for high-efficient antimony selenide

thin-film solar cells. *Materials Today Physics* 2022, 27(100772), 100772.

[93] Liang, G. X., Chen, M. D., Ishaq, M., Li, X. R., Tang, R., Zheng, Z. H., Su, Z. H., Fan, P., Zhang, X. H., Chen, S., Crystal growth promotion and defects healing enable minimum open-circuit voltage deficit in antimony selenide solar cells. *Adv. Sci.* 2022, 9(9), 2105142.

[94] Liang, G. X., Luo, Y. D., Chen, S., Tang, R., Zheng, Z. H., Li, X. J., Liu, X. S., Liu, Y. K., Li, Y. F., Chen, X. Y., Su, Z. H., Zhang, X. H., Ma, H. L., Fan, P., Sputtered and selenized Sb_2Se_3 thin-film solar cells with open-circuit voltage exceeding 500 mV. *Nano Energy* 2020, 73, 104806.

[95] Guo, H. F., Zhao, C., Xing, Y. L., Tian, H. J., Yan, D. C., Zhang, S., Jia, X. G., Qiu, J. H., Yuan, N. Y., Ding, J. N., High-efficiency Sb_2Se_3 Solar cells modified by potassium hydroxide. *J. Phys. Chem. Lett.* 2021, 12, 12352-12359.

[96] Bhattacharya, R. N., Pramanik, P., A photoelectrochemical cell based on chemically deposited Sb_2Se_3 thin film electrode and dependence of deposition on various parameters. *SoEnM* 1982, 6, 317-322.

[97] Messina, S., Nair, M. T. S., Nair, P. K., Antimony selenide absorber thin films in all-chemically deposited solar cells. *Journal of The Electrochemical Society* 2009, 156(5), H327.

[98] Guijarro, N., Lutz, T., Lana-Villarreal, T., O'Mahony, F., Gómez, R., Haque, S. A., Toward antimony selenide sensitized solar cells: efficient charge photogeneration at spiro-ometad/Sb_2Se_3/metal oxide heterojunctions. *J. Phys. Chem. Lett.* 2012, 3(10), 1229-1421.

[99] Wang, L., Li, D. B., Li, K., Chen, C., Deng, H. X., Gao, L., Zhao, Y., Jiang, F., Li, L. Y., Huang, F., He, Y. S., Song, H. S., Niu, G. D., Tang, J., Stable 6%-efficient Sb_2Se_3 solar cells with a ZnO buffer layer. *Nat. Energy* 2017, 2(4).

[100] Chen, C., Wang, L., Gao, L., Nam, D., Li, D. B., Li, K. H., Zhao, Y., Ge, C., Cheong, H., Liu, H., Song, H. S., Tang, J., 6.5% certified efficiency Sb_2Se_3 solar cells using PbS colloidal quantum dot film as hole-transporting layer. *ACS Energy Lett.* 2017, 2(9), 2125-2132.

[101] Guo, H. F., Chen, Z. W., Wang, X., Cang, Q. F., Jia, X. G., Ma, C. H., Yuan, N. Y., Ding, J. N., Enhancement in the efficiency of Sb_2Se_3 thin-film solar cells by increasing carrier concertation and inducing columnar growth of the grains. *Solar RRL* 2018, 3(3), 1800224.

[102] Chen, C., Li, K. H., Chen, S. Y., Wang, L., Lu, S. C., Liu, Y. H., Li, D. B., Song, H. S., Tang, J., Efficiency improvement of Sb_2Se_3 solar cells via grain boundary inversion. *ACS Energy Lett.* 2018, 3(10),

2335-2341.

[103] Yuan, C. C., Zhang, L. J., Liu, W. F., Zhu, C. F., Rapid thermal process to fabricate Sb_2Se_3 thin film for solar cell application. *Sol. Energy* 2016, 137, 256-260.

[104] Li, Z. Q., Chen, X., Zhu, H. B., Chen, J. W., Guo, Y. T., Zhang, C., Zhang, W., Niu, X. N., Mai, Y. H., Sb_2Se_3 thin film solar cells in substrate configuration and the back contact selenization. *Sol. Energy Mater. Sol. Cells* 2017, 161, 190-196.

[105] Li, G., Li, Z. Q., Liang, X. Y., Guo, C. S., Shen, K., Mai, Y. H., Improvement in Sb_2Se_3 solar cell efficiency through band alignment engineering at the buffer/absorber interface. *ACS Appl Mater Interfaces* 2019, 11(1), 828-834.

[106] Tang, R., Zheng, Z. H., Su, Z. H., Li, X.-J., Wei, Y.-D., Zhang, X. H., Fu, Y. Q., Luo, J., Fan, P., Liang, G. X., Highly efficient and stable planar heterojunction solar cell based on sputtered and post-selenized Sb_2Se_3 thin film. *Nano Energy* 2019, 64(103929), 103929.

[107] Tang, R., Chen, S., Zheng, Z. H., Su, Z. H., Luo, J. T., Fan, P., Zhang, X. H., Tang, J., Liang, G. X., Heterojunction annealing enabling record open-circuit voltage in antimony triselenide solar cells. *Adv. Mater.* 2022, 34(14), 2109078.

Chapter II: Sb_2Se_3 thin-film solar cells using Al^{3+} doped CdS buffer layer

2.1 Introduction

As a promising environment-friendly light-absorbing semiconductor material, antimony selenide (Sb_2Se_3) has attracted wide interest owing to its optoelectronic properties. Sb_2Se_3 thin film as a binary compound possesses a high light absorption coefficient (greater than 10^5 cm^{-1}), suitable direct bandgap (≈ 1.17 eV), and interesting carrier mobility (≈ 10 cm^2 V^{-1} s^{-1}).[1, 2] A single junction solar cell can yield a maximum theoretical power conversion efficiency (PCE) above 30% originating from the Shockley–Queisser detail-balance model.[3, 4] Covalently bonded $[Sb_4Se_6]_n$ ribbons are vertically stacked by van der Waals force interactions and form Sb_2Se_3 with a 1D crystal structure, exhibiting conspicuous anisotropic properties.[5] Furthermore, high constituent abundance, low toxicity, cost-effectiveness, and simple fabrication process facilitate the application of high-efficiency thin-film solar cells in large-scale manufacturing. In recent years, remarkable progress has been made in the PCE of Sb_2Se_3-based photovoltaic devices. To date, the efficiency of 9.2%,[6] 10.12%[2], and 10.57%[7] for the core–shell-structured, substrate-structured, and superstrate-structured Sb_2Se_3 thin-film solar cells were prepared through closed space sublimation (CSS), injection vapor deposition (IVD) and additive-assisted chemical bath deposition (CBD) method, respectively. Moreover, series connected antimony selenosulfide monolithic integrated photovoltaic modules have achieved a PCE of 7.43%.[8] However, the highest efficiency of Sb_2Se_3 thin-film solar cells remains considerably lower than the theoretical value and far inferior to that of the well-studied $CuInGaSe_2$ (CIGS) thin-film solar cells.

In fact, several major affecting factors impede improvement in device efficiency, such as defects at the bulk and interface, the band alignment of heterojunction, and the device structure.[9] Particularly for the substrate-structured Sb_2Se_3 thin-film solar cells, the buffer layer and absorber layer characteristics play a critical role in a desirable heterojunction.[10] An excellent heterojunction is obviously favored for optimizing band alignment and facilitating the generation, separation, and transportation efficiency of

charge carriers, thereby enhancing the optoelectronic performance of devices. According to previous works,[2, 11] CdS films are regarded as the most appreciable and effective buffer layers for high-quality heterojunctions in Sb_2Se_3 devices. However, some theoretical and experimental results pointed out that the main factor that deteriorates device performance is the high density of interfacial defects ($\approx 10^{11}$ cm^{-3})[12, 13] between Sb_2Se_3 and CdS. In addition, the unsatisfactory conduction band offset (CBO) at the Sb_2Se_3/CdS heterojunction was deemed a major limiting factor for device performance enhancement. A number of approaches, such as interfacial modification and element doping, have been used to improve heterojunction quality, enhance carrier transport, and minimize recombination. In this regard, incorporating doping elements, such as oxygen (O),[14] potassium (K),[15] zinc (Zn),[16] and indium (In),[17] presents a positive effect that optimizes the energy band alignment between Sb_2Se_3 absorber layer and CdS buffer layer. For example, it has demonstrated that the introduction of Zn could promote tuning interface band alignment and carrier transport, and thus the short–circuit current density was visibly enhanced.[16] The CdS:In buffer layer with an enlarged bandgap (the bandgaps of CdS and In:CdS thin film are estimated to be 2.36 and 2.40 eV) can effectively reduce charge recombination and result in efficient charge transport.[17] In addition, doping O elements into the CdS buffer layer can effectively modify the band alignment from a “cliff-like” structure to a “spike-like” structure at the CdS:O/Sb_2Se_3 interface.[14] Thus, doping appropriate elements into the CdS layer can be considered as an effective approach for optimizing heterojunction quality and improving efficiency.

In this chapter, heterojunction quality and the performance of Sb_2Se_3 thin-film solar cells were efficiently enhanced by incorporating Al^{3+} cations into the CdS buffer layer. The modified optoelectronic properties and corresponding improvement in the mechanism were systematically studied, and the effect of Al^{3+} doping on bandgap alignment tuning and carrier transport dynamics within Sb_2Se_3/CdS:Al solar cells were carefully investigated.

2.2 Preparation of Sb_2Se_3 thin-film solar cells

2.2.1 Preparation of Sb_2Se_3 absorber layer

Mo-coated glass as a back contact layer was employed for the Sb_2Se_3 solar cells fabrication. An effective combination reaction involving RF magnetron sputtering and selenization of Sb metallic precursors was used for fabricating Sb_2Se_3 thin films, as shown in Figure 2.1. The Mo-coated glass was entirely cleaned in an ultrasonic bath using detergent, ethanol, and deionized water. Before the magnetron sputtering process, the back pressure of the vacuum chamber was kept below 7.0×10^{-4} Pa. The optimized sputtering power and pressure were set at 35 W and 0.5 Pa to reach high-quality Sb thin film with fewer voids and benign adhesion. The flow rate of argon was 30 sccm, and the sputtering process was conducted for 40 min.

Sequentially, an effective post-selenization heat treatment was applied to induce in-situ combination reaction and self-assembled growth of Sb_2Se_3 thin films with high crystallinity. As depicted in Figure 2.1a, the sputtered precursors and 0.2 g of selenium (Se) powder with high purity (> 99.99%) were separately placed into the chambers of a vacuum tubular furnace for selenization. The chambers were evacuated using a mechanical pump before introducing high-purity argon (Ar) gas. During the annealing process, the working pressure of the two chambers was kept at 5×10^4 Pa. Both the Se powder side temperature and the Sb precursor side temperature were kept at 410 °C and ramped up to the set values at a heating rate of 20 °C/min. The furnace was naturally cooled down to room temperature once the selenization was finished.

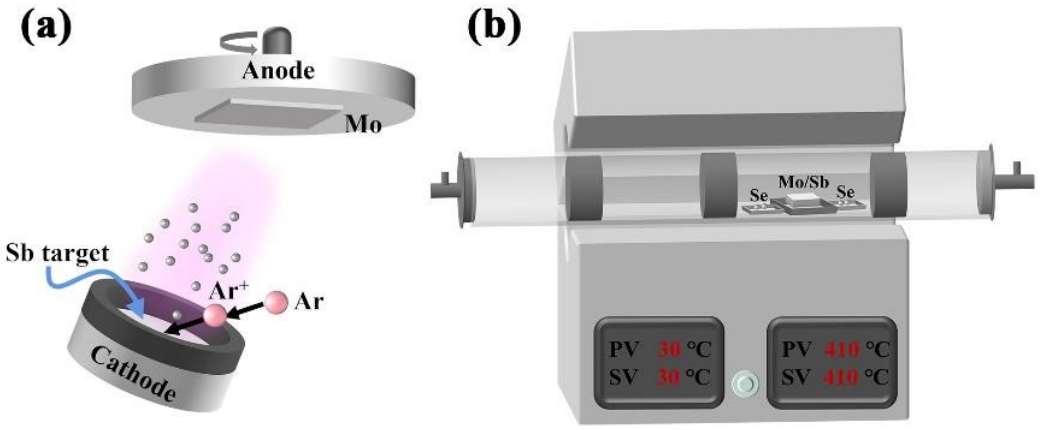

Figure 2.1 *Schematic diagram of the preparation process of Sb_2Se_3 thin films. (a) RF magnetron sputtering process for Sb precursor thin film. (b) Selenization heat treatment for Sb_2Se_3 thin film[18].*

2.2.2 Preparation of CdS:Al buffer layer

After finishing the preparation of the Sb_2Se_3 absorber layer, the pristine cadmium sulfide (CdS) buffer layer was then deposited onto the well-crystalline Sb_2Se_3 thin film employing the chemical bath deposition (CBD) technique. The aqueous solution of $CdSO_4$ (0.015 M), thiourea (0.75 M), and ammonium hydroxide (≥ 28%) were subsequently added to deionized water. The samples were fully stirred into the well-mixed solution that was then placed in a preheated 80°C water bath with continuous stirring for 9 min. After completing the chemical reaction, the samples were rinsed with deionized water and dried in an oven at around 60°C.

For Al doping, appropriate amount of $AlCl_3$ (99.999%, Aladdin) powder was weighed and completely dissolved in an organic solvent of 2-methoxy ethanol to prepare Al^{3+} solution with variable concentration, i.e., 0.1, 0.3, 0.5, and 0.7 M. Different concentration Al^{3+} solution was spin-coated on the surface of Sb_2Se_3/CdS film and then heat treatment was conducted on a hot plate at various temperatures (i.e., 260, 280, 300, and 320 °C) and for different durations (i.e., 1, 3, 5, and 7 min). A schematic illustration of Al-doped CdS film deposition via spin coating and post-annealing process is depicted in Figure 2.2. The thickness of the Al-doped CdS buffer layer was ≈ 70 nm.

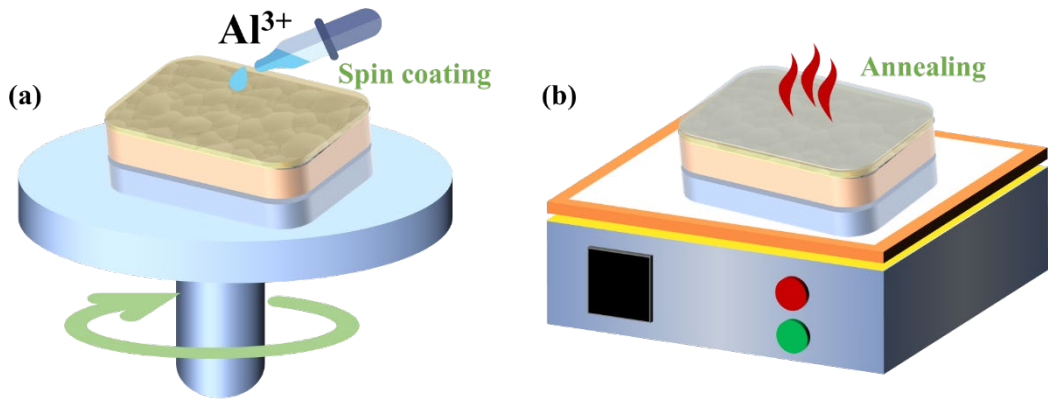

Figure 2.2 *A schematic illustration of Al-doped CdS film deposition: (a) spin coating and (b) subsequent post-annealing process.*

2.2.3 Preparation of the whole thin-film solar cells

Indium tin oxide (ITO), used as a windows layer, was subsequently covered on the surface of the Al-doped CdS film via direct current (DC) magnetron sputtering method. The sputtering procedure was performed with a power of 120 W, and a relatively low deposition pressure of 0.4 Pa. Pure Ar gas and oxygen (O_2) gas were introduced at a flow rate of 40 and 30 sccm, respectively. The surface of the device was divided into small squares with an identical active area of 0.075 cm^2. Ag electrodes were thermally evaporated onto the ITO surface to form metallic contact. Figure 2.3 shows a schematic diagram of the fabrication process of this thin-film solar cell with the configuration of Glass/Mo/Sb_2Se_3/CdS:Al/ITO/Ag. It is important to note that the pristine CdS thin films were utilized as the buffer layer to construct a device with the configuration of Glass/Mo/Sb_2Se_3/CdS/ITO/Ag for comparative purposes.

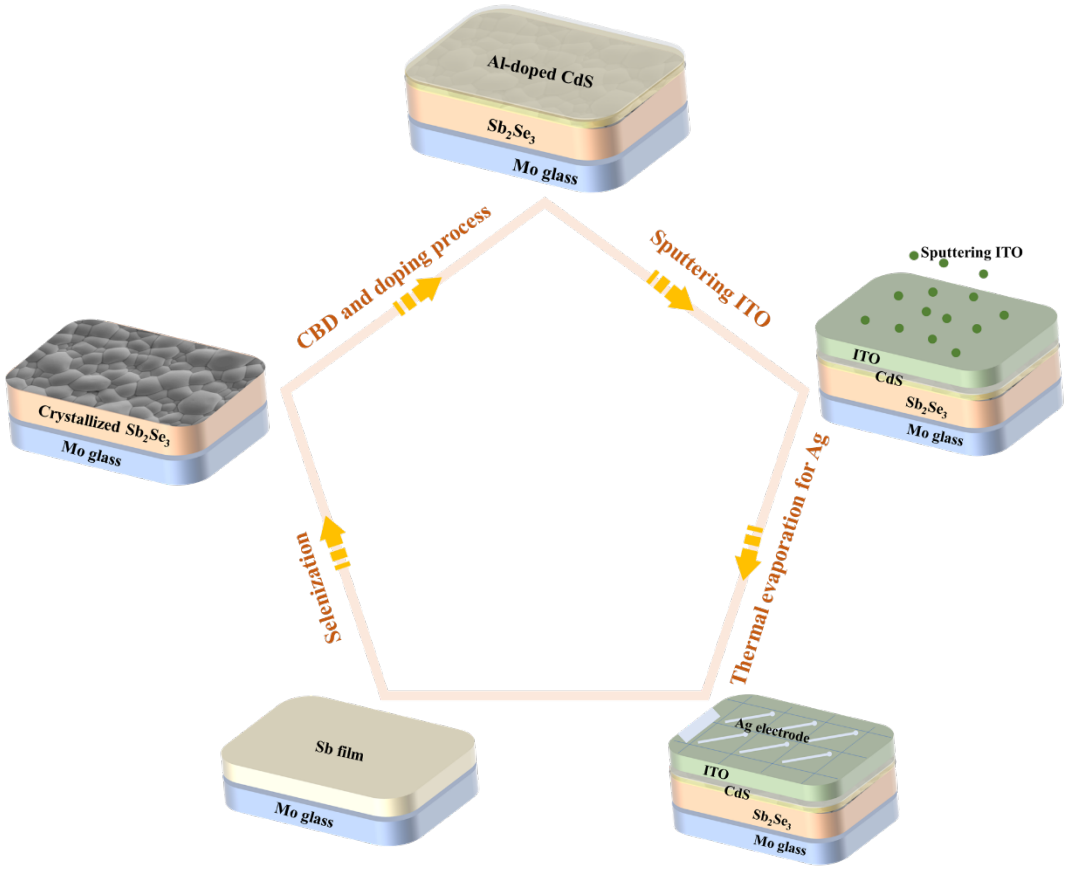

Figure 2.3 *Schematic illustration of the preparation process of the substrate structured Sb_2Se_3/CdS:Al thin-film solar cells.*

2.3 Characterization of Sb_2Se_3 absorber layer

2.3.1 X-ray diffraction (XRD) analysis

The crystal structure of the Sb_2Se_3 thin film and crystal orientation and crystallinity were characterized through XRD analysis. The XRD pattern of the Sb_2Se_3 absorber layer is provided in Figure 2.4. Distinctly, the diffraction peaks of the as-prepared Sb_2Se_3 thin film matched well with the information provided by orthorhombic Sb_2Se_3 (JCPDS Card No. 15–0861) without any secondary phase, suggesting the absence of detectable impurities. As Sb_2Se_3 consists of covalently bonded $[Sb_4Se_6]_n$ ribbons stacked by van der Waals force, an appropriate crystallographic orientation is critical to control the crystalline quality of Sb_2Se_3 thin films and their charge carrier transport

ability.[19] Three prominent diffraction peaks: (221), (211), and (002) demonstrated preferential crystallographic orientation along (hk1) of the Sb_2Se_3 thin film. Sb_2Se_3 crystal grains grown along the (hk1) orientation are conducive to the transport of photoexcited carriers.[10, 20] Thus, the as-fabricated Sb_2Se_3 thin film is theoretically a promising material that could reduce interfacial recombination and improves device performance.

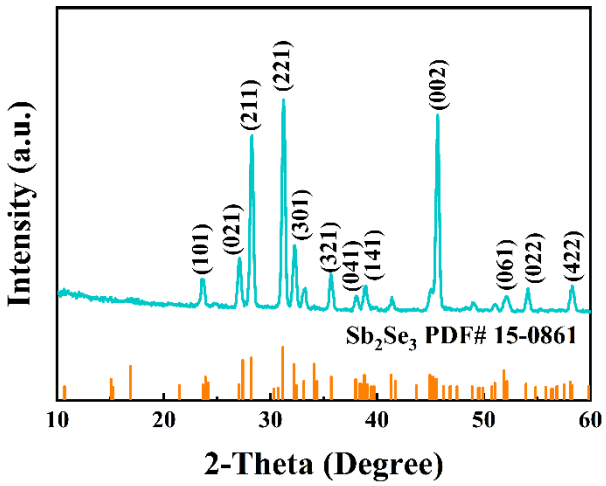

Figure 2.4 *XRD patterns of Sb_2Se_3 absorber thin films.*

2.3.2 Scanning electron microscope (SEM) analysis

The SEM top-view image is shown in Figure 2.5. Highly crystalline, compact, and uniform surface is observed, along with the absence of visible voids. We analyzed the grain size distribution using the SEM image. The detailed frequency histogram versus Sb_2Se_3 grain size distribution is depicted in Figure 2.6. The average grain size was ≈ 1.2 µm, which was comparable to the thickness of the absorber layer, indicating effective restraining of recombination losses resulting from the grain boundaries. Therefore, a high-quality Sb_2Se_3 absorber layer with a preferred orientation, high crystallinity, and compact, uniform, and large crystal grains was obtained, which could be favorable for improved device performance.

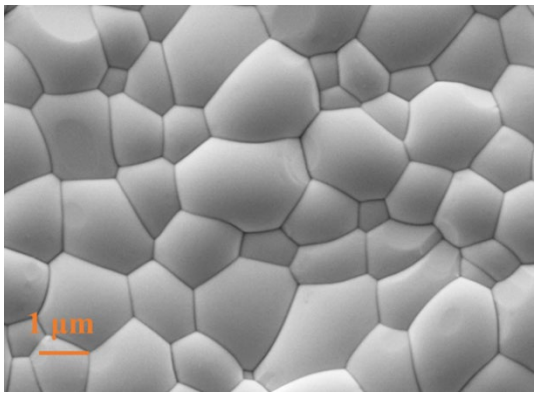

Figure 2.5 *Top-view SEM image of Sb_2Se_3 absorber thin films.*

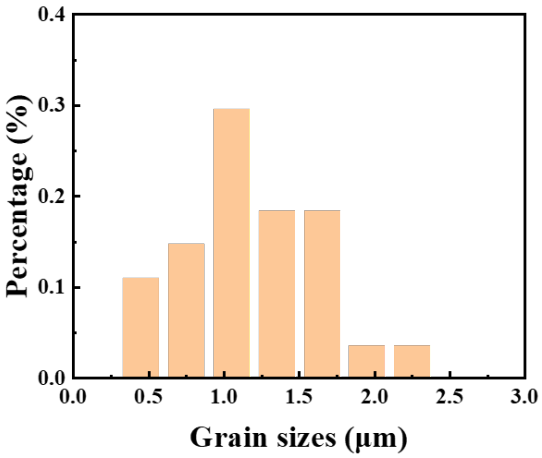

Figure 2.6 *Grain size distributions of the Sb_2Se_3 thin films.*

2.4 Investigation of CdS:Al buffer layer

2.4.1 Optimization of CdS:Al buffer layer

Apart from the absorber layer, the buffer layer is a key factor for improving device performance. Herein, a deep investigation of CdS:Al thin films was carried out to optimize the heterojunction. To evaluate the applicability of Al doping, various Al concentration-dependent Sb_2Se_3 thin-film solar cells were prepared with the substrate configuration Mo/Sb_2Se_3/CdS:Al/ITO/Ag. Annealing treatment has been proven to be an indispensable factor in obtaining high-quality Al-doped CdS thin films.[21] Therefore, the effect of annealing temperature and duration was first investigated to optimize the

annealing treatment process. Various devices were fabricated by using four different annealing temperatures of CdS:Al films. Obviously, this group of efficiency boxes shows a maximum, and the device with 280 °C-annealing for CdS:Al film was at the top with the highest PCE (Figure 2.7). At the same time, the corresponding average values of FF and J_{SC} are higher than other groups of annealing temperatures for CdS:Al film.

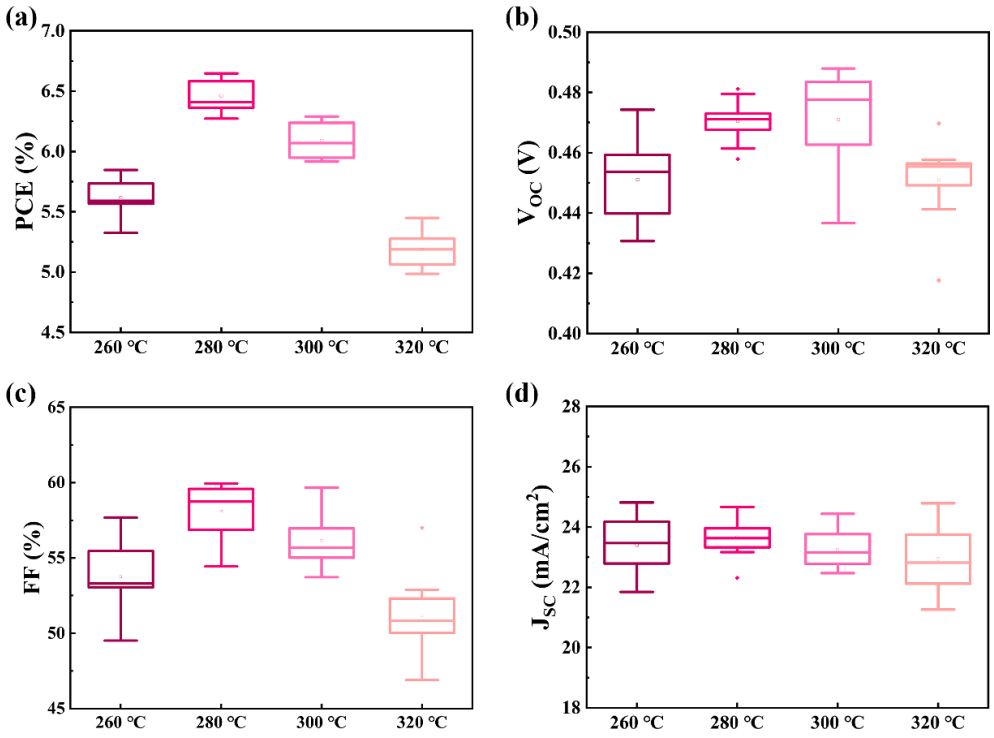

Figure 2.7 *Statistical boxplots of (a) PCE; (b) V_{OC}; (c) FF; (d) J_{SC} for Sb_2Se_3 solar cells based on Al-doped CdS buffer layer as a function of annealing temperatures. The edges of the box represent the 25th and 75th percentiles; the whisker length defines the upper inner and lower inner fence values; the line in the middle of the box marks out the median value, and the crosses the minimum and maximum values.*

Similarly, the annealing durations were studied and the results are summarized in Figure 2.8. An overall improvement in device performance, especially the PCE was obtained for the device with 5 min annealing of CdS:Al films. In summary, an optimized annealing temperature of 280 °C and annealing time of 5 min are found through systematic investigation for improving the photovoltaic performance.

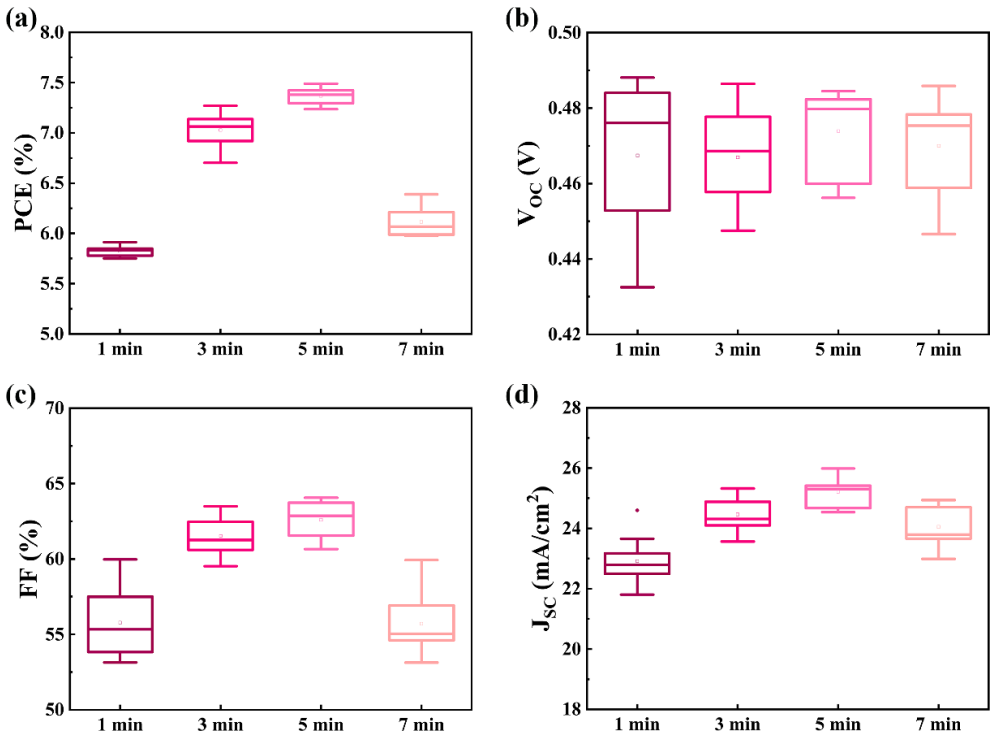

Figure 2.8 *Statistical boxplots of (a) PCE; (b) V_{OC}; (c) FF; (d) J_{SC} for Sb_2Se_3 solar cells based on Al-doped CdS buffer layer as a function of annealing durations.*

The pristine CdS-based sample and the Al^{3+} doped counterparts with various concentrations (i.e., 0.1, 0.3, 0.5, and 0.7 M), labeled as A0, A1, A2, A3, and A4, have been used to fabricated substrate structured solar cells with configuration of Mo/Sb_2Se_3/CdS/ITO/Ag or Mo/Sb_2Se_3/CdS:Al/ITO/Ag to examine the impact of the Al^{3+} doping. The statistical distributions of the key performance parameters of devices are presented in Figure 2.9a–d and Table 2.1. It was found that the PCE revealed a gradual enhancement with increasing Al concentration from 0.1 to 0.5 M and then dramatically decreased under a high doping concentration of 0.7 M. The variation tendency of FF and J_{SC} of all the devices was semblable, implying that excessive Al^{3+} doping into CdS (device-A4 with 0.7 M Al^{3+}) would deteriorate the performance of the device. The device utilizing the CdS:Al buffer layer with 0.5 M Al^{3+} doping demonstrated the highest device efficiency. These results indicated a strong correlation between the cation doping concentration of the CdS buffer layer and PCE of the device. Herein, based on the trends of device performance analysis above, the discussion of

device performance improvement mechanism will be limited to the representative device-A0 (without Al^{3+} doping), device-A1 (low Al^{3+} doping concentration), and device-A3 (optimal Al^{3+} doping concentration).

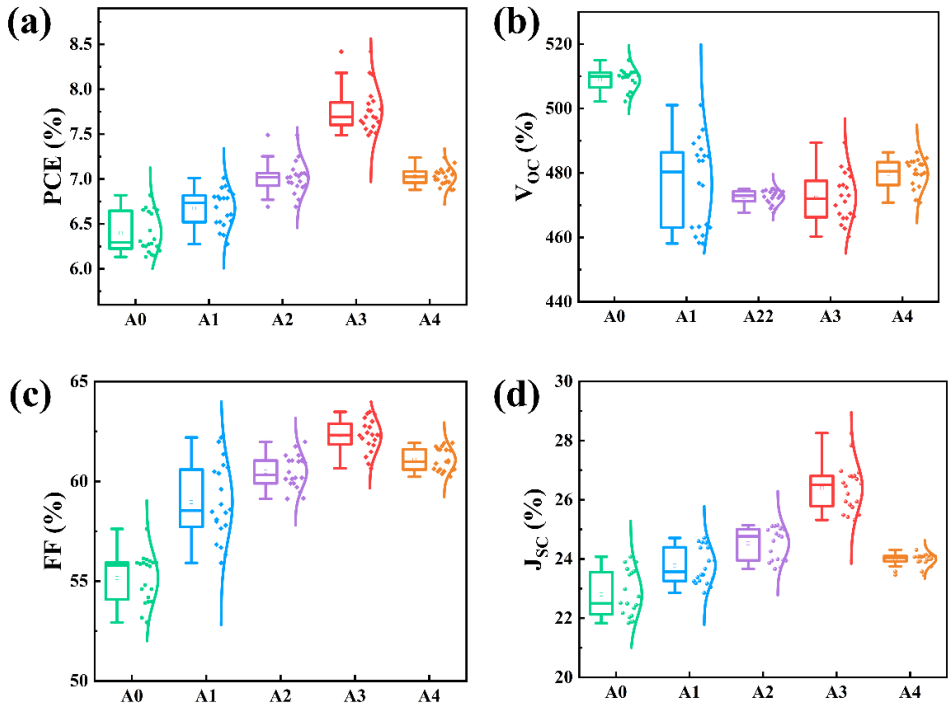

Figure 2.9 *Statistical box-plots of (a) PCE; (b) V_{OC}; (c) FF; (d) J_{SC} for the representative Sb_2Se_3 solar cells based on Al-doped CdS buffer layer as a function of doping concentrations.*

Table 2.1 The key photovoltaic performance parameters of Sb_2Se_3 solar cells with various Al-doping concentrations.

Devices	**Concentration (mol)**	**PCE (%)**	***V*OC (mV)**	**FF (%)**	***J*SC (mA/cm²)**
A1	0.1	7.01	489	61.12	23.47
A2	0.3	7.49	475	62.75	25.14
A3	0.5	8.41	489	60.87	28.26
A4	0.7	7.24	484	61.92	24.15
A0	0	6.82	515	57.92	22.98

2.4.2 Characterization of CdS:Al buffer layer

To investigate the correlation between the variation of E_g and the effect of the Al doping behavior, X-ray photoelectron spectroscopy (XPS) characterizations were used in pristine CdS (A0) and the representative Al-doped CdS (A3) samples, along with a qualitative analysis of constituent elements and valence states. The spectra of the measured thin films were calibrated according to the peak of standard C 1s (284.68 eV).[22] The high-resolution XPS spectra of Cd, S, and Al elements fitted by the Gaussian method are displayed in Figure 2.10. According to Cd and S XPS spectra, no obvious differences can be identified in elemental chemical states between the two thin films, indicating the absence of phase transition or surface oxidation after doping. As shown in Figure 2.10a, the Cd 3d peaks presented two characteristic peaks corresponding to $3d_{5/2}$ and $3d_{3/2}$, located at 404.9 and 411.7 eV, respectively.[23] In Figure 2.10b, the position of the peaks centered at 161.4 and 162.5 eV of the S 2p spectrum was fitted by two main peaks ($2p_{3/2}$ and $2p_{1/2}$), which were associated with the only S^{2-} ion states belonging to CdS. The major peaks of Cd and S elements were assigned to high-resolution spectral deconvolution elemental states of CdS. Meanwhile, an observable peak of the Al 2p core levels for the A3 thin film in Figure 2.10c was obtained at a binding energy of 74.5 eV, indicating that the Al ion was successfully incorporated into the CdS film.[24]

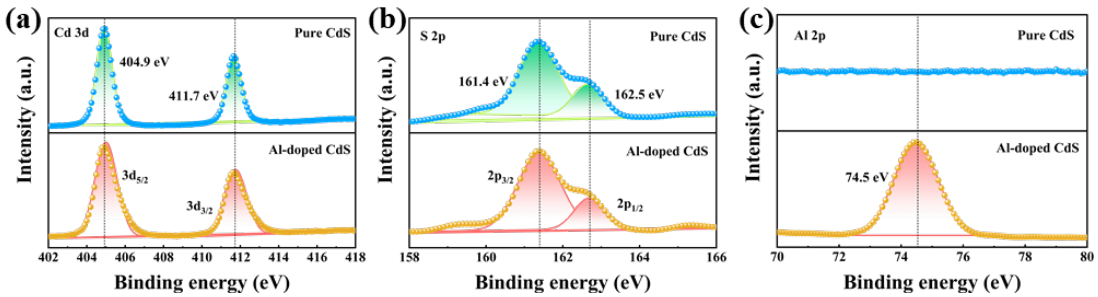

Figure 2.10 *XPS analysis of Cd 3d (a), S 2p (b), and Al 2p (c) for the representative pristine CdS and Al-doped CdS thin films.*

To examine the surface electrical properties of pristine CdS (A0) and Al-doped CdS (A3) samples, we carried out Kelvin probe force microscopy (KPFM) measurements. AFM micrograph (Figure 2.11a, b) and the contact potential differences (V_{CPD}, the difference between the probe and sample; Figure 2.11c, d) of the two samples are shown in Figure 2.11. By taking line profiles along the marked area, the potential mappings compared with topography were obtained (Figure 2.11e, f). As can be observed in the two samples, GBs possessed a high V_{CPD} compared with the grain surface (GS), corresponding to a low work function, indicating that the E_F of GBs was closer to the vacuum level, which is schematically depicted in Figure 2.11g, h. This increase in V_{CPD} at the GBs impeded carrier transport across the horizontal direction. By contrast, the low V_{CPD} at GS was ascribed to the relatively small lateral potential difference thus photogenerated electrons and holes were effectively separated along the aligned $[Sb_4Se_6]_n$ ribbons.[25] In the comparison of the surface potentials of the two thin films, the contact potential differences for samples with incorporated Al cation (≈ 15 mV) were smaller than that for the pristine CdS samples (≈ 30 mV). This result indicated less energy variation at the Fermi level and reduced band fluctuation in the Al-doped CdS samples.[26] Consequently, the lower V_{CPD} in Al-doped CdS sample is beneficial for charge carrier extraction and collection, facilitating carrier transport and thereby improving device performance.

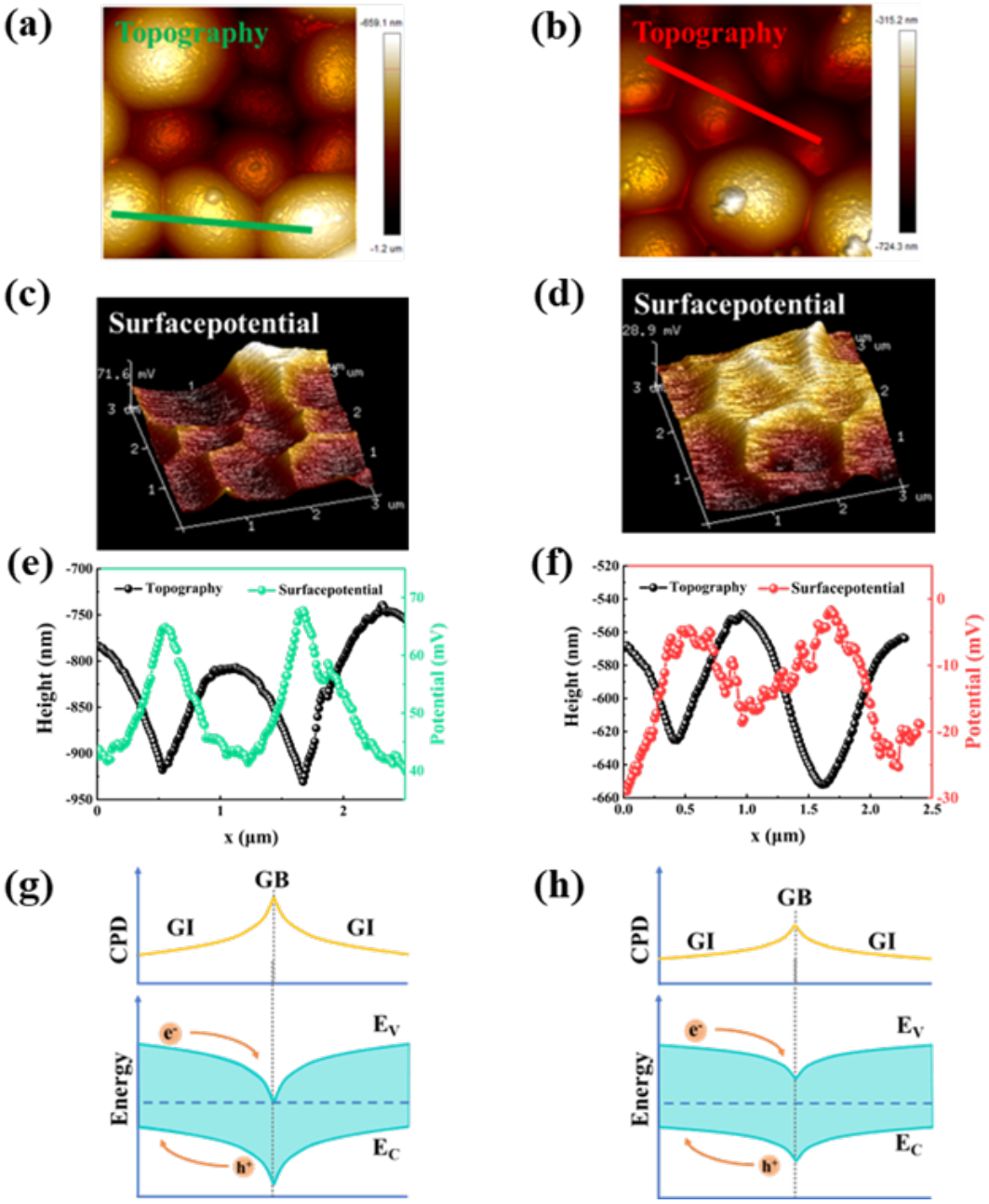

Figure 2.11 *KPFM analysis of the representative pristine CdS (A0) and Al-doped CdS (A3) samples. (a), (b) Topography. (c), (d) Surface potential differences. (e), (f) Topography and Surface potential line profile (acquired from scanning the green line in (a) and (b)) for pristine CdS and Al-doped CdS thin film. (g), (h) The schematic diagrams corresponding to KPFM results.*

2.5 Characterization of Sb_2Se_3/CdS:Al heterojunction

2.5.1 Morphology and microstructure properties analysis

A cross-sectional SEM image of the A3 sample and the schematic structure is provided in Figure 2.12. The Sb_2Se_3 absorber layer, CdS:Al buffer layer and ITO window layer were ≈ 1200, 70, and 400 nm thick, respectively. The heterojunction between the Sb_2Se_3 absorber layer and CdS:Al buffer layer presented good adhesion and a compact and pinhole-free interface without abrupt interfacial boundary. In addition, the Sb_2Se_3 thin film consisted of large and compact crystal grains, confirming an effective combination reaction during the selenization of sputtered Sb precursor under sufficient Se vapor.[27] This high-quality heterojunction interface should considerably reduce charge carrier recombination and current leakage, facilitating the collection of photogenerated carriers and the enhancement of J_{SC}.[27, 28]

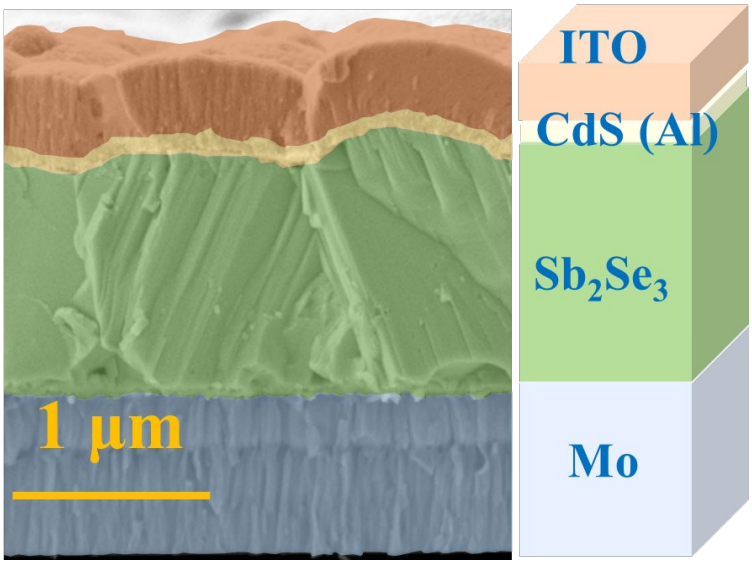

Figure 2.12 *The cross-sectional SEM image of the A3 sample and the schematic structure.*

2.5.2 Interface properties and doping behavior at heterojunction analysis

Transmission electron microscope (TEM) measurement was further performed on the sample-A3 for the investigation of the Sb_2Se_3/CdS:Al heterojunction interface. The distinct cross-section TEM morphology of the Sb_2Se_3/CdS:Al interface is shown in Figure 2.13a1. A highly compact and void-free structure was observed, demonstrating a well-adherent Sb_2Se_3/CdS:Al heterojunction interface, which is consistent with the cross-sectional SEM image presented in Figure 2.12. High-resolution TEM (HRTEM) was subsequently conducted at the Al ion doping interface, which revealed benign lattice-matching characteristics (Figure 2.13a2) corresponding to the compact and smooth feature in Figure 2.13a1. Such an interface minimizes the current leakage and the interfacial carrier recombination.[29] According to the atomic resolution high angle annular dark field scanning transmission electron microscopy (HAADF-STEM) images (Figure 2.13b1) obtained near the region of the Sb_2Se_3/CdS:Al interface (the yellow rectangle in Figure 2.13a2), the measured lattice fringe of 0.329 nm matched well with the (111) plane of hexagonal CdS. Figure 2.13 b2 displays the HAADF-STEM images of the bulk absorber layer (corresponding to the rose-red rectangle obtained from Figure 2.13a2). A Sb_2Se_3 crystal with 1D crystal structure consisted of units $[Sb_4Se_6]_n$ ribbons formed by van der Waals forces and combined in the (001) direction by covalent Sb–Se bonds, which is favorable for carrier transport.[2] Figure 2.13c1 exhibits the intensity line profiles of a row of atoms corresponding to the yellow rectangle marked in Figure 2.13b1. Notably, the atomic scale shows evident variation in column intensity, pointing out an abnormal peak with lower intensity. It is likely to imply that the original site Cd atoms were substituted by another cation that possesses a relatively smaller atomic number, that is, Al atoms from doping. Finally, the elemental composition distribution of the cross-section of the device was characterized through scanning transmission electron microscopy combined with energy dispersive X-ray spectroscopy mapping (Figure 2.13d). Each corresponding element in the absorber and buffer layers showed a uniform distribution, implying the successful doping of Al cation. Overall, Al doping

into CdS can improve the heterojunction, with smooth microstructural Sb_2Se_3/CdS:Al interface, which enhanced device performance.

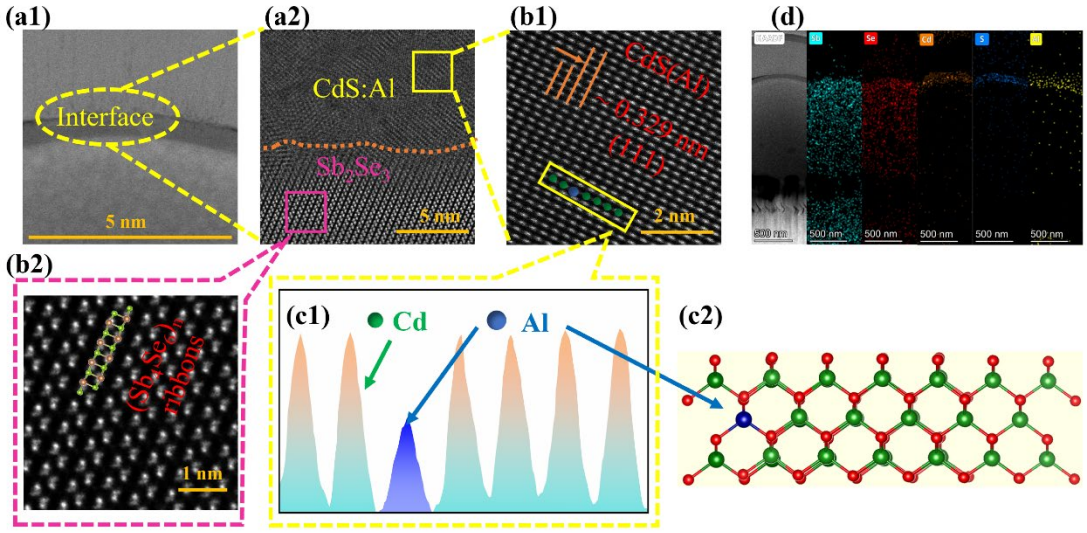

Figure 2.13 *TEM characterization of the champion Sb_2Se_3/CdS:Al device. (a1) Cross-section TEM image of the Sb_2Se_3/CdS:Al heterojunction interface. (a2) HRTEM image of the heterojunction interface. HAADF-STEM image taken from CdS:Al buffer layer (b1) and Sb_2Se_3 absorber layer (b2). (c1) The intensity profiles of the HAADF signals obtained from the marked yellow rectangular frame in Figure 2.13b1. (c2) the corresponding atomic configuration of CdS:Al buffer layer. (d) The EDS elements mapping of Sb_2Se_3/CdS:Al heterojunction interface, including Sb, Se, Cd, S, and Al.*

2.6 Effects of Al-doping concentration on the photovoltaic performance

The *J–V* curves of the representative A1, A3, and A0 devices under the standard AM 1.5 G light illumination are shown in Figure 2.14a. The A0 device presented a V_{OC} of 515 mV, FF of 57.6%, and J_{SC} of 23.0 mA cm^{-2}, thus achieving a PCE of 6.82%. By contrast, a competitive PCE of 8.41% was achieved for the A3 device, along with the major device parameters, that is, a V_{OC} of 489 mV and simultaneous increases in FF to 60.9% and J_{SC} to 28.3 mA cm^{-2}. As can be seen in the statistical distributions of the key photovoltaic parameters of the devices in Figure 2.9, a set of 20 devices for each

category was utilized to check the reproducibility of the devices. The acceptable performance variation within all single-category devices indicated the good reproducibility of a substrate-structured device with the controllable preparation process of the device. Interestingly, the obvious promotion of J_{SC} for the Al-doped devices may be ascribed to the enhanced effectiveness of carrier collection and extraction and minimized carrier recombination loss at the interface of Sb_2Se_3/CdS:Al.[30] To investigate the device stability, the device was stored in ambient air without any special encapsulation for over 60 days. The efficiency of the champion device was measured every 10 days and the statistical results are given in Figure 2.14b. The A3 sample presented excellent device stability since the PCE was maintained at relatively high levels throughout the whole period, with only a slight performance degradation of PCE falling from 8.41% to 8.03% after long-term exposure to ambient air without any protection.

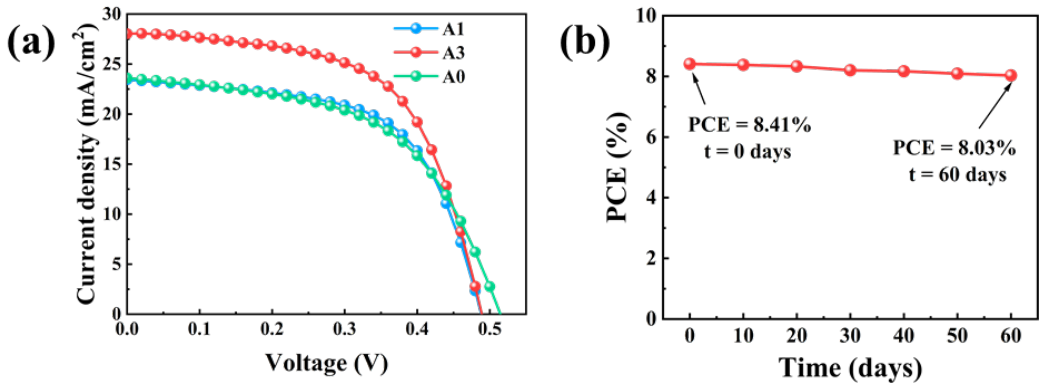

Figure 2.14 *(a) Current density–voltage (J–V) curves, and (b) PCE evolution of the champion device after 60 days storage in ambient air without encapsulation.*

External quantum efficiency (EQE) characterization was applied to further explore photocurrent generation, as shown in Figure 2.15. All devices displayed broad photo-response ranging from UV to near-infrared region and possessed excellent quantum response, showing maximum EQE values of 90%, which are consistent with the strong light absorption of the intrinsically narrow bandgap of Sb_2Se_3 thin films.[31, 32] Importantly, the A3 device with appropriate Al cation incorporation exhibited

considerable improvement in photocurrent generation at the visible region of 400–600 nm, compared with a non-doped counterpart. This variation indicated less light absorption loss by the buffer layer, along with the reduced carrier recombination loss at the Sb_2Se_3/CdS:Al heterojunction interface.[33] The optimization of device performance can be attributed to the appropriate concentration of Al cation doping in the CdS buffer layer, which not only alleviated the recombination loss of photo-generated carriers but also improved the carrier transport efficiency. The integrated J_{SC} values were calculated from EQE data according to the following equation:[34]

$$J_{SC} = \int F(\lambda)\, EQE(\lambda) d\lambda \qquad (2\text{-}1)$$

where F(λ) is the photon flux and EQE(λ) is the measured EQE density. The integrated J_{SC} values for A1, A3, and A0 devices were 21.61, 25.33, and 21.10 mA cm^{-2}, respectively. Since part of the incident light might be blocked by the electrode probe during EQE measurement, the integrated J_{SC} should be, in reality, slightly lower. The J_{SC} variation agreed well with the *J–V* measurement results upon Al cation doping.

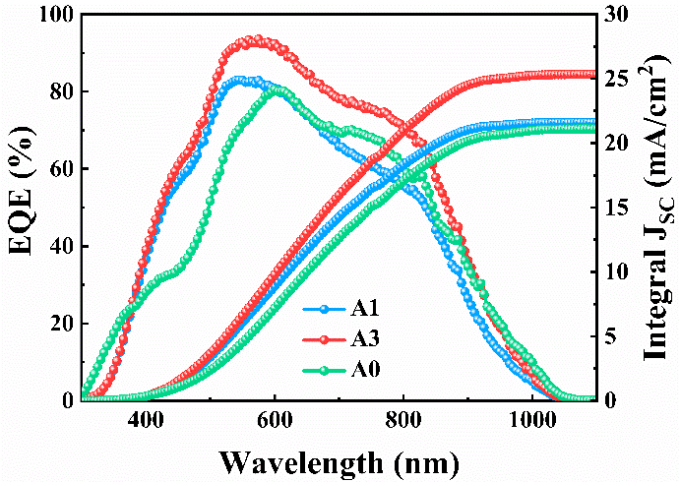

Figure 2.15 *External quantum efficiency (EQE) together with integrated J_{SC} of the representative A1, A3, and A0 devices, respectively.*

Dark *J–V* measurements were conducted under a bias voltage of −1 to 1 V, and the electrical properties of the representative devices were estimated. The three devices (A0, A1, and A3) showed evident rectifying characteristics, as indicated by the *J–V* curves in Figure 2.16a. Subsequently, shunt conductance (*G*), series resistance (R_s), diode

ideality factor (A), and reverse saturation current density (J_0), were compared according to the dark J–V curves and the following single exponential diode formula with the Site's method:

$$J = J_O\left(exp\left[\frac{q}{AkT}(V - JR_sS)\right] - 1\right) + G\left(\frac{V - JR_sS}{S}\right) - J_L \quad (2\text{-}2)$$

By introducing two parameters R_s^* and G^* linked to the area and to simplify this formula. It was assumed that $G^* << R_s^*$, the formula (2-2) can be written as follows:

$$J = J_O\left(exp\left[\frac{q}{AkT}(V - JR_s^*)\right] - 1\right) + G^*(V - JR_s^*) - J_L \quad (2\text{-}3)$$

$$J = J_O exp\left[\frac{q}{AkT}(V - JR_s^*)\right] + G^*V - J_L \quad (2\text{-}4)$$

where S is the surface area. $R_s^* = R_s \cdot S$ ($\Omega \cdot cm^2$) and $G^* = G/S$ (S/cm^2) are referred to as normalized series resistance and shunt conductance respectively, or simply as common series resistance R_s and shunt conductance G for the follow of this chapter. The G_{sh} values were 3.18, 2.46, and 3.72 mS cm^{-2} for A1, A3, and A0, respectively, through extracting the flat zone of the plot of dJ/dV versus V with the reverse bias condition (Figure 2.16b). The values of R_s and A were derived from the curves of dV/dJ versus $(J+J_{SC})^{-1}$, as shown in Figure 2.16c, by calculating the intercept of the Y-axis and the slope as AkT/q, respectively. The R_s value was 2.07 Ω cm^2 (R_{A3}) in the A3 device then increased to 3.69 Ω cm^2(R_{A0}) in the A0 device. The A values were 2.05, 1.84, and 2.07 for A1, A3, and A0 devices, respectively. By plotting the semi-logarithmic ln(J+J_{SC}−GV) versus V−RJ (Figure 2.16d), the J_0 values for the A3 and A0 devices were 6.6×10^{-4} and 1.1×10^{-3} mA cm^{-2}, respectively. In fact, the results of A and J_0 were utilized as effective standards that reflect the carrier recombination due to of defects at the interface and in the bulk.[35] Notably, a low A value implied that doping Al into CdS reduced carrier recombination losses in the devices exhibited in Table 2.2. Moreover, the smaller J_0 indicated effective carrier transportation and further inhibited shunting paths.[36, 37] Hence, under an appropriate Al doping concentration in CdS, considerably improved Sb_2Se_3/CdS:Al junction quality was achieved, as evidenced by the preferable A, small J_0, and decreased G, leading to the greatly enhanced J_{SC} for the A3 sample.[30]

Table 2.2 *Electrical properties for the pristine CdS and Al-doped CdS buffer layer based Sb_2Se_3 solar cells.*

Devices	G (mS/cm^2)	R_S (Ω cm^2)	A	J_0 (mA/cm^2)
A1	3.18	2.93	2.05	9.9×10^{-4}
A3	2.46	2.07	1.84	6.6×10^{-4}
A0	3.72	3.69	2.21	1.1×10^{-3}

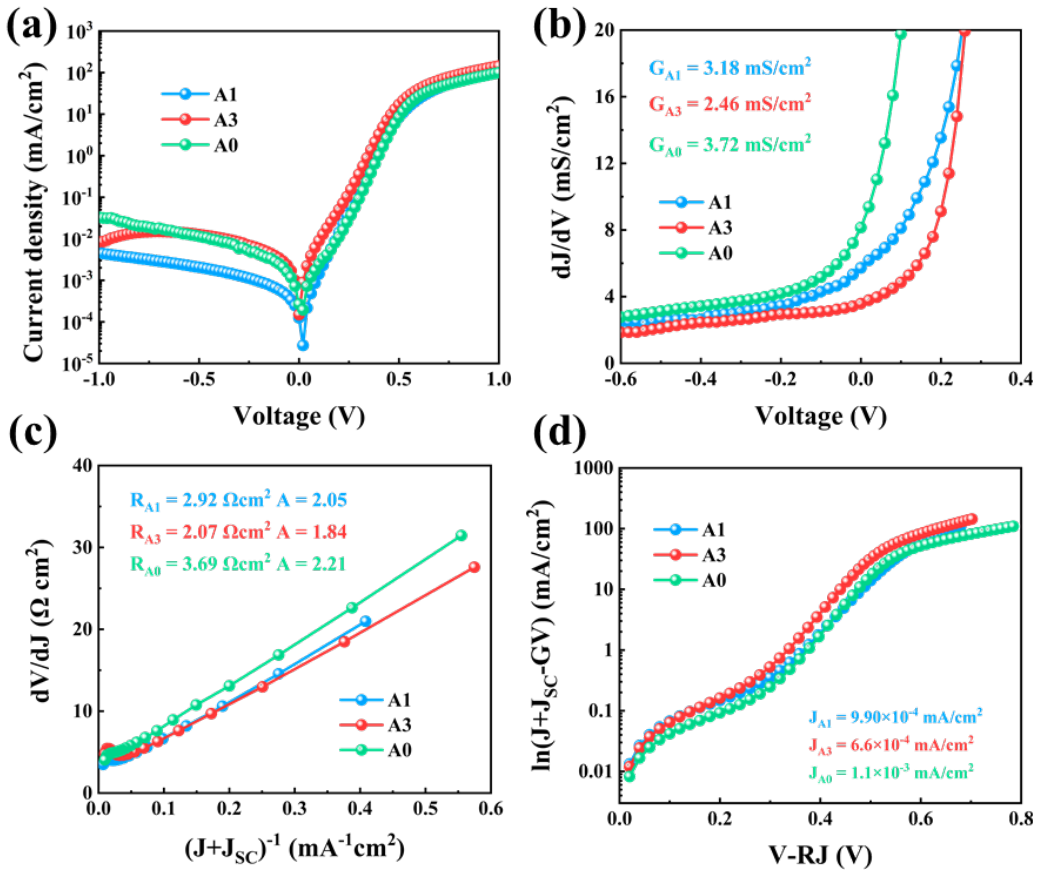

Figure 2.16 *Dark J–V electrical behaviors of the representative A1, A3, and A0 devices. (a) Dark J–V curves, (b) Shunt conductance (G) characterizations. (c) Series resistance (R) and ideality factor (A) characterizations. (d) Reverse saturation current density (J_0) characterizations.*

2.7 The band alignment analysis of the Sb_2Se_3/CdS:Al solar cells

Herein, given that device performance is closely associated with band alignment, the band structures of the Al^{3+} doped (A3) and pristine CdS (A0) samples were investigated using UPS measurements. As depicted in Figure 2.17, the cutoff edge (E_{cutoff}) values of binding energy near the surfaces of the A3 and A0 samples were 16.96 and 16.30 eV, respectively. Additionally, by extrapolating the linear region of low binding energy, the energy gaps (E_{onset}) between the valence band maximum and Fermi energy were 2.02 and 1.68 eV, respectively.

Additionally, the bandgap (E_g) values of the Al^{3+} doped and pristine CdS buffer layers can also be determined from the EQE spectra by analyzing d(EQE)/dλ as a function of wavelength. The estimated value of E_g was determined from the maximum of the first derivative of the EQE with respect to wavelength (d(EQE)/dλ).[38] The calculated results are presented in Figure 2.18, with the estimated E_g values of 2.49 for the A3 buffer layer, and 2.41 eV for the A0 buffer layer, respectively, revealing slight enlargement after Al cation doping.

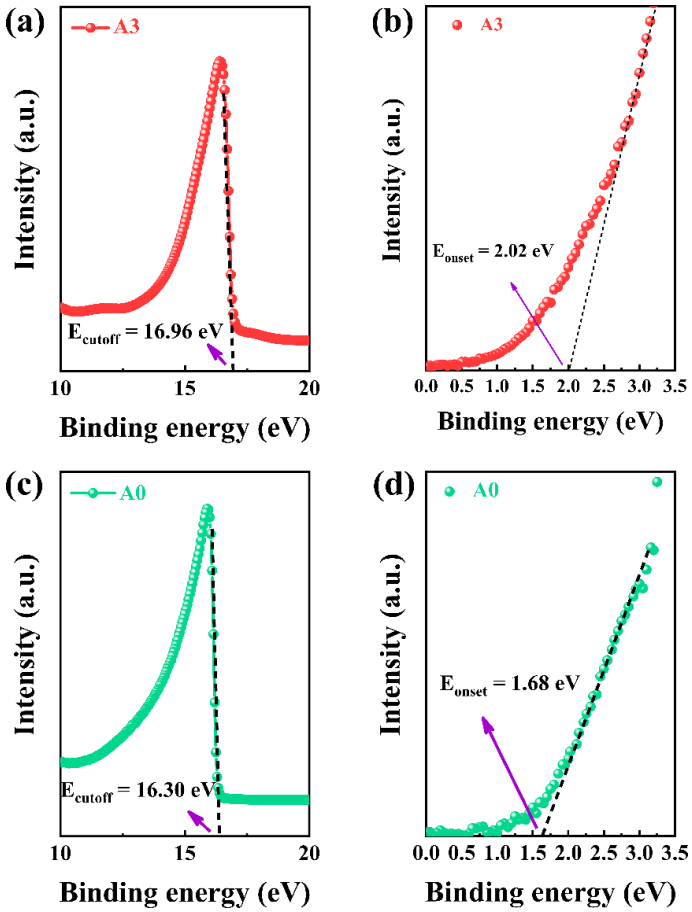

Figure 2.18 *UPS characterizations of A3 (Al-doped) (a) and A0 (undoped) (b)CdS samples.*

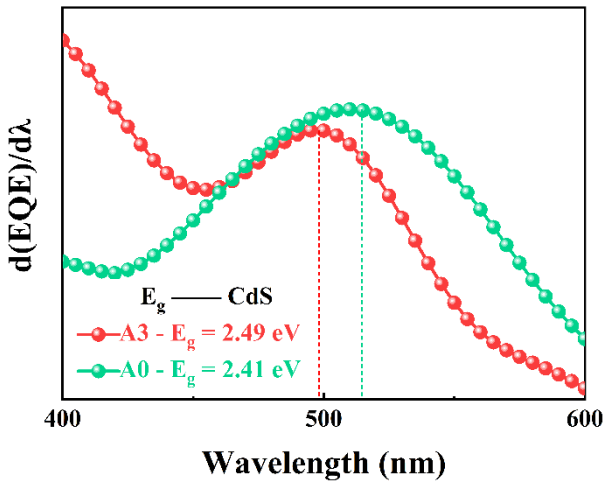

Figure 2.18 *The E_g values of the Al^{3+} doped and pristine CdS buffer layers obtained from EQE spectra.*

Thus, the energy band information of the buffer layers including conduction band (E_C), valence band (E_V), and Fermi levels (E_F) can be calculated from the E_{cutoff} and E_{onset} values according to the following equations:[39, 40]

$$\varphi = h\upsilon - E_{cutoff} \quad (2\text{-}5)$$

$$E_V = \varphi + E_{onset} \quad (2\text{-}6)$$

$$E_C = E_V - E_g \quad (2\text{-}7)$$

where φ is the work function, $h\upsilon$ is the UV photoelectron energy of 21.22 eV, and E_g is the band gap of the two samples calculated from the EQE spectrum. The energy band levels information were summarized in Table 2.3. The schematic diagrams of the band alignment for the pristine CdS device and Al-doped CdS device are depicted in Figure 2.19. Particularly, the energy level information of Sb_2Se_3 was obtained from the literature, *which suggests E_C and E_V to be −3.98 eV and −5.19* eV.[41] As can be seen, the CBO values of Sb_2Se_3/CdS and Sb_2Se_3/CdS:Al heterojunction were −0.21 and 0.19 eV, respectively. In the former device, a negative CBO (often referred to as "cliff-like") of −0.21 eV was found between the Sb_2Se_3/CdS interface, as clarified in Figure 2.19a. This "cliff-like" band alignment intrinsically attenuated band bending because the low point of the conduction band in the CdS buffer layer in this case was located farther from the quasi-Fermi level of electrons.[42] More importantly, weak band bending would lower the barriers for charge carriers approaching the interface. As a result, electrons and holes near the Sb_2Se_3/CdS interface accumulated after they were separated by the electric field, and thus the probability of charge recombination via deep interfacial defects increased. By contrast, a positive CBO (often referred to as "spike-like") of 0.19 eV was observed after the device was treated with Al doping in the CdS buffer layer (Figure 2.19b). Contrary to "cliff-like" band alignment, this "spike-like" band alignment prevented charge carriers from piling up in the vicinity of the heterojunction interface by increasing barriers that prevented charge carriers from reaching the interface.[32] Interface recombination can therefore be effectively restrained, giving rise to considerable promotion of carrier collection and ultimately the enhancement of J_{SC}. However, an extremely large "spike-like" CBO would inversely

block photogenerated electrons reaching the CdS buffer side and diminish the device J_{SC} and PCE. The CBO of our device (0.19 eV) was within the suitable range (0 < CBO < 0.4 eV) according to the values for the most efficient thin-film solar cells.[43] This optimal CBO between the heterojunction band alignment would efficiently suppress non-radiative recombination in the Sb_2Se_3/CdS:Al interface without affecting charge collection efficiency. Thus, we can deduce that doping Al into the CdS buffer layer leads to the reasonable optimization of energy band alignment.

Table 2.3 The energy band levels information for pristine CdS and Al^{3+} doped CdS samples.

Samples	E_V	E_C	E_g
A0	6.60	4.19	2.41
A3	6.28	3.79	2.49

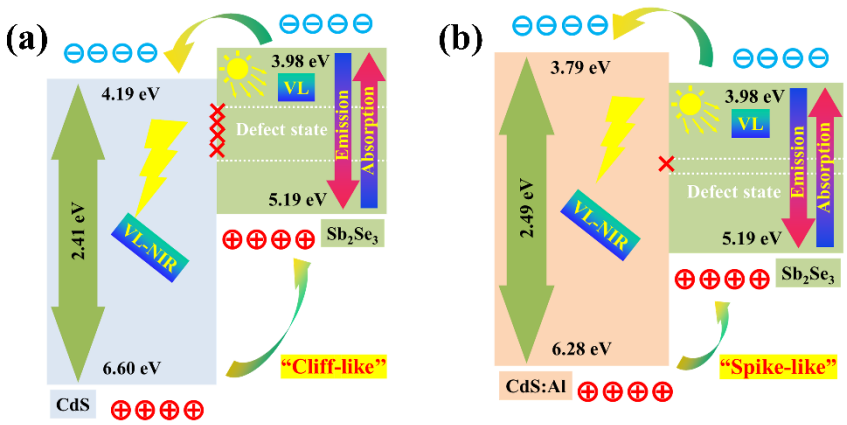

Figure 2.19 *Schematic illustration of the band alignment for pristine CdS (a) and Al^{3+} doped CdS (b) devices.*

2.8 Defect investigation in Sb_2Se_3/CdS:Al solar cells

Defects often act as recombination centers deteriorating device performance. Significantly, the defect states and the qualitative defect density of the devices should be thoroughly investigated.

First, space charge limited current (SCLC) mode was applied to characterize the defect states of our devices.[44] The *J–V* logarithmic curves for the A0, A1, and A3 devices under dark conditions are displayed in Figure 2.20. In general, the curves can be classified according to their exponent *n* values: the ohmic region of low voltage (n=1, yellow rectangle),[45] trap-filled limit (TFL) region of middle voltage (n>3, red rectangle), and child region of high voltage (n=2, green rectangle). The TFL voltage (V_{TFL}) was defined as the cross point of the TFL and ohmic regions. The current density abruptly increased when the bias voltage exceeded the V_{TFL}, representing the trap states are entirely filled by the injected carriers in the TFL region.[46] Thus, the obtained values were 0.25, 0.22, and 0.19 V for the A0, A1, and A3 devices, respectively. The defect density N_{trap} of the device can be determined as follows:[46]

$$N_{trap} = \frac{2\varepsilon\varepsilon_0 V_{TFL}}{eL^2} \quad (2\text{-}8)$$

where ε_0 represents the vacuum dielectric constant, ε represents the relative dielectric constant of Sb_2Se_3 (generally selected as 15.1),[32] L is the thickness of Sb_2Se_3 thin films, and *e* is the elementary charge. According to the formula, N_{trap} decreases with V_{TFL}. The obtained N_{trap} values for Al-doped CdS devices were smaller than that for the A0 devices, calculated as 2.55×10^{14}, 2.20×10^{14}, and 2.90×10^{14} cm^{-3} for the A1, A3, and A0 devices, respectively. Fewer defect recombination centers at the grain boundaries and Sb_2Se_3/CdS:Al interface led to higher quality Sb_2Se_3 absorber layer and the doped CdS buffer layer.[47]

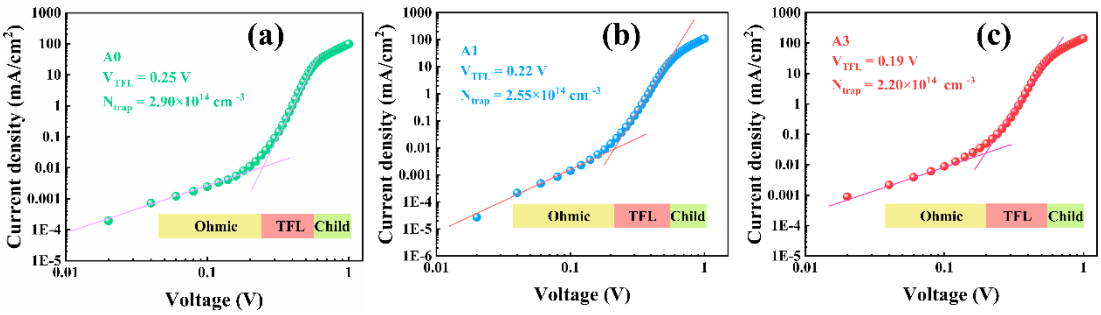

Figure 2.20 *Logarithmic J–V curves of the A1, A3, and A0 devices, respectively, showing Ohmic, TFL, and Child region.*

It is also meaningful to investigate the behavior of interface defect recombination, which always plays a crucial role in unveiling device performance improvement mechanisms. Herein, capacitance–voltage (*C–V*) profiling and deep-level capacitance profiling (DLCP) characterizations, regarding as a vital electrical property characterization techniques, were further carried out to estimate the concentration and properties of interfacial defects for our solar cells. Generally, *C–V* characterization, driven by DC voltage, represents the response of interface defects, bulk defects, and free carriers. DLCP characterization, driven by a small AC voltage under different bias voltages at 100 kHz, reflects the response of bulk defects and free carriers.[48] Thus, the discrepancy at zero bias between the *C–V*-measured defect density (N_{CV}) and the DLCP-measured defect density (N_{DLCP}) is connected to the interfacial defect density (N_i) of Sb_2Se_3 devices. Therefore, the interfacial defect density of the device can be calculated as the subtraction of N_{DLCP} from N_{CV}. The *C–V* and DLCP characterizations as a function of the depletion region width (W_d) are displayed in Figure 2.21, according to the following expressions:[49]

$$N_{CV} = \frac{-2\varepsilon_{r,n}N_D}{\left(\frac{d\left(1/C^2\right)}{dV}\right)qA^2\varepsilon_0\varepsilon_{r,p}\varepsilon_{r,n}N_D + 2\varepsilon_{r,p}} \tag{2-9}$$

$$N_{DLCP} = -\frac{C_0^3}{2q\varepsilon_0\varepsilon_{r,p}A^2C_1} \tag{2-10}$$

$$W_d = \frac{\varepsilon_0\varepsilon_{r,p}A}{C_0} \tag{2-11}$$

where A symbolizes the device area, ε_0 represents the vacuum permittivity, $\varepsilon_{r,n}$ and N_D are the relative permittivity and the doping density of CdS, respectively. $\varepsilon_{r,p}$ is the relative permittivity of Sb_2Se_3. C_0 and C_1 are two quadratic fitting parameters originating from the C–V curves. The detailed analysis data of C–V and DLCP profiling are shown in Table 2.4. The interfacial defect density decreased after Al doping of CdS. Specifically, the calculated N_i value for the A0 device was 4.90×10^{16} cm^{-3}, and the corresponding value for the A1 and A3 devices decreased to 3.93×10^{16} and 3.08×10^{16} cm^{-3}, respectively, demonstrating lower defect density and reduced recombination loss at the optimal Sb_2Se_3/CdS:Al interface.

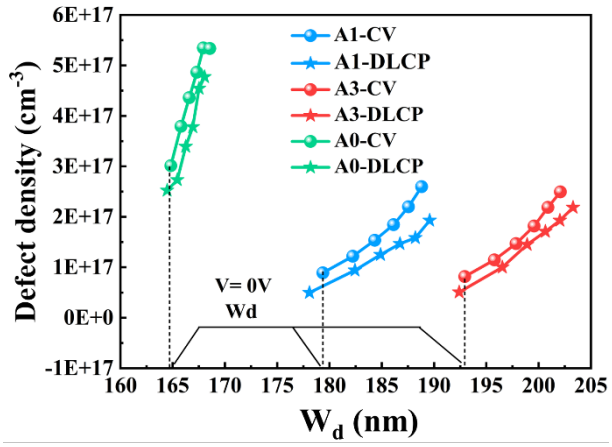

Figure 2.21 *C–V and DLCP profiling of A1, A3, and A0 devices, respectively.*

Table 2.4 *Doping density calculated from C–V and DLCP profiling of the A1, A3, and A0 devices.*

Devices	W_d (nm)	N_{CV} (cm^{-3})	N_{DLCP} (cm^{-3})	N_i (cm^{-3})
A1	179	8.90×10^{16}	4.97×10^{16}	3.93×10^{16}
A3	193	8.16×10^{16}	5.08×10^{16}	3.08×10^{16}
A0	165	3.01×10^{17}	2.50×10^{17}	4.90×10^{16}

In addition, the Al-doped A3 device possessed a large W_d of 193 nm, which is conducive to carrier extraction and light absorption in the device [27] and obviously enhances the J_{SC} values and performance of the Al-doped devices.

Deep-level transient spectroscopy (DLTS) analysis consists of extracting the emission rates of deep levels from a transient capacitance (ΔC). These transients result from a voltage or optical pulse applied to the junction. In its simplest application, DLTS allows for the determination of deep trap parameters such as the type of the defect (majority or minority carrier trap), activation energy, capture cross sections and trap concentration. [50, 51] The DLTS results of the A0 and A3 device are exhibited in Figure 2.22a, containing positive peaks and negative DLTS signal peaks. The positive peaks in the DLTS curves can be ascribed to majority carrier traps, whereas negative peaks represent minority carrier traps. Herein, positive and negative curves correspond to hole and electron traps in the Sb_2Se_3 absorber,[50] respectively. The defect information of the two categories of devices is calculated and summarized in Table 5, including the value of defect active energy (E_r), defect density (N_T), and capture cross-section (σ). Especially, the E_r (E_C–E_T or E_T–E_V, wherein, E_T, E_C, and E_V are the defect energy level, conduction band edge, and valance band edge, respectively) of the defects was obtained through the linear fitting of DLTS signal derived Arrhenius plot points (Figure 2.22b).[50, 52] One positive and one negative peak were found in both devices, demonstrating one hole trap defect and one electron trap defect, which are denoted as H1 and E1, respectively. The corresponding energy level of the negative peak for the A3 device was detected at 0.225 eV, with an N_T and σ of 2.28×10^{14} cm^{-3} and 1.98×10^{-20} cm^2, respectively. The A0 device exhibited a similar defect type E1 located at ≈ 0.251 eV, which was close to the intrinsic Fermi level (E_F), along with an adversely increased N_T of 3.73×10^{14} cm^{-3} and the largest σ of 6.56×10^{-20} cm^2. According to the calculated results of energy level, the defect type E1 can be assigned as Se vacancy (V_{Se}) defect, agreeing well with our previous works on the Sb_2Se_3 thin films, fabricated by sputtering and selenization technique.[32, 41, 53] In addition, in the positive peaks, a defect type denoted as H1 (E_r = 0.303 eV, $N_T = 2.50 \times 10^{14}$ cm^{-3}, and $\sigma = 5.88 \times 10^{-21}$

cm^2) was obtained for the A3 device, whereas the A0 device displayed a similar hole trap H1 (E_r = 0.377 eV, $N_T = 4.57 \times 10^{14}$ cm^{-3}, and $\sigma = 4.55 \times 10^{-20}$ cm^2), which can be assigned to selenium antistite (Se_{Sb}) according to the DFT calculations.[54] Notably, the decreased defect density and capture cross-section of the Sb_2Se_3 device with the doping of Al cation in CdS improved device performance.

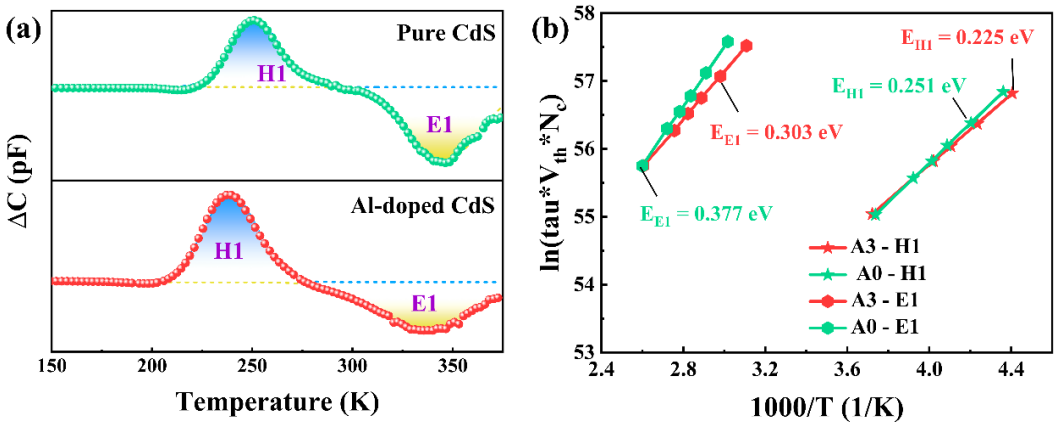

Figure 2.22 *(a) Deep-level transient spectroscopy (DLTS) signals from pristine CdS A0 and Al-doped CdS A3 devices. (b) Arrhenius plots obtained from DLTS signals.*

Furthermore, the index $N_T \times \sigma$ is another effective pathway to investigate the defect feature for thin-film solar cells, according to the following equation:[32]

$$\tau_{trap} = \frac{1}{v_t \sigma N_T} \tag{2-12}$$

where σ and N_T are the capture cross-section and defect density acquired from DLTS results, v_t is the carrier thermal velocity, which is $\approx 10^7$ cm s^{-1} at room temperature in the bulk of semiconductors.[55, 56] As listed in Table 2.5 and the histogram displayed in Figure 2.23), the obviously decreased value $N_T \times \sigma$ demonstrated the effective passivation of the two major defects (E1 and H1) in our devices owing to the Al cation doped into the CdS buffer layer and the post-annealing treatment. With undoped CdS, the photogenerated electrons and holes are likely to be captured and result in poor trap-assisted recombination, ultimately reducing the minority carrier lifetime and decreasing J_{SC}.[57] After the doping of Al cation into the CdS buffer layer, the capture cross-section of H1 dramatically decreased by nearly one order of magnitude. The carriers captured

by shallow trap states are emitted again in an extremely short time because of the small capture cross-section.

Table 2.5 *Defect characteristics of the A3 and A0 devices.*

Devices	Defect	E_T (eV)	N_T (cm^{-3})	σ (cm^2)	$N_T \times \sigma$ (cm^{-1})
A3	E1	E_C – 0.303eV	2.50×10^{14}	5.88×10^{-20}	1.47×10^{-6}
	H1	E_V + 0.225 eV	2.28×10^{14}	1.98×10^{-21}	4.54×10^{-6}
A0	E1	E_C – 0.377eV	4.57×10^{14}	4.55×10^{-20}	2.08×10^{-5}
	H1	E_V + 0.251 eV	3.73×10^{14}	6.56×10^{-20}	2.44×10^{-5}

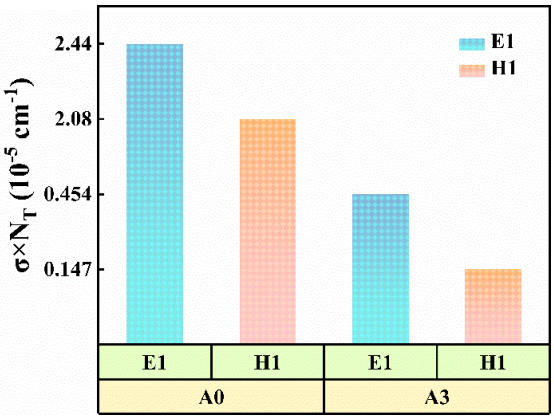

Figure 2.23 *Histogram of the calculated σ × N_T values of traps in Sb_2Se_3 devices.*

The energy states and defect levels of the two devices are revealed in Figure 2.24a, b, respectively. In the A0 device, the corresponding defect level E1 extracted from the Arrhenius plots was located at 0.377 eV below E_C, and the H1 defect was located at 0.251 eV above E_V, which was closer to the position of intrinsic E_F. These conditions can lead to severe defect-assisted recombination because of the detrimental pining effect. By contrast, in the A3 device, the defect levels E1 and H1 were detected at 0.303 eV below E_C and 0.225 eV above E_V. The effectively passivated harmful defects will minimize the pining effect, facilitating the split of the quasi-Fermi levels of holes and electrons, and enhancing J_{SC}.

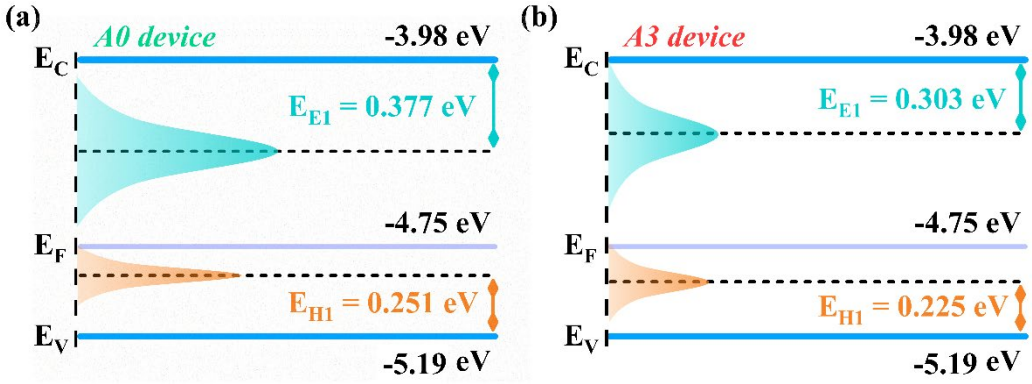

Figure 2.24 *Schematic diagram of defect energy states and defect levels in A0 (a) and A3 (b) devices.*

To elucidate the behavior of defect recombination and carriers' transport dynamic mechanism, electrochemical impedance spectroscopy (EIS) measurements were carried out for the A0 and A3 devices. The corresponding Nyquist plots of the EIS spectrum and equivalent circuit diagrams of the devices are represented in Figure 2.25. The impedance spectra were fitted by the equivalent circuit, which was composed of two modules. The first part belongs to the Sb_2Se_3/CdS:Al heterojunction interface and the second part represents the remaining devices. The series resistance (R_S) obtained by the intercept of the X-axis represents the contact and material resistance of the whole cell, and the recombination resistance (R_{rec}) is equal to the diameter of the impedance spectrum semicircle and represents the defect recombination resistance of the heterojunction interface.[36] Notably, the R_S value of the A3 device (21.33 Ω) was smaller than that of the A0 device (23.52 Ω) because of carrier transfer enhanced by the incorporation of Al cation (Figure 2.25b). The values of R_{rec} for the A0 and A3 devices were 13637 and 2826 Ω, respectively, which implied efficient defect passivation at the Sb_2Se_3/CdS:Al interface. The enhanced carrier generation, separation, and transport and the reduced recombination led to the overall enhancement of Al-doped device performance.

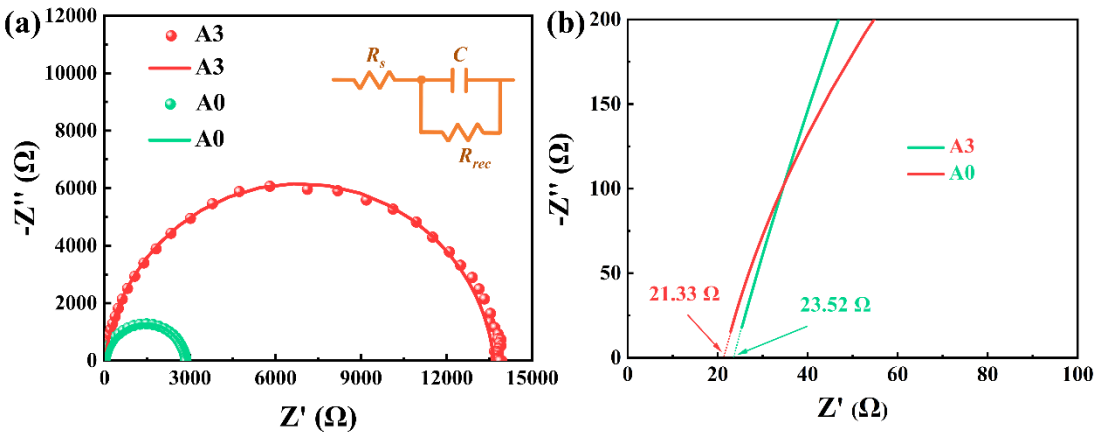

Figure 2.25 *(a) Nyquist plots of the impedance for A0 device and A3 device (inset equivalent circuit employed to fit the Nyquist plots), experimental data are shown as dotted circles and the fitted results are shown as solid lines. (b)The intercept of the X-axis*

2.9 Conclusions

In this chapter, we have demonstrated an effective strategy of Al^{3+} cation doping in the CdS buffer layer through spin-coating and post-annealing methods. The Sb_2Se_3 devices with substrate configuration of Mo/Sb_2Se_3/CdS:Al/ITO/Ag were constructed. The characteristics of Sb_2Se_3/CdS:Al heterojunction, and the key device performance were systematically investigated, and comprehensive analysis was also conducted on the band alignment and defect properties of the Sb_2Se_3 devices. As a result, Al doping in CdS significantly optimized the band alignment and the heterojunction interface quality, leading to the facilitation of charge carrier transport and the reduction of interface recombination. Meanwhile, post-annealing treatment was beneficial to passivate bulk defects and defect-assisted recombination. Finally, after the introduction of 0.5 mol Al^{3+} ion to the CdS buffer layer and annealing at 280 °C for 5 min, the thin-film device achieved a high PCE of 8.41% and showed a dramatic increase in J_{SC} (from 22.98 mA/cm^2 to 28.26 mA/cm^2), which was closely related to the suppression of defect-assisted recombination at the heterojunction interface, the optimization of band

alignment with ideal CBO, and the enhancement of carrier transport efficiency. This work provides an effective and facile method for fabricating efficient Sb_2Se_3 thin-film solar cells, broadening the development of chalcogenide-based photovoltaic devices.

2.10 References

[1] Lian, W. T., Cao, R., Li, G., Cai, H. L., Cai, Z. Y., Tang, R. F., Zhu, C. F., Yang, S. F., Chen, T., Distinctive deep-level defects in non-stoichiometric Sb_2Se_3 photovoltaic materials. *Adv. Sci.* 2022, 9(9), 2105268.

[2] Duan, Z. T., Liang, X. Y., Feng, Y., Ma, H. Y., Liang, B. L., Wang, Y., Luo, S. P., Wang, S. F., Schropp, R. E. I., Mai, Y. H., Li, Z. Q., Sb_2Se_3 thin-film solar cells exceeding 10% power conversion efficiency enabled by injection vapor deposition technology. *Adv. Mater.* 2022, 34(30), 2202969.

[3] Tao, W. J., Zhu, L. L., Li, K. H., Chen, C., Chen, Y. Z., Li, Y. J., Li, X. F., Tang, J., Shang, H. H., Zhu, H. M., Coupled electronic and anharmonic structural dynamics for carrier self-trapping in photovoltaic antimony chalcogenides. *Adv. Sci.* 2022, 9(25), 2202154.

[4] Shockley, W., Queisser, H. J., Detailed balance limit of efficiency of p-n junction solar cells. *J. Appl. Phys.* 1961, 32(3), 510-519.

[5] Cai, H. L., Cao, R., Gao, J. X., Qian, C., Che, B., Tang, R. F., Zhu, C. F., Chen, T., 界面 sbcl3 on CdS-Interfacial engineering towards enhanced photovoltaic performance of Sb_2Se_3 solar cell. *Adv. Funct. Mater.* 2022, 32(46), 2208243.

[6] Li, Z. Q., Liang, X. Y., Li, G., Liu, H. X., Zhang, H. Y., Guo, J. X., Chen, J. W., Shen, K., San, X. Y., Yu, W., Schropp, R. E. I., Mai, Y. H., 9.2%-efficient core-shell structured antimony selenide nanorod array solar cells. *Nat. Commun.* 2019, 10, 125.

[7] Zhao, Y. Q., Wang, S. Y., Li, C., Che, B., Chen, X. L., Chen, H. Y., Tang, R. F., Wang, X. M., Chen, G. L., Wang, T., Gong, J. B., Chen, T., Xiao, X. D., Li, J. M., CBD-10.57%--Regulating deposition kinetics via a novel additive-assisted chemical bath deposition technology enables fabrication of 10.57%-efficiency Sb_2Se_3 solar cells. *Energy Environ. Sci.* 2022, 15, 5118-5128.

[8] Han, W. H., Gao, D., Tang, R. F., Ma, Y. Y., Jiang, C. H., Li, G., Chen, T., Zhu, C. F., Efficient $Sb_2(S,Se)_3$ solar modules enabled by hydrothermal deposition. *Solar RRL* 2021, 5(3), 202000750.

[9] Gao, Q. Q., Yuan, S. J., Zhou, Z. J., Kou, D. X., Zhou, W. H., Meng, Y. N., Qi, Y. F., Han, L. T., Wu, S. X., Over 16% Efficient Solution-Processed $Cu(In,Ga)Se_2$ Solar Cells via Incorporation of Copper-Rich Precursor Film. *Small* 2022, 18(39), 2203443.

[10] Wang, W. H., Cao, Z. X., Wu, L., Chen, G. L., Ao, J. P., Luo, J. S., Zhang, Y., Interface etching leads to the inversion of the conduction band offset between the CdS/Sb_2Se_3 heterojunction and high-efficient Sb_2Se_3 solar cells. *ACS Appl. Energy Mater.* 2022, 5(2), 2531-2541.

[11] Liang, G. X., Luo, Y. D., Chen, S., Tang, R., Zheng, Z. H., Li, X. J., Liu, X. S., Liu, Y. K., Li, Y. F., Chen, X. Y., Su, Z. H., Zhang, X. H., Ma, H. L., Fan, P., Sputtered and selenized Sb_2Se_3 thin-film solar cells with open-circuit voltage exceeding 500 mV. *Nano Energy* 2020, 73, 104806.

[12] Wen, X. X., Chen, C., Lu, S. C., Li, K. H., Kondrotas, R., Zhao, Y., Chen, W. H., Gao, L., Wang, C.,

Zhang, J., Niu, G. D., Tang, J., Vapor transport deposition of antimony selenide thin film solar cells with 7.6% efficiency. *Nat. Commun.* 2018, 9(2179), 2179.

[13] Chen, Y. J., Wang, Y. Y., Wang, R., Hu, X. B., Tao, J. H., Weng, G. E., Zhao, C. H., Chen, S. Q., Zhu, Z. Q., Chu, J. H., Akiyama, H., Importance of interfacial passivation in the high efficiency of Sb_2Se_3 thin-film solar cells: numerical evidence. *ACS Appl. Energy Mater.* 2020, 3(11), 10415-10422.

[14] Ou, C. Z., Shen, K., Li, Z. Q., Zhu, H. B., Huang, T. L., Mai, Y. H., Bandgap tunable CdS:O as efficient electron buffer layer for high-performance Sb_2Se_3 thin film solar cells. *Sol. Energy Mater. Sol. Cells* 2019, 194, 47-53.

[15] Ning, H., Guo, H. F., Zhang, J. Y., Wang, X., Jia, X. G., Qiu, J. H., Yuan, N. Y., Ding, J. N., Enhancing the efficiency of Sb_2S_3 solar cells using dual-functional potassium doping. *Sol. Energy Mater. Sol. Cells* 2021, 221, 110816.

[16] Chen, C., Liu, X. X., Li, K. H., Lu, S. C., Wang, S. Y., Li, S., Lu, Y., He, J. G., Zheng, J. J., Lin, X. T., Tang, J., High-efficient Sb_2Se_3 solar cell using $Zn_xCd_{1-x}S$ n-type layer. *Appl. Phys. Lett.* 2021, 118(17), 172103.

[17] Wu, C. Y., Jiang, C. H., Wang, X. M., Ding, H. H., Ju, H. X., Zhang, L. J., Chen, T., Zhu, C. F., Interfacial engineering by Indium-doped CdS for high efficiency solution processed $Sb_2(S_{1-x}Se_x)_3$ solar cells. *ACS Appl. Mater. Interfaces* 2019, 11(3), 3207-3213.

[18] Luo, P., Imran, T., Ren, D. L., Zhao, J., Wu, K. W., Zeng, Y. J., Su, Z. H., Fan, P., Zhang, X. H., Liang, G. X., Chen, S., Electron transport layer engineering induced carrier dynamics optimization for efficient Cd-free Sb_2Se_3 thin-film solar cells. *Small* 2023, 20(4), 2306516.

[19] Li, K. H., Chen, C., Lu, S. C., Wang, C., Wang, S. Y., Lu, Y., Tang, J., Orientation engineering in low-dimensional crystal-structural materials via seed screening. *Adv. Mater.* 2019, 31(44), 1903914.

[20] Rijal, S., Li, D. B., Awni, R. A., Xiao, C. X., Bista, S. S., Jamarkattel, M. K., Heben, M. J., Jiang, C. S., Al-Jassim, M., Song, Z. N., Yan, Y. F., Templated growth and passivation of vertically oriented antimony selenide thin films for high-efficiency solar cells in substrate configuration. *Adv. Funct. Mater.* 2021, 32(10), 2110032.

[21] Wang, S. Y., Zhao, Y. Q., Yao, L. Q., Li, C., Gong, J. B., Chen, G. L., Li, J. M., Xiao, X. D., Efficient and stable all-inorganic $Sb_2(S, Se)_3$ solar cells via manipulating energy levels in MnS hole transporting layers. *Sci. Bull.* 2022, 67(3), 263-269.

[22] Chen, S., Liu, T. X., Chen, M. D., Ishaq, M., Tang, R., Zheng, Z. H., Li, X. J., Qiao, X. S., Liang, G. X., Crystal growth promotion and interface optimization enable highly efficient Sb_2Se_3 photocathodes for solar hydrogen evolution. *Nano Energy* 2022, 99, 107417.

[23] Leng, M. Y., Chen, C., Xue, D. J., Gong, J. B., Liu, Y. H., Li, K. H., Xiao, X. D., Wang, G., Tang, J., Sb_2Se_3 solar cells employing metal-organic solution coated CdS buffer layer. *Sol. Energy Mater. Sol. Cells* 2021, 225(111043), 111043.

[24] Jiang, M., Wu, Z. J., Zhang, X. Y., Cai, Y. Y., Wang, W. Z., Liang, Y. J., Synergetic effect of surface plasmon resonance and Schottky junction to drastically boost solar-driven photoelectrochemical hydrogen production and photocatalytic performance of CdS/Al nanorod arrays. *Energy Convers. Manage.* 2022, 268, 115978.

[25] Yang, W., Kim, J. H., Hutter, O. S., Phillips, L. J., Tan, J. W., Park, J., Lee, H., Major, J. D., Lee, J. S., Moon, J., Benchmark performance of low-cost Sb_2Se_3 photocathodes for unassisted solar overall water splitting. *Nat. Commun.* 2020, 11(1), 861.

[26] Vishwakarma, M., Kumar, M., Hendrickx, M., Hadermann, J., Singh, A. P., Batra, Y., Mehta, B. R., Enhancing the hydrogen evolution properties of kesterite absorber by Si-doping in the surface of CZTS

thin film. *Adv. Mater. Interfaces* 2021, 8(10), 2002124.

[27] Luo, Y. D., Tang, R., Chen, S., Hu, J. G., Liu, Y. K., Li, Y. F., Liu, X. S., Zheng, Z. H., Su, Z. H., Ma, X. F., Fan, P., Zhang, X. H., Ma, H. L., Chen, Z. G., Liang, G. X., An effective combination reaction involved with sputtered and selenized Sb precursors for efficient Sb_2Se_3 thin film solar cells. *Chem. Eng. J.* 2020, 393, 124599.

[28] Yang, Z. L., Wang, X. M., Chen, Y. Z., Zheng, Z. F., Chen, Z., Xu, W. Q., Liu, W. M., Yang, Y., Zhao, J., Chen, T., Zhu, H. M., Ultrafast self-trapping of photoexcited carriers sets the upper limit on antimony trisulfide photovoltaic devices. *Nat. Commun.* 2019, 10, 4540.

[29] Liang, G. X., Liu, T. X., Ishaq, M., Chen, Z. J., Tang, R., Zheng, Z. H., Su, Z. H., Fan, P., Zhang, X. H., Chen, S., Heterojunction interface engineering enabling high onset potential in Sb_2Se_3/CdS photocathodes for efficient solar hydrogen production. *Chem. Eng. J.* 2022, 431.

[30] Wang, W. H., Cao, Z. X., Wang, H. H., Luo, J. S., Zhang, Y., Remarkable Cd-free Sb_2Se_3 solar cell yield achieved by interface band-alignment and growth orientation screening. *J. Mater. Chem. A* 2021, 9(47), 26963-26975.

[31] Liu, D., Tang, R. F., Ma, Y. Y., Jiang, C. H., Lian, W. T., Li, G., Han, W. H., Zhu, C. F., Chen, T., Direct hydrothermal deposition of antimony triselenide films for efficient planar heterojunction solar cells. *ACS Appl. Mater. Interfaces* 2021, 13(16), 18856-18864.

[32] Liang, G. X., Chen, M. D., Ishaq, M., Li, X. R., Tang, R., Zheng, Z. H., Su, Z. H., Fan, P., Zhang, X. H., Chen, S., Crystal growth promotion and defects healing enable minimum open-circuit voltage deficit in antimony selenide solar cells. *Adv. Sci.* 2022, 9(9), 2105142.

[33] Su, Z. H., Sun, K. W., Han, Z. L., Cui, H. T., Liu, F. Y., Lai, Y. Q., Li, J., Hao, X. J., Liu, Y. X., Green, M. A., Fabrication of Cu_2ZnSnS_4 solar cells with 5.1% efficiency via thermal decomposition and reaction using a non-toxic sol-gel route. *J. Mater. Chem. A* 2014, 2(2), 500-509.

[34] Saliba, M., Etgar, L., Current density mismatch in perovskite solar cells. *ACS Energy Lett.* 2020, 5(9), 2886-2888.

[35] Shen, K., Zhang, Y., Wang, X. Q., Ou, C. Z., Guo, F., Zhu, H. B., Liu, C., Gao, Y. Y., Schropp, R. E. I., Li, Z. Q., Liu, X. H., Mai, Y. H., nip-
Efficient and stable planar n-i-p Sb_2Se_3 solar cells enabled by oriented 1D trigonal selenium structures. *Adv. Sci.* 2020, 7(16), 2001013.

[36] Wang, W. H., Cao, Z. X., Zuo, X., Wu, L., Luo, J. S., Zhang, Y., Double interface modification promotes efficient Sb_2Se_3 solar cell by tailoring band alignment and light harvest. *J. Energy Chem.* 2022, 70, 191-200.

[37] Guo, H. F., Zhao, C., Xing, Y. L., Tian, H. J., Yan, D. C., Zhang, S., Jia, X. G., Qiu, J. H., Yuan, N. Y., Ding, J. N., High-efficiency Sb_2Se_3 Solar cells modified by potassium hydroxide. *J. Phys. Chem. Lett.* 2021, 12, 12352-12359.

[38] Bae, D., A Comparative Study of (Cd,Zn)S Buffer Layers for Cu(In,Ga)Se2 Solar Panels Fabricated by Chemical Bath and Surface Deposition Methods. *Materials* 2020, 13, 1622.

[39] Luo, Y. D., Chen, M. D., Tang, R., Azam, M., Chen, S., Zheng, Z. H., Su, Z. H., Fan, P., Ma, H. L., Liang, G. X., Zhang, X. H., Energy band alignment for Cd-free antimony triselenide substrate structured solar cells by Co-sputtering ZnSnO buffer layer. *Sol. Energy Mater. Sol. Cells* 2022, 240, 111721.

[40] Whitten, J. E., Ultraviolet photoelectron spectroscopy: Practical aspects and best practices. *Appl. Surf. Sci. Adv.* 2023, 13, 100384.

[41] Tang, R., Zheng, Z. H., Su, Z. H., Li, X.-J., Wei, Y.-D., Zhang, X. H., Fu, Y. Q., Luo, J., Fan, P., Liang, G. X., Highly efficient and stable planar heterojunction solar cell based on sputtered and post-

selenized Sb_2Se_3 thin film. *Nano Energy* 2019, 64(103929), 103929.

[42] Yan, C., Huang, J. L., Sun, K. W., Johnston, S., Zhang, Y. F., Sun, H., Pu, A. B., He, M. R., Liu, F. Y., Eder, K., Yang, L. M., Cairney, J. M., Ekins-Daukes, N. J., Hameiri, Z., Stride, J. A., Chen, S. Y., Green, M. A., Hao, X. J., Cu_2ZnSnS_4 solar cells with over 10% power conversion efficiency enabled by heterojunction heat treatment. *Nat. Energy* 2018, 3(9), 764-772.

[43] Li, Y., Wang, K., Huang, D. W., Li, L. T., Tao, J. H., Ghany, N. A. A., Jiang, F., $Cd_xZn_{1-x}S/Sb_2Se_3$ thin film photocathode for efficient solar water splitting. *Appl. Catal., B* 2021, 286(1), 119872.

[44] Chen, K., Wu, P., Yang, W. Q., Su, R., Luo, D. Y., Yang, X. Y., Tu, Y. G., Zhu, R., Gong, Q. H., Low-dimensional perovskite interlayer for highly efficient lead-free formamidinium tin iodide perovskite solar cells. *Nano Energy* 2018, 49, 411-418.

[45] Fan, P., Chen, G. J., Chen, S., Zheng, Z. H., Azam, M., Ahmad, N., Su, Z. H., Liang, G. X., Zhang, X. H., Chen, Z. G., Quasi-vertically oriented Sb_2Se_3 thin-film solar cells with open-circuit voltage exceeding 500 mV prepared via close-space sublimation and selenization. *ACS Appl. Mater. Interfaces* 2021, 13(39), 46671-46680.

[46] Lin, J. H., Mahmood, A., Chen, G. J., Ahmad, N., Chen, M. D., Fan, P., Chen, S., Tang, R., Liang, G. X., Crystallographic orientation control and defect passivation for high-efficient antimony selenide thin-film solar cells. *Materials Today Physics* 2022, 27(100772), 100772.

[47] Wang, C., Lu, S. C., Li, S., Wang, S. Y., Lin, X. T., Zhang, J., Kondrotas, R., Li, K. H., Chen, C., Tang, J., Efficiency improvement of flexible Sb_2Se_3 solar cells with non-toxic buffer layer via interface engineering. *Nano Energy* 2020, 71(104577).

[48] Wen, X. X., Lu, Z. H., Wang, G. C., Washington, M. A., Lu, T. M., Efficient and stable flexible Sb_2Se_3 thin film solar cells enabled by an epitaxial CdS buffer layer. *Nano Energy* 2021, 85, 106019.

[49] Chen, G. J., Luo, Y. D., Abbas, M., Ishaq, M., Zheng, Z. H., Chen, S., Su, Z. H., Zhang, X. H., Fan, P., Liang, G. X., Suppressing buried interface nonradiative recombination losses toward high-efficiency antimony triselenide solar cells. *Adv. Mater.* 2023, 36(5), 2308522.

[50] Lian, W. T., Jiang, C. H., Yin, Y. W., Tang, R. F., Li, G., Zhang, L. J., Che, B., Chen, T., Revealing composition and structure dependent deep-level defect in antimony trisulfide photovoltaics. *Nat. Commun.* 2021, 12(1), 3260.

[51] Lang, D. V., Deep-level transient spectroscopy: a new method to characterize traps in semiconductors. *J. Appl. Phys.* 1974, 45(7), 3023-3032.

[52] Tang, R. F., Wang, X. M., Lian, W. T., Huang, J. L., Wei, Q., Huang, M. L., Yin, Y. W., Jiang, C. H., Yang, S. F., Xing, G. C., Chen, S. Y., Zhu, C. F., Hao, X. J., Green, M. A., Chen, T., Hydrothermal deposition of antimony selenosulfide thin films enables solar cells with 10% efficiency. *Nat. Energy* 2020, 5(8), 587-595.

[53] Tang, R., Chen, S., Zheng, Z. H., Su, Z. H., Luo, J. T., Fan, P., Zhang, X. H., Tang, J., Liang, G. X., Heterojunction annealing enabling record open-circuit voltage in antimony triselenide solar cells. *Adv. Mater.* 2022, 34(14), 2109078.

[54] Chen, C., Tang, J., Open-circuit voltage loss of antimony chalcogenide solar cells: status, origin, and possible solutions. *ACS Energy Lett.* 2020, 5(7), 2294-2304.

[55] Wang, S. Y., Zhao, Y. Q., Che, B., Li, C., Chen, X. L., Tang, R. F., Gong, J. B., Wang, X. M., Chen, G. L., Chen, T., Li, J. M., Xiao, X. D., A novel multi-sulfur source collaborative chemical bath deposition technology enables 8%-efficiency Sb_2S_3 planar solar cells. *Adv. Mater.* 2022, 34(41), 2206242.

[56] Sze, S. M., *Semiconductor devices: physics and technology*. Wiley: 2002; p 48.

[57] Hadke, S., Huang, M. L., Chen, C., Tay, Y. F., Chen, S. Y., Tang, J., Wong, L., chalcogenide--

Emerging chalcogenide thin films for solar energy harvesting devices. *Chem. Rev.* 2022, 122(11), 10170-10265.

Chapter III: Rapid thermal annealing of Sb_2Se_3 thin-film solar cells with 9.03% efficiency

3.1 Introduction

In recent years, there has been significant progress in enhancing the PCE of Sb_2Se_3-based solar cells, with a current record standing at 10.57%.[1] However, to approach its theoretical PCE limit of over 30%,[2] the improvement of Sb_2Se_3 absorber layer quality and optimization of grain orientation remain the key factors. Existing literature suggests that achieving large crystal grains, a voids-free and compact morphology, along with benign orientation in the Sb_2Se_3 absorber layer leads to remarkable photoelectric characteristics for the entire device, thereby promoting its efficiency.[3, 4] In this regard, the fabrication of a high-quality Sb_2Se_3 thin film is deemed crucial for maximizing the performance of an Sb_2Se_3 device.

Various thin film deposition approaches have been employed to fabricate high-quality Sb_2Se_3 films with preferential orientation along the (hk1) crystal plane. As mentioned in chapter II, these approaches include vapor transport deposition (VTD),[5] close-spaced sublimation (CSS),[6] magnetron sputtering deposition (MSD),[7] rapid thermal processing (RTP),[8, 9] chemical bath deposition (CBD),[1] thermal evaporation (RTE),[10] hydrothermal deposition (HD)[11], and injection vapor deposition (IVD).[12] Among these thin film deposition techniques, RTP approach has emerged as a successful method capable of preparing high-quality thin films for both laboratory-scale research and commercial production. Firstly, the vacuum-based RTP reaction process, involving chemical vapor deposition and/or physical vapor deposition, takes place within a vacuum environment, which effectively mitigates the adverse impact of dust particles on the morphology of the film during the deposition process. The vacuum condition plays a vital role in ensuring the quality control of thin film preparation during the typical thin film deposition process.[13] Additionally, simplifying operations not only facilitates experimental accuracy but also enables large-scale production.[14] In contrast, traditional thermal evaporation approaches often suffer from longer-duration reactions and challenges in controlling grain growth due to slower heating and cooling rates. In contrast, the RTP commonly takes place in a shorter-duration reaction process,

providing instantaneous heat to the samples within a relatively brief period. This RTP thermal treatment process rapidly activates the sample atoms, inducing grain nucleation and crystallization, thereby increasing crystallinity and enhancing surface smoothness.[15] In addition, the accelerated heat conduction during RTP heat treatment expedites diffusion reaction, thereby mitigating or even preventing the film from oxidation, which is commonly observed in slower traditional thermal evaporation approaches. Moreover, it is noteworthy to mention that the use of the RTP approach can significantly reduce a number of undesirable defects at the surface and in the bulk of film, which typically originate from long-time annealing processes conducted at excessive temperatures.[16] Numerous strategies associated with RTP have been successfully employed in photovoltaic devices to fabricate and optimize the absorber thin film, thereby enabling the enhancement of device performance. For instance, the incorporation of potassium (K) into the solution-processed $Cu(In,Ga)(S,Se)_2$ device followed by selenization through RTP has proven effective in increasing the crystallization and modifying the surface of CIGSSe.[17] The photoelectric performance of $Cu_2ZnSn(S_xSe_{1-x})_4$ thin-film solar cells has shown significant improvement, particularly in terms of open-circuit voltage (V_{oc}), as a result of optimizing different selenization annealing process using RTP.[18] Low-temperature RTP annealing of the $(Ag,Cu)_2ZnSnSe_4$/CdS junction has proven advantageous in significantly reducing interface recombination, thereby enhancing the V_{oc} and fill factor (FF) of the device.[19] Therefore, in consideration of the aforementioned literature pertaining to other thin films utilized in solar cells, it is imperative to allocate greater attention toward comprehending both the crystal growth mechanism and the mechanism for suppressing defects in RTP-Sb_2Se_3 thin films and solar cells, aiming for further enhancement of the overall cell performance.

In this chapter, the Sb_2Se_3 layer has been prepared on the Mo-coated substrate by selenizing the sputtered-Sb metallic precursor. Notably, the selenization procedure was carried out using a rapid-heating tube furnace. Through a comprehensive investigation of the grain growth process during the RTP selenization, we systematically examined

the effects of Sb_2Se_3 thin film morphology and microstructure on photoelectric characteristics and defect properties. Fundamentally, the optimization of the RTP selenization process (including pre-selenization, selenization temperature and duration) enables improved crystallization, preferred crystal orientation, and enhanced carrier transportation, which is conducive to mitigating trap recombination and reducing defect density.

3.2 Preparation and characterization of Sb_2Se_3 thin film

3.2.1 Preparation of Sb_2Se_3 thin film

As in chapter II, Sb metallic precursor thin film was deposited on cleaned Mo-coated soda-lime glass substrate by RF magnetron sputtering. The sputtering deposition process was conducted in a vacuum chamber with a residual pressure below 7.0×10^{-4} Pa. 35 W was selected as the suitable sputtering power. Argon gas filled the whole chamber with a flow rate of 30 sccm. The sputtering pressure was kept at 0.5 Pa during the deposition of 40 min to obtain a thickness of 600 nm. Sequentially, the Sb_2Se_3 layer was prepared by an effective rapid thermal process, during which 0.2 g Se power (99.999% purity, Aladdin) was used as the Se source which was separated into two quartz crucibles. These two crucibles were placed on each side of the graphite box, as shown in Figure 3.1a. The Sb metallic precursor samples were kept in the middle of the graphite box. In order to let the sample be heated evenly, the whole graphite box was placed at the center of the heating zone. The RTP treatment was carried out in argon gas with a pressure of 0.05 MPa. It is important to notice that the vacuum tubular furnace needs to be purified with argon to remove air before the treatment. Heat-up time (pre-selenization duration) was varied from 60 s to 300 s at an interval of 60 s to determine the best duration. The RTP-selenization procedures were conducted at the temperatures of 370, 390, and 410°C, respectively. The selenization durations were

selected to be 5, 15, and 25 min. Especially, different ramping rates were applied to heating process.

The temperature-time curves of the RTP technique employed in this study and the normal thermal processing (NTP) are presented in Figure 3.1b. It should be noted that NTP requires a significantly longer heating time, approximately five times that of RTP. In chapter II, NTP technique has been used with a rate of 20°C/min to obtain a selenization temperature of 410°C, corresponding to a set time of 1200 seconds with pre-selenization duration. As is known, this prolonged pre-selenization can adversely impact both crystal growth and the overall selenization process.[16] Additionally, it is worth mentioning that a graphite box was utilized to house both the Se source and the sample, which were positioned on the top of an AlN support along with a thermocouple beneath them. This arrangement proves advantageous in maintaining stable sample temperatures throughout experimentation. The impact of favorable pre-selenization durations on crystal growth and defect formation within the bulk Sb_2Se_3 absorber layer will be studied.

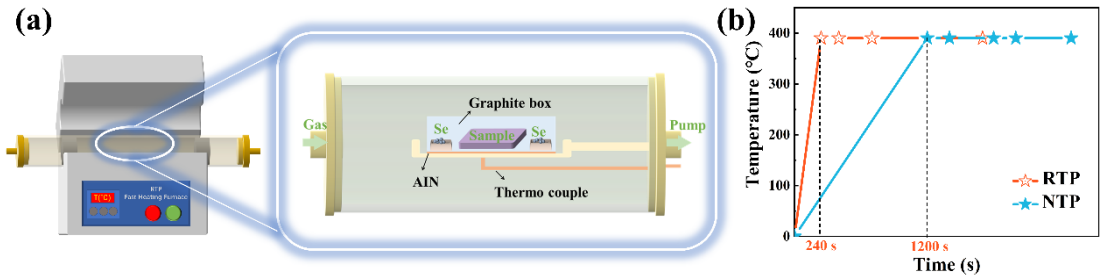

Figure 3.1 *The RTP preparation process of Sb_2Se_3 thin film.*

3.2.2 Influence of pre-selenization time on morphology and crystallinity of Sb_2Se_3 thin film

Exploration of how to optimize crystal growth has been considered as a crucial prerequisite for the superior quality of Sb_2Se_3 absorber thin films in the application of photovoltaic devices.[20] Therefore, the nucleation crystallization process of Sb_2Se_3 thin film was initially investigated by varying the pre-selenization duration from 60 s to 300

s at intervals of 60 s. For clarity, the Sb_2Se_3 samples prepared through RTP with the aforementioned pre-selenization duration were denoted as R60, R120, R180, R240, and R300, respectively. The microstructure characteristics, including X-ray diffraction (XRD), scanning electron microscopy (SEM), and electron backscatter diffraction (EBSD), were employed to monitor the evolution of morphology variation and preferred orientation for RTP-Sb_2Se_3 grain growth.

Figure 3.2a-c shows the XRD patterns of the as-prepared thin films that underwent pre-selenization at different durations (i.e., 60, 120, 180, 240, and 300 s) at 410°C without selenization. It is evident from the XRD patterns that all the diffraction peaks of the R60 thin film correspond to orthorhombic Sb (JCPDS#35–0732) with dominant orientation along the [012], [104], [110]and [202] directions (Figure 3.2a). Concurrently, the diffraction peak belonging to Sb still could be observed in the XRD pattern of the R120 sample; however, it exhibits a relatively weakened intensity. This observation was further confirmed by the quantified texture coefficient (TC) analysis (Figure 3.2b). Especially, the diffraction peaks of Sb_2Se_3 can be detected, predominantly exhibiting an orientation characterized by (hk0).

TC, considered as an indicator of preferred crystal orientation, is utilized to quantitatively examine the orientation preference by focusing on the dominant diffraction peaks. The TC values were calculated using the following formula quote:[21]

$$TC_{hkl} = \frac{I_{hkl}}{I_{0\,hkl}} \Big/ \left(\frac{1}{N} \sum_{i=1}^{N} \frac{I_{h_i k_i l_i}}{I_{0\,h_i k_i l_i}} \right) \tag{3-1}$$

where $I_{0(hkl)}$ and $I_{(hkl)}$ are the diffraction peak intensities of (hkl) planes in the standard XRD pattern of Sb (JCPDS#35–0732) and the measured XRD result, respectively. Four main diffraction peaks were selected for the TC calculation. A high TC value of a diffraction peak demonstrates preferential crystal orientation along this specific direction. It is evident that the (012), (104), and (110) peaks can be consistently detected with gradually diminishing intensity. This observation inferred that the Sb metallic film was consumed gradually.

Then, XRD spectra for R180 revealed the obvious diffraction peaks of (211) and (221) assigned to the orthorhombic phase of Sb_2Se_3 (JCPDS#15–0861), indicating the presence of $(Sb_4Se_6)_n$ chains on the Mo substrate. However, there are still remaining diffraction peaks for the R180 film at positions (020) and (120), which are detrimental to carrier transport. The diffraction peaks for R240 sample exhibit prominent peaks that are in good agreement with the standard card (JCPDS#15–0861) for the orthorhombic phase of Sb_2Se_3 indicating the absence of any detectable impurity and successful formation of favorable Sb_2Se_3 grains. Furthermore, analysis of the TC in Figure 3.2c reveals a weakened [hk0] orientation and strengthened [hk1] orientation (mainly (211) and (221)), indicating that an appropriate pre-selenization duration can facilitate better crystallization and favorable growth orientation.

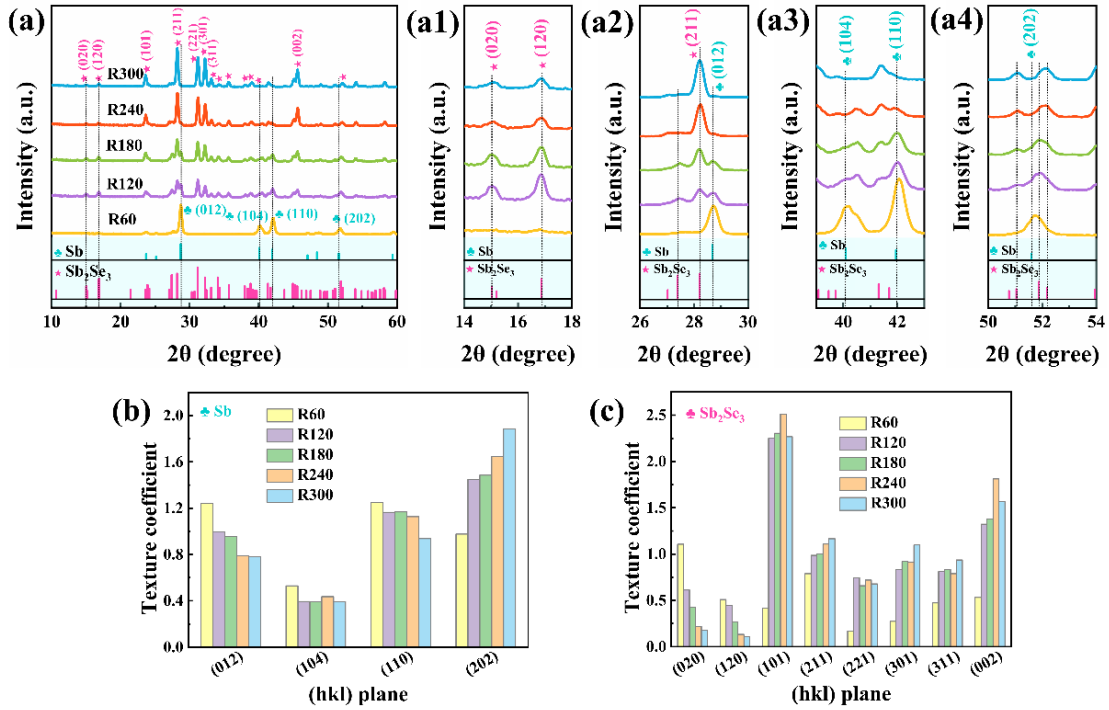

Figure 3.2 *(a) The XRD patterns and (a1–a4) the corresponding detailed diffraction peaks. Texture coefficients of Sb (b) and Sb_2Se_3 (c) for the above samples at 410°C.*

The surface SEM images of Sb_2Se_3 films with different pre-selenization durations are presented in Figure 3.3a-e, while the corresponding cross-section SEM images can be found in Figure 3.3a1-e1. As shown in Figure 3.3a, the surface of the sample lacks

noticeable crystal characteristics but instead displays small ripple-like grains, aligning with the typical surface morphology of Sb film as previously reported in our study.[22] The cross-sectional image in Figure 3.3a1 indicates minimal alteration, which is further supported by the XRD diffraction peaks observed in Figure 3.2a for the R60 sample, confirming their attribution to the Sb metallic precursor.

After a pre-selenization duration of 120 s, dispersed and squamous single Sb_2Se_3 seeds irregularly appear on the surface of the sample (Figure 3.3b), leading to a progressive increase in thickness. In Figure 3.3b1, only an ultra-thin layer of particles on the upper surface initiated the selenization reaction, indicating partial selenization of the Sb layer. The formation of these seeds was confirmed by the presence of weak Sb_2Se_3 diffraction peaks in the corresponding XRD spectra for the R120 sample.

Then, numerous small Sb_2Se_3 grains could be spotted on the sample surface with poor compactness and a few pinholes when 180 s was applied for the pre-selenization duration, indicating an inadequate intermediate stage of pre-selenization reaction (Figure 3.3c). The existence of these minute grains leads to considerable grain boundary area, facilitating the formation of trap centers and increasing the probability of minority carriers (electrons) recombination at the grain boundary.[23] Additionally, a few larger grains with sizes approaching 800 nm, accompanied by distinct micro-voids, were observed in the cross-section (Figure 3.3c1).

Subsequently, by increasing the pre-selenization duration to 240 s, the Sb_2Se_3 thin films demonstrated remarkable compactness and uniformity, accompanied by a noticeable increase in grain size to approximately 1 μm (Figure 3.3d). Such film comprises large grains nearly matching the thickness of the entire Sb_2Se_3 layer, exhibiting excellent adhesion to the Mo substrate (Figure 3.3d1). These larger grains and strong adhesion align well with the corresponding XRD spectra which displayed prominent peaks without any detectable impurities for the R240 sample (Figure 3.2a).

Afterward, the prolonged duration of pre-selenization (300 s) made little difference in crystallization as the Sb_2Se_3 grain sizes remained essentially constant (Figure 3.3e). However, discrete space appeared between the absorber layer and the Mo substrate

(Figure 3.3e1), resulting in poor adhesion. Prominent growth in Sb_2Se_3 grain development was observed within the range of pre-selenization durations from 60 s to 300 s, indicating a dynamic process of the nucleation crystallization growth for the Sb_2Se_3 absorber thin film. Consequently, a model illustrating this dynamic crystal growth during the RTP process will be proposed and discussed later on.

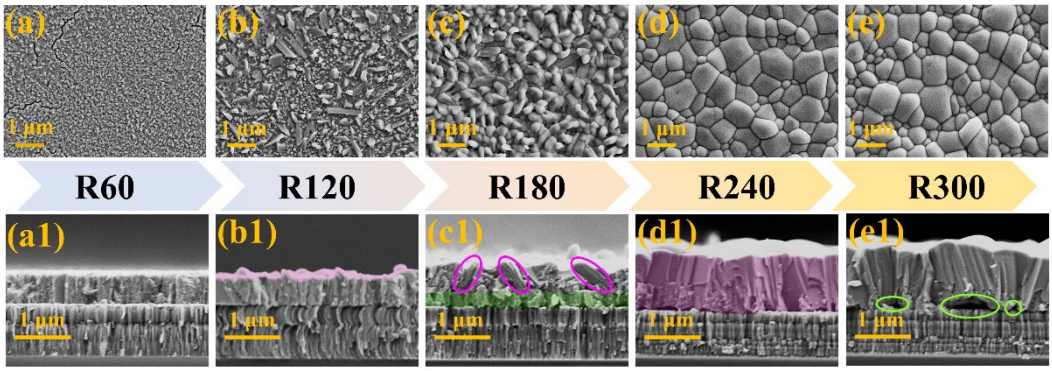

Figure 3.3 *(a–e) The surface SEM images and (a1–e1) the cross-sectional SEM images of Sb_2Se_3 thin films under the pre-selenization duration of 60, 120, 180, 240, and 300 s for 410°C.*

In general, EBSD measurement, an SEM-based technique, is widely regarded as a valuable tool for investigating the characteristics of grain boundaries and in-plane orientations in Sb_2Se_3 films.[24] Figure 3.4a presents the microtopography SEM image of the R240 sample obtained through EBSD measurement. Furthermore, Figure 3.4b illustrates the EBSD crystallographic orientation mapping of the Sb_2Se_3 film along the Z direction using inverse pole figure (IPF), while providing colored orientation IPF maps within it. Blue, yellow, or pink colors can be observed within a small scanned area in the IPF-Z mapping, demonstrating that several crystal grains exhibit out-of-plane misorientations, which can be ascribed to the non-negligible surface roughness. However, a dominant red color is evident in the EBSD map image, implying highly quasi-(001) orientated growth in the Sb_2Se_3 film. It is worth mentioning that this quasi-(001) orientation promotes carrier transportation and enhances device performance.

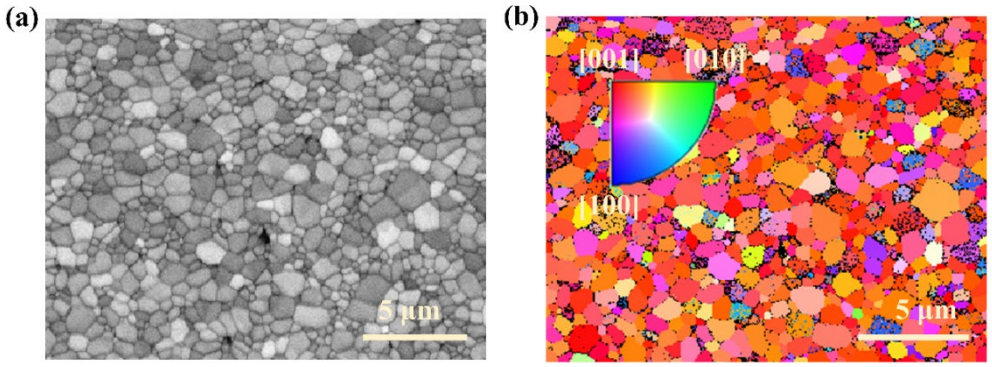

Figure 3.4 *(a) Microtopography image of the R240 sample using in electron backscatter diffraction (EBSD), (b) corresponding EBSD mapping in IPF-Z component.*

3.2.3 Nucleation crystallization growth model for pre-selenization process of Sb_2Se_3

The schematic diagram in Figure 3.5 illustrates the crystal growth model of the Sb_2Se_3 absorber thin film through selenization of Sb precursors using the RTP technique. The Sb precursors with amorphous features were deposited on the Mo substrate via RF magnetron sputtering. Primarily, during the initial duration, the Sb films (sample R60) remained in a pre-reaction state due to the limited selenium atmosphere, characterized by a deficiency in selenium. Consequently, the Se atoms merely diffuse within the vacuum furnace without participating in the reaction, leading to negligible deviation from the as-deposited Sb metallic precursor. It was found that during the initial growth stage, a significant amount of Se atoms diffuses and combines with Sb atoms to form Sb_2Se_3 molecules as the pre-selenization duration extends. Owing to the squamous and granulated morphology of Sb_2Se_3 grains, the resulting surface of the sample was discontinuous, chaotic, and uncompact at this stage. The selenization would take place progressively from the surface of the Sb film toward the Mo substrate, leading to a double-layer structure comprising an upper layer of Sb_2Se_3 and the bottom layer of Sb. Subsequently, continuously extending the pre-selenization duration up to 180 s can effectively promote crystallization while facilitating numerous Se evaporation diffusion

throughout the entire thickness. The downward diffusion of Se continues to react with upward Sb to form Sb_2Se_3 molecules until the bottom Sb atoms are completely consumed. However, because of the limited pre-selenization duration, the combination reaction imparts less energy to the bottom grains. As a result, a double-layer structure is formed within the Sb_2Se_3 grains layer, comprising an upper layer consisting of large Sb_2Se_3 grains and a bottom layer consisting of fine Sb_2Se_3 grains. At the final stage of crystal growth, large compact grains in vertical growth distribute evenly across the complete Sb_2Se_3 absorber layer under sufficient Se scenario as more pre-selenization duration is employed. Such improved crystallization and grain distribution not only effectively prevent carrier recombination at grain boundaries but also facilitate carrier transport within the Sb_2Se_3 absorber layer. It is evident that excessively prolonging the pre-selenization duration would adversely impact the crystallization of the Sb_2Se_3 film, resulting in visible voids between the Sb_2Se_3 layer and the substrate. With excessive pre-selenization, it is possible to speculate that the formation of substantial voids is triggered by Se re-evaporating. Therefore, it can be inferred that an appropriate pre-selenization duration plays a key role in achieving high-quality Sb_2Se_3 thin film.

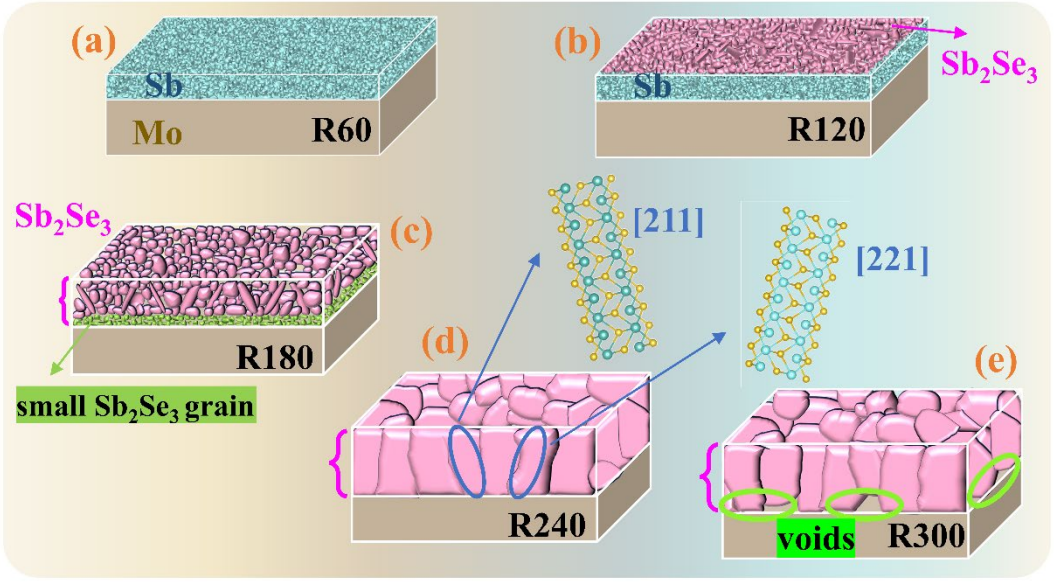

Figure 3.5 *Schematic illustration of Sb_2Se_3 thin films under various pre-selenization conditions of 60, 120, 180, 240, and 300 s, denoted as R60, R120, R180, R240, and R300 samples at 410°C.*

3.2.4 Investigation of the topography and surface potential distribution of Sb_2Se_3 thin films

To elucidate the disparity in morphology evolution of the aforementioned absorber thin films, we conducted Kelvin probe force microscopy (KPFM) measurements, which detects variations in electrostatic forces between the probe tip and material surface, arising from differences in their Fermi levels. This is achieved by applying a direct bias voltage equivalent to the contact potential difference (V_{CPD}). Consequently, upon introducing the bias voltage to the samples, surface potential can be determined using a simple equation as follows:[25]

$$\varphi_S = \varphi_T - eV_{CPD} \tag{3-2}$$

where φ_S is the potential of the sample, and φ_T is the potential of the probe. The surface topography and the corresponding distribution of V_{CPD} values are displayed in Figure 3.6a, b, respectively. The surface morphology of the three samples exhibited conformity with that observed in the top-view SEM images. The color contrast bar accurately represented the distribution of V_{CPD} values extracted from the KPFM signal. Since the R60 and R120 samples underwent partial pre-selenization without complete growth into Sb_2Se_3, the obtained thin film comprised a mixture of Sb and Sb_2Se_3. Therefore, discussion regarding KPFM and the subsequent characteristics will be confined to R180, R240, and R300 samples. One can easily distinguish the grain boundary (GB) and the grain internal (GI) in most scanning areas due to the noticeable color difference observed in the three samples (Figure 3.6b), which manifests a varying potential difference between the GB and the GI. It is important to highlight that this potential difference, caused by fluctuations in band structures, directly impacts carrier transportation in space. As depicted in Figure 3.6b for the three samples, the V_{CPD} at GB was higher than that of GI, resulting in a lower potential at GB compared with GI, leading to strong band bending at GB, which also can be quantitatively calculated by the following expression based on the Equation:[18]

$$\varphi_{GI} - \varphi_{GB} = eV_{CPD(GB)} - eV_{CPD(GI)} \tag{3-3}$$

where φ_{GI} and φ_T are the potentials of the GI and GB, respectively. In theory, a higher V_{CPD} at GB hinders the horizontal carrier transportation, while a lower V_{CPD} at GI effectively promotes the vertical separation of electrons and holes along the aligned $[Sb_4Se_6]_n$ ribbons. However, upon further comparison of the potential difference change between the GB and the GI among the three samples, it is observed that sample R240 exhibits a smaller potential difference than both sample R180 and sample R300. Meanwhile, as depicted in Figure 3.6c, the average V_{CPD} ($V_{CPD(GB)}$-$V_{CPD(GI)}$) between GB and the GI was about 39.7, 25.1, and 47.9 mV for the R180, R240, and R300 samples, respectively. These imply a decrease in the disparity of Fermi levels, leading to reduced fluctuations in energy bands within the R240-Sb_2Se_3 thin film. The decreased average V_{CPD} can be attributed to the presence of larger Sb_2Se_3 grains and fewer grain boundaries within the R240 sample as previously discussed during SEM analysis.[26] To some extent, the undesired characteristics of crystal defects, such as the small grain size and non-uniform distribution of grains in R180 film, as well as pin-holes in R300 film, also exist in the thin film. These defects may generate more surface trap states at GB, resulting in a higher degree of band bending that negatively impacts device performance. The favorable average V_{CPD} results obtained from the R240 sample suggest a more suitable band structure with minimal band bending (Figure 3.6d), which is advantageous for reducing substantial carrier recombination and enhancing charge carrier transport and collection.

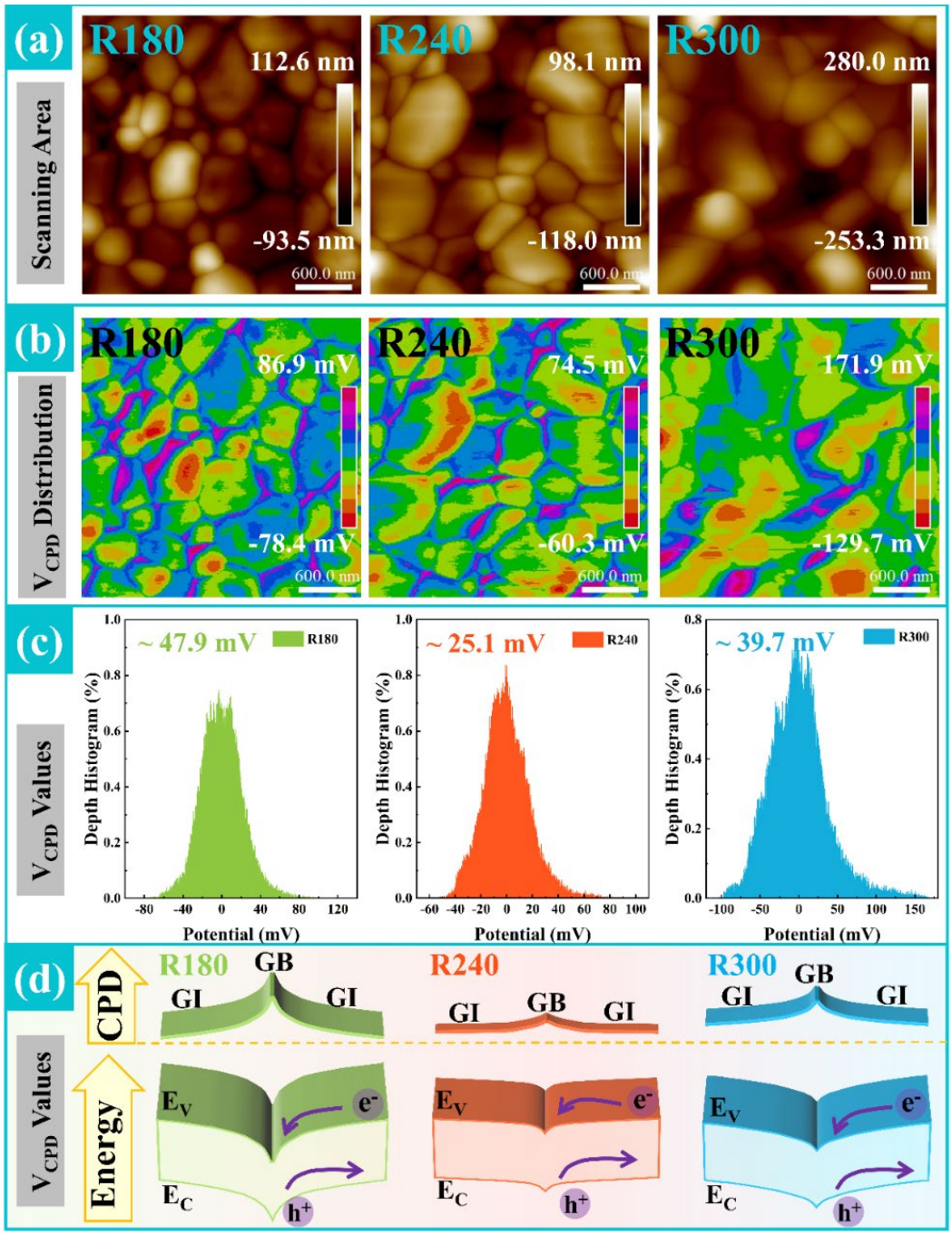

Figure 3.6 *Topography and surface potential of Sb_2Se_3 samples according to Kelvin probe force microscopy (KPFM) characterization. (a) Topography, (b) surface potential distribution, (c) corresponding values of surface potential, and (d) schematic diagrams of the energy band structure and CPD near the GB for R180, R240, and R300 samples, respectively at 410°C.*

3.2.5 Influence of selenization temperature and duration on morphology and crystallinity of Sb_2Se_3 thin film

Based on the aforementioned analysis, it can be preliminarily concluded that pre-selenization conducted at 240 s is optimal for promoting the growth of high-quality Sb_2Se_3 crystals. Furthermore, the investigation aims to identify the optimal temperature and duration required for selenization to achieve Sb_2Se_3 thin film with desirable microstructure and preferred orientation.

The selenization temperatures were conducted at 370, 390, and 410 ^oC to investigate their impact on the morphology and crystal orientation of the absorber thin film by using SEM and XRD. The surface morphologies of the Sb_2Se_3 absorber thin films annealed at different temperatures for a selenization duration of 15 min are depicted in Figure 3.7. Notably, the grain sizes of the three absorber thin films were found to be significantly increased with the increasing temperatures, suggesting remarkable improvement in crystallization and growth (Figure 3.8). This finding aligns with the XRD patterns and corresponding TC values presented in Figure 3.9, while the XRD patterns demonstrate the absence of any detectable impurities in all samples. However, it was observed that voids appear on both sides (the surface and the cross-section) of the thin film annealed at 410 ^oC, which can be attributed to the excessive selenization temperature leading to accelerated Se evaporation. Therefore, better morphology and crystallinity of Sb_2Se_3 thin film can be achieved under a selenization temperature of 390 ^oC.

Following an analysis of the impact of selenization temperature, selenization durations of 0, 5, 15, and 25 mins were chosen to further optimize the Sb_2Se_3 absorber layer. It was found that increasing the duration of selenization led to a notable improvement in both grain size and microstructure for a selenization temperature of 390^oC (Figure 3.10).

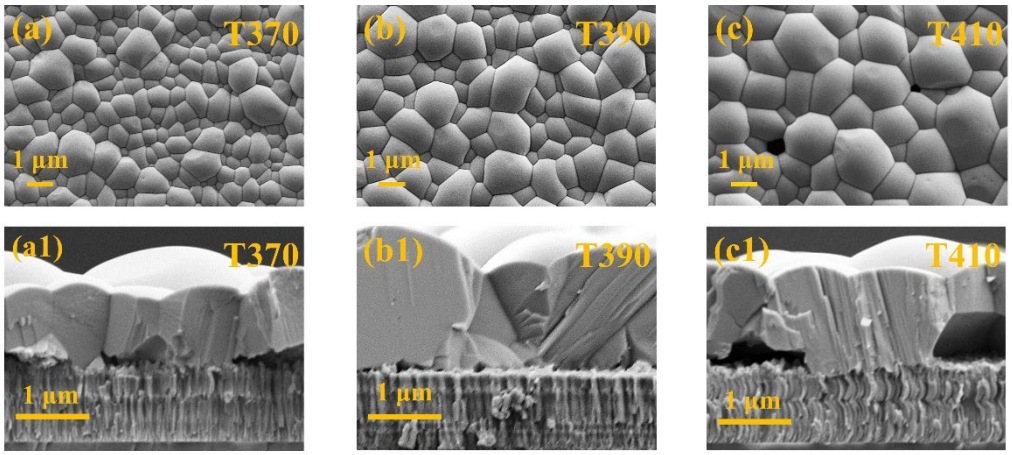

Figure 3.7 *(a–c) The surface SEM images and (a1–c1) the cross-sectional SEM images of Sb_2Se_3 thin films at different selenization temperatures of 370, 390, and 410°C with 240 s for pre-selenization and with a selenization duration of 15 min.*

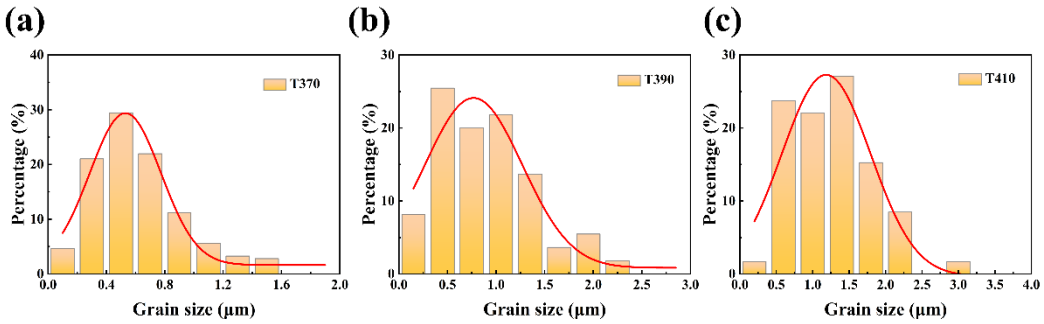

Figure 3.8 *The detailed frequency histograms versus grain size distribution for Sb_2Se_3 thin films at different selenization temperatures.*

In comparison to samples (D0 sample) without subsequent selenization processes, the Sb_2Se_3 grain size increased approaching 1.3 µm (Figure 3.11), resulting in significantly improved uniformity and flatness in the D15 Sb_2Se_3 sample. However, the D25 sample exhibited visible voids in both the Sb_2Se_3 bulk and at the back interface, despite the presence of large grains in the thin film.

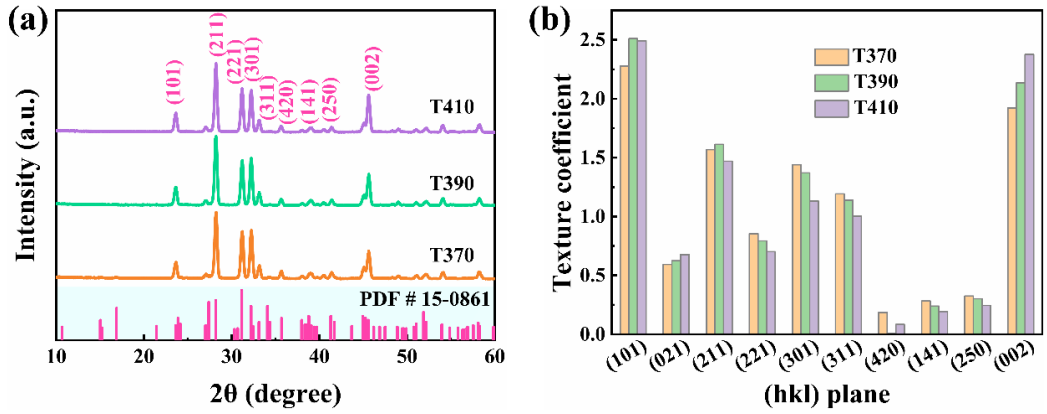

Figure 3.9 *(a) XRD patterns and corresponding TC values of the prominent diffraction peaks for Sb_2Se_3 thin films at different selenization temperatures for a selenization duration of 15 min.*

To some extent, this signifies the quality of the selenized Sb_2Se_3 thin film is dependent on an appropriate selenization duration. The XRD patterns demonstrate that all the films present prominent diffraction peaks that align well with the standard orthorhombic Sb_2Se_3 (PDF#15–0861) (Figure 3.12).[27] Furthermore, the TC values indicate that the D15 sample displays a distinct preferred orientation of [211] and [221] with high crystallinity, which has been proven to enhance carrier transport. Overall, excellent quality of Sb_2Se_3 thin film was achieved when the selenization process was performed at the optimal scenario of 390 °C for 15 min.

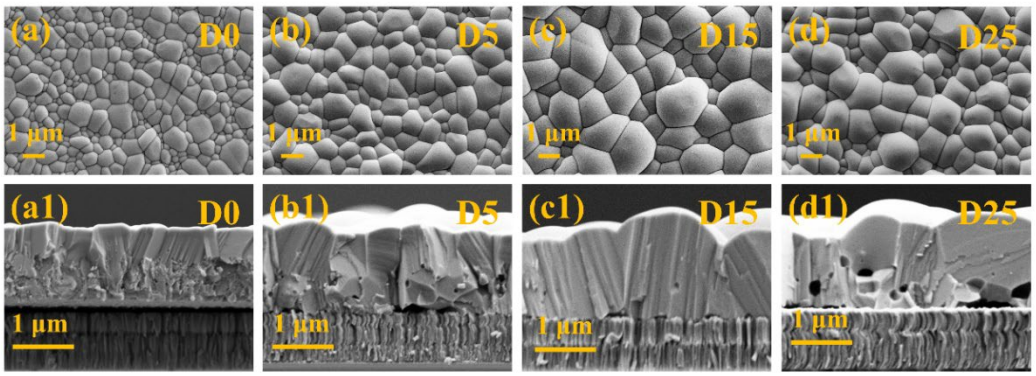

Figure 3.10 *(a–d) The surface SEM images and (a1–d1) the cross-sectional SEM images for Sb_2Se_3 thin films at different selenization durations of 0, 5, 15, and 25 mins for a selenization temperature of 390°C.*

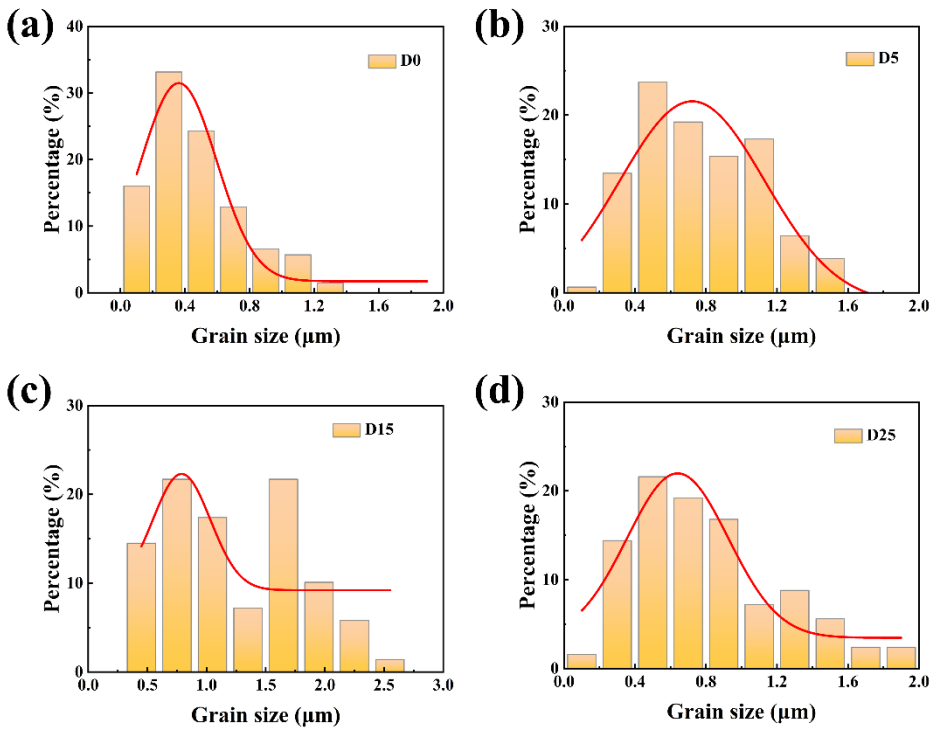

Figure 3.11 *The detailed frequency histograms versus grain size distribution for Sb_2Se_3 thin films at different selenization durations.*

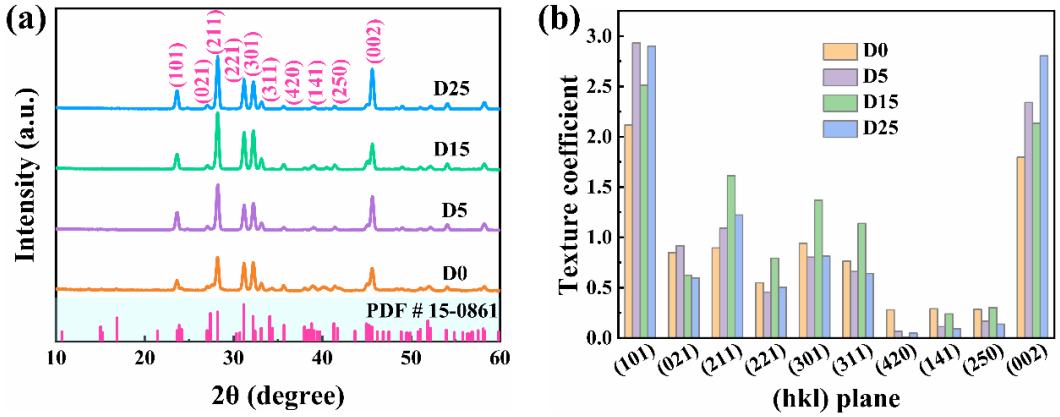

Figure 3.12 *(a) XRD patterns and corresponding TC values of the prominent diffraction peaks for Sb_2Se_3 thin films with different selenization durations for a selenization temperature of 390 °C.*

3.3 Preparation and characterization of Sb_2Se_3 thin film solar cells

3.3.1 Preparation and characterization of Sb_2Se_3 thin film solar cells

The cadmium sulfide (CdS) buffer layer with a thickness of 70~80 nm was directly deposited onto the RTP-Sb_2Se_3 absorber layer by chemical bath deposition (CBD). Cadmium sulfate ($3CdSO_4 \cdot 8H_2O$) aqueous solution (0.015 M, 20 mL), thiourea aqueous solution (0.75 M, 20 mL), and ammonium hydroxide aqueous solution (14.8 M, 20 mL) were subsequently added to deionized water (140 mL). The samples were soaked into the mixed solution and the CBD process lasted 8 min at 80 °C. After the CBD process, a 0.5 M Al^{3+} solution was incorporated into the CBD-CdS thin film by spin-coating at a speed of 2000 r/min, followed by annealing on a hotplate in the air at 280 ºC for 5min (A3 condition of chapter II).

Indium tin oxide (ITO) windows layer with a thickness of 300~400 nm was subsequently deposited on the surface of Al-doped CdS film via the magnetron sputtering technique. The working pressure and sputtering power were kept at 0.4 Pa and 120 W during the sputtering process, respectively. The sputtering duration was fixed at 25 min without additional in-situ heat treatment.

Silver (Ag) granules were thermally evaporated onto the surface of the ITO windows layer forming the Ag electrodes.

Finally, the device was divided, by knife, into small identical areas with an active area of 0.135 cm^2. A substrate configuration of Mo/Sb_2Se_3/CdS:Al/ITO/Ag was constructed for the Sb_2Se_3 thin film solar cells (Figure 3.13).

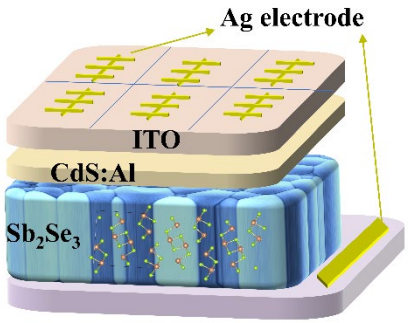

Figure 3.13 *The schematic structure of the Sb_2Se_3 thin film solar cells.*

3.3.2 Photovoltaic performance of the Sb_2Se_3 thin film solar cells

Different Sb_2Se_3 devices were fabricated and characterized to compare the influence of different pre-selenization durations of the Sb_2Se_3 absorber layer on device performance with a selenization temperature and duration of 390 °C and 15 min, respectively. The corresponding photovoltaic parameters are listed in Table 3.1 and current density–voltage (*J–V*) curves of the representative Sb_2Se_3 devices with different preparation conditions of the Sb_2Se_3 absorber layers are shown in Figure 3.14 for in-depth assessment and analysis. The device utilizing the R240 absorber presents a significant superiority in all the key PV parameters, delivering the highest V_{OC} of 495 mV, a *FF* of 62.95%, a J_{SC} of 28.97 mA/cm^2, yielding the best PCE of 9.03% under the AM 1.5 G solar irradiation. It should be noted that the best result obtained by the NTP method in Chapter II is 8.41%.

Table 3.1 *Summary of key parameters for the devices R180, R240, and R300 selenized at 390 °C for 15 min.*

Devices	***PCE*** **(%)**	V_{OC} **(mV)**	***FF*** **(%)**	J_{SC} **(mA/cm^2)**
R180	6.04	452	56.53	23.66
R240	9.03	495	62.95	28.97
R300	6.27	476	53.07	24.84

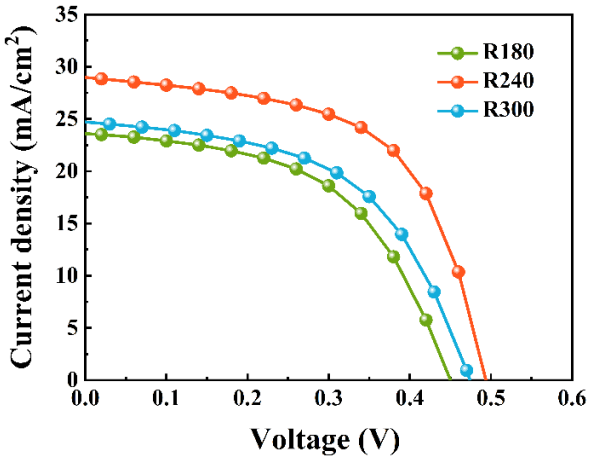

Figure 3.14 *J–V curves of the devices R180, R240, and R300.*

The external quantum efficiency (EQE) spectra, which reflect the photo-response of the devices and the integrated J_{SC} are presented in Figure 3.15a, aligning well with the aforementioned *J–V* measurement results. Device-R240 exhibited a significantly enhanced photo-response within the spectral range of 550 to 1000 nm, resulting in the highest integral J_{SC}, which could be attributed to the improvement of the absorber layers. In general, the fabrication procedures for all functional layers was consistent across devices, with the exception of specific parameters used in the selenization process for Sb_2Se_3 layers in each device. Moreover, a stronger spectral response represents enhanced carrier collection and separation capability, thereby indicating better device performance owing to superior absorber quality characterized by compactness and large crystal grains. Additionally, the bandgap of the Sb_2Se_3 absorber layers can be estimated by fitting the regions corresponding to the band edges obtained from plotting $(E\times\ln(1-EQE))^2$ versus energy (Figure 3.15b).[28] This analysis reveals a slight reduction of the bandgap which is decreased to 1.26 eV for the optimized absorber layer. Particularly, the enhanced spectral response in wavelengths greater than 900 nm can reasonably be attributed to a narrower bandgap resulting from the improvement in the absorber layer.[28]

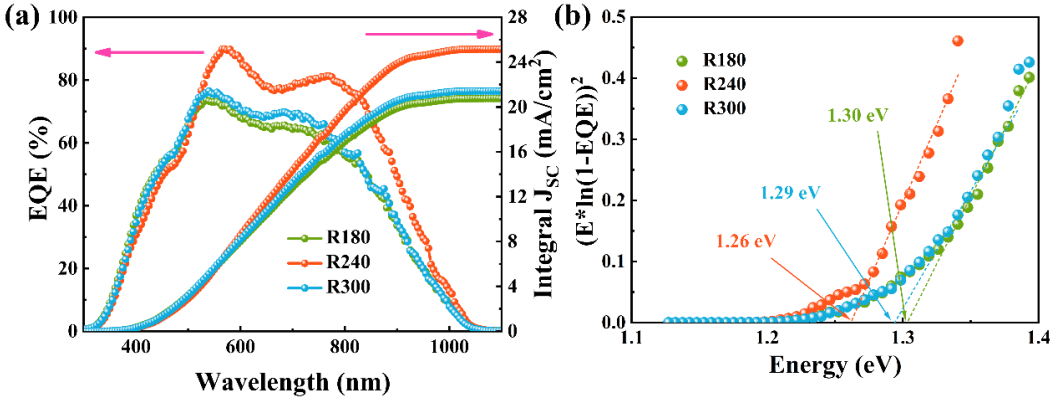

Figure 3.15 *(a) external quantum efficiency (EQE) spectra, (b) bandgap derived from the EQE data.*

The electrical properties of the three devices were characterized by evaluating diode performance parameters based on dark *J–V* results (Figure 3.16a) and the detailed calculation is illustrated as follows, including shunt conductance (*G*), series resistance (*R*), diode ideality factor (*A*), and reverse saturation current density (J_0), which can be illustrated by a general single exponential diode equation (equation (2-4) of chapter II). The *G* values was obtained by the *dJ*/*dV* vs. *V* plot. The *G* values of device-R180, device-R240 and device-R300 were 4.32, 1.61 and 3.34 mS/cm^2, respectively. Next, by calculating the derivation of $r(J)=dV/dJ$ and plotting the *dV*/*dJ* against $(J+J_{SC})^{-1}$, both the value of *R* and *A* can be obtained, through the formula:

$$r(J) \equiv \frac{dV}{dJ} = R + \frac{AkT}{q}\frac{1-G\frac{dV}{dJ}}{(J+J_L-GV)} = R + V_0\frac{1-G\frac{dV}{dJ}}{(J+J_L-GV)} \quad (3\text{-}4)$$

The Y-intercept yielded the *R* values, which were determined to be 6.86, 2.55, 2.91 Ω cm^2 for the R180, R240, and R300 devices, respectively. Meanwhile, the *A* values were estimated to be 1.99, 1.75, and 1.86 for the corresponding three devices by fitting the slope of *AkT*/*q*. Furthermore, the J_0 values were extracted by analyzing the plot of $\ln(J+J_{SC}-GV)$ against *V*–*RJ*, and the calculating formula is presented as follows:

$$ln(J + J_L - GV) = lnJ_0 + \frac{q}{AkT}(V - RJ) = lnJ_0 + \frac{V-RJ}{V_0} \quad (3\text{-}5)$$

The J_0 values were determined to be 2.11×10^{-3}, 5.33×10^{-4}, and 8.96×10^{-4} mA/cm^2 for the corresponding three samples.

The calculated results are summarized in Table 3.2. Noticeable reductions in *G* emerged as a perfect absorber layer was utilized to construct the solar cells for device-R240 (Figure 3.16b). In fact, the *A* and J_0 serve as effective indicators reflecting the recombination extent of defects at both the interface and absorber bulk. Apparently, superior performance is associated with lower values of *A* (1.75) and J_0 (5.33×10^{-4} mA/cm^2) observed in device-R240 (Figure 3.16c, d), indicating enhanced carrier transportation and suppressed carrier recombination. In addition, the device-R240 exhibited a decrease in R (2.55 Ω) compared to the other two devices, demonstrating an improved FF consistent with the *J–V* results. Hence, with an appropriate pre-selenization duration, significant enhancement in the quality of Sb_2Se_3 absorber layer was achieved, resulting in a considerable improvement in J_{SC} and FF, as confirmed by the desirable *A*, small J_0, and reduced *R* value.

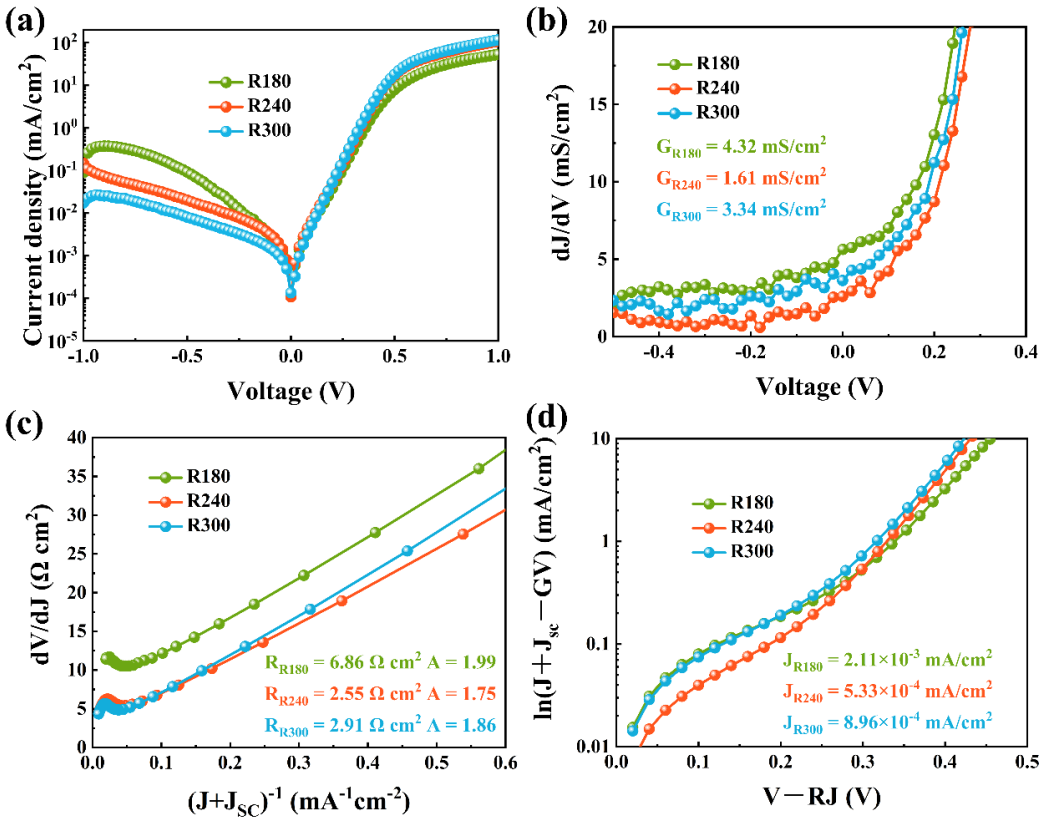

Figure 3.16 *Electrical behavior of the representative R180, R240, and R300 devices. (a) Dark J–V curves, (b) shunt conductance (G), (c) series resistance (R) and ideality factor (A), (d) reverse saturation current density (J_0).*

Table 3.2 *Summary of the diode performance parameters of the three representative devices.*

Devices	G (mS/cm²)	R (Ω cm²)	A	J_0 (mA/cm²)
R180	4.32	6.86	1.99	2.11×10^{-3}
R240	1.61	2.55	1.75	5.33×10^{-4}
R300	3.34	2.91	1.86	8.96×10^{-4}

3.3.3 The band alignment analysis of Sb_2Se_3 device

To gain further insights into the impact of optimizing the properties of the absorber layer on the evolution of band alignment in the heterojunction, we conducted ultra-violet photoelectron spectroscopy (UPS) analysis. Figure 3.17a-c displays information regarding the cutoff edge (E_{cutoff}) and the energy gaps (E_{onset}) obtained by extrapolating the linear region of binding energy.[29] Moreover, He I was employed as the ultraviolet photoelectron energy during UPS measurement. The band level can be calculated based on the equation (2-5), (2-6), and (2-7) as mentioned in chapter II.

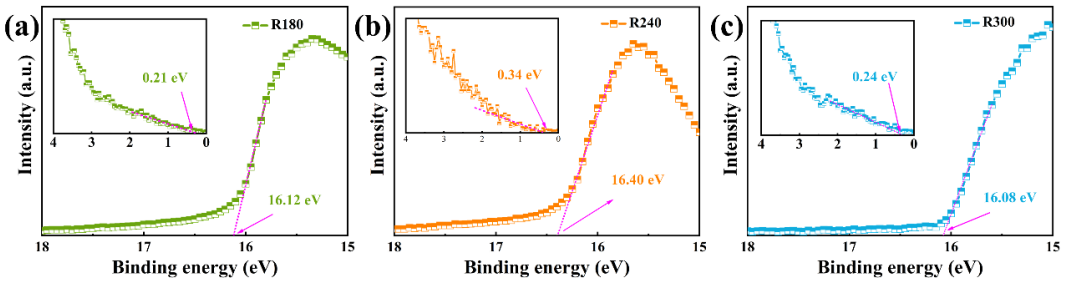

Figure 3.17 *UPS characterizations of the (a) R180 sample, (b) R240 sample, and (c) R300 sample.*

The calculated results of the band level for the three samples are summarized in Table 3.3. The schematic diagram in Figure 3.18 illustrates the calculated valence band

maximum (VBM), conduction band minimum (CBM), and Fermi level (E_F) for the band alignment. Notably, the corresponding information regarding the energy band of CdS buffer layer was obtained from our previous report.[2] As depicted in the schematic diagram, the desirable VBM and CBM offsets for the three samples exhibited a good alignment with the buffer layer, thereby significantly facilitating the transport of photogenerated carriers. It has been reported that a positive value of conduction band offset (CBO) ranging from 0 to 0.4 eV is more advantageous for achieving high-performance semiconductor devices.[20, 30] In terms of the R180, R240, and R300 samples, a distinct "spike-like" band alignment was observed at their heterojunction with CBO values of 0.31, 0.16, and 0.38 eV, respectively, which align well within the appropriate range of 0 to 0.4 eV. Interestingly, in comparison with the R180 and R300 samples, the R240 sample exhibited a more favorable CBO value. Such a notable "spike-like" band alignment effectively impedes defects-assisted recombination carriers at the interface, leading to enhanced charge separation and efficient carrier transportation, which is conducive to improving the overall device performance. Consequently, this greatly reinforces the justification for employing Sb_2Se_3 films fabricated using the RTP technique as the absorber layer in thin-film solar cells. In addition, the R240 sample demonstrates an evident P-type conductive property as its E_F is found to be closer to the VBM, which is attributed to the favorable morphology and crystallization as aforementioned in the SEM and XRD analysis.

Table 3.3 *The energy band levels information for samples R180, R240, and R300.*

Devices	E_{cutoff} (eV)	E_{cutoff} (eV)	Work function (eV)	*VBM* (eV)	*CBM* (eV)	E_g (eV)
R180	16.12	0.21	5.12	5.31	4.01	1.30
R240	16.40	0.34	4.82	5.16	3.90	1.26
R300	16.08	0.24	5.14	5.38	4.09	1.29

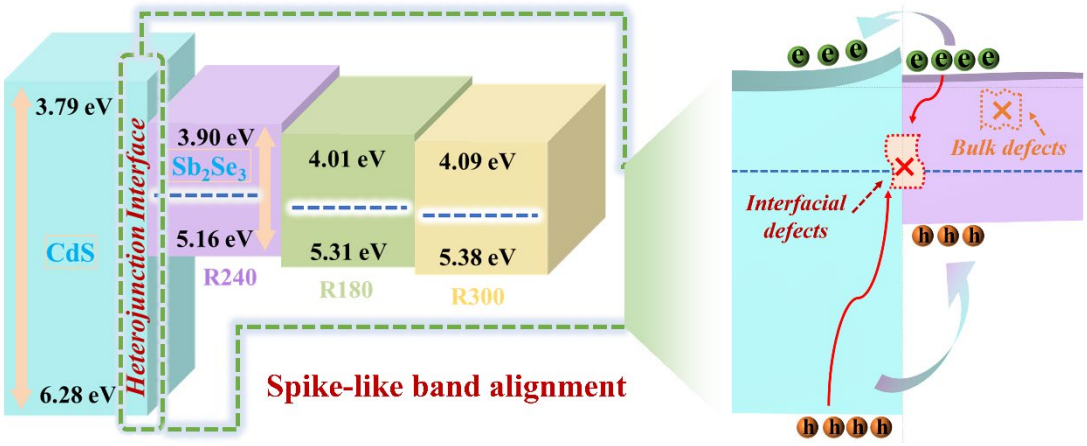

Figure 3.18 *Schematic diagram of the band alignment for the samples R180 (green), R240 (purple), and R300 (yellow).*

3.3.4 Defect property analysis of Sb_2Se_3 device

To better understand the defect states of the corresponding devices (R180, R240, and R300), a space charge-limited current (SCLC) model based on logarithmic dark *J–V* characteristics was applied. Figure 3.19a-c shows the logarithmic *J–V* curves of R180, R240, and R300 respectively. The V_{TFL} value can be determined by the formulation (2-8) mentioned in chapter II.

The estimated V_{TFL} values associated to device-180, device-240, and device-300 were 0.20, 0.16, and 0.19 V, respectively. The obtained N_{trap} of device-R180 and device-R300 exceeded 2.0×10^{14} cm^{-3}, suggesting more defect recombination losses in these two devices. Notably, the N_{trap} value decreased to 1.86×10^{14} cm^{-3} for device-R240, indicating fewer trap states and defect recombination centers in the R240 absorber thin film. It agrees well with its superior thin film quality characterized by larger grains, absence of pin-holes, improved compactness, and favorable orientation.

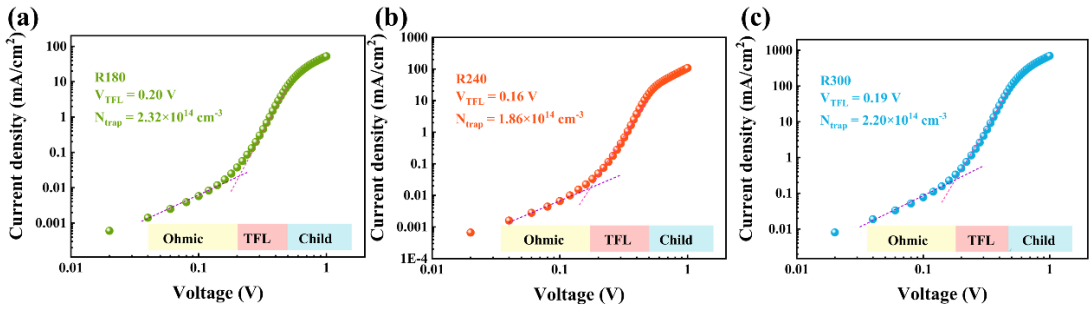

Figure 3.19 *Logarithmic J–V curves of the (a) device-R180, (b) device-R240, and (c) device-R300.*

In general, the presence of defects is a significant challenge that impacts the development of solar cells in their quest for enhanced conversion efficiency. Hence, it is imperative to unveil the origin and characteristics of these detrimental defects. In this regard, we conducted capacitance–voltage (*C–V*) and drive-level capacitance profiling (DLCP), which are recognized as crucial characterization techniques to investigate the behavior associated with recombination due to interface defects. *C–V* characterization predominantly involves the response of free carriers, bulk defects, and interfacial defects. Conversely, DLCP characterization is primarily more sensitive to free carriers and bulk defects, with less susceptibility to interface state conditions.[31] Hence, the interfacial defect density (N_i) can be derived by subtracting the DLCP-calculated defect density (N_{DLCP}) from the defect density (N_{CV}) calculated through *C–V* as the used formulations (2-9), (2-10), and (2-11) in chapter II.[32]

The detailed analysis data are shown in Figure 3.20, and Table 3.4, respectively. The N_{DLCP} values for these three devices were approximately 10^{17} cm^{-3}, while the calculated values for device-R240 decreased to 1.51×10^{17} cm^{-3}, compared to those observed in device-R180 (1.57×10^{17} cm^{-3}) and device-R300 (2.21×10^{17} cm^{-3}). This indicates that the R240 absorber exhibits a decreased bulk defect density attributable to the structural transformation of Sb_2Se_3 thin films, transitioning from fine crystals with poor compactness to large and more uniformly distributed crystals without pinholes. However, the N_{CV} results for these three devices exhibited significantly higher values compared to their corresponding N_{DLCP} results, indicating the presence of severe defects

at the interface. Device-R240 demonstrated a lower interfacial defect density (3.92×10^{16}, relative to 6.60×10^{16} of device-R180 and 7.10×10^{16} cm^{-3} of device-R300), which is advantageous to suppressing the interfacial defect and alleviating the defect-assisted recombination in the device-R240. The observed reduction in defect density, both within the Sb_2Se_3 thin film and at the interface, suggests an enhancement in the overall quality of the bulk Sb_2Se_3 absorber and at its surface, resulting in the mitigation of defects. Additionally, the *C–V* and DLCP data are the function of depletion region width (W_d) which also plays a significant role in the performance of the photovoltaic device. The wider W_d (defined as the X value at zero bias) of device-R240 is beneficial to enhancing light absorption and facilitating the separation and extraction of electron–hole pairs, which could significantly enhance the key performance parameters, particularly the J_{SC} value of the solar cell.

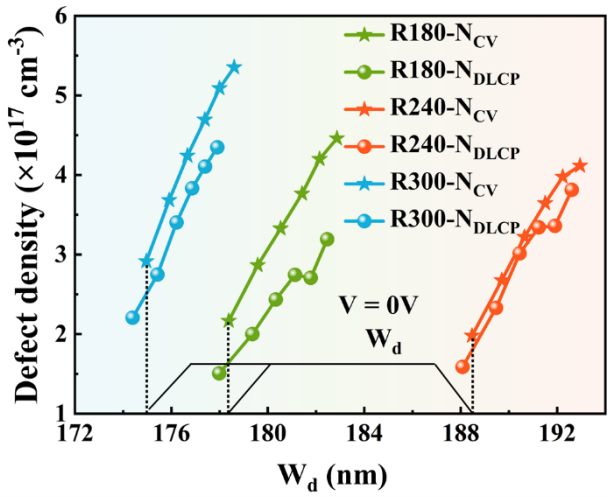

Figure 3.20 *Plots of interfacial defect density versus the depletion region width (W_d) to the heterojunction extrapolated from C−V and DLCP results.*

Table 3.4 *Interfacial defect density of the R180, R240, and R300 devices measured with C–V and DLCP.*

Devices	W_d (nm)	N_{CV} (cm^{-3})	N_{DLCP} (cm^{-3})	N_i (cm^{-3})	V_{bi} (mV)
R180	178	2.17×10^{17}	1.59×10^{17}	6.60×10^{16}	536

R240	188	1.98×10^{17}	1.51×10^{17}	3.92×10^{16}	595
R300	175	2.92×10^{17}	2.21×10^{17}	7.10×10^{16}	558

Further, temperature-dependent V_{OC} (V_{OC}–T) was analyzed to explore the activation energy (E_a) of the recombination–dominated mechanism, as described by the following equation:[31]

$$V_{OC} = \frac{E_a}{q} - \frac{Ak_BT}{q} \times ln\left(\frac{J_0}{J_L}\right) \quad (3\text{-}6)$$

where q is the elementary charge; T is the temperature; k_B is the Boltzmann's constant; J_0 is reverse saturation current, and J_L is the photocurrent. In general, two major recombination mechanisms commonly exist in photovoltaic devices, i.e., space charge region recombination-dominated ($E_a = E_g$) and interface recombination-dominated ($E_a < E_g$).[30] By linearly fitting, the E_a can be estimated by determining the intercept on the Y-axis in Figure 3.21. It is noteworthy that both device-R180 and device-R300 exhibit significantly lower E_a values compared to their respective bandgap values (1.30 and 1.29 eV, as derived from EQE data in Figure 3.15b), as well as device-R240. This observation reinforces the idea that besides conventional Shockley–Read–Hall (SRH) recombination, interface recombination significantly impacts the overall performance of the devices. In contrast, the device-R240 exhibits an enhanced E_a of 1.25 eV, which closely matches its bandgap value of 1.26 eV, effectively reducing unwanted interface recombination. The improvement in E_a deficit is primarily attributed to the utilization of a high-quality Sb_2Se_3 thin film (sample R240) with compact and pinhole-free surface morphology characteristics, resulting in superior adhesion at the Sb_2Se_3/CdS heterojunction interface.

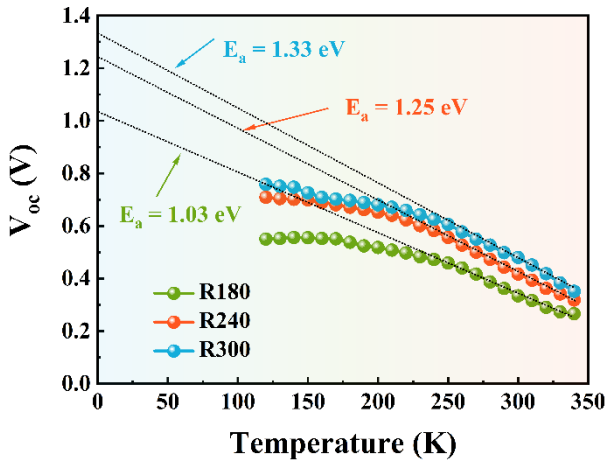

Figure 3.21 *Plots of V_{OC}–T profiles for the three representative devices.*

To gain deeper insights into the electric field information within the space charge region, a comprehensive analysis was performed on the *C–V* data obtained at 50 kHz using the Mott-Schottky model. Considering the device structure employed in this study, which involves a single-sided P–N junction of Sb_2Se_3/CdS heterojunction, the capacitance and the bias voltage applied during the measurements can be summarized with the following equation:[33]

$$\frac{A_d^2}{C^2} = \frac{2(V+V_{bi})}{q\varepsilon_0\varepsilon_S N_A} \tag{3-7}$$

where ε_0 is the vacuum permittivity; ε_S is the relative permittivity of the Sb_2Se_3; A_d is the area of the device; V_{bi} is the built-in voltage, respectively. Figure 3.22 displays the plots of $1/C^2$ against V, where the V_{bi} values could be acquired by fitting the X intercept under the bias voltage. Importantly, the capacitance of the device is dominated by the pseudo-capacitance in the space at this point.[22] From the fitting results, with the adjustment of absorber films via optimized pre-selenization duration, the V_{bi} in the Sb_2Se_3/CdS P–N junction is increased from 536 (device-R180) to 595 mV (device-R240). This demonstrates a significant enhancement of downward band bending which is correlated with a more favorable "spike-like" configuration. As a consequence, photogenerated carriers will be repelled from reaching the interface, effectively limitting Schottky-Read-Hall (SRH) recombination in this space charge region. Meanwhile, due to the passivation of deep-level interfacial defect, a greater downward

band bending is more favorable to decrease the interfacial defect density, echoing the above analysis results of *C–V* and DLCP.

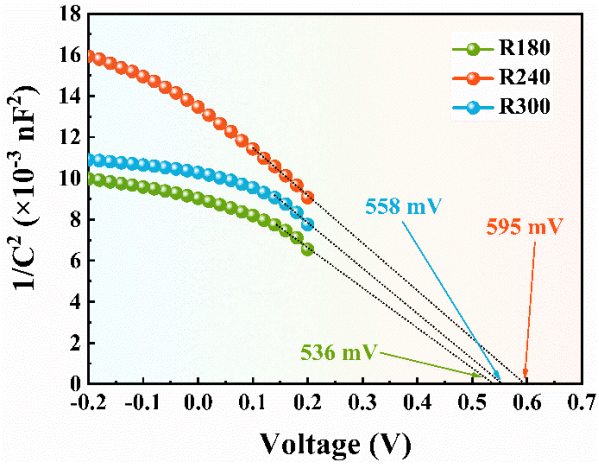

Figure 3.22 *Mott-Schottky plots with a linear fit of the voltage.*

The capacitance-mode deep-level transient spectroscopy (C-DLTS) methodology is widely employed for detecting electrically active defects in solar cells by measuring changes in the charge state of deep defect centers at different temperatures. This technique relies on the detection of signals originating from minority carrier traps by analyzing the transient capacitance of the p-n junction.[34] The C-DLTS was applied to explore the defect dynamics, particularly targeting electrically active defects. As evidenced in the DLTS spectra (Figure 3.23a), all samples exhibit two distinct peaks, indicating the presence of a hole trap (referred to as H1) and an electron trap (referred to as E1). It has been reported that the positive peak and the negative peak correspond to majority carrier traps and the minority carrier traps, respectively.[42] Furthermore, through linear fitting of the signal points surrounding the DLTS peak, detailed DLTS parameters such as defect activation energy (E_a), defect density (N_T), and capture cross section (σ) were extracted from the Arrhenius plot, which is summarized in Figure 3.23b and Table 3.5. By further comparing the defect levels of the devices, it is observed that the H1 defect demonstrates an E_a value closely approximating 300−400 meV (relative to VBM) across all devices. Similarly, the E1 defect displays a comparable

trend, with E_a values ranging from 200−300 meV (relative to CBM), implying that they might derive from the same types of defects.

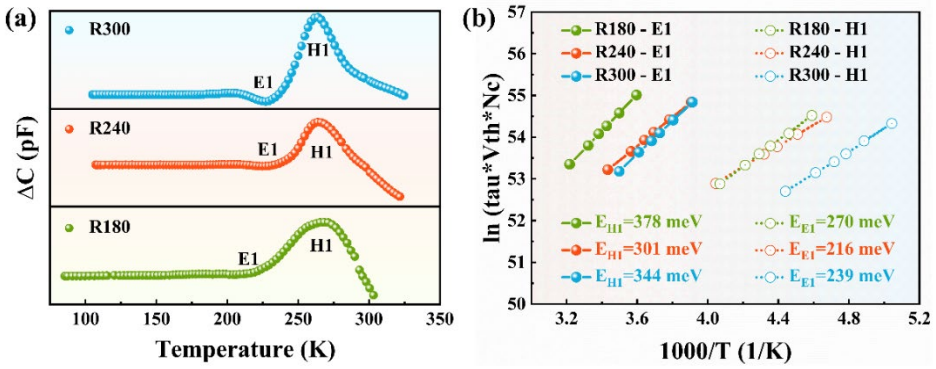

Figure 3.23 *(a) C−DLTS signals. (b) Arrhenius plots derived from C−DLTS signals.*

Table 3.5 *Defect properties of the representative devices measured by C-DLTS.*

Devices	Defect	E_a (eV)	σ (cm^2)	N_T (cm^{-3})	$N_T \times \sigma$ (cm^{-1})
R180	E1	0.271	3.79×10^{-18}	3.52×10^{13}	1.33×10^{-5}
	H1	0.378	9.11×10^{-18}	1.76×10^{14}	1.60×10^{-3}
R240	E1	0.216	2.66×10^{-19}	8.09×10^{12}	2.15×10^{-6}
	H1	0.301	1.27×10^{-18}	1.43×10^{14}	1.82×10^{-4}
R300	E1	0.230	2.03×10^{-18}	9.29×10^{12}	1.89×10^{-5}
	H1	0.344	9.40×10^{-17}	2.70×10^{14}	2.54×10^{-2}

Specifically, the activation energies of the aforementioned defects align well with the theoretical findings derived from the first-principal calculation,[35] the H1 and E1 defects are being attributed to the selenium anti-stites (Se_{Sb}) and selenium vacancy (V_{Se}), respectively. As previously reported, the amphoteric defect known as Se_{Sb}, which exhibits comparable capture cross-sections for both holes and electrons, has been identified as a dominant defect in Sb_2Se_3 solar cells. This defect functions as an efficient trapping center, thereby significantly increasing the probability of carrier recombination.

To further analyze the defect energy levels and density intuitively, a schematic diagram illustrating the energy band structures for these three devices was meticulously crafted and presented in Figure 3.24a-c to evaluate the impact of defect behavior on device performance. Asit is widely known, defect density and capture cross-section are considered a useful indicator to estimate the device quality.[12]

However, it was observed that the defect levels of E1 and H1 in device-R180 and device-R300 were found to be comparatively deeper than those observed in device-R240, accompanied by significantly larger σ and higher N_T. Defects situated at deep levels within the band gap (close to mid-gap) tend to function as more effective carrier recombination centers compared to shallow defects positioned near the band edge, which results in exacerbation of carrier recombination within these defects.[36] The larger σ in the device leads to more severe trap-assisted recombination, thereby increasing the N_T. Conversely, in the device-R240 with a smaller σ, holes are promptly emitted again after being captured by the shallow defect state, resulting in a considerable decrease in N_T. We reasonably attributed this significant improvement in defect dynamics to the enhanced quality of the absorber layer for device R240.

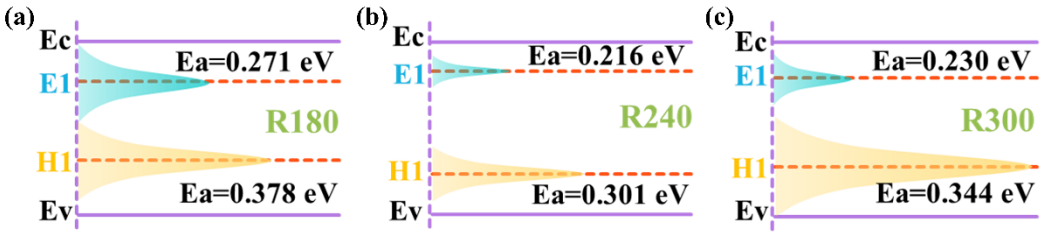

Figure 3.24 *Schematic illustration of the band energy levels and defect energy levels for the R180 sample (a), R240 sample (b), and R300 sample (c), respectively.*

More importantly, the product $N_T \times \sigma$ is considered a pivotal indicator for characterizing the defect dynamic and trap lifetime (τ_{trap}) which is proportional to $(N_T \times \sigma)^{-1}$.[37, 38] The photogenerated holes and electrons are easily prone to be captured by V_{Se} and Se_{Sb} defects if the defect possesses an enlarged σ, leading to substantial losses in carrier lifetime and non-radiative recombination. As shown in Table 3.5, the $N_T \times \sigma$ values for

both E1 and H1 of device-R240 exhibits a significant reduction by one order of magnitude compared to those of device-R180 and device-R300. This finding suggests a prolonged carrier lifetime and efficient inhibition of photogenerated carrier recombination, ascribed to the large crystal size and the removal of pinholes within the absorber layer. Consequently, device-R240 demonstrates a reduced capture cross-section, lower defect density, and longer carrier lifetime. This effectively diminishes its potential as a recombination center, facilitating deep-level defect passivation and inhibiting carrier recombination. As a result, the device's performance is significantly enhanced, particularly in terms of J_{SC}.

To gain a more profound understanding of defect properties, admittance spectroscopy (AS) analysis focusing on the capacitance spectrum for defect characterization was carried out on the Sb_2Se_3 devices. The evaluation of defect density was performed by examining capacitance–frequency–temperature (*C–f–T*) spectra at various temperatures ranging from 330 K to 180 K, with an interval of 10 K for three categories of Sb_2Se_3 devices, as depicted in Figure 3.25a-c.

Angular frequency (ω) at the maximum of the $\omega dC/d\omega$ plot was denoted as the inflection point frequency (ω_0) for the *C–f–T* curve. Herein, only one peak was distinguished from each $\omega dC/d\omega$ plots which can be attributed to one defect level. According to the formular $\omega_0=2\pi f_0$, the Arrhenius plots of $ln\ \omega_0/T^2$ vs. 1000/T were calculated (Figure 3.25d-f). Additionally, the activation energy (E_a) and ω_0 can be concluded in the following equation:[39]

$$\omega_0 = 2\pi v_0 T^2 exp\left(\frac{-E_a}{kT}\right) \tag{3-8}$$

where k is the Boltzmann constant, v_0 is the attempt-to-escape frequency ($s^{-1}\cdot K^{-2}$), ω_0 is the inflection angular frequency of the electronic transition and E_a is the defect activation energy. The slopes of linearly fitting the Arrhenius plots allowed for deducing the defect activation energy E_a.

Furthermore, the distribution of the defect was fitted by Gaussian method using the Kimerling model based on the following equations:[40]

$$E(\omega) = kT\ ln\left(\frac{2\pi v_0 T^2}{\omega}\right) \tag{3-9}$$

$$N_t\big(E(\omega)\big) = -\frac{V_d}{qW}\frac{dC}{d\omega}\frac{\omega}{kT} \tag{3-10}$$

where V_d is the built-in potential of the P–N junction, ω is the angular frequency, and $N_t(E(\omega))$ is the defect density. The defect densities and distribution are plotted in Figure 3.25g-i. As shown in Table 3.6, the E_a values obtained for the device-R180, device-R240, and device-R300 were 435, 377, and 424 meV. The corresponding defect density of the three devices were calculated to be 1.04×10^{17}, 1.25×10^{16}, and 8.13×10^{17} cm^{-3}, respectively.

Combined with the previous first-principles results, there mainly exist two intrinsic defects belonging to the Sb_2Se_3 device, which could be ascribed to selenium vacancy (V_{Se}) defect and antimony antisite (Sb_{Se}) defect.[41] Considering the selenization scenario during the Sb_2Se_3 preparation and the variation of defect energy, it is tentatively speculated that both two types of defects may occur in our Sb_2Se_3 devices. Notably, only one defect level was detected in the corresponding results of admittance spectroscopy. Therefore, we reasonably infer that V_{Se} defect and/or Sb_{Se} defect are likely to be the deterioration defects in our devices. The difference in activation energy (E_a) of the defects among the three devices is likely associated with the fluctuation of energy bands caused by the unique microstructure of the Sb_2Se_3 absorber layer, consequently influencing the band alignment of the heterojunction. Notably, device-R240 with the best-performance absorber layer possesses a lower defect activation energy and reduced integrated defect densities (Table 3.6). Defects with higher activation energy and increased defect density tended to act as more efficient recombination centers, consequently impeding the carrier transport and weakening the complete device performance. Therefore, the significant decrease in both defect activation energy and defect density observed in the device-R240 can be attributed to significant optimization of absorber layer quality, effectively reducing recombination within bulk Sb_2Se_3 and thereby contributing to an overall enhancement in device performance.

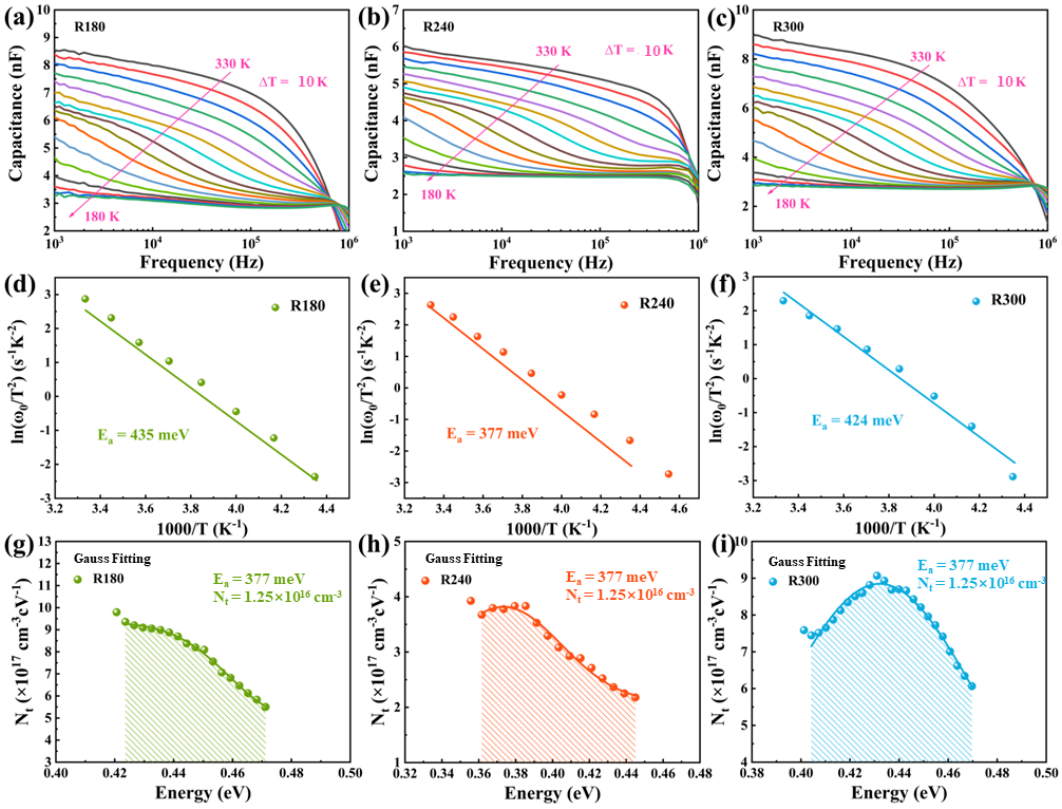

Figure 3.25 *(a–c) Capacitance–frequency–temperature (C–f–T) spectra, (d–f) Arrhenius plots determined from the derivative of the C–f–T data (The lines are the linearly fitting of the Arrhenius plots. The calculated defect activation energies (E_a) for the defect are displayed in the figure), and (g–i) defect densities derived from the C–f–T spectra of device-R180, device-R240, and device-R300, respectively.*

Table 3.6 *Defect parameters of the three representative devices characterized by admittance spectroscopy.*

Devices	E_a (meV)	N_t (cm^{-3})
R180	435	1.04×10^{17}
R240	377	1.25×10^{16}
R300	424	8.13×10^{17}

3.3.5 Photogenerated Carrier Transport Dynamics Analysis

To further monitor the photogenerated carrier transport dynamics, transient absorption spectroscopy (TAS) was carried out on the above three devices. TAS is a technique

used to study the dynamic behavior of materials following photoexcitation. It captures the transient changes between the excited state and the ground state of the molecules or materials and to understand their electronic and structural dynamic on ultrafast timescales.[42] From the 2D TAS mapping illustrated in Figure 3.26a-c, a distinct photoinduced absorption (PIA) peak at approximately 720 nm was observed for all the devices, which could be ascribed to the capture of photogenerated carriers (minority carriers for Sb_2Se_3 thin film is electron). Subsequently, the TAS signal was fitted using a bi-exponential model, and the comprehensive fitting parameters, involving a short (τ_1) and long (τ_2) decay lifetime, are summarized in Figure 3.27 and Table 3.7 It should be noted that the τ_1 and τ_2 are attributed to interface/surface recombination and bulk recombination, respectively. Remarkably, the decay lifetimes (both τ_1 and τ_2) of all three devices exhibited a significant increase due to enhancement in the absorber layer quality, particularly the long decay lifetime (τ_2, from 1093 to 7549 ps).

The kinetic curves presented in Figure 3.26 were normalized and fitted using a typical biexponential decay kinetic model based on the TAS mapping, as follows:[43]

$$y = A_1 e^{\left(-\frac{x}{\tau_1}\right)} + A_2 e^{\left(-\frac{x}{\tau_2}\right)} \quad (3\text{-}10)$$

The value of average lifetime (τ) was estimated from the fitting parameters (A_1, A_2, τ_1, and τ_2) based on the following equation:

$$\tau = \frac{\left(A_1\tau_1^2 + A_2\tau_2^2\right)}{A_1\tau_1 + A_2\tau_2} \quad (3\text{-}11)$$

where τ_1 and τ_2 represent the short decay lifetime and the long decay lifetime, respectively. A_1, and A_2 are their corresponding weighted coefficients.

A far superior average lifetime of the sample (R240) with the best microstructure is found to be 7477 ps, which is comparable to the impressive lifetimes observed in high-efficiency Sb_2Se_3 thin-film solar cells.[1, 5, 28, 44] These findings demonstrate that the carrier extraction and/or transport efficiency were improved, leading to a significant mitigation of current leakage. Consequently, the dominant bulk recombination process was greatly alleviated, aligning closely with the findings from the SEM analysis as mentioned above. The observed sharp increase in the long decay lifetime can be

attributed to the efficient passivation of Se_{Sb} defects and the reduction of capture cross-section occurring in the bulk of Sb_2Se_3 absorber film, which echoes well DLTS results. Eventually, the prolonged delay lifetime of the photogenerated carrier could potentially contribute to the J_{SC} enhancement in the Sb_2Se_3 device.

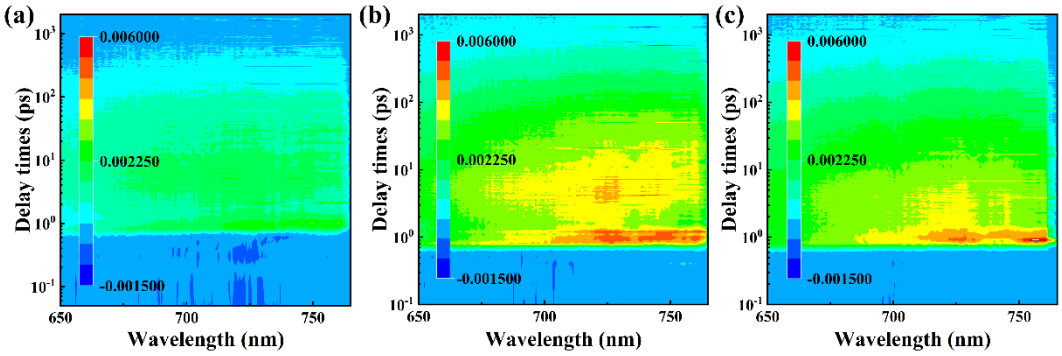

Figure 3.26 *TAS spectra for the R180 sample (a), R240 sample (b), and R300 sample (c), respectively.*

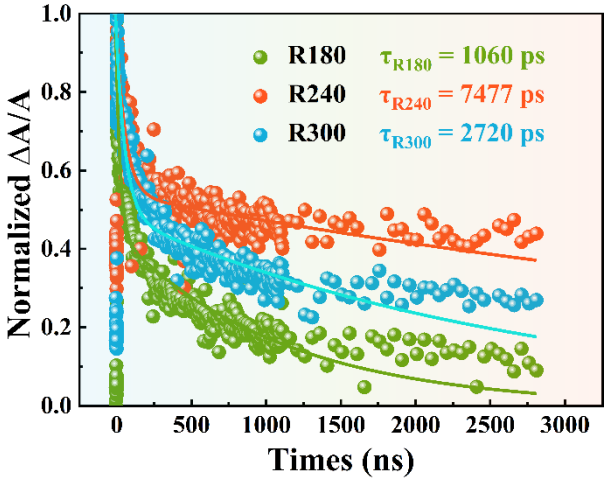

Figure 3.27 *Transient kinetic traces of the decay of the PIA peak at 720 nm for the R180 sample, R240 sample, and R300 sample, respectively.*

Table 3.7 *Fitted parameters for kinetic curves.*

Devices	A_1	τ_1 **(ps)**	A_2	τ_2 **(ps)**	T **(ps)**
R180	0.56	1093	0.44	28	1060
R240	0.54	7549	0.46	60	7477
R300	0.51	2780	0.49	62	2720

3.4 Conclusions

In summary, we have demonstrated the successful fabrication of a high-quality Sb_2Se_3 thin film by controlling the nucleation crystal process based on the RTP pre-selenization technique. Through a systematic investigation of crystal microstructure and orientation, an improved quality of Sb_2Se_3 absorber film was obtained with favorable orientation, smoother morphology, excellent crystallinity, and reduced voids/pin-holes on the surface and in the bulk Sb_2Se_3. It has been illustrated that these characteristics not only facilitate the extraction, collection, and transport of photogenerated carriers but also enhance the conductivity while prolonging the lifetime of minority carriers. Additionally, they contribute to reducing the intrinsic defects in Sb_2Se_3 and promote the quality of heterojunction with enhanced adhesion and more desirable "spike-like" band alignment. Thus, effective reduction of carrier recombination is achieved in both the bulk Sb_2Se_3 and at the heterojunction interface, leading to a reduced defect density and an overall improvement in device performance. The champion device delivered a high efficiency of 9.03% with a superior J_{SC} of 28.97 mA/cm^2. This study offers a comprehensive insight into the influence of crystal growth on the defect properties and optoelectrical performance in photovoltaic devices.

3.5 References

[1] Zhao, Y. Q., Wang, S. Y., Li, C., Che, B., Chen, X. L., Chen, H. Y., Tang, R. F., Wang, X. M., Chen, G. L., Wang, T., Gong, J. B., Chen, T., Xiao, X. D., Li, J. M., Regulating deposition kinetics via a novel additive-assisted chemical bath deposition technology enables fabrication of 10.57%-efficiency Sb_2Se_3 solar cells. *Energy Environ. Sci.* 2022, 15, 5118-5128.

[2] Luo, Y. D., Chen, G. J., Chen, S., Ahmad, N., Muhammad, A., Zheng, Z. H., Su, Z. H., Cathelinaud, M., Ma, H. L., Chen, Z. G., Fan, P., Zhang, X. H., Xing, L. G., Carrier transport enhancement mechanism in highly efficient antimony selenide thin-film solar cell. *Adv. Funct. Mater.* 2023, 33(14), 2213941.

[3] Liang, G. X., Chen, M. D., Ishaq, M., Li, X. R., Tang, R., Zheng, Z. H., Su, Z. H., Fan, P., Zhang, X. H., Chen, S., Crystal growth promotion and defects healing enable minimum open-circuit voltage deficit in antimony selenide solar cells. *Adv. Sci.* 2022, 9(9), 2105142.

[4] Li, K. H., Chen, C., Lu, S. C., Wang, C., Wang, S. Y., Lu, Y., Tang, J., Orientation engineering in low-dimensional crystal-structural materials via seed screening. *Adv. Mater.* 2019, 31(44), 1903914.
[5] Wen, X. X., Chen, C., Lu, S. C., Li, K. H., Kondrotas, R., Zhao, Y., Chen, W. H., Gao, L., Wang, C., Zhang, J., Niu, G. D., Tang, J., Vapor transport deposition of antimony selenide thin film solar cells with 7.6% efficiency. *Nat. Commun.* 2018, 9(2179), 2179.
[6] Li, Z. Q., Liang, X. Y., Li, G., Liu, H. X., Zhang, H. Y., Guo, J. X., Chen, J. W., Shen, K., San, X. Y., Yu, W., Schropp, R. E. I., Mai, Y. H., 9.2%-efficient core-shell structured antimony selenide nanorod array solar cells. *Nat. Commun.* 2019, 10, 125.
[7] Tang, R., Zheng, Z. H., Su, Z. H., Li, X.-J., Wei, Y.-D., Zhang, X. H., Fu, Y. Q., Luo, J., Fan, P., Liang, G. X., Highly efficient and stable planar heterojunction solar cell based on sputtered and post-selenized Sb_2Se_3 thin film. *Nano Energy* 2019, 64(103929), 103929.
[8] Wen, X. X., Lu, Z. H., Yang, X. K., Chen, C., Washington, M. A., Wang, G. C., Tang, J., Zhao, Q., Toh, M. L., Vertically aligned one-dimensional crystal-structured Sb_2Se_3 for high-efficiency flexible solar cells via regulating selenization kinetics. *ACS Appl Mater Interfaces* 2023, 15(18), 22251-22262.
[9] Yuan, C. C., Zhang, L. J., Liu, W. F., Zhu, C. F., Rapid thermal process to fabricate Sb_2Se_3 thin film for solar cell application. *Sol. Energy* 2016, 137, 256-260.
[10] Liu, X. S., Chen, J., Luo, M., Leng, M. Y., Xia, Z., Zhou, Y., Qin, S. K., Xue, D. J., Lv, L., Huang, H., Niu, D. M., Tang, J., Thermal evaporation and characterization of Sb_2Se_3 thin film for substrate Sb_2Se_3/CdS solar cells. *ACS Appl Mater Interfaces* 2014, 6(13), 10687-10695.
[11] Liu, D., Tang, R. F., Ma, Y. Y., Jiang, C. H., Lian, W. T., Li, G., Han, W. H., Zhu, C. F., Chen, T., Direct hydrothermal deposition of antimony triselenide films for efficient planar heterojunction solar cells. *ACS Appl. Mater. Interfaces* 2021, 13(16), 18856-18864.
[12] Duan, Z. T., Liang, X. Y., Feng, Y., Ma, H. Y., Liang, B. L., Wang, Y., Luo, S. P., Wang, S. F., Schropp, R. E. I., Mai, Y. H., Li, Z. Q., Sb_2Se_3 thin-film solar cells exceeding 10% power conversion efficiency enabled by injection vapor deposition technology. *Adv. Mater.* 2022, 34(30), 2202969.
[13] Pan, X. Y., Pan, Y. L., Shen, L. Y., Wang, L. J., Wang, R., Weng, G. E., Jiang, J. C., Hu, X. B., Chen, S. Q., Yang, P. X., Chu, J. H., Tao, J. H., All-Vacuum-Processed $Sb_2(S,Se)_3$ Thin Film Photovoltaic Devices via Controllable Tuning Seed Orientation. *Adv. Funct. Mater.* 2023, 33, 2214511.
[14] Koo, J., Jeon, S., Oh, M., Cho, H.-i., Son, C., Kim, W. K., Optimization of Se layer thickness in Mo/CuGa/In/Se precursor for the formation of $Cu(InGa)Se_2$ by rapid thermal annealing. *Thin Solid Films* 2013, 535, 148-153.
[15] Liu, X. S., Liu, Y. J., Zhang, S. Q., Sun, X. M., Zhuang, Y. G., Liu, J. L., Wang, G., Cheng, K., Du, Z. L., Regulating deposition pressures during rapid thermal evaporation processes to enable efficient Sb_2Se_3 solar cells. *Small Methods* 2023, 8(1), 2300728.
[16] Vinayakumar, V., Hernández, C. R. O., Shaji, S., Avellaneda, D. A., Martinez, J. A. A., Krishnan, B., Effects of rapid thermal processing on chemically deposited antimony sulfide thin films. *Materials Science in Semiconductor Processing-Mater. Sci. Semicond. Process.* 2018, 80, 9-17.
[17] Zhao, Y. H., Gao, Q. Q., Yuan, S. J., Chang, Q. Q., Liang, T., Su, Z. H., Ma, H. L., Chen, S., Liang, G. X., Fan, P., Zhang, X. H., Wu, S. X., Defects passivation and crystal growth promotion by solution-processed K doping strategy toward 16.02% efficiency $Cu(In,Ga)(S,Se)_2$ solar cells. *Chem. Eng. J.* 2022, 436, 135008.
[18] Yu, Z. X., Li, C. H., Chen, S., Zheng, Z. H., Fan, P., Li, Y. F., Tan, M. L., Yan, C., Zhang, X. H., Su, Z. H., Liang, G. X., Unveiling the Selenization Reaction Mechanisms in Ambient Air-Processed Highly Efficient Kesterite Solar Cells. *Adv. Energy Mater.* 2023, 13(19), 2300521.

[19] Gong, Y. C., Zhu, Q., Li, B. Y., Wang, S. S., Duan, B., Lou, L. C., Xiang, C. X., Jedlicka, E., Giridharagopal, R., Zhou, Y. G., Dai, Q., Yan, W. B., Chen, S. Y., Meng, Q. B., Xin, H., Elemental de-mixing-induced epitaxial kesterite/CdS interface enabling 13%-efficiency kesterite solar cells. *Nat. Energy* 2022, 7(10), 966-977.

[20] Hu, Y., Huang, L., Che, B., Wang, H. L., Liu, A. X., Zhu, C. F., Tang, R. F., Chen, T., Molecular induced patching process improving film quality for high-efficiency Cd-free antimony selenosulfide solar cells. *Adv. Funct. Mater.* 2024, 2314974.

[21] Deng, H., Cheng, Y. S., Chen, Z. K., Lin, X., Wu, J. H., Zheng, Q., Zhang, C. X., Cheng, S. Y., Flexible Substrate-Structured Sb_2S_3 Solar Cells with Back Interface Selenization. *Advanced Function Materterials* 2023, 33(12), 2212627.

[22] Luo, Y. D., Tang, R., Chen, S., Hu, J. G., Liu, Y. K., Li, Y. F., Liu, X. S., Zheng, Z. H., Su, Z. H., Ma, X. F., Fan, P., Zhang, X. H., Ma, H. L., Chen, Z. G., Liang, G. X., An effective combination reaction involved with sputtered and selenized Sb precursors for efficient Sb_2Se_3 thin film solar cells. *Chem. Eng. J.* 2020, 393, 124599.

[23] Spalatu, N., Krautmann, R., Katerski, A., Karber, E., Josepson, R., Hiie, J., Acik, I. O., Krunks, M., Screening and optimization of processing temperature for Sb_2Se_3 thin film growth protocol: Interrelation between grain structure, interface intermixing and solar cell performance. *Sol. Energy Mater. Sol. Cells* 2021, 225, 111045.

[24] Wen, X. X., Lu, Z. H., Li, B. X., Wang, G.-C., Washington, M. A., Zhao, Q., Lu, T.-M., Free-standing [001]-oriented one-dimensional crystal-structured antimony selenide films for self-powered flexible near-infrared photodetectors. *Chem. Eng. J.* 2023, 462, 142026.

[25] Wang, W. H., Cao, Z. X., Wu, L., Chen, G. L., Ao, J. P., Luo, J. S., Zhang, Y., Interface etching leads to the inversion of the conduction band offset between the CdS/Sb_2Se_3 heterojunction and high-efficient Sb_2Se_3 solar cells. *ACS Appl. Energy Mater.* 2022, 5(2), 2531-2541.

[26] Chen, G. J., Luo, Y. D., Abbas, M., Ishaq, M., Zheng, Z. H., Chen, S., Su, Z. H., Zhang, X. H., Fan, P., Liang, G. X., Suppressing buried interface nonradiative recombination losses toward high-efficiency antimony triselenide solar cells. *Adv. Mater.* 2023, 36(5), 2308522.

[27] Liang, G. X., Luo, Y. D., Chen, S., Tang, R., Zheng, Z. H., Li, X. J., Liu, X. S., Liu, Y. K., Li, Y. F., Chen, X. Y., Su, Z. H., Zhang, X. H., Ma, H. L., Fan, P., Sputtered and selenized Sb_2Se_3 thin-film solar cells with open-circuit voltage exceeding 500 mV. *Nano Energy* 2020, 73, 104806.

[28] Tang, R., Chen, S., Zheng, Z. H., Su, Z. H., Luo, J. T., Fan, P., Zhang, X. H., Tang, J., Liang, G. X., Heterojunction annealing enabling record open-circuit voltage in antimony triselenide solar cells. *Adv. Mater.* 2022, 34(14), 2109078.

[29] Zhou, R., Li, X. Z., Wan, L., Niu, H. H., Wang, H., Yang, X., Wang, X. Z., Hou, J., Xu, J. Z., Xu, B. M., Bulk heterojunction antimony selenosulfide thin-film solar cells with efficient charge extraction and suppressed recombination. *Adv. Funct. Mater.* 2023, 34(6), 2308021.

[30] Luo, P., Imran, T., Ren, D. L., Zhao, J., Wu, K. W., Zeng, Y. J., Su, Z. H., Fan, P., Zhang, X. H., Liang, G. X., Chen, S., Electron transport layer engineering induced carrier dynamics optimization for efficient Cd-free Sb_2Se_3 thin-film solar cells. *Small* 2023, 20(4), 2306516.

[31] Liang, G. X., Li, C. H., Zhao, J., Fu, Y., Yu, Z. X., Zheng, Z. H., Su, Z. H., Fan, P., Zhang, X. H., Luo, J. T., Ding, L. M., Chen, S., Self-powered broadband kesterite photodetector with ultrahigh specific detectivity for weak light applications. *SusMat* 2023, 3(5), 557-728.

[32] Lin, J. H., Chen, G. J., Ahmad, N., Muhammad, I., Chen, S., Su, Z. H., Fan, P., Zhang, X. H., Zhang, Y., Liang, G. X., Back contact interfacial modification mechanism in highly-efficient antimony selenide

thin-film solar cells. *J. Energy Chem.* 2023, 80, 256-264.

[33] Hu, Y. J., Chen, Z. X., Xiang, Y., Cheng, C. H., Liu, W. F., Zhan, W. S., Enhanced efficiency of the Sb_2Se_3 thin-film solar cell by the anode passivation using an organic small molecular of TCTA. *J. Semicond.* 2023, 44(8).

[34] Guo, H. F., Huang, S., Zhu, H. C., Zhang, T. Y., Geng, K. J., Jiang, S., Gu, D., Su, J., Lu, X. L., Zhang, H., Zhang, S., Qiu, J. H., Yuan, N. Y., Ding, J. N., Enhancement in the efficiency of Sb_2Se_3 solar cells by triple function of lithium hydroxide modified at the back contact interface. *Adv Sci* 2023, 10(31), 2304246.

[35] Chen, C., Tang, J., Open-circuit voltage loss of antimony chalcogenide solar cells: status, origin, and possible solutions. *ACS Energy Lett.* 2020, 5(7), 2294-2304.

[36] Gu, Y. H., Liang, W. H., Che, Y. X., Cai, Z. Y., Xiao, P., Yang, J. J., Zang, R. X., Wang, H., Wu, X. J., Chen, T., Solvent annealing enabling reconstruction of cadmium sulfide film for improved heterojunction quality and photovoltaic performance of antimony selenosulfide solar cells. *Adv. Funct. Mater.* 2023, 2311577.

[37] Liu, C., Wu, S. H., Gao, Y. Y., Feng, Y., Wang, X. L., Xie, Y. F., Zheng, J. Z., Zhu, H. B., Li, Z. Q., Schropp, R. E. I., Shen, K., Mai, Y. H., Band gap and defect engineering for high-performance cadmium-free $Sb_2(S,Se)_3$ solar cells and modules. *Adv. Funct. Mater.* 2022, 32(49), 2209601.

[38] Wang, S. Y., Zhao, Y. Q., Che, B., Li, C., Chen, X. L., Tang, R. F., Gong, J. B., Wang, X. M., Chen, G. L., Chen, T., Li, J. M., Xiao, X. D., A novel multi-sulfur source collaborative chemical bath deposition technology enables 8%-efficiency Sb_2S_3 planar solar cells. *Adv. Mater.* 2022, 34(41), 2206242.

[39] Chen, S., Luo, P., Ren, D. L., Duan, C. Y., Ma, X. F., Su, Z. H., Zheng, Z. H., Fan, P., Liang, G. X., Tang, R., An effective engineering with simultaneous carrier density enhancement and interface optimization enables efficient Sb_2Se_3 solar cells. *Applied Surface Science* 2023, 619(156783), 156783.

[40] Luo, Y. D., Chen, M. D., Tang, R., Azam, M., Chen, S., Zheng, Z. H., Su, Z. H., Fan, P., Ma, H. L., Liang, G. X., Zhang, X. H., Energy band alignment for Cd-free antimony triselenide substrate structured solar cells by Co-sputtering ZnSnO buffer layer. *Sol. Energy Mater. Sol. Cells* 2022, 240, 111721.

[41] Chen, M. D., Ishaq, M., Ren, D. L., Ma, H. L., Su, Z. H., Fan, P., Le Coq, D., Zhang, X. H., Liang, G. X., Chen, S., Interface optimization and defects suppression via NaF introduction enable efficient flexible Sb_2Se_3 thin-film solar cells. *J. Energy Chem.* 2024, 90, 165-175.

[42] Zhang, J., Zhu, B., Zhang, L., Yu, J., Femtosecond transient absorption spectroscopy investigation into the electron transfer mechanism in photocatalysis. *Chem. Commun.* 2023, 59(6), 688-699.

[43] Huang, L., Yang, J. J., Xia, Y. J., Xiao, P., Cai, H. L., Liu, A. X., Wang, Y., Liu, X. S., Tang, R. F., Zhu, C. F., Chen, T., $InCl_3$-modified SnO_2 as an electron transporting layer for Cd-free antimony selenide solar cells. *J. Mater. Chem. A* 2023, 11(32), 16963-16972.

[44] Cai, H. L., Cao, R., Gao, J. X., Qian, C., Che, B., Tang, R. F., Zhu, C. F., Chen, T., Interfacial engineering towards enhanced photovoltaic performance of Sb_2Se_3 solar cell. *Adv. Funct. Mater.* 2022, 32(46), 2208243.

Chapter IV: Cd-free Sb_2Se_3 thin-film solar cells with co-sputtered ZnSnO buffer layer

4.1 Introduction

Nair et al. were among the first ones to employ Sb_2Se_3 as a photoactive absorber layer and obtained a comparatively lower power conversion efficiency (PCE) of 0.66%.[1] Since then, this new type of photovoltaics has been substantially studied and significant improvements have been achieved in the last few years. The highest efficiencies of Sb_2Se_3-based PV devices are reported to be 10.12% and 10.57% with the substrate-structured Glass/Mo/$MoSe_2$/Sb_2Se_3/CdS/ZnO/AZO[2] and superstrated structured Glass/FTO/CdS/Sb_2Se_3/spiro-OMeTAD/Au,[3] respectively. To date, chemical bath-deposited CdS thin film is commonly employed as electron transport layer (ETL) in Sb_2Se_3 solar cells, which is an issue due to the toxicity of Cd.[4] In addition, the relative narrow band gap (2.4 eV) of CdS thin film instigated optical loss in the short wavelength response range.[5] Therefore, it is crucial to substitute a larger band gap and green ETL for CdS for further development of Sb_2Se_3-based photovoltaic. Extensive investigation has been carried out to explore alternative wide band gap ETLs, such as Zn (O,S),[6] SnO_2,[7] ZnO,[8] $Zn_{1-x}Sn_xO$ (ZTO)[9] and Zn-doped TiO_2.[10, 11]

Among these buffer layers, ZTO has been studied for high-efficiency CIGS.[9, 12] and CZTS [13] solar cells. However, research on the ZTO buffer layer for Sb_2Se_3 solar cells has been rarely reported. A commonly employed technique for ZTO film deposition is the atomic layer deposition (ALD),[13, 14] which is unavoidably associated with the drawbacks of slow deposition rate and expensive precursors for the perspective of mass production at the industrial level. Magnetron sputtering is considered to be an efficient technique owing to its lower deposition temperature, excellent compactness of film, high deposition rate, and avoidance of liquid-based waste. In this chapter, we developed ZnSnO layers via the magnetron co-sputtering method to substitute the hazardous CdS film for ZTO/Sb_2Se_3-based devices. The effect of Zn/Sn in ZTO film on solar cells (substrate structured Glass/Mo/Sb_2Se_3/ZTO/ITO/Ag) performance and the corresponding charge transfer mechanism were studied systematically.

4.2 Preparation and characterization of Sb_2Se_3/ZTO heterojunction

4.2.1 Sb_2Se_3 thin film preparation

Mo-coated glass was employed as the substrate for the device fabrication. Before deposition, the substrates with the size of 2×2 cm were successively cleaned using sonication in deionized water and ethanol each for 10 min with the assistance of an ultrasonic cleaning machine, finally rinsed with deionized water and dried with N_2 stream. Just after the cleaning process, the magnetron sputtering technique was employed for the fabrication of Sb metallic precursor thin film with a highly pure and dense sputtering target. Figure 4.1a gives the schematic illustration of the preparation process. Before performing the sputtering procedure, the chamber pressure was evacuated to a residual pressure below 7.0×10^{-4} Pa. To ensure the deposition of high-compact thin film, the optimized pressure, and sputtering power were 0.5 Pa and 35 W, and the argon gas flow rate was kept at 42.5 sccm during the deposition. Unless otherwise specified, no intentional heating was applied to the samples during this deposition process. The sputtering time was set to be 40 min to obtain an Sb metallic precursor thin film with a thickness of 600 nm.

Subsequently, the Sb metallic precursor thin film was subjected to a selenization process to grow a high-crystallinity Sb_2Se_3 thin film. As can be seen in Figure 4.1b, two ceramic boats each containing 0.1 g Se powder (>99.99%) and the as-sputtered Sb samples were put into the furnace together. The pressure was set at 5×10^4 Pa during the selenization, operating with a mechanical pump. The selenization process temperature and time were set at 410 ˚C and 15 min, respectively. After finishing the procedure of selenization, the samples were naturally cooled down to room temperature and then taken out from the furnace.

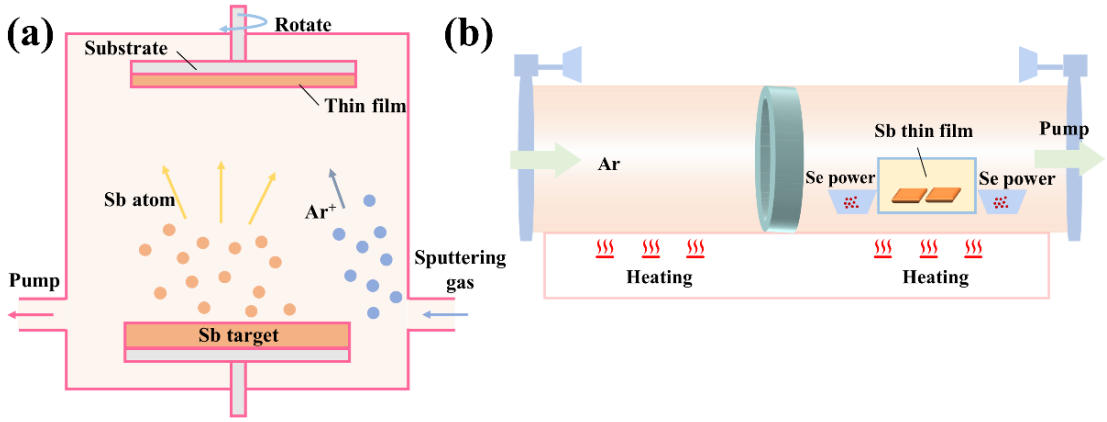

Figure 4.1 *Schematic illustration of the fabrication process of Sb_2Se_3 absorber layer. (a) Sb precursor thin film deposited by RF magnetron sputtering, (b) Sb_2Se_3 thin film obtained by post-selenization heat treatment.*

4.2.2 ZTO thin film preparation

For the deposition of $Zn_{1-x}Sn_xO$ ETL, ZnO and SnO_2 target materials were employed in the RF magnetron co-sputtering process The deposition process can be seen from Figure 4.2. Additionally, ZnO and SnO_2 films were also fabricated onto the glass substrates for comparison. The co-sputtering process begins running with the working pressure of 1 Pa. Furthermore, only high-purity argon gas was flowed (at 30 sccm) into the vacuum chamber as a sputtering gas for the co-sputtering. The sample holder was rotated at the speed of 30 rpm to obtain uniform thin film thickness. The ZTO film composition was controlled by varying the RF powers of ZnO and SnO_2 targets during co-sputtering. Table 4.1 shows the different power ratios of ZnO and SnO_2 targets resulting in various ratios of Sn/(Sn+Zn), denoted as ZTO1, ZTO2, ZTO3, and ZTO4.

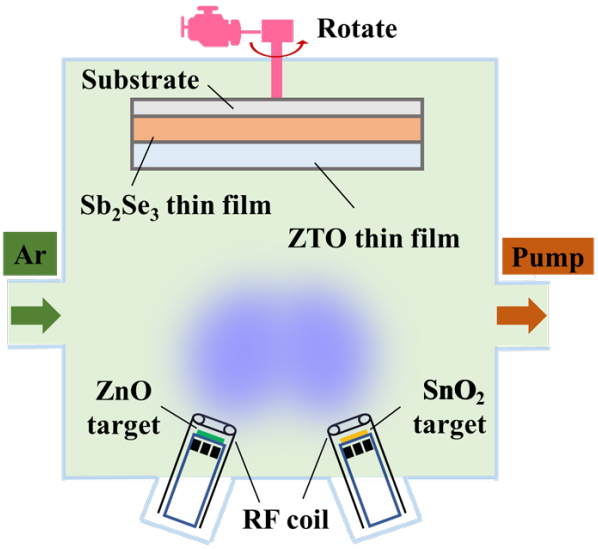

Figure 4.2 *Schematic illustration of the fabrication process of ZTO buffer layer deposited via RF magnetron co-sputtering method.*

Table 4.1 *Co-sputtering parameters and optical band gap of ZTO films.*

Sample	Sn/(Zn+Sn)	E_g (eV)	Power ratio ZnO:SnO_2	Thickness (nm)
ZnO	0	3.21	–	102.4
ZTO 1	0.29	3.17	8 : 2	45.8
ZTO 2	0.38	3.64	6 : 4	44.3
ZTO 3	0.43	3.75	1 : 1	20.3
ZTO 4	0.56	3.42	4 : 6	53.5
SnO_2	1	3.25	–	91.2

4.2.3 Optical band gaps and elemental chemical states analysis of ZTO thin film

$Zn_{1-x}Sn_xO$ thin films were deposited on glass substrates (Soda-Lime Glass, SLG), The evaluation of Sn/(Zn+Sn) and optical properties were characterized. Figure 4.3a shows the transmittance measurements of $Zn_{1-x}Sn_xO$ films and the ratio of Sn/(Zn+Sn) estimated from energy dispersive spectroscopy (EDS) is given in Table 4.1. A lower cut-off edge at wavelength 450 nm was observed from the transmission spectra of

corresponding samples. The optical band gap (E_g) can be acquired using the given relations:

$$\alpha = d^{-1} ln(T^{-1}) \tag{4-1}$$

$$\alpha hv = A\left(hv - E_g\right)^n \tag{4-2}$$

where d is the thickness, and α is the absorption coefficient; T is the transmittance from the measurement. The second relation gives the Tauc plot, in which n is an index related to the nature of the film surface, whether it is crystalline or not.[15] Herein, we use n = 0.5 for calculation. Figure 4.3b shows the Tauc plots of the ZTO films together with ZnO and SnO_2 films and the band gap is obtained by extrapolating the linear portion of the plot to its abscissa-intercept. The band gap of ZTO can be tuned by different chemical compositions through varying sputtering powers of the ZnO target and SnO_2 target, as detailed in Table 4.1. The Figure 4.3c indicates the variation in the band gap as a function of the relative ratio of Sn/(Zn+Sn). Once enhancing the Sn ratio in ZTO films, the band gap values were firstly slightly decreased from 3.21 to 3.17 eV for pure ZnO and $Zn_{0.71}Sn_{0.29}O$, respectively, then greatly increased to 3.75 eV for $Zn_{0.57}Sn_{0.43}O$ and finally decreased to 3.25 eV for pure SnO_2. The corresponding band gap value was slightly higher, but the variation trend as a function of the Sn/(Zn+Sn) ratio was in good agreement with the previous reports.[16] Thus, it is believed that the optimized Sn concentration could lead to achieving an appropriate band alignment for ZTO/Sb_2Se_3 heterojunction.

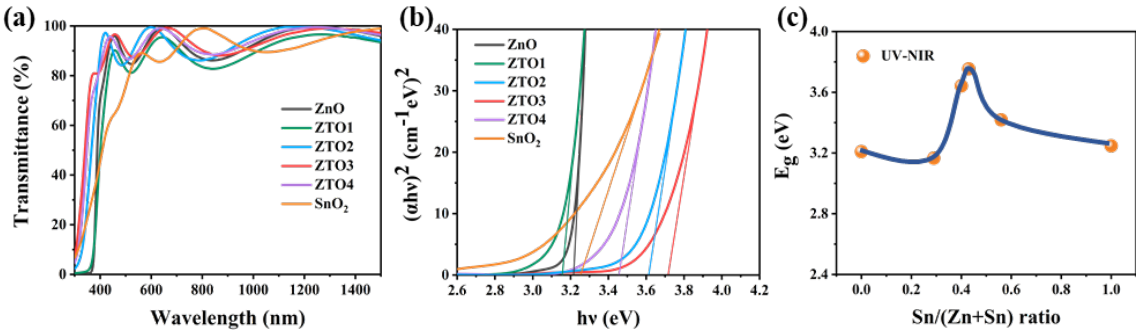

Figure 4.3 *(a) Internal transmittance spectra of $Zn_{1-x}Sn_xO$ films. (b) Tauc plot of $(\alpha hv)^2$ versus photo energy (hv). (c) Optical band gaps extracted from Tauc plot analysis as a function of Sn/(Zn+Sn).*

To investigate the elemental chemical states of the ZTO thin films, we performed X-ray photoelectron spectroscopy (XPS) measurements for qualitative and quantitative analysis. The full range XPS spectrum of the ZTO3 revealed the presence of a traceable amount of Carbon (C) (Figure 4.4), which could be attributed to the environmental absorption of quite a few organics on the surface of the film during sample preparation and/or during the XPS measurements.[17] It is noted that the occurrence of the C peak position conforms to the conventional C 1s peak (284.68 eV).[5] Furthermore, the XPS spectrum validates the existence of Zn, O, and Sn in the corresponding ZTO3 film. Figure 4.5 indicates the two characteristic peaks related to Zn $2p_{3/2}$ and Zn $2p_{1/2}$, which indicate simply the presence of Zn^{2+}. The photoelectron peaks of Sn $3d_{5/2}$ and Sn $3d_{3/2}$ also were detected at 486.3 eV and 494.7 eV, respectively (Figure 4.5). The peak position for Sn matched well with the previously reported work about ZTO.[18] Eventually, the XPS analysis confirmed the formation of the ZTO3 phase by RF co-sputtering method and indicated an efficient authentic technique for ZTO film synthesis.

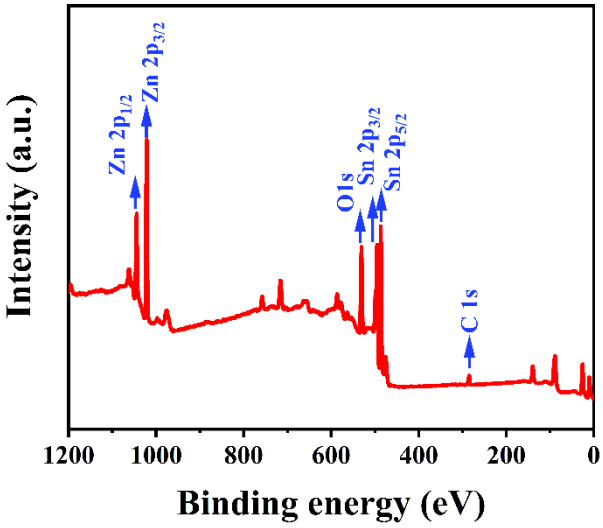

Figure 4.4 *The XPS pattern of ZTO3 film.*

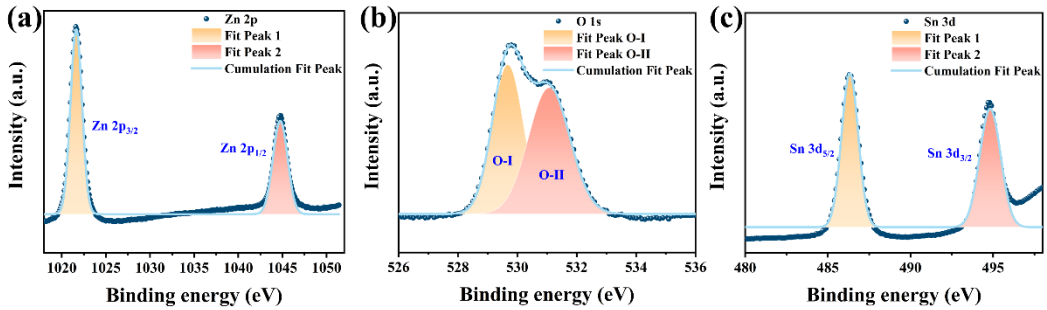

Figure 4.5 *The peaks of Zn 2p (a), O 1s (b) and Sn 3d (c) determined by XPS spectra.*

4.2.4 Energy band structure analysis of Sb_2Se_3/ZTO heterojunction

To further analyze the energy level alignment of multiple layers of the whole device, we have carried out ultraviolet photoelectron spectroscopy (UPS) measurements. Figure 4.6 exhibits the secondary electron cutoff (E_{cutoff}) and valence band (E_{onset}) spectrum of ZTO films along with ZnO and SnO_2 films. Herein, we have employed the mathematical equations, already described in Chapter II (2-5), (2-6), (2-7), to obtain the energy band levels (conduction band (E_C), valence band (E_V)) of corresponding ZTO films.[19] Thus, by analyzing the UPS spectrum and band gap, the energy level diagram of the whole device along with ZnO and SnO_2 films is represented in Figure 4.7, where the energy levels of Sb_2Se_3 and ITO were taken from works of the works of literature.[20, 21] To obtain high device performance, the E_C alignment of the absorber layer with the corresponding E_C of ETL is one of the most important factors.[17, 22] Furthermore, it is important to note that a suitable conduction band offset (CBO) within the range 0~0.4 eV, corresponding to "spike"-like band alignment, is crucial for better performance of solar cells.[23, 24] In Figure 4.7, it can be observed that the CBO offset for the ZTO2 and ZTO3 devices was measured at 0.27 eV and 0.18 eV, respectively. This indicates that there is a short "spike-like" alignment at the interface which would not inhibit the electron transport, thus favorable for obtaining an efficient device. In addition, an appreciable E_V edge also makes ZTO3 a successful hole-blocking film which results in a reduction of non-radiative recombination at the interface. The appropriate band

alignment of Sb_2Se_3/ZTO3 heterojunction further demonstrated that the prepared ZTO3 film is extremely preferable as an electron transport layer for Sb_2Se_3-based devices.

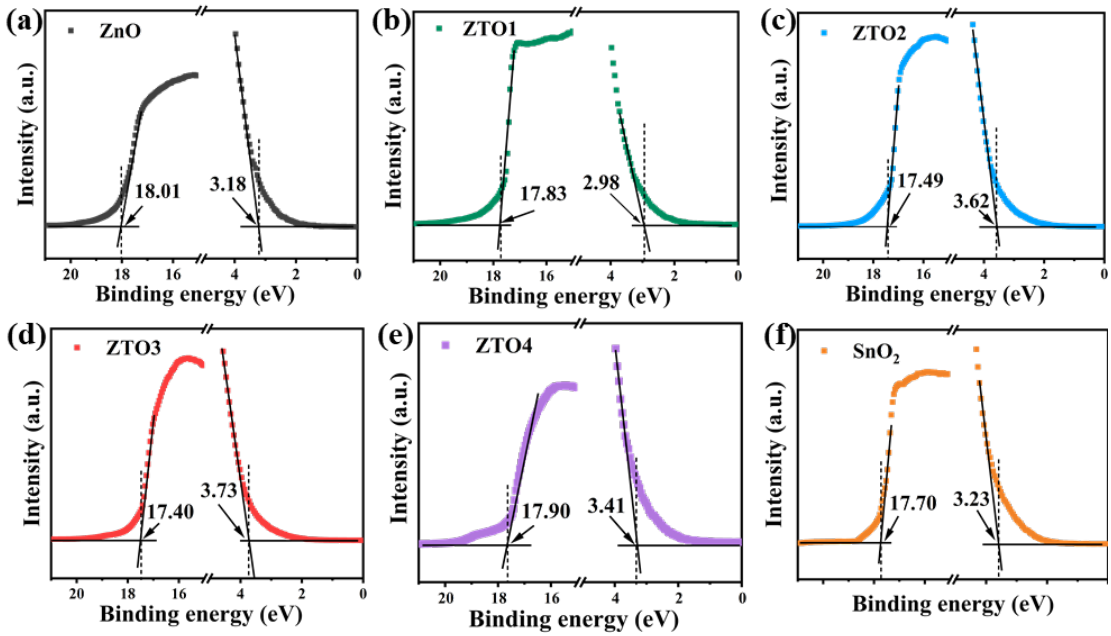

Figure 4.6 *UPS spectra of $Zn_{1-x}Sn_xO$ films, (a) ZnO, (b) ZTO1, (c) ZTO2, (d) ZTO3, (e) ZTO4, (f) SnO_2, used to derive E_{cutoff} edge and E_{onset} position.*

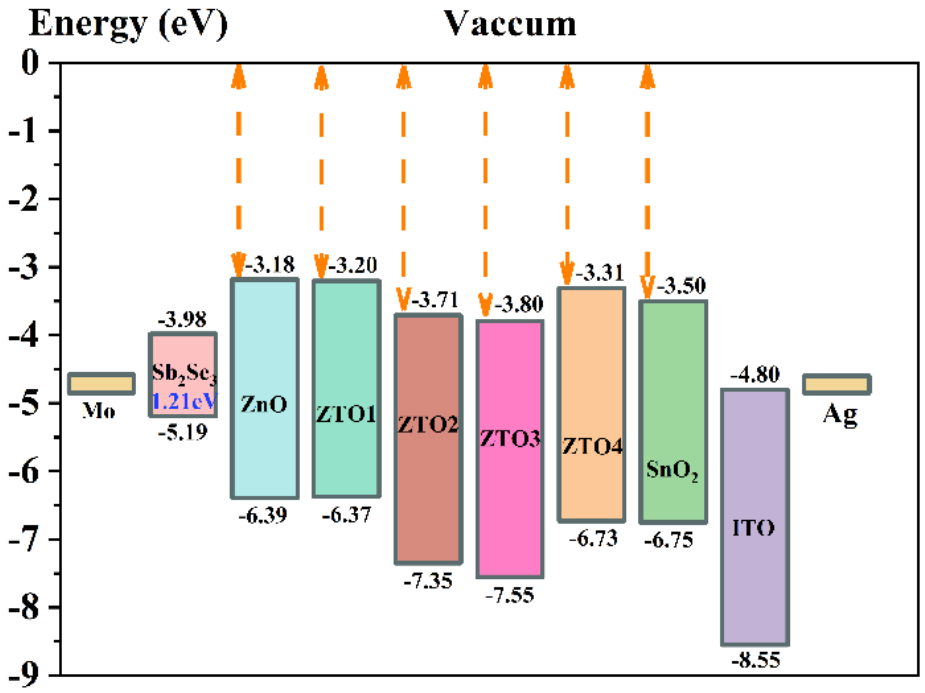

Figure 4.7 *Band gap alignment schematic diagram for the Sb_2Se_3/ZTO device.*

4.3 Preparation and characterization of Sb_2Se_3/ZTO thin-film solar cells

4.3.1 Preparation of solar cells

Indium tin oxide (ITO) window layer was sputtered on the ZTO film by a sequential process, using magnetron sputtering with the working parameters of 120 W, 0.4 Pa, a flow rate of 30 sccm and 7 sccm for argon and oxide gas, respectively (Figure 4.8a). To complete the device structure, Ag metallic contact was deposited on the ITO film through thermal evaporation. Finally, the active area of the devices was mechanically engraved into small squares. The active area of the Sb_2Se_3/ZTO devices is about 0.14 cm^2. Figure 4.8b indicates the adopted device structure of the Sb_2Se_3-based solar cells (Mo/Sb_2Se_3/ZTO/ITO/Ag). The photo of the solar cells is shown in (Figure 4.8c).

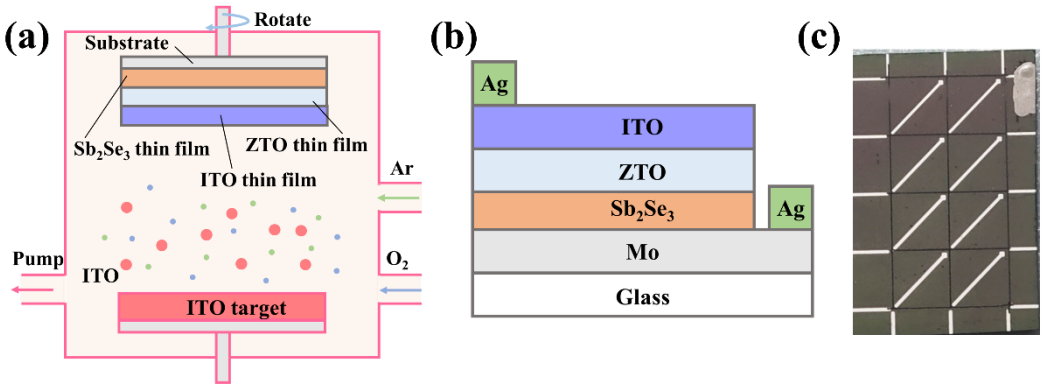

Figure 4.8 *(a) ITO layer preparation by magnetron sputtering, (b) Schematic configuration of the final Sb_2Se_3/ZTO thin-film solar cell, (c) image of the final Sb_2Se_3/ZTO thin-film solar cells.*

4.3.2 Device performance of the Sb_2Se_3/ZTO solar cells

The ZTO thin films were used to construct four batches of substrate-structured solar cells (ZTO1, ZTO2, ZTO3, and ZTO4), and the statistical distributions of the key performance parameters containing open–circuit voltage (V_{OC}), short–circuit current density (J_{SC}), fill factor (FF), and PCE are presented in Figure 4.9a–d. All four batches

of devices, each with a set of thirty-five synchronously fabricated sub-cells demonstrated acceptable variation of device performance, which authenticated quite good uniformity for these buffer layers and fabrication process. However, the Sb_2Se_3 devices constructed with ZTO1 and ZTO4 exhibited poor performance, and the highest efficiency with these buffer layers was even lower than 2%. Thus, the following device characteristics will be restricted to the ZTO2 and ZTO3-based devices. Apparently, the ZTO3 device with a slightly larger value of V_{OC}, J_{SC}, and FF than those of ZTO2, indicates probably a better band alignment of the Sb_2Se_3/ZTO heterojunction of the device. Moreover, the stable performance of the device based on optimized ZTO3 films shows promising indications for their potential application.

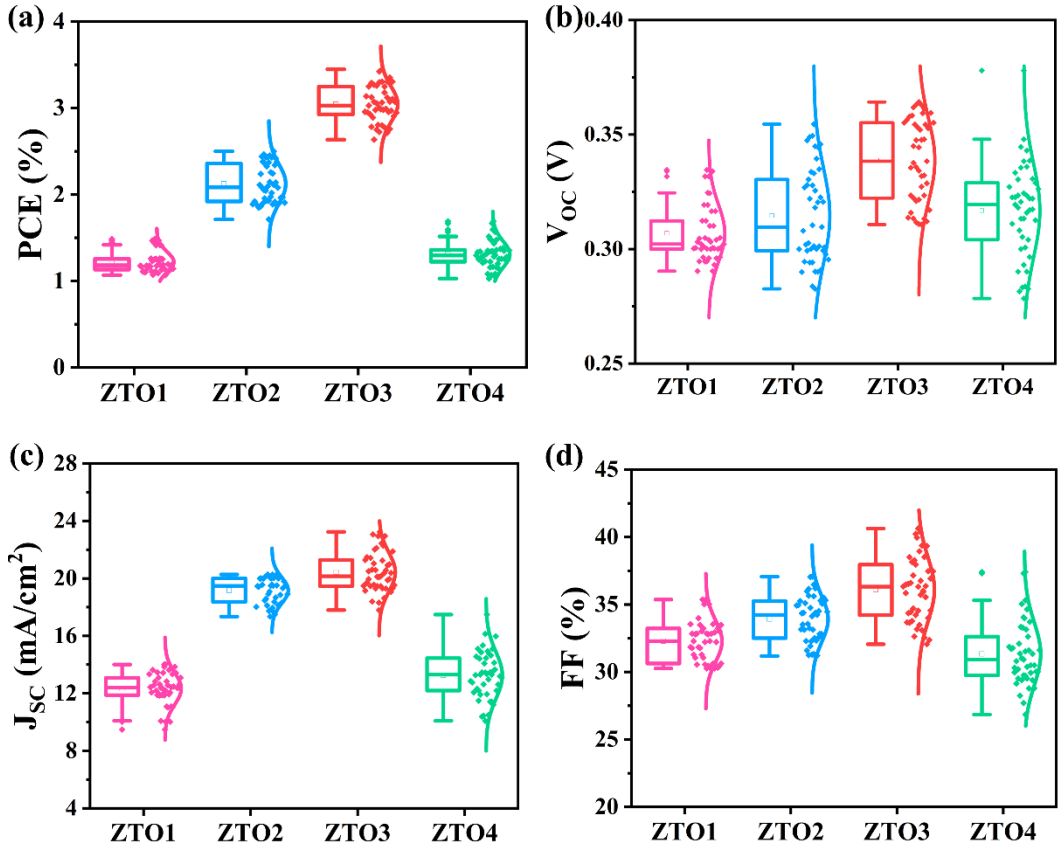

Figure 4.9 *Statistical distribution of the performance parameters including (a) PCE, (b) V_{OC}, (c) J_{SC}, and (d) FF for different Sb_2Se_3/ZTO devices.*

The representative *J–V* characteristics and detailed device parameters of ZTO/Sb_2Se_3 devices (ZTO2 and ZTO3) are given in Figure 4.10a and Table 4.2. It can be observed

that the ZTO2 devices exhibited a J_{SC} of 20.26 $mAcm^{-2}$, V_{OC} of 354 mV, and FF of 37.06%, thus acquiring a PCE of 2.50%. The ZTO3 device delivered a PCE of 3.44% with an obvious improvement of V_{OC} to 364 mV, J_{SC} to 23.23 $mAcm^{-2}$, and FF to 40.63%, respectively. Along with the better energy band alignment, the improved performance of ZTO3 can also be attributed to large grains of the absorber layer, smooth interfacial boundary, crack-free interface, and strong adhesion between the photoactive and charge extracting films,[21] as shown in the inset of Figure 4.10a. As shown in Figure 4.10b, the EQE analysis of the ZTO2 and ZTO3 devices indicated identical wide photo responses within the wavelengths from 300 to 1100 nm, which coincided efficiently with the narrow band gap of Sb_2Se_3. The integrated J_{SC} obtained from EQE results were 19.59 and 22.58 $mAcm^{-2}$ for ZTO2 and ZTO3 devices, respectively. The corresponding integrated J_{SC} values were in excellent agreement with the values acquired from (*J–V* measurements Figure 4.10a). Importantly, a sharp decline at the range below the wavelength of ~520 nm for cells with a CdS buffer can be observed (Figure 4.10b). The essential EQE improvement in the spectral region of 400-500 nm is attributed to the employment of a wider band gap ZTO thin film in comparison to the CdS-based device,[25] due to the absorption of the CdS ETL itself.[26, 27]

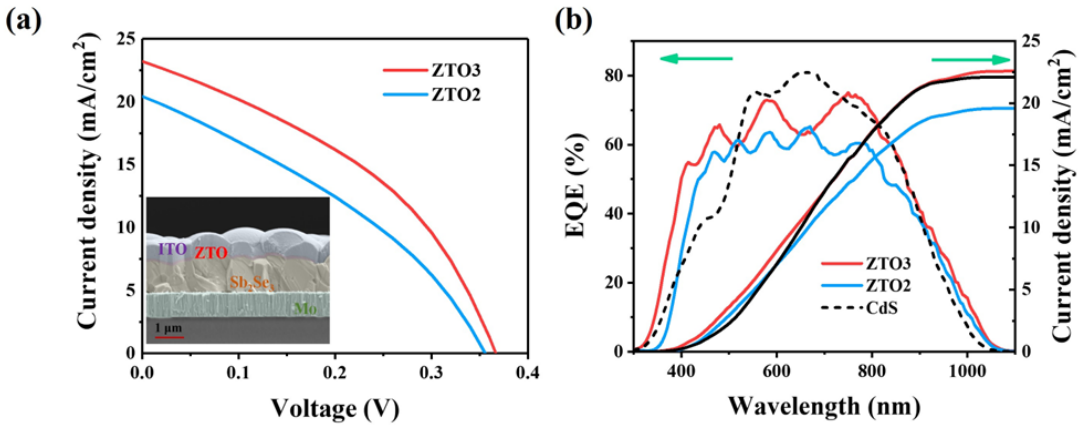

Figure 4.10 *Device performance. (a) J–V curves of ZTO2 and ZTO3 devices. (b) External quantum efficiency (EQE) spectra and integrated J_{SC} of Sb_2Se_3 devices with ZTO and CdS buffer layers, respectively.*

Table 4.2 *Device performance parameters of ZTO2 and ZTO3 devices.*

Samples	PCE (%)	V_{OC} (mV)	J_{SC} (mA/cm^2)	FF (%)	Integrated J_{SC} (mA/cm^2)
ZTO2	2.50	354	20.26	37.06	19.59
ZTO3	3.44	364	23.23	40.63	22.58

4.3.3 Defect analysis in Sb_2Se_3/ZTO solar cells

In order to investigate the interfacial characteristics of the fabricated solar cells (ZTO2 and ZTO3), capacitance-voltage (*C–V)* and deep-level capacitance profiling (DLCP) characterizations were carried out. Based on the literature,[29, 30] we have calculated the interfacial defect density (N_{CV}) and bulk defect density (N_{DLCP}) of the corresponding devices. The respective curves of N_{CV} and N_{DLCP} against the profiling depth x (Figure 4.11) can be calculated according to the equation (2-9), (2-10), and (2-11), mentioned in Chapter II.[31] Herein, it should be noted that $\varepsilon_{r,n}$, and $\varepsilon_{r,p}$ are related to the relative permittivity of ZTO and Sb_2Se_3, respectively. It can be clearly seen that there is a large difference between N_{CV} and N_{DLCP} curves for ZTO2 in comparison to the device ZTO3, illustrating that an optimized ZTO buffer layer is highly important to decrease the interfacial defect density and the recombination loss at the Sb_2Se_3/ZTO interface. In addition, the interface defect density has been calculated and summarized in Table 4.3, the value for ZTO2 devices (6.7×10^{15} cm^{-3}) is approximately twice that of ZTO3 devices (3.3×10^{15} cm^{-3}). This result is closely associated with the much better band alignment of the ETL and absorber layers for the optimized ZTO3 device. Thus, it is assumed that the enhancement in V_{OC} of the ZTO3 device is attributed to the diminished interface defect density. Moreover, it can be observed that the ZTO3 device possesses a slightly larger depletion width (W_d=188 nm, the corresponding depletion width when voltage=0 V) than that of the ZTO2 device (164 nm), which indicates a better photon penetration to the absorber and carrier extraction capability of the device.

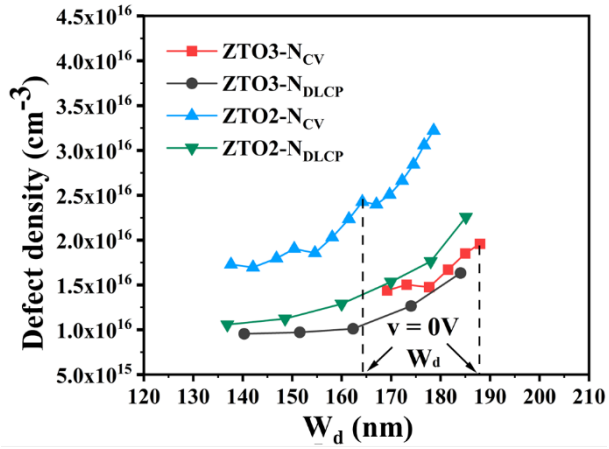

Figure 4.11 *C–V and DLCP profiles of ZTO2 and ZTO3 devices.*

Table 4.3 *Interfacial defect density calculated from C–V and DLCP of ZTO2 and ZTO3 devices.*

Samples	N_{CV} (cm^{-3})	N_{DLCP} (cm^{-3})	Interface defect density (cm^{-3})	Depth (nm)
ZTO2	2.43×10^{16}	1.76×10^{16}	6.7×10^{15}	164
ZTO3	1.96×10^{16}	1.63×10^{16}	3.3×10^{15}	188

C–V measurements were also carried out to distinguish the interfacial built-in voltage (V_{bi}) of the fabricated ZTO2 and ZTO3 devices. As illustrated in $1/C^2$–*V* curves (Figure 4.12), the V_{bi} values can be evaluated by extracting the curve to abscissa-intercept and linear fitting. The V_{bi} value of ZTO2 and ZTO3 devices obtained from $1/C^2$–*V* curves were 324 mV and 458 mV, respectively. The V_{bi} for ZTO3 is larger than that of the ZTO2 device, signifying a greatly improved band alignment for the ZTO3 device, which validated the results of the above *C–V* and DLCP analysis.

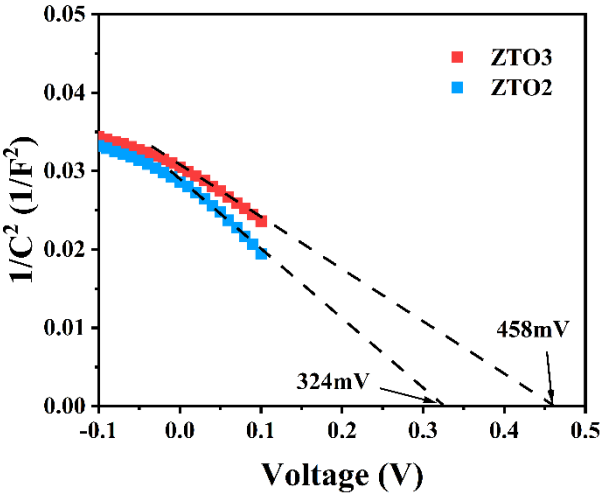

Figure 4.12 *$1/C^2$–V plots of the representative ZTO2 and ZTO3 devices.*

To investigate the electrical behaviors of the representative ZTO2 and ZTO3 devices, dark *J–V* characteristics were estimated. It can be observed from dark current measurements that the ZTO3 device, as compared to the ZTO2, displays better characteristics and higher dark current density, as given in Figure 4.13a. This specifies that the ZTO3/Sb_2Se_3 interface can diminish non-radiative recombination loss and enhance the interfacial contact quality, which can result in an improvement in device parameters in terms of J_{SC} and FF.[16, 32] Figure 4.13b presents the *dJ/dV* against *V* plot. The shunt conductance (G) values of the ZTO2 and ZTO3 devices are 7.69 and 6.50 mS/cm^2, respectively. In Figure 4.13c, the diode ideality factor (A)and the series resistance (R) are obtained by plotting *dV/dJ* against $(J+J_{SC})^{-1}$ to find a slope of AkT/q and the intercept of the ordinate-axis, respectively. The series resistance R_{ZTO3} of the device ZTO3 (2.09 Ω.cm^2) is smaller than that of the device ZTO2 (3.68 Ω.cm^2). In addition, the ideality factor A values of the devices ZTO2 and ZTO3 are 2.33 and 1.75, respectively, implying less interfacial recombination for the device ZTO3. These results confirm an improved Sb_2Se_3/ZTO heterojunction in ZTO3.

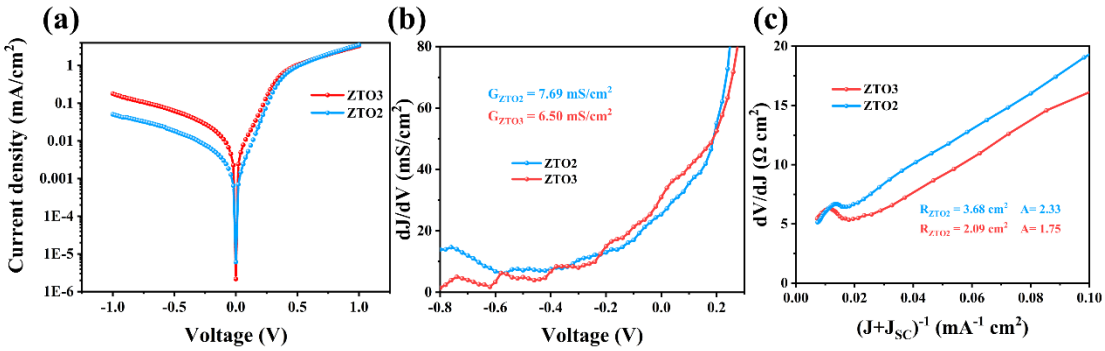

Figure 4.13 *Dark J–V characteristic for ZTO2 and ZTO3 devices. (a) Dark J–V curves, (b) shunt conductance (G), (c) series resistance (R), and ideality factor (A).*

Figure 4.14 presents the electrochemical impedance spectrum (EIS) in dark conditions to examine the interface charge transfer mechanism. As shown in the inset in Figure 4.14, the impedance results were simulated by employing an equivalent circuit model to fit the experimental plot. The recombination resistance (R_{rec}) values of the ZTO2 and ZTO3 devices were directly obtained from the arc's diameter length and were 846.5 Ω and 1473 Ω respectively. In other words, the devices using ZTO3 film as a buffer layer show higher recombination resistance, which better obstructs the photogenerated carriers' recombination.

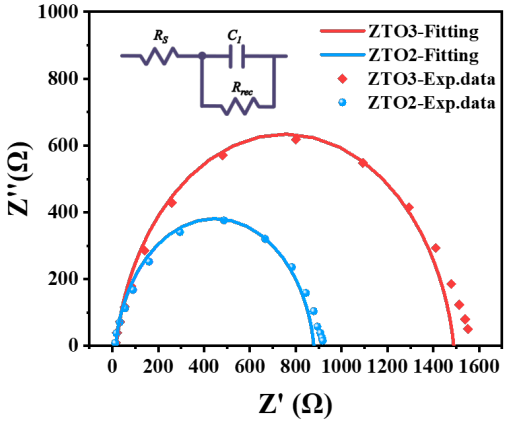

Figure 4.14 *Nyquist plots of the impedance for the ZTO2 and ZTO3 devices (inset equivalent circuit employed to fit the Nyquist plots), experimental data are shown as dotted circles and the fitted results are shown as solid lines.*

Admittance spectroscopy (AS) has been recognized as a powerful technique to explore the activation energies along with the properties of defects in thin film solar cells.[33, 34] For the sake of further evaluating the energy distribution of defect density and charge recombination mechanisms of fabricated solar cells, *C–f–T* analysis was implemented at the temperature varying from 120 to 300 K with steps of 20 K. Figure 4.15 demonstrates the *C–f–T* spectra of the optimized device (3.44%, ZTO3). The inflection points at different temperatures were obtained by the Arrhenius plot. The corresponding values of inflection point frequency (ω_0) and the defect activation energies (E_a) were extracted from the slopes that were fitted using the relation (3-8) mentioned in Chapter III.[26, 35] According to the capacitance spectra, we obtained two different defect levels labeled as D1 and D2 with E_a values of 219 meV and 331 meV, respectively (Figure 4.15b).

According to the reported work,[15] the capacitance at smaller frequency range is attributed to the result of free charge density and deep-level traps, while the capacitance at large frequency range is only considered as the result of the response of free charge density. The scattering of defect densities was fitted according to the formula (3-9) and (3-10) mentioned in Chapter III.[36]

In Figure 4.15c–d, the defect density distribution spectra of D1 and D2 are Gaussian fitted to overlap the plots of N_t versus $E_{(\omega)}$, and the extracted values of defect density were 3.45×10^{15} cm^2eV^{-1} and 5.31×10^{16} cm^2eV^{-1} for the defect type of D1 and D2, respectively. The defect density of the optimized device here is larger than that of the Sb_2Se_3-based devices with improved performance, reported in previous work,[21, 26] which indicates that there are more deep-level defects in the bulk and interface of the device in this work using Cd-free buffer layer. These defects likely act as recombination centers, which significantly deteriorate the performance of the device.

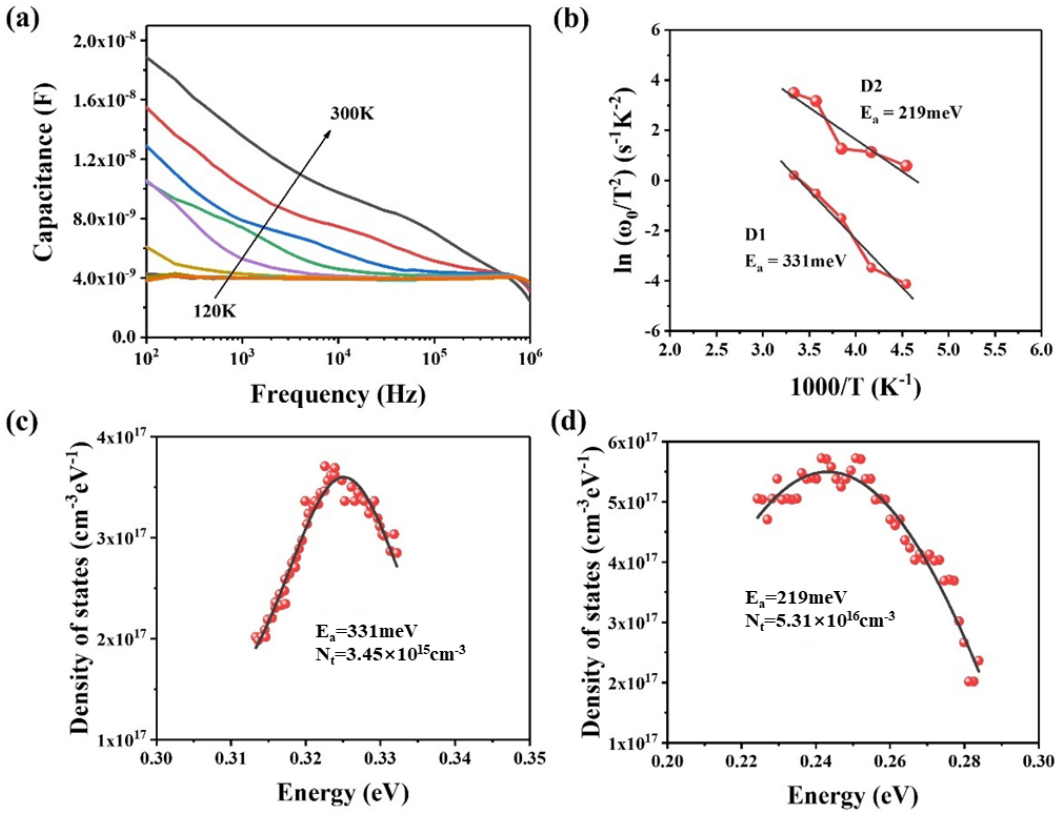

Figure 4.15 *(a) Temperature-dependent admittance measurements of the champion device. (a) Capacitance–frequency–temperature (C–f–T) spectra. (b) Defect activation energies of the ZTO3 device. Defect distributions of D1 (c) and D2 (d) of the ZTO3 device derived from the admittance spectra.*

4.4 Conclusions

An RF magnetron co-sputtering technique has been employed for the deposition of $Zn_{1-x}Sn_xO$ ETLs to fabricate Cd-free substrate-structured Sb_2Se_3-based devices. The ratio of Zn and Sn in ZTO film can be tuned to modify its optical band gap and energy level for better alignment with Sb_2Se_3 absorber, which has a significant effect on the device performance. Sb_2Se_3-based PV devices with the configuration Glass/Mo/Sb_2Se_3/ZTO/ITO/Ag were first developed with the optimized $Zn_{0.57}Sn_{0.43}O$ buffer layer, demonstrating an encouraging efficiency of 3.44%. The uniformity of a relatively high number of devices is already quite acceptable at this level. In comparison

with the PV cells using CdS buffer layer, the Sb_2Se_3-based solar cells using the ZTO buffer layer, studied here, still have much higher defect density, especially in the interface. The reduction of these defects will be necessary to significantly increase the efficiency of these Cd-free solar cells.

4.5 References

[1] Messina, S., Nair, M. T. S., Nair, P. K., Antimony selenide absorber thin films in all-chemically deposited solar cells. *Journal of The Electrochemical Society* 2009, 156(5), H327.

[2] Duan, Z. T., Liang, X. Y., Feng, Y., Ma, H. Y., Liang, B. L., Wang, Y., Luo, S. P., Wang, S. F., Schropp, R. E. I., Mai, Y. H., Li, Z. Q., Sb_2Se_3 thin-film solar cells exceeding 10% power conversion efficiency enabled by injection vapor deposition technology. *Adv. Mater.* 2022, 34(30), 2202969.

[3] Zhao, Y. Q., Wang, S. Y., Li, C., Che, B., Chen, X. L., Chen, H. Y., Tang, R. F., Wang, X. M., Chen, G. L., Wang, T., Gong, J. B., Chen, T., Xiao, X. D., Li, J. M., Regulating deposition kinetics via a novel additive-assisted chemical bath deposition technology enables fabrication of 10.57%-efficiency Sb_2Se_3 solar cells. *Energy Environ. Sci.* 2022, 15, 5118-5128.

[4] Leng, M. Y., Chen, C., Xue, D. J., Gong, J. B., Liu, Y. H., Li, K. H., Xiao, X. D., Wang, G., Tang, J., Sb_2Se_3 solar cells employing metal-organic solution coated CdS buffer layer. *Sol. Energy Mater. Sol. Cells* 2021, 225(111043), 111043.

[5] Du, Q., Li, B. Y., Shi, S., Zhang, K. Z., Zhang, Y. X., Cheng, S. Q., Zhou, Z. Q., Liu, F. F., Sun, S. L., Sun, Y., Liu, W., Relationship between the intermediate phases of the sputtered Zn(O,S) buffer layer and the conduction band offset in Cd-free Cu(In,Ga)Se_2 solar cells. *Crystengcomm* 2020, 22(26), 4416-4426.

[6] Larsson, F., Donzel-Gargand, O., Keller, J., Edoff, M., Törndahl, T., Atomic layer deposition of Zn(O,S) buffer layers for Cu(In,Ga)Se_2 solar cells with KF post-deposition treatment. *Sol. Energy Mater. Sol. Cells* 2018, 183, 8-15.

[7] Guo, H. F., Chen, Z. W., Wang, X., Cang, Q. F., Ma, C. H., Jia, X. G., Yuan, N. Y., Ding, J. N., Significant increase in efficiency and limited toxicity of a solar cell based on Sb_2Se_3 with SnO_2 as a buffer layer. *J. Mater. Chem. C* 2019, 7(45), 14350-14356.

[8] Wen, X. X., He, Y. S., Chen, C., Liu, X. S., wang, L., Yang, B., Leng, M. Y., Song, H. B., Zeng, K., Li, D. B., Li, K. H., Gao, L., Tang, J., Magnetron sputtered ZnO buffer layer for Sb_2Se_3 thin film solar cells. *Sol. Energy Mater. Sol. Cells* 2017, 172, 74-81.

[9] Saadat, M., Amiri, O., Rahdar, A., Optimization of (Zn,Sn)O buffer layer in Cu(In,Ga)Se_2 based solar cells. *Sol. Energy* 2019, 189, 464-470.

[10] Wang, W. H., Cao, Z. X., Wang, H. H., Luo, J. S., Zhang, Y., Remarkable Cd-free Sb_2Se_3 solar cell yield achieved by interface band-alignment and growth orientation screening. *J. Mater. Chem. A* 2021, 9(47), 26963-26975.

[11] Ishaq, M., Chen, S., Farooq, U., Azam, M., Deng, H., Su, Z. H., Zheng, Z. H., Fan, P., Song, H. S., Liang, G. X., High open-circuit voltage in full-inorganic Sb_2S_3 solar cell via modified Zn-doped TiO_2 electron transport layer. *Solar RRL* 2020, 4(12).

[12] Nakamura, M., Yamaguchi, K., Kimoto, Y., Yasaki, Y., Kato, T., Sugimoto, H., Cd-free

$Cu(In,Ga)(Se,S)_2$ thin-film solar cell with record efficiency of 23.35%. *IEEE Journal of Photovoltaics* 2019, 9(6), 1863-1867.

[13] Ericson, T., Larsson, F., Törndahl, T., Frisk, C., Larsen, J., Kosyak, V., Hägglund, C., Li, S., Platzer-Björkman, C., Zinc-tin-oxide buffer layer and low temperature post annealing resulting in a 9.0% efficient cd-free Cu_2ZnSnS_4 solar cell. *Solar RRL* 2017, 1(5).

[14] Cui, X., Sun, K. W., Huang, J. L., Lee, C. Y., Yan, C., Sun, H., Zhang, Y. F., Liu, F. Y., Hossain, M. A., Zakaria, Y., Wong, L. H., Green, M., Hoex, B., Hao, X. J., Enhanced heterojunction interface quality to achieve 9.3% efficient Cd-free Cu_2ZnSnS_4 solar cells using atomic layer deposition ZnSnO buffer layer. *Chemistry of Materials* 2018, 30(21), 7860-7871.

[15] Liang, G. X., Luo, Y. D., Chen, S., Tang, R., Zheng, Z. H., Li, X. J., Liu, X. S., Liu, Y. K., Li, Y. F., Chen, X. Y., Su, Z. H., Zhang, X. H., Ma, H. L., Fan, P., Sputtered and selenized Sb_2Se_3 thin-film solar cells with open-circuit voltage exceeding 500 mV. *Nano Energy* 2020, 73, 104806.

[16] Li, X. L., Su, Z. H., Venkataraj, S., Batabyal, S. K., Wong, L. H., 8.6% efficiency CZTSSe solar cell with atomic layer deposited Zn-Sn-O buffer layer. *Sol. Energy Mater. Sol. Cells* 2016, 157, 101-107.

[17] Kang, L. L., Zhao, L., Jiang, L. X., Yan, C., Sun, K. W., Ng, B. K., Gao, C. H., Liu, F. Y., In situ growth of $CuSbS_2$ thin films by reactive co-sputtering for solar cells. *Materials Science in Semiconductor Processing* 2018, 84, 101-106.

[18] Lu, S. C., Zhao, Y., Chen, C., Zhou, Y., Li, D., Li, K. H., Chen, W., Wen, X. X., Wang, C., Kondrotas, R., Lowe, N., Tang, J., Sb_2Se_3 thin-film photovoltaics using aqueous solution sprayed SnO_2 as the buffer layer. *Adv. Electron. Mater.* 2018, 4(1), 1700329.

[19] Kamruzzaman, M., Chaoping, L., Yishu, F., Farid Ul Islam, A. K. M., Zapien, J. A., Atmospheric annealing effect on TiO_2/Sb_2S_3/P3HT heterojunction hybrid solar cell performance. *RSC Advances* 2016, 6(101), 99282-99290.

[20] Wang, W. H., Wang, X. M., Chen, G., Chen, B. W., Cai, H. L., Chen, T., Chen, S. Y., Huang, Z. G., Zhu, C. F., Zhang, Y., Promising $Sb_2(S,Se)_3$ solar cells with high open voltage by application of a TiO_2/CdS double buffer layer. *Solar RRL* 2018, 2(11), 1800208.

[21] Tang, R., Zheng, Z. H., Su, Z. H., Li, X.-J., Wei, Y.-D., Zhang, X. H., Fu, Y. Q., Luo, J., Fan, P., Liang, G. X., Highly efficient and stable planar heterojunction solar cell based on sputtered and post-selenized Sb_2Se_3 thin film. *Nano Energy* 2019, 64(103929), 103929.

[22] Barkhouse, D. A. R., Haight, R., Sakai, N., Hiroi, H., Sugimoto, H., Mitzi, D. B., Cd-free buffer layer materials on $Cu_2ZnSn(S_xSe_{1-x})_4$: Band alignments with ZnO, ZnS, and In_2S_3. *Appl. Phys. Lett.* 2012, 100(19).

[23] Minemoto, T., Matsui, T., Takakura, H., Hamakawa, Y., Negami, T., Hashimoto, Y., Uenoyama, T., Kitagawa, M., Theoretical analysis of the effect of conduction band offset of window/CIS layers on performance of CIS solar cells using device simulation. *Sol. Energy Mater. Sol. Cells* 2001, 67(1), 83-88.

[24] Tang, R., Chen, S., Zheng, Z. H., Su, Z. H., Luo, J. T., Fan, P., Zhang, X. H., Tang, J., Liang, G. X., Heterojunction annealing enabling record open-circuit voltage in antimony triselenide solar cells. *Adv. Mater.* 2022, 34(14), 2109078.

[25] Ahmad, N., Zhao, Y. H., Ye, F., Zhao, J., Chen, S., Zheng, Z. H., Fan, P., Yan, C., Li, Y. Y., Su, Z. H., Zhang, X. H., Liang, G. X., Cadmium-free kesterite thin-film solar cells with high efficiency approaching 12%. *Adv. Sci.* 2023.

[26] Luo, Y. D., Tang, R., Chen, S., Hu, J. G., Liu, Y. K., Li, Y. F., Liu, X. S., Zheng, Z. H., Su, Z. H., Ma, X. F., Fan, P., Zhang, X. H., Ma, H. L., Chen, Z. G., Liang, G. X., An effective combination reaction involved with sputtered and selenized Sb precursors for efficient Sb_2Se_3 thin film solar cells. *Chem. Eng.*

J. 2020, 393, 124599.

[27] Ishaq, M., Deng, H., Yuan, S., Zhang, H., Khan, J., Farooq, U., Song, H., Tang, J., Efficient double buffer layer $Sb_2(SexS_{1-x})_3$ thin film solar cell via single source evaporation. *Solar RRL* 2018, 2(10), 1800144.

[28] Lee, J., Enkhbat, T., Han, G., Sharif, M. H., Enkhbayar, E., Yoo, H., Kim, J. H., Kim, S., Kim, J., Over 11 % efficient eco-friendly kesterite solar cell: Effects of S-enriched surface of $Cu_2ZnSn(S,Se)_4$ absorber and band gap controlled (Zn,Sn)O buffer. *Nano Energy* 2020, 78, 105206.

[29] Luo, Y. D., Chen, G. J., Chen, S., Ahmad, N., Muhammad, A., Zheng, Z. H., Su, Z. H., Cathelinaud, M., Ma, H. L., Chen, Z. G., Fan, P., Zhang, X. H., Xing, L. G., Carrier transport enhancement mechanism in highly efficient antimony selenide thin-film solar cell. *Adv. Funct. Mater.* 2023, 33(14), 2213941.

[30] Lin, J. H., Chen, G. J., Ahmad, N., Muhammad, I., Chen, S., Su, Z. H., Fan, P., Zhang, X. H., Zhang, Y., Liang, G. X., Back contact interfacial modification mechanism in highly-efficient antimony selenide thin-film solar cells. *J. Energy Chem.* 2023, 80, 256-264.

[31] Chen, G. J., Luo, Y. D., Abbas, M., Ishaq, M., Zheng, Z. H., Chen, S., Su, Z. H., Zhang, X. H., Fan, P., Liang, G. X., Suppressing buried interface nonradiative recombination losses toward high-efficiency antimony triselenide solar cells. *Adv. Mater.* 2023, 36(5), 2308522.

[32] Liang, G. X., Chen, M. D., Ishaq, M., Li, X. R., Tang, R., Zheng, Z. H., Su, Z. H., Fan, P., Zhang, X. H., Chen, S., Crystal growth promotion and defects healing enable minimum open-circuit voltage deficit in antimony selenide solar cells. *Adv. Sci.* 2022, 9(9), 2105142.

[33] Chen, M. D., Ishaq, M., Ren, D. L., Ma, H. L., Su, Z. H., Fan, P., Le Coq, D., Zhang, X. H., Liang, G. X., Chen, S., Interface optimization and defects suppression via NaF introduction enable efficient flexible Sb_2Se_3 thin-film solar cells. *J. Energy Chem.* 2024, 90, 165-175.

[34] Hu, X. B., Tao, J. H., Weng, G. E., Jiang, J. C., Chen, S. Q., Zhu, Z. Q., Chu, J. H., Investigation of electrically-active defects in Sb_2Se_3 thin-film solar cells with up to 5.91% efficiency via admittance spectroscopy. *Sol. Energy Mater. Sol. Cells* 2018, 186, 324-329.

[35] Chen, G. J., Tang, R., Chen, S., Zheng, Z. H., Su, Z. H., Ma, H. L., Zhang, X. H., Fan, P., Liang, G. X., Crystal Growth Promotion and Defect Passivation by Hydrothermal and Selenized Deposition for Substrate-Structured Antimony Selenosulfide Solar Cells. *ACS Appl. Mater. Interfaces* 2022, 14(28), 31986-31997.

[36] Luo, P., Imran, T., Ren, D. L., Zhao, J., Wu, K. W., Zeng, Y. J., Su, Z. H., Fan, P., Zhang, X. H., Liang, G. X., Chen, S., Electron transport layer engineering induced carrier dynamics optimization for efficient Cd-free Sb_2Se_3 thin-film solar cells. *Small* 2023, 20(4), 2306516.

GENERAL CONCLUSIONS

Sb_2Se_3 solar cells are one of the most promising novel thin-film solar cells with attractive photoelectric properties, low toxicity, and earth element abundance. The low efficiency compared to its theoretical limits is the primary obstacle to applications. The unfavorable absorber quality and unsatisfactory band alignment are the significant impediments to improving device performance. This PhD thesis is based on the fabrication of Sb_2Se_3 thin-film solar cells using sputtering and selenization of Sb precursors. The objective is to address the above issues from three aspects: improvement of the quality of the Sb_2Se_3/CdS interface by doping the buffer layer, optimization of the quality of the Sb_2Se_3 absorber layer, and replacement of the CdS with ZnSnO for alternative Cd-free buffer layer. The following results and conclusions have been obtained.

(1) Heterojunction interface engineering of Al^{3+} doped into CdS buffer layer

To optimize the band alignment and to reduce interfacial defect density of the Sb_2Se_3/CdS heterojunction, a strategy of Al^{3+} cation doping in CdS buffer layer was introduced in Sb_2Se_3 solar cells. This doping significantly alleviated the current leakage, minimized the recombination loss, and enhanced the quality of the heterojunction interface. Further studies show that the band alignment of the optimized Sb_2Se_3/CdS:Al heterojunction was modified to be a “spike-like” structure, which prevents the charge carriers from piling up in the vicinity of the heterojunction interface. As a result, the optimized band alignment, the reduced interface recombination, and the enhanced carrier transport effectively result in the improvement of device performance. The best Sb_2Se_3/CdS:Al device delivers an interesting efficiency of 8.41%, accompanied with an increase of *J*sc to 28.26 mA/cm^2.

(2) Absorber growth engineering by rapid thermal processing

The undesirable defects, originating from prolonged annealing, is associated with the presence of fine grain and distinct voids existing at the bottom of the Sb_2Se_3 absorber

layer, thereby still constraining the enhancement of device efficiency. We proposed an effective rapid thermal annealing for better control of Sb_2Se_3 absorber layer growth. An improved quality of Sb_2Se_3 absorber film was obtained with high crystallinity, preferred crystal orientation, smoother morphology, and reduced voids/pin-holes on the surface and in the bulk. This high-quality Sb_2Se_3 absorber is favorable for the extraction, and the transport of photogenerated carriers as well as for the longer lifetime of minority carriers. These characteristics also contribute to mitigating intrinsic defects of bulk Sb_2Se_3 and enhancing the adhesion of Mo/Sb_2Se_3 contact. Thus, effective reduction of carrier recombination is achieved in both the bulk Sb_2Se_3 and at the heterojunction interface, leading to a reduced defect density and an overall improvement in device performance. The efficiency of Sb_2Se_3 solar cells is increased to 9.03% with a superior *J*sc of 28.97 mA/cm^2.

(3) Alternative Cd-free buffer layer: ZnSnO

The optical loss induced by the relatively narrow band gap of CdS and its toxicity are still a huge concern restraining its application perspective. We have developed a more environmentally-friendly ZnSnO layer via the magnetron co-sputtering method to substitute the hazardous CdS film for Sb_2Se_3/ZnSnO-based devices. By tuning the ZnSnO composition, an optimized “spike-like” band alignment with a conduction band offset of 0.18 eV was obtained for the $Zn_{0.57}Sn_{0.43}O$ buffer layer. The analytical results show this buffer layer with a wider band gap can provide additional photo-generated carriers thanks to the photo-response improvement from ~330 nm to ~520 nm. The best device with the Cd-free structure of Glass/Mo/Sb_2Se_3/ZnSnO/ITO/Ag has achieved an interesting power efficiency of 3.44%, demonstrating a possibility to eliminate the widely used toxic buffer layer of CdS.

Further efficiency enhancement of Sb_2Se_3 solar cells is crucial to make them commercially viable in the future. Potential methods for improving efficiency include modification of the back contact interface, modulation of defects, and optimization of device configuration.

(1) Modification of the back contact interface

The back contact interface between Mo back electrode and Sb_2Se_3 film makes it easy to form a barrier for charge carriers. Based on experience with CIGS and CZTS solar cells, an intermediate layer such as MoO_2 or WO_3 can be considered to block the possible reaction between Mo and Sb_2Se_3.

(2) Modulation of defects

Due to the chemically binary but physically multinary character of Sb_2Se_3, the complex type of defects and the high defect density continue to pose challenges for Sb_2Se_3 thin-film solar cells. The presence of such defects may contribute to low V_{OC} due to the pinning of the Fermi level within the bandgap. Therefore, a comprehensive understanding of these defects is essential to address the bottleneck of efficiency enhancement. Future studies could focus on defect analysis, combined with theoretical calculations and experimental characterization to get deeper insights into the formation energy, energy level, type, and density of different defects in Sb_2Se_3 devices. Additionally, optimizing film preparation conditions to reduce intrinsic and bulk defect densities is also crucial.

(3) Optimization of device configuration

The device configuration directly affects the generation and the transport of charge carriers. Several methods could be tested for optimizing the device configuration. Firstly, new device structures such as multilayer structures could be useful for improving light absorption and carrier collection efficiency. Secondly, an anti-reflection layer on the surface of the device should reduce the light loss. Thirdly, novel buffer layers could also be necessary for better performance as well as for eliminating the toxic Cd.

PUBLICATION LIST

1. **Luo Y.**, Chen M., Tang R., Azam M., Chen S., Zheng Z., Su Z., Fan P., Ma H., Liang G., Energy band alignment for Cd-free antimony triselenide substrate structured solar cells by Co-sputtering ZnSnO buffer layer. Sol. Energy Mater. Sol. Cells, 2022, 240, 111721.

2. **Luo Y.**, Chen G., Chen S., Ahmad N., Azam M., Zheng Z., Carrier transport enhancement mechanism in highly efficient antimony selenide thin-film solar cell. Adv. Funct. Mater., 2023, 33, 2213941.

3. Azam M., **Luo Y.**, Tang R., Chen S., Zheng Z., Su Z., Hassan A., Fan P., Ma H., Chen T., Liang G., Zhang X., Organic chloride salt interfacial modified crystallization for efficient antimony selenosulfide solar cells. ACS Appl. Mater. Interfaces, 2022, 14, 4276-4284.

4. Chen G., **Luo Y.**, Muhammad A., Muhammad I., Zheng Z., Chen S., Suppressing buried interface nonradiative recombination losses toward high-efficiency antimony triselenide solar cells. Adv. Mater., 2023, 36, 2308522.

5. Duan C., **Luo Y.**, Hu C., Hu W., Ishaq M., Chen S., Su Z., Li J., Tang R., Zhao J., Liang G., Light-absorber engineering induced defect passivation for efficient antimony triselenide solar cells. Journal of Alloys and Compounds, 2024, 1000, 175130.

6. **Luo Y.**, Ma H., Ahmad N., U. Shah A., Zheng Z., Chen S., Su Z., Zhao J., Zhang X., Liang G., Rapid thermal-driven crystal growth and defect suppression in antimony selenide thin film for efficient solar cells (In revision)

COLLEGE SCIENCES DE LA MATIERE
DOCTORAL DES MOLECULES
BRETAGNE ET MATERIAUX

Université de Rennes

Titre : Développement de nouvelles couches tampons et processus de recuit rapide pour des cellules solaires à couche mince Sb_2Se_3 efficaces

Mots clés : Sb_2Se_3, cellules solaires à film mince, couche tampon, couche d'absorbeur, alignements de bande, recombinaison de défauts

Résumé : Dans ce travail de thèse, le comportement de l'interface de l'hétérojonction, le processus de croissance des grains cristallins et la couche tampon des cellules solaires à base de Sb_2Se_3 ont été étudiés.
La qualité de l'absorbeur et l'alignement des bandes d'énergie sont identifiés comme des paramètres clés pour réduire la densité de défauts et pour faciliter la séparation et le transport des porteurs de charge photogénérés.
Une stratégie de dopage d'Al^{3+} dans la couche tampon de CdS a été introduite dans les cellules solaires Sb_2Se_3. L'alignement des bandes d'énergie et la qualité de l'interface p-n ont été considérablement améliorés. Une courbure de bandes type "Spike-like" a été obtenue pour la meilleure cellule solaire avec un rendement de 8,41%. Deuxièmement, un procédé de recuit thermique rapide a également été développé et optimisé afin d'améliorer la qualité de la couche absorbeur de Sb_2Se_3 avec une densité de défauts réduite. Le rendement des cellules solaires est augmenté à 9,03%.
De plus, nous avons essayé de remplacer la couche tampon CdS toxique par un film ZnSnO respectueux de l'environnement avec en plus un band-gap plus large. Un rendement intéressant de 3,44% a été obtenue pour ces cellules solaires de Sb_2Se_3 sans Cd.

Title : Development of new buffer layers and rapid annealing process for efficient Sb_2Se_3 thin-film solar cells.

Keywords : Sb_2Se_3, thin-film solar cells, buffer layer, absorber layer, band alignments, defect recombination

Abstract: In this thesis, heterojunction interface behavior, grain growth process and alternative buffer layer of Sb_2Se_3 based solar cells were investigated.
The absorber quality and the band alignment are identified as key parameters for reducing defect density and for facilitating the separation and the transport of photogenerated charge carriers.
A strategy of Al^{3+} doping into the CdS buffer layer was introduced in Sb_2Se_3 solar cells. The band alignment and the interface quality have been significantly improved. A "spike-like" structure was obtained for the best device with an efficiency of 8.41%.
Secondly, a rapid thermal annealing process has also been developed and optimized in order to improve the quality of Sb_2Se_3 absorber film with reduced defect density. The efficiency of the Sb_2Se_3 solar cells is increased to 9.03%.
In addition, we have tried to replace the toxic CdS buffer layer with an environmentally friendly ZnSnO film with moreover a wider band gap. An interesting power conversion efficiency of 3.44% was achieved for the Cd-free Sb_2Se_3 thin-film solar cells.